

Applications and environmental impacts of carbon-based nanoparticles and microparticles

Shawninder Chahal

Department of Chemical Engineering

McGill University

Montreal, Canada

November 2022

A thesis submitted to McGill University in partial fulfillment of the requirements of the degree
of Doctor of Philosophy

© Shawninder Chahal 2022

Acknowledgements

I would like to thank Prof. Nathalie Tufenkji for her supervision and guidance over the years, both before and during my PhD studies. Her input and feedback always led to more thorough and comprehensive research. I would also like to thank past and present members of the Biocolloids and Surfaces Laboratory for their support over the years. Specifically, I would like to thank Jun-Ray Macairan, Nariman Yousefi, Laura M. Hernandez, and Hemanshu Anand for collaborating with me on several of my thesis projects. I would also like to thank Sara Matthews for teaching me how to work with fruit flies and Eva Roubeau Dumont for helpful discussions on statistical analysis methods and revising the French version of my thesis abstract.

Many collaborators from beyond the lab helped make this thesis possible. I would like to thank Prof. Rafik Naccache, Prof. Stéphane Bayen, Prof. Subhasis Ghoshal, Prof. Valérie Gravel, Peiyong Wang, and Vinicius Bueno for being great collaborators. I would also like to acknowledge Mohini Ramkaran for assistance with AFM imaging, David Liu and S Kelly Sears for assistance with TEM imaging, and Shimin Fan, Parghat Gopal, and Ilias Hader for assistance with setting up experiments at Macdonald Campus.

I would also like to acknowledge the various funding organizations that supported me throughout my PhD, particularly NSERC for a PGS D scholarship, McGill University for a MEDA fellowship, the EUL fund in the Department of Chemical Engineering, and EcotoQ (FRQNT).

I want to thank my family and friends for always supporting and encouraging me throughout my life.

Abstract

Carbon dots (CDs) are carbon nanoparticles typically less than 10 nm in size. They have similar properties to the widely studied quantum dots (QDs), which are semiconductor nanoparticles that have applications in a variety of fields, including bioimaging, photovoltaics, and light-emitting diodes to name a few. Cadmium-derived QDs are among the most popular, but their toxic nature has resulted in many jurisdictions imposing an outright ban on cadmium in consumer goods. While there has been increasing interest in CDs as a more sustainable alternative to QDs, there are considerable knowledge gaps regarding their optimal synthesis and potential *in vivo* toxicity.

In our first study, we optimized the stoichiometry of a green CD synthesis resulting in nitrogen-doped CDs with a quantum yield of 65 %. While our study confirmed the long-established viewpoint that nitrogen-doping can increase the quantum yield of CDs, we found that a model consisting only of the oxygen-to-carbon ratio and the fraction of total oxygen found in the CD's carboxyl groups was a better predictor of quantum yield than a model that implemented the nitrogen content of the CDs.

We then performed a direct comparison of the toxicity of nitrogen-doped and sulfur/nitrogen-codoped CDs with CdTeQDs in the fruit fly, *Drosophila melanogaster*. We found clear toxicity on larva-to-adult development with a half maximal effective concentration (EC₅₀) of 46 mg CdTeQD per kg food whereas no toxicity from the CDs was observed over the 10 – 100 mg/kg range studied. Moreover, no toxicity was observed in the reproductive performance, climbing ability, larvae crawling, mass, and locomotor activity of *Drosophila melanogaster* after exposure to a sublethal CD concentration of 100 mg/kg and a sublethal CdTeQD concentration of 5 mg/kg.

While CDs have the potential to increase the sustainability of many applications, they are still primarily found in a lab setting. Therefore, we examined another class of anthropogenic carbon-based material that is more widespread in the environment and consumer goods. In the environment, plastics can break down into microplastics and nanoplastics due to mechanical abrasion and UV irradiation. While extensive research has been done on aquatic microplastic pollution, few studies have researched the effects of microplastics in a terrestrial context. In our third study, we exposed *Drosophila melanogaster* to high-density polyethylene (HDPE) microplastics (<38 μm). Scanning electron microscopy also confirmed the presence of nano-sized HDPE (median size: 228 nm). We found that the HDPE did not negatively impact the reproductive performance of the flies over four generations and that the pupae raised on 100 mg/kg HDPE across all generations even had a 5.7 % higher eclosion fraction than those raised on control food. In addition, no toxicity was observed in the development of larvae into adults, climbing ability, larvae crawling, or mass.

Our final study examined the effect of HDPE microplastics (<1 mm) and eight common pharmaceutically active compounds found in wastewater on soil microbial community composition, soil enzyme activity, and strawberry plant growth. The experiments were performed outdoors over two growing seasons. We found that the compounds were able to significantly alter the soil microbial community composition but had no effect when mixed with 100 mg/kg HDPE, showing that the microplastics may have minimized their impact on the soil microbial community. We also found little-to-no effects on the soil enzyme activity and plant growth.

Overall, this work contributes to our understanding of the impact of anthropogenic carbon-based microparticles and nanoparticles in soil environments. This research advances our understanding on the sustainable synthesis and use of CDs as a less toxic alternative to QDs. It

also advances our understanding of the effects of microplastics and nanoplastics in terrestrial environments.

Résumé

Les points de carbone (PC) sont des nanoparticules de carbone de généralement moins de 10 nm ayant des propriétés semi-conductrice similaires aux points quantiques (PQ). Ils ont tous deux des applications dans une variété de domaines, tel que la bioimagerie, les photovoltaïques et les diodes électroluminescentes. Les PQ dérivés du cadmium sont parmi les plus populaires, mais leur utilisation dans les produits de consommation a été interdite à cause de leur toxicité. Bien qu'il y ait un intérêt croissant pour les PC en tant qu'alternative plus durable aux PQ, il existe un manque de connaissances concernant leur synthèse optimale et leur toxicité potentielle.

Dans une première étude, nous avons optimisé la stœchiométrie d'une synthèse de PC par des méthodes de chimie verte, produisant des PC dopés à l'azote avec un rendement quantique de 65 %. Nous avons découvert qu'un modèle composé uniquement du rapport oxygène-carbone et de la fraction d'oxygène total trouvée dans les groupes carboxyle des PC était un meilleur prédicteur du rendement quantique qu'un modèle qui implémentait la teneur en azote des PC.

Nous avons ensuite comparé la toxicité des PC dopés à l'azote, et dopés au soufre et à l'azote, avec les PQ CdTe chez *Drosophila melanogaster*. Le développement de la larve à l'adulte a été fortement impacté par les PQ CdTe, avec une concentration létale à 50 % (CL₅₀) de 46 mg/kg, mais aucune toxicité observée des PC avec des concentrations allant jusqu'à 100 mg/kg. Aucun effet n'a été observé dans les performances reproductives, la capacité d'escalade, le rampeement des larves, la masse et l'activité locomotrice après exposition à des concentrations sous-létales de 100 mg PC/kg et de 5 mg PQ CdTe/kg.

Bien que les PC aient le potentiel d'augmenter la durabilité de nombreuses applications, ils sont encore principalement trouvés dans des laboratoires. Par conséquent, nous avons examiné une autre classe de matériaux à base de carbone qui est plus répandue dans l'environnement et les

produits de consommation. Dans l'environnement, les plastiques peuvent se décomposer en microplastiques et nanoplastiques suite à l'abrasion mécanique et l'irradiation UV. Bien que des recherches approfondies aient été menées sur la pollution aquatique par les microplastiques, l'effets des microplastiques en milieu terrestre reste peu étudié. Dans une troisième étude, nous avons exposé *Drosophila melanogaster* à des microplastiques et nanoplastiques en polyéthylène haute densité (PEHD) (<38 µm). La présence de PEHD nanométrique (taille médiane : 228 nm) a également été confirmée par microscopie à balayage électronique. Nous avons trouvé que le PEHD n'avait pas d'impact négatif sur les performances de reproduction des mouches sur quatre générations, mais au contraire celles-ci avaient une fraction d'éclosion supérieure de 5,7 %. De plus, aucune toxicité n'a été observée dans le développement des larves en adultes, la capacité d'escalade, le rampelement des larves ou la masse.

Notre étude finale a examiné l'effet des microplastiques PEHD (<1 mm) et de huit composés pharmaceutique actifs présents dans les eaux usées, sur la composition de la communauté microbienne du sol, l'activité enzymatique du sol et la croissance des fraisiers. Les expériences ont été réalisées à l'extérieur durant deux étés. La composition de la communauté microbienne du sol a été significativement impactée par l'exposition aux composés chimiques, mais aucun effet n'a été trouvé lorsque ces mêmes composés étaient mélangés à 100 mg/kg de PEHD. Cela suggère que les microplastiques peuvent avoir minimisé leur impact sur la communauté microbienne du sol. Peu ou pas d'effets ont été observés sur l'activité enzymatique du sol et la croissance des plantes.

Table of contents

Acknowledgements.....	i
Abstract.....	ii
Résumé.....	v
Table of contents.....	vii
List of figures.....	xvi
List of tables.....	xxix
List of additional graphics	xxxii
List of abbreviations	xxxiii
Chapter 1: Introduction.....	1
1.1 Motivations for research.....	1
1.2 Research objectives	3
1.3 Contributions to original knowledge.....	4
1.4 Contributions of the authors.....	7
1.5 Background on microplastics toxicity in terrestrial environments.....	10
1.6 References	13
Preamble to Chapter 2.....	18
Chapter 2: Green synthesis of carbon dots and their applications	19
Abstract.....	19
Abstract Graphic	20

2.1 Introduction.....	20
2.2 Synthesis	21
2.2.1 What makes a synthesis green?.....	21
2.2.2 Green synthesis methods.....	22
2.2.3 Carbon source	24
2.2.4 Purification.....	26
2.3 Properties	27
2.3.1 Size.....	27
2.3.2 Optical properties.....	29
2.3.3 Chemical composition	31
2.4 Applications	34
2.4.1 Chemical sensing	34
2.4.2 Bioimaging.....	36
2.4.3 Biomedicine	38
2.4.4 Ink	38
2.4.5 Catalysis.....	39
2.5 Conclusions and outlook.....	40
Conflicts of interest.....	41
Acknowledgements.....	42
References.....	43

Electronic supplementary information.....	55
References.....	56
Preamble to Chapter 3.....	62
Chapter 3: Green synthesis of high quantum yield carbon dots from phenylalanine and citric acid:	
Role of stoichiometry and nitrogen doping	64
Abstract	64
Abstract Graphic	65
Synopsis	65
Keywords	65
3.1 Introduction.....	65
3.2 Experimental.....	67
3.2.1 Chemicals.....	67
3.2.2 Synthesis of Carbon Dots.....	68
3.2.3 Characterization	69
3.2.4 Quantum Yield.....	69
3.2.5 Ion Sensing.....	70
3.2.6 Statistical Analysis.....	71
3.3 Results and Discussion	71
3.3.1 Nitrogen Doping and Quantum Yield.....	71
3.3.2 Chemistry of CDs	74

3.3.3 Fluorescence and UV-Vis Spectroscopy	79
3.3.4 Structural Characterization of CDs	82
3.3.5 Ion Sensing.....	83
3.4 Conclusions.....	85
Acknowledgements.....	86
Supporting Information Content.....	86
References.....	87
Supporting Information.....	98
XPS Analysis	110
FTIR Analysis.....	111
Size Analysis.....	112
Preamble to Chapter 4.....	113
Chapter 4: A comparison of carbon dot and CdTe quantum dot toxicity in <i>Drosophila melanogaster</i>	114
Abstract.....	114
4.1 Introduction.....	115
4.2 Experimental.....	117
4.2.1 Synthesis of NCDs.....	117
4.2.2 Synthesis of SCDs.....	117
4.2.3 Purification of carbon and quantum dots.....	117

4.2.4	Characterization of carbon dots and quantum dots.....	118
4.2.5	<i>Drosophila melanogaster</i> husbandry.....	119
4.2.6	Larvae collection.....	119
4.2.7	Carbon dioxide anesthesia	120
4.2.8	Developmental toxicity	120
4.2.9	Sublethal toxicity assays	121
4.2.9.1	Reproductive performance assay	121
4.2.9.2	Larval crawling assay	122
4.2.9.3	Climbing and fly mass assay.....	122
4.2.9.4	Locomotor activity monitoring.....	123
4.2.10	Lightsheet imaging.....	123
4.2.11	Statistical analysis.....	124
4.3	Results and discussion	125
4.3.1	Characterization of carbon and quantum dots	125
4.3.2	Developmental toxicity	126
4.3.3	Reproductive performance.....	130
4.3.4	Fly mass assay.....	132
4.3.5	Larvae crawling and fly climbing assays.....	135
4.3.6	Locomotor activity.....	136
4.3.7	Nanoparticle uptake analysis	137

4.4 Conclusions.....	138
Acknowledgements.....	139
References.....	141
Supplementary information	147
Preamble to Chapter 5.....	156
Chapter 5: Multigenerational effects of weathered polyethylene microplastics on <i>Drosophila melanogaster</i>	157
Abstract.....	157
5.1 Introduction.....	158
5.2 Experimental.....	160
5.2.1 Preparation of weathered high-density polyethylene microplastics	160
5.2.2 Scanning electron microscopy	161
5.2.3 Fourier-transform infrared spectroscopy	161
5.2.4 Maintenance of <i>Drosophila melanogaster</i>	162
5.2.5 Developmental toxicity.....	163
5.2.6 Multigenerational reproductive assay	164
5.2.7 Larval crawling assay	165
5.2.8 Climbing assay.....	166
5.2.9 Fly mass measurements	166
5.2.10 Lightsheet fluorescence microscopy.....	167

5.2.11 Statistical analysis	168
5.3 Results and discussion	169
5.3.1 Size and imaging of microplastics	169
5.3.2 Fourier-transform infrared spectroscopy	170
5.3.3 Developmental toxicity	171
5.3.4 Multigenerational reproductive assay	175
5.3.5 Sublethal toxicity assays	180
5.3.6 Lightsheet fluorescence microscopy	182
5.4 Conclusions	184
Acknowledgements	185
References	186
Supplementary information	191
Preamble to Chapter 6	194
Chapter 6: Effect of emerging contaminants on soil microbial community composition, soil enzyme activity, and strawberry plant growth in polyethylene microplastic-containing soils...	195
Abstract	195
6.1 Introduction	196
6.2 Experimental	199
6.2.1 Production of high-density polyethylene microplastics	199
6.2.2 Preparation of contaminated soils	200

6.2.3 Strawberry field experiment	201
6.2.4 Soil sampling	202
6.2.5 Chemical contaminants analysis	202
6.2.6 Soil microbial community composition.....	204
6.2.7 Soil enzyme activity measurements.....	204
6.2.8 Strawberry plant growth	206
6.2.9 Statistical analysis.....	206
6.3 Results and discussion	208
6.3.1 Characterization of HDPE microplastics	208
6.3.2 Contaminant transport.....	209
6.3.3 Effect on soil microbial community composition.....	213
6.3.4 Effect on soil enzyme activity.....	218
6.3.5 Effect on strawberry plant growth	222
6.4 Conclusions.....	225
Acknowledgements.....	226
References.....	228
Supplementary information	239
Calculation of enzyme activity	252
Qiime2 commands	254
Significance tests	256

Chapter 7: Comprehensive discussion	264
7.1 Gaps in the green carbon dot synthesis literature	264
7.2 Understanding the relationship between carbon dot synthesis conditions, chemical structure, and optical properties	267
7.3 Relative toxicity of carbon dots and CdTe quantum dots in <i>Drosophila melanogaster</i> ...	270
7.4 Ecotoxicology of HDPE microplastics	272
7.5 References.....	277
Chapter 8: Conclusions and summary	279
Bibliography of non-manuscript chapters.....	284

List of figures

Figure 2.1. a) A diverse set of locally sourced renewable precursors can be used for the green synthesis of CDs. A reference list of these images can be found in Table S2.1 of the Electronic Supplementary Information (ESI). b) Sankey diagram showing the number of green-synthesized CD publications reporting various pathways from carbon source to CD. For this diagram, it is assumed that the purification steps followed the order: 1) filtration, 2) centrifugation, 3) dialysis, although this was not always the case, and this assumption was made for illustrative purposes only. A hybrid precursor indicates that both a renewable raw material and renewable refined compound were used. The most common synthesis route uses a renewable raw material in a hydrothermal synthesis followed by one or more purification steps. A reference list can be found in Table S2.2 of the ESI. 25

Figure 2.2. (a) HR-TEM images of CDs synthesized from black pepper (inset: lattice spacing). Adapted from Open Access ref⁴³. Copyright 2018 Vasimalai *et al.*; licensee Beilstein-Institut. (b) HR-TEM images of hollow CDs synthesized from bovine serum albumin. The hollow design allows for this CD to be used in drug delivery applications. Adapted with permission from ref⁴⁶. Copyright 2013 Elsevier Ltd. (c) Fluorescence spectra of a CD synthesized from maize at different excitation wavelengths. These CDs displayed green colour at their peak fluorescence emission. Adapted with permission from ref¹⁷. Copyright 2017 Springer Science Business Media Dordrecht. Empirical cumulative distribution function plots of (d) CD size as measured by TEM and (e) fluorescence quantum yield. (f) Peak excitation and emission wavelengths of green-synthesized CDs. Counts are shown next to their respective bins and indicate the number of publications reporting CDs with properties in that bin's range. Peak emission and excitation generally move in the same direction. A reference list can be found in Table S2.2 of the ESI. 28

Figure 2.3. (a, b, c, d, e) XPS spectra of CDs showing nitrogen and sulfur doping. The use of *Allium fistulosum* in synthesis gave access to an abundant and diverse set of biomolecules contained within the plant resulting in an elementally diverse CD with a high sulfur content. Reproduced from RSC ref ²⁵. Copyright 2019 the Centre National de la Recherche Scientifique (CNRS) and The Royal Society of Chemistry. (f) Plot showing the diverse range of the O:C and N:C ratios of green-synthesized CDs reported in the literature. Counts are shown next to their respective bins and indicate the number of publications reporting CDs with properties in that bin's range. N:C and O:C are atomic ratios. XPS data from publications were assumed to be in atomic percent whereas elemental data from other types of instrumentation were either explicitly stated as atomic ratios or converted from their mass ratios. A reference list can be found in Table S2.2 of the ESI..... 33

Figure 2.4. Zebrafish imaging using CDs synthesized from gynostemma. It is demonstrated that the probes localize in the digestive system. The CDs exhibit blue, green, or red fluorescence depending on the excitation source used. Reprinted with permission from ref ⁶⁵. Copyright 2019 American Chemical Society. 37

Figure 2.5. (a) Inkjet printing using CDs synthesized from oriental plane leaves. (b) Invisible pattern made from CD ink under visible light. (c, d, e, f) Fluorescent patterns made from CD ink under UV light. Scale bar = 1 cm. Reproduced from RSC ref ⁶⁸. Copyright 2013 The Royal Society of Chemistry..... 39

Figure 3.1. (a) Quantum yield of CDs vs phenylalanine mole fraction (balance is citric acid) in water at an excitation wavelength of 350 nm. (b) Nitrogen to carbon ratios for various phenylalanine mole fractions. Blue diamonds represent (N:C)_{CD}. Green curved line represents

(N:C)_R. Red line shows a linear trend for $0.05 \leq x_p \leq 0.90$. (c) Quantum Yield vs (N:C)_{CD} as determined by XPS. Error bars represent 2 standard errors of the mean (N=3). 72

Figure 3.2. FTIR spectra of (a) P₂₅-CDs, P₅₀-CDs, and P₇₅-CDs and (b) P₉₅-CDs and P₁₀₀-CDs. Dashed lines in (a) are to show alignment of peaks between CD types. Shaded regions in (b) are to highlight similarities and differences in certain regions. 76

Figure 3.3. Comparison of the actual QY (blue diamonds) to the QY calculated from Equation 3.4 (black line). 78

Figure 3.4. Fluorescence heat maps of (a) P₉₅-CDs and (b) P₁₀₀-CDs over a range of excitation and emission wavelengths using an excitation and emission slit width of 3 nm. Absorbance spectra of (c) P₉₅-CDs and P₁₀₀-CDs, and (d) P₂₅-CDs, P₅₀-CDs, and P₇₅-CDs. Fluorescence heat maps and absorbance spectra were normalized to their respective maximum peaks. 81

Figure 3.5. AFM images of (a) P₉₅-CDs and (b) P₁₀₀-CDs. TEM images of (c) P₉₅-CDs and (d) P₁₀₀-CDs. TEM images have been cropped to match the scale of AFM images. Uncropped images can be found in Figure S3.9. 82

Figure 3.6. Relative fluorescence of P₉₅-CDs exposed to a) 1000 μM of various ions and b) Fe³⁺ at various concentrations. Error bars show 2 standard errors of the mean (N=3). 84

Figure S3.1. C_{1s}, N_{1s}, and O_{1s} XPS peak deconvolution for a), d), g) P₂₅-CDs, b), e), h) P₅₀-CDs, and c), f), i) P₇₅-CDs, respectively. 101

Figure S3.2. C_{1s}, N_{1s}, and O_{1s} XPS peak deconvolution for a), c), e) P₉₅-CDs and b), d), f) P₁₀₀-CDs, respectively. 102

Figure S3.3. FTIR spectra of P₉₅-CDs and P₁₀₀-CDs. This figure shows the same data as Figure 3.2b, but the P₁₀₀-CD spectra has been normalized to match the peaks between the two CDs at ~3200 cm⁻¹ instead of at ~1100 cm⁻¹. 103

Figure S3.4. FTIR spectra of CDs, citric acid (CA), and phenylalanine (Phe). Normalized to each spectrum's most prominent peak.	104
Figure S3.5. Principal component analysis (PCA) of the 14-dimensional XPS data (<i>i.e.</i> (N:C) _{CD} and (O:C) _{CD} , and the relative amount of each bond type in the 5 C _{1s} features, 3 N _{1s} features, and 4 O _{1s} features) on the first two principal components (PCs). Percentage of total variance explained by each PC is indicated in brackets.....	105
Figure S3.6. Fluorescence heat maps of (a) P ₂₅ -CDs, (b) P ₅₀ -CDs, and (c) P ₇₅ -CDs, over a range of excitation and emission wavelengths using an excitation and emission slit width of 3 nm. Fluorescence heat maps were normalized to their respective maximum peaks.....	105
Figure S3.7. Fluorescence lifetime decay fit to a biexponential function of a) P ₉₅ -CD and P ₁₀₀ -CD and b) P ₉₅ -CD with and without 50 μM Fe ³⁺	106
Figure S3.8. Histogram of (a) P ₉₅ -CD and (b) P ₁₀₀ -CD size distribution from TEM.	106
Figure S3.9. Original TEM images of (a) P ₉₅ -CDs and (b) P ₁₀₀ -CDs as shown in Figure 3.5c,d.	107
Figure S3.10. Raman spectrum of P ₉₅ -CDs. The fluorescence from the CDs is obscuring the Raman signal.	107
Figure S3.11. Relative fluorescence of P ₉₅ -CDs exposed to Fe ³⁺ and Pd ²⁺	108
Figure S3.12. Fe ³⁺ sensing data in the form of a) fluorescence emission spectra at an excitation wavelength of 350 nm and b) absorbance spectra.	108
Figure S3.13. Absorbance of Fe ³⁺ and fluorescence of P ₉₅ -CDs. All spectra are normalized to their respective maximum. P ₉₅ -CD excitation spectra was performed at an emission wavelength of 376 nm. P ₉₅ -CD emission spectra was performed at an excitation wavelength of 350 nm.	109

Figure 4.1. Number of (a) pupae and (b) flies that emerged from approximately twenty first instar larvae raised on 0, 10, 40, 70, or 100 mg/kg NCD, SCD, or CdTeQD treated food by day 14. The mean (c) pupation and (d) eclosion time of the pupae and flies in (a) and (b), respectively. Grey squares represent the mean of data points in that column and error bars represent $2 \times$ the standard error of the mean. Legend labels have the format X-Y where X is the treatment and Y is the experimental block ID..... 128

Figure 4.2. Number of (a) pupae and (b) flies that emerged after allowing one female and one male fly that were raised on CTRL (0 mg/kg), NCD (100 mg/kg), SCD (100 mg/kg), or CdTeQD (5 mg/kg) treated food to mate for 10 days. Grey squares represent the mean of data points in that column and error bars represent $2 \times$ the standard error of the mean. Legend labels have the format X-Y where X is the treatment and Y is the experimental block ID..... 132

Figure 4.3. Average mass of (a) female and (b) male flies that were raised on CTRL (0 mg/kg), NCD (100 mg/kg), SCD (100 mg/kg), or CdTeQD (5 mg/kg) treated food. Grey squares represent the mean of data points in that column and error bars represent $2 \times$ the standard error of the mean. Legend labels have the format X-Y where X is the treatment and Y is the experimental block ID. 134

Figure 4.4. (a) Average number of larval contractions per minute and (b) fraction of flies able to climb 10 cm within 10 s. Larvae and flies were raised on CTRL (0 mg/kg), NCD (100 mg/kg), SCD (100 mg/kg), or CdTeQD (5 mg/kg) treated food. Grey squares represent the mean of data points in that column and error bars represent $2 \times$ the standard error of the mean. Legend labels have the format X-Y where X is the treatment and Y is the experimental block ID..... 135

Figure 4.5. Locomotor activity measured as average number of infrared beam breaks per day of male flies raised on CTRL (0 mg/kg), NCD (100 mg/kg), SCD (100 mg/kg), or CdTeQD (5 mg/kg)

treated food. Grey squares represent the mean of data points in that column and error bars represent $2 \times$ the standard error of the mean. The standard errors are relatively small due to the large sample size and may be difficult to see in the figure. Legend labels have the format X-Y where X is the treatment and Y is the experimental block ID. 137

Figure 4.6. Lightsheet images of female flies from day 11 raised on a) CTRL (0 mg/kg), b) CdTeQD (5 mg/kg), c) NCD (100 mg/kg), or d) SCD (100 mg/kg) treated food. Red light shows fluorescence from SCD and CdTeQDs. Blue fluorescence is from the fly's autofluorescence. NCDs also emit blue light and are therefore not easily visible..... 138

Figure S4.1. TEM images of a) NCDs and b) SCDs. Insets show their respective size distributions. 147

Figure S4.2. FTIR spectra of CdTeQDs, NCDs, and SCDs. 147

Figure S4.3. XPS spectra of NCDs showing a) survey scan, b) C_{1s} spectra, c) O_{1s} spectra, and d) N_{1s} spectra. 148

Figure S4.4. XPS spectra of SCDs showing a) survey scan, b) C_{1s} spectra, c) O_{1s} spectra, d) N_{1s} spectra, and e) S_{2p} spectra. 149

Figure S4.5. Fluorescence spectra of CdTeQDs, NCDs, and SCDs. The CdTeQDs were excited under 561 nm light, whereas the NCDs and SCDs were excited under 405 nm. 150

Figure S4.6. UV-Vis spectra of CdTeQDs, NCDs, and SCDs. 151

Figure S4.7. Number of (a) pupae and (b) flies that emerged from approximately twenty first instar larvae raised on 0, 10, 40, 70, or 100 mg/kg CdTeQD treated food by day 14. Squares represent the mean of data points in that column and error bars represent $2 \times$ the standard error of the mean. Legend labels have the format X-Y where X is the treatment and Y is the experimental block ID. Red curve represents the Hill equation that was fit to the corresponding data. 152

Figure S4.8. Eclosion fraction representing the fraction of pupae raised on 0, 10, 40, 70, or 100 mg/kg NCD, SCD, or CdTeQD treated food that successfully eclosed into flies by day 14. Grey squares represent the mean of data points in that column and error bars represent $2 \times$ the standard error of the mean. Legend labels have the format X-Y where X is the treatment and Y is the experimental block ID..... 153

Figure S4.9. The mean (c) pupation and (d) eclosion time of the pupae and flies that emerged from approximately twenty first instar larvae raised on 0, 10, 40, 70, or 100 mg/kg SCD, or CdTeQD treated food by day 14. Squares represent the mean of data points in that column and error bars represent $2 \times$ the standard error of the mean. Legend labels have the format X-Y where X is the treatment and Y is the experimental block ID. Lines represents a linear regression that was fit to the corresponding data. 154

Figure S4.10. Number of (a) pupae and (b) flies that emerged after allowing one female and one male fly that were raised on CTRL (0 mg/kg), NCD (100 mg/kg), SCD (100 mg/kg), or CdTeQD (5 mg/kg) treated food to mate over 10 days. Grey squares represent the mean of data points in that column and error bars represent $2 \times$ the standard error of the mean. Legend labels have the format X-Y where X is the treatment and Y is the experimental block ID. 155

Figure 5.1. (a) SEM image showing nano-sized HDPE fragments. (a-inset) Size distribution of 2495 microplastic fragments taken from eight SEM images at $2500\times$ magnification. The fragments likely formed during mechanical and/or UV weathering. We note that this histogram does not cover the entire distribution of the microplastics used in this study, but instead focuses on the distribution of sub-micrometer sized plastic particles. (b) SEM image showing aggregated HDPE microplastics. (c) Dark-field microscopy image of HDPE microplastics..... 170

Figure 5.2. Total number of (a) pupae and (b) flies that emerged from approximately 20 *Drosophila melanogaster* 1st instar larvae raised in control (CTRL) food or food containing 0.1, 1, 10, or 100 mg HDPE microplastics per kg food. Mean (c) pupation and (d) eclosion time of the same eggs described in (a) and (b), respectively. Legend labels are formatted as X-Y, where X is the treatment, and Y is the experimental block ID. Grey squares represent the mean value of all markers that appear in that column and error bars represent $2 \times$ the standard error of the mean. 173

Figure 5.3. Total number of (a) pupae and (b) flies that emerged from approximately 20 *Drosophila melanogaster* 1st instar larvae raised in control (CTRL) food or food containing 1000 or 10 000 mg HDPE microplastics per kg food after 14 days. Mean (c) pupation and (d) eclosion time of the same eggs described in (a) and (b), respectively. Legend labels are formatted as X-Y, where X is the treatment, and Y is the experimental block ID. Grey squares represent the mean value of all markers that appear in that column and error bars represent $2 \times$ the standard error of the mean. 174

Figure 5.4. Total number of (a) pupae and (b) flies that emerged from eggs laid by a *Drosophila melanogaster* mating pair over 4 days. The eggs were laid and raised on control (CTRL) food or food containing 100 mg HDPE microplastics per kg food. The pupae and flies were monitored over 16 days starting when the mating pair was first isolated and transferred to their respective test tube. Mean (c) pupation and (d) eclosion time of the same eggs described in (a) and (b), respectively. Legend labels are formatted as X-Y, where X is the stream ID as indicated in Table 5.1, and Y is the experimental block ID. Grey squares represent the mean value of all markers that appear in that column and error bars represent $2 \times$ the standard error of the mean. The flies were monitored over 4 generations..... 178

Figure 5.5. (a) Average number of contractions per minute for larvae. (b) The fraction of flies able to climb 10 cm within 10 s. The average mass of (c) female and (d) male flies. Larvae and flies were raised on control (CTRL) food or food containing 100 mg HDPE microplastics per kg food. Larvae were sampled 4 days after eggs were laid. Adult flies were sampled 11 days after eggs were laid. Legend labels are formatted as X-Y, where X is the treatment, and Y is the experimental block ID. Grey squares represent the mean value of all markers that appear in that column and error bars represent $2 \times$ the standard error of the mean. 181

Figure 5.6. Lightsheet images of female flies (day 10) raised on (a) control and (b) 10 000 mg/kg HDPE food. The red signal represents HDPE and is found mainly on the surface of the flies.. 183

Figure S5.1. FTIR spectra from: HDPE suspension filtrate which passed through a 0.2 μ m filter, unweathered HDPE microplastics, and UV weathered HDPE microplastics. The spectra of all samples were virtually identical and consistent with the spectra for HDPE. “HDPE Unweathered” and “HDPE Weathered” spectra were measured three times and one spectra from each was selected to show here as a representative sample. “HDPE Filtrate” spectra was measured once. 191

Figure S5.2. Eclosion fraction of *Drosophila melanogaster* that were raised on (a) 0, 0.1, 1, 10, or 100 mg/kg HDPE microplastics and (b) 0, 1000, or 10 000 mg/kg HDPE microplastics. Legend labels are formatted as X-Y, where X is the treatment, and Y is the experimental block ID. Grey squares represent the mean value of all markers that appear in that column and error bars represent $2 \times$ the standard error of the mean. Eclosion fraction is defined here as the fraction of pupae that successfully eclosed into adult flies..... 192

Figure S5.3. Eclosion fraction of *Drosophila melanogaster* that were raised on three streams of food treatments (Table 5.1). Legend labels are formatted as X-Y, where X is the stream ID as indicated in Table 5.1, and Y is the experimental block ID. Grey squares represent the mean value

of all markers that appear in that column and error bars represent $2 \times$ the standard error of the mean. The flies were monitored over 4 generations. Eclosion fraction is defined here as the fraction of pupae that successfully eclosed into adult flies. 193

Figure 6.1. Leachate mass data for (a) gemfibrozil, (b) triclosan, (c) carbamazepine, and (d) sulfamethoxazole in control (CTRL), chemical contaminants + 100 mg HDPE microplastic kg^{-1} soil (CP100), and chemical contaminants (C) treated soils. No leachate data was collected for the intervals including day 52 – 363, 392 – 456. For each timepoint, treatments with the same letter have no significant difference between them. Markers represent individual replicates. Grey squares represent the means. Error bars show $2 \times$ the standard error of the mean. 211

Figure 6.2. Concentration of (a) gemfibrozil, (b) triclosan, (c) carbamazepine, and (d) sulfamethoxazole in control (CTRL), chemical contaminants + 100 mg HDPE microplastic kg^{-1} soil (CP100), and chemical contaminants (C) treated soils. For each timepoint, treatments with the same letter have no significant difference between them. Markers represent individual replicates. Grey squares represent the means. Error bars show $2 \times$ the standard error of the mean. 212

Figure 6.3. Soil microbial community composition based on the relative abundance of phyla found in control (CTRL), 10 mg HDPE microplastic kg^{-1} soil (P10), 100 mg HDPE microplastic kg^{-1} soil (P100), chemical contaminants + 100 mg HDPE microplastic kg^{-1} soil (CP100), and chemical contaminants (C) treated soils. PRE (pre-treatment) is a composite sample of the uncontaminated soils. Row labels have the following nomenclature: A-B-C, where A is the treatment, B is the replicate ID, and C is the timepoint. 214

Figure 6.4. Principal coordinate analysis (PCoA) of the weighted UniFrac distance of the soil microbial communities' ASVs in control (CTRL), 10 mg HDPE microplastic kg^{-1} soil (P10), 100 mg HDPE microplastic kg^{-1} soil (P100), chemical contaminants + 100 mg HDPE microplastic kg^{-1}

¹ soil (CP100), and chemical contaminants (C) treated soils. PRE (pre-treatment) is a composite sample of the uncontaminated soils. Ellipses represent the zone where 95 % of samples from a bivariate normal distribution with the same mean and covariance matrix as the respective treatment would be drawn from. Numbers in brackets indicate the amount of variance captured by that principal coordinate (PC)..... 216

Figure 6.5. (a) β -glucosidase, (b) chitinase, and (c) xylan 1,4- β -xylosidase activities over the course of two growing seasons in control (CTRL), 10 mg HDPE microplastic kg⁻¹ soil (P10), 100 mg HDPE microplastic kg⁻¹ soil (P100), chemical contaminants + 100 mg HDPE microplastic kg⁻¹ soil (CP100), and chemical contaminants (C) treated soils. For each time point, treatments with the same letter have no significant difference between them. Markers represent individual replicates. Grey squares represent the means. Error bars show 2 × the standard error of the mean. 220

Figure 6.6. (a) Dry biomass of the remaining plant without any strawberry fruit, (b) total yield of fresh strawberries, (c) number of leaves, and (d) number of flower stalks in control (CTRL), 10 mg HDPE microplastic kg⁻¹ soil (P10), 100 mg HDPE microplastic kg⁻¹ soil (P100), chemical contaminants + 100 mg HDPE microplastic kg⁻¹ soil (CP100), and chemical contaminants (C) treated soils. For each time point, treatments with the same letter have no significant difference between them. Markers represent individual replicates. Grey squares represent the means. Error bars show 2 × the standard error of the mean. 223

Figure S6.1. Top-down view of outdoor layout of strawberry pots (green rectangles)..... 243

Figure S6.2. Approximate location of strawberry plants, irrigation, and soil sampling in each pot. The mixing was performed in an aluminum tray near the pot, before being transferred to glassware for transportation and further analysis in a lab setting..... 244

Figure S6.3. Fluorescence of 4-methylumbelliferone (MUB) in buffer at various concentrations and after NaOH addition. This plot shows that the fluorescence of MUB is linearly correlated to its concentration when the MUB concentration is below 1.92 μM . The highest concentration shown here is equivalent to Well C in Table S6.6. 245

Figure S6.4. Images of HDPE microplastics taken under a stereomicroscope in dark-field mode. 246

Figure S6.5. Leachate mass data for (a) acetaminophen, (b) caffeine, (c) ibuprofen, and (d) sulfanilamide in control (CTRL), chemical contaminants + 100 mg HDPE microplastic kg^{-1} soil (CP100), and chemical contaminants (C) treated soils. No leachate data was collected for the intervals including day 52 – 363, 392 – 456. For each timepoint, treatments with the same letter have no significant difference between them. Markers represent individual replicates. Grey squares represent the mean. Error bars show $2 \times$ the standard error of the mean. 247

Figure S6.6. Concentration of (a) acetaminophen, (b) caffeine, and (c) ibuprofen in control (CTRL), chemical contaminants + 100 mg HDPE microplastic kg^{-1} soil (CP100), and chemical contaminants (C) treated soils. For each timepoint, treatments with the same letter have no significant difference between them. Markers represent individual replicates. Grey squares represent the mean. Error bars show $2 \times$ the standard error of the mean. 248

Figure S6.7. Shannon’s diversity index of control (CTRL), 10 mg HDPE microplastic kg^{-1} soil (P10), 100 mg HDPE microplastic kg^{-1} soil (P100), chemical contaminants + 100 mg HDPE microplastic kg^{-1} soil (CP100), and chemical contaminants (C) treated soils. PRE (pre-treatment) is a composite sample of the uncontaminated soils. For each timepoint, treatments with the same letter have no significant difference between them. No letters are present for PRE, since there were

no other treatments to compare it to on day 0. Markers represent individual replicates. Grey squares represent the mean. Error bars show $2 \times$ the standard error of the mean. 249

Figure S6.8. Principal coordinate analysis (PCoA) of the weighted UniFrac distance of the soil microbial communities' amplicon sequence variants in control (CTRL), 10 mg HDPE microplastic kg^{-1} soil (P10), 100 mg HDPE microplastic kg^{-1} soil (P100), chemical contaminants + 100 mg HDPE microplastic kg^{-1} soil (CP100), and chemical contaminants (C) treated soils. PRE (pre-treatment) is a composite sample of the uncontaminated soils. Ellipses represent the zone where 95 % of samples from a bivariate normal distribution with the same mean and covariance matrix as the respective treatment would be drawn from. Numbers in brackets indicate the amount of variance captured by that principal coordinate (PC). This figure shows the same data as Figure 6.4, but with markers representing treatments and colour representing time to better illustrate the temporal effects on the microbial community composition. 250

Figure S6.9. Phosphatase activity over the course of two growing seasons in control (CTRL), 10 mg HDPE microplastic kg^{-1} soil (P10), 100 mg HDPE microplastic kg^{-1} soil (P100), chemical contaminants + 100 mg HDPE microplastic kg^{-1} soil (CP100), and chemical contaminants (C) treated soils. Day 6 and 35 data were omitted due to a potential contamination of the MUB-linked substrates. For each timepoint, treatments with the same letter have no significant difference between them. Markers represent individual replicates. Grey squares represent the mean. Error bars show $2 \times$ the standard error of the mean. 251

List of tables

Table 2.1. Processing parameters and properties of CDs synthesized by green methods.	23
Table 2.2. Summary of the sensing properties of green-synthesized CDs.	35
Table S2.1. References for images in Figure 2.1. All images are in the public domain.....	55
Table S2.2. References for data shown in Figures 2.1b, 2.2d, 2.2e, 2.2f, 2.3f.	55
Table S3.1. Synthesis concentrations at various phenylalanine mole fractions.	98
Table S3.2. Summary of the elemental composition of CDs, on the basis of carbon (C), nitrogen (N), and oxygen (O). Uncertainties show 2 standard errors of the mean (N = 3).	98
Table S3.3. XPS data. Relative amount of sp^2 , sp^3 , C-N/C-O, C=N/C=O, and O-C=O groups from the deconvolution of C_{1s} peaks. Relative amount of C-NH-C/pyridinic N, C-N(C)-C/N-C=O/pyrrolic N, and $-NH_3^+$ /graphitic N groups from the deconvolution of N_{1s} peaks. Relative amount of COOH, C=O, C-O, and C-OH groups from the deconvolution of O_{1s} peaks. Uncertainties show 2 standard errors of the mean (N = 3).	99
Table S3.4. Table of parameters and corresponding coefficient of determination (R^2) of the function: $QY = \beta_0 + \beta_1z_1 + \beta_2z_2 + \beta_3z_3 + \beta_4z_1z_2$ where z_i is the standard score of: (i=1) (O:C) _{CD} , (i=2) relative amount of COOH oxygen (from O_{1s} spectra), and (i=3) (N:C) _{CD}	100
Table S3.5. Table of means (μ_i) and standard deviations (σ_i) for the features: (i=1) (O:C) _{CD} , (i=2) relative amount of COOH oxygen (from O_{1s} spectra), and (i=3) (N:C) _{CD} . Values are used to calculate the standard score (z_i) as follows: $z_i = \frac{x_i - \mu_i}{\sigma_i}$ where x_i is the real value of: (i=1) (O:C) _{CD} , (i=2) relative amount of COOH oxygen (from O_{1s} spectra), and (i=3) (N:C) _{CD}	100
Table 5.1. There are three treatment streams. This table shows the type of food, <i>i.e.</i> , control (CTRL) or 100 mg/kg HDPE, each generation was fed for each stream. For example, BF1 flies were raised on 100 mg kg ⁻¹ HDPE microplastics from egg to adult.	165

Table 6.1. Size distribution on a mass basis of HDPE microplastics in both years of the study. Microplastics were first passed through a ~1 mm mesh size sieve before further use.	208
Table S6.1. Chemical contaminants stock solution.	239
Table S6.2. Spiked chemical contaminant concentration [mg per kg fresh soil] in C and CP100 pots and their octanol-water partition coefficient ($\log K_{OW}$), molar mass, and chemical structure.	240
Table S6.3. The composition of the fertilizer used on soils.	241
Table S6.4. Enzyme and substrate pairings. (MUB = 4-methylumbelliferyl)	241
Table S6.5. Weighted UniFrac distance of the soil microbial communities' amplicon sequence variants pairwise PERMANOVA results for control (CTRL), 10 mg HDPE microplastic kg^{-1} soil (P10), 100 mg HDPE microplastic kg^{-1} soil (P100), chemical contaminants + 100 mg HDPE microplastic kg^{-1} soil (CP100), and chemical contaminants (C) treated soils. PRE (pre-treatment) is a composite sample of the uncontaminated soils. $q < 0.05$ is significant.	242
Table S6.6. Each plate contained the following types of wells.	253
Table S6.7. Significance testing for contaminants leachate samples found in Figures 6.1 and S6.5. HB = Holm-Bonferroni.	256
Table S6.8. Significance testing for contaminants soil samples found in Figures 6.2 and S6.6. HB = Holm-Bonferroni.	258
Table S6.9. Post hoc analysis for contaminants soil samples found in Figure 6.2.	258
Table S6.10. Significance testing for enzyme activities found in Figures 6.5 and S6.9. HB = Holm-Bonferroni.	259
Table S6.11. Post hoc analysis for enzyme activities found in Figures 6.5 and S6.9.	260

Table S6.12. Significance testing for plant growth found in Figure 6.6. HB = Holm-Bonferroni, LUT = Lookup table. 260

Table S6.13. Significance testing for Shannon entropy found in Figure S6.7. HB = Holm-Bonferroni. 261

Table S6.14. Significance testing for phylum-level relative abundance found in Figure 6.3. HB = Holm-Bonferroni..... 261

Table S6.15. Post hoc analysis for phylum-level relative abundance found in Figure 6.3..... 263

List of additional graphics

Abstract graphic 2.1. A visual depiction of the abstract for Chapter 2.....	20
Abstract graphic 3.1. A visual depiction of the abstract for Chapter 3.....	65
Scheme 3.1 Proposed mechanism of the initial synthesis steps for the reaction of citric acid and phenylalanine.	68

List of abbreviations

Abbreviation	Full name
(N:C) _{CD}	nitrogen-to-carbon atomic ratio of the carbon dots
(N:C) _R	nitrogen-to-carbon atomic ratio of the reactants
(O:C) _{CD}	oxygen-to-carbon atomic ratio of the carbon dots
(O:C) _R	oxygen-to-carbon atomic ratio of the reactants
AFM	atomic force microscopy
AI	absorbance increase
ANOVA	analysis of variance
ASV	amplicon sequence variant
C	chemical contaminants
CA	citric acid
CD	carbon dot
CdTeQD	cadmium telluride quantum dot
CP100	chemical contaminants + 100 mg HDPE microplastic kg ⁻¹ soil
CTRL	control
EC	Enzyme Commission (number) (Chapter 6)
EC ₁	1 % maximal effective concentration
EC ₅₀	Half maximal effective concentration
EDTA	ethylenediaminetetraacetic acid
ESI	electronic supplementary information (Chapter 2) electrospray ionization (Chapter 6)
F0	parental flies
F1	1 st filial generation
F2	2 nd filial generation
F3	3 rd filial generation
F4	4 th filial generation
FI	fluorescence increase
FQ	fluorescence quenching

FTIR	Fourier-transform infrared (spectroscopy)
HCD	hollow carbon dot
HDPE	high-density polyethylene
HPLC	high-performance liquid chromatography
HR-TEM	high resolution transmission electron microscopy
IC ₅₀	half maximal inhibitory concentration
IDL	instrument detection limit
K _{ow}	octanol-water partition coefficient
LC ₅₀	lethal concentration, 50 %
LD ₅₀	lethal dose, 50 %
LDPE	low-density polyethylene
LOD	limit of detection
<i>m/z</i>	mass-to-charge ratio
MKP	monopotassium phosphate
MUB	4-methylumbelliferone / 4-methylumbelliferyl-(linked)
N:C	nitrogen-to-carbon (atomic ratio)
NCD	nitrogen-doped carbon dots
O:C	oxygen-to-carbon (atomic ratio)
P:C	phosphorus-to-carbon (atomic ratio)
P10	10 mg HDPE microplastic kg ⁻¹ soil
P100	100 mg HDPE microplastic kg ⁻¹ soil
P ₀ -CD	carbon dots synthesized from a solute containing 0 mol% phenylalanine
P ₅ -CD	carbon dots synthesized from a solute containing 5 mol% phenylalanine
P ₁₀ -CD	carbon dots synthesized from a solute containing 10 mol% phenylalanine
P ₂₅ -CD	carbon dots synthesized from a solute containing 25 mol% phenylalanine
P ₅₀ -CD	carbon dots synthesized from a solute containing 50 mol% phenylalanine
P ₇₅ -CD	carbon dots synthesized from a solute containing 75 mol% phenylalanine
P ₉₀ -CD	carbon dots synthesized from a solute containing 90 mol% phenylalanine

P ₉₅ -CD	carbon dots synthesized from a solute containing 95 mol% phenylalanine
P ₁₀₀ -CD	carbon dots synthesized from a solute containing 100 mol% phenylalanine
PC	principal component/coordinate
PCA	principal component analysis
PCoA	principal coordinate analysis
PCR	polymerase chain reaction
PERMANOVA	permutational multivariate analysis of variance
PET	polyethylene terephthalate
Phe	phenylalanine
PRE	pre-treatment
PTFE	polytetrafluoroethylene
PVC	polyvinyl chloride
PVDF	polyvinylidene fluoride
QD	quantum dot
QY	quantum yield
R ²	coefficient of determination
RO	reverse osmosis
S:C	sulfur-to-carbon (atomic ratio)
SCD	sulfur, nitrogen co-doped carbon dots
SEM	scanning electron microscopy
SI	supporting/supplementary information
TEM	transmission electron microscopy
TPC	meso-tetraphenylchlorin
UV	ultraviolet
x_p	phenylalanine mole fraction
XPS	X-ray photoelectron spectroscopy
λ_{em}	emission wavelength
λ_{ex}	excitation wavelength

Chapter 1: Introduction

1.1 Motivations for research

Carbon-based nanoparticles and microparticles have been gaining attention recently, both as a potentially less toxic alternative to certain metallic nanoparticles¹ and due to their occurrence in terrestrial environments.² Whereas some heavy metal nanoparticles have shown to exhibit toxicity greater than their respective ions,³ the environmental impact of carbon-based particles in terrestrial environments is less clear. This thesis examines the applications and environmental impacts of two classes of carbon-based nanoparticles and microparticles, carbon dots (CDs) and high-density polyethylene (HDPE) microplastics.

Carbon dots are carbon nanoparticles typically less than 10 nm in size and share many similar properties to quantum dots (QDs) which are typically derived from heavy metals. Both are well known for their visible light fluorescence and superior resistance to photobleaching when compared to organic dyes.⁴ They also find themselves used for a variety of applications including bioimaging,⁵ chemical sensing,⁶ photovoltaics,⁷ light-emitting diodes,⁸ catalysis,⁹ and more. Some of the most popular and widely studied QDs are those derived from cadmium. Notably, CdTeQDs are highly customizable with well established methods for functionalizing their surface and controlling their size which in turn controls their peak excitation and emission wavelengths. However, these remarkable features come at a cost. Cadmium is known to be highly toxic,¹⁰ and as a result faces restrictions or outright bans in many jurisdictions for use in commercial goods.¹¹ CDs are an attractive alternative to Cd-derived QDs since they typically have considerably lower toxicity.¹ Moreover, due to their carbon-based nature, they are increasingly being synthesized from renewable raw materials such as plants without the need for any solvents other than water.¹² However, CDs have their fair share of drawbacks. While the fluorescence mechanism of QDs is

thoroughly understood to derive from the quantum confinement effect, as made evident by the size dependence of its peak fluorescence wavelength, the underlying mechanisms for CD fluorescence remain unclear, with most CDs exhibiting a peak fluorescence in the blue to green region of the visible light spectrum. It also remains unclear why some CDs have very high fluorescence quantum yields, whereas others are very low. These shortcomings prevent CDs from replacing more tunable, heavy metal based QDs. Another concern is that although CDs are known to have less toxicity than Cd-derived QDs, they are not entirely nontoxic. Few studies directly compare the toxicity of CDs and QDs under similar conditions to assess their relative toxicity.

While CDs are a remarkable class of nanoparticles with the potential to be used in a variety of applications, they are not widely used in consumer products or industrial processes and as a result, they are not currently widespread in our environment. However, another anthropogenic carbon-based material is found in virtually every sector of the economy and our daily lives. Plastics have become ubiquitous in our environment due to the fact that the vast majority of plastic is either released into the environment or ends up in a landfill upon disposal.¹³ Over time these plastics degrade, breaking down into smaller particles.¹⁴ Although definitions vary, microplastics are generally considered to be plastic particles ~1 – 5000 μm in size,¹⁵ whereas smaller particles are sometimes referred to as nanoplastics. While much of the global effort against microplastic pollution is focused on their effects in aquatic environments such as oceans, recent advances in detection methods have revealed that the majority of microplastic pollution is found in terrestrial environments.² Of particular concern is how this microplastic pollution can affect agriculture. When microplastics enter wastewater streams, they make their way to wastewater treatment plants where they are often settled out in sewage sludge.¹⁶ This microplastic-containing sludge is then treated and converted into biosolids which can then be applied to agricultural soils as fertilizer.¹⁷

While research investigating the ecotoxicology of nanoplastics and microplastics has become increasingly common, many studies are centered around commercially available polystyrene beads due to their widespread availability. While this is a good starting point for the literature as a whole, there exists a wide array of polymers, sizes, and shapes, that make up microplastics that require further investigation. Moreover, due to their route of entry into agricultural soils *via* wastewater, they are often found in conjunction with many common pharmaceutically active compounds such as household drugs and antibiotics. While it is important to measure the toxicity of microplastics themselves, we also need to understand their interactions with other compounds known for inducing biological responses. Moreover, since macroplastics are often viewed as having little-to-no toxicity, the effect of nanoplastics and microplastics should therefore be investigated over a longer duration to see if trends that were not observed in acute exposure studies begin to emerge under chronic exposure conditions.

1.2 Research objectives

The goal of this thesis is to:

- Conduct a thorough literature review on the green synthesis of CDs and identify the knowledge gaps that must be filled to bring their performance and tunability on par with CDs synthesized from non-renewable precursors.
- Identify the role that reactant stoichiometry plays in determining the chemical structure of CDs and the role that the resulting chemical structure plays in fluorescence quantum yield.
- Perform a direct comparison of the toxicity of nitrogen-doped and sulfur/nitrogen-codoped CDs with CdTe QDs in the model organism *Drosophila melanogaster*.

- Evaluate the effects of acute and chronic HDPE microplastic exposure on *Drosophila melanogaster*.
- Determine the long-term effects of HDPE microplastic exposure on soil microbial community composition, soil enzyme activity, and strawberry plant growth and assess their ability to amplify or inhibit a biological response from pharmaceutically active compounds.

1.3 Contributions to original knowledge

This thesis aims to make considerable contributions towards filling current knowledge gaps surrounding the sustainability of anthropogenic carbon-based nanoparticles and microparticles. Chapter 2 consists of a comprehensive literature review on the green synthesis of CDs and their applications. It concludes with an outlook of the field and suggestions of where future research should be directed to close the knowledge gap between green synthesized CDs and those synthesized from non-renewable compounds. This can be achieved by better understanding how the precursors and synthesis conditions used impact the chemical structure and size of the CD, and then how chemical structure and size may impact the ability of CDs to perform in various applications. Chapter 3 is an investigation of the role of reactant stoichiometry and nitrogen doping on the fluorescence quantum yield of CDs. In a green synthesis involving nine different ratios of citric acid and phenylalanine, an optimal ratio was found which produced CDs with a quantum yield of 65 %. While it has been well established in the CD literature that nitrogen-doping typically increases quantum yield,¹⁸ this work showed that while quantum yield can increase with nitrogen content in the CD, it is not always the case. A model was constructed from the resulting CDs' chemical structures as determined by X-ray photoelectron spectroscopy which found that minimizing the oxygen-to-carbon ratio and the fraction of oxygen contained in carboxyl groups

would increase the quantum yield of the CDs. The resulting CDs were also shown to function as Fe³⁺ sensors.

Many studies have examined the toxicity of CDs and QDs, but few have compared the two directly in parallel. Moreover, it is important to note that while CDs are considered less toxic than CdTeQDs they are by no means non-toxic and in sufficiently high concentrations can induce a toxic response depending on their chemical structure. Therefore, although it is important to examine their toxicity under a variety of conditions, it is also necessary to have a positive control in the form of a substance that the CD is presumably trying to replace in some application. Chapter 4 directly compares the toxicity of nitrogen-doped and sulfur/nitrogen-codoped CDs with that of CdTeQDs in the model organism *Drosophila melanogaster*. By performing the comparison under the same conditions, the relative toxicity of the nanoparticles can be better assessed. In general, there was no toxicity observed from the CDs in the 10 – 100 mg/kg range evaluated, but the CdTeQDs had an EC₅₀ of 46 mg/kg food and induced considerable developmental delays. This allows us to put into perspective the extent to which CDs may be safer to use than CdTeQDs.

Chapter 5 shifts focus to a type of anthropogenic carbon-based particle that is more prevalent in the environment. While many studies have examined the toxicity of nanoplastics and microplastics, the field has largely focussed on studying the effects of polystyrene nanobeads and microbeads on aquatic organisms. This is in stark contrast to the fact that the majority of microplastic pollution is found in terrestrial environments,² and that most plastics are made of polyethylene or polypropylene.¹³ Moreover, microplastics found in the environment typically consist of a variety of shapes and sizes, whereas commercial beads tend to have a spherical shape and a more uniform size distribution. In addition, while it is certainly important to measure the acute toxicity of microplastics, in the absence of such toxicity it becomes especially important to

assess the long-term or chronic effects of exposure to microplastics. This thesis studies the effects of long-term exposure to weathered HDPE microplastics in animal, plant, and soil microorganisms. The toxicity of HDPE microplastics in *Drosophila melanogaster* was evaluated. In addition to a standard developmental toxicity assay over a concentration range of 0.1 – 10 000 mg/kg HDPE in food, which found no toxicity in larvae-to-adult development, the reproductive performance of the flies over four generations was measured. While no toxicity was observed, the pupae exposed to 100 mg/kg HDPE microplastics across all generations successfully eclosed into adult flies 5.7 % more often than flies raised on control food.

A common route of entry for microplastics into agricultural soils is through biosolids or sewage sludge.¹⁷ Biosolids are derived from wastewater sewage sludge and therefore often contain a variety of pharmaceutically active compounds as a result. Chapter 6 examines the effect of microplastics and these compounds individually and together on soil microbial community composition, soil enzyme activity, and strawberry plant growth. While the majority of microplastic studies are conducted in a controlled environment such as an environmental chamber, this work studied these effects over the span of two years in an outdoor study to more closely represent real-world conditions. No overall impact was observed from any of the treatments on plant growth or soil enzyme activity, but the pharmaceutically active compounds were able to significantly alter the microbial community composition when compared to the control soil. However, the key finding of this chapter was that when these pharmaceutically active compounds were added to soil containing 100 mg/kg HDPE microplastics, there was no longer any significant difference in the soil microbial community composition when compared to the control.

1.4 Contributions of the authors

Chapter 2: Green synthesis of carbon dots and their applications

Citation: *RSC Adv.*, 2021, 11, 25354

Authors: Shawninder Chahal, Jun-Ray Macairan, Nariman Yousefi, Nathalie Tufenkji, Rafik Naccache

Contributions: SC extracted information from the literature, wrote the manuscript, made figures and tables. JRM extracted information from the literature, wrote the first draft of the “Applications” section, and revised the manuscript. All authors conceptualized, edited, and revised the manuscript.

Chapter 3: Green synthesis of high quantum yield carbon dots from phenylalanine and citric acid: Role of stoichiometry and nitrogen doping

Citation: *ACS Sustainable Chem. Eng.*, 2020, 8, 14, 5566–5575

Authors: Shawninder Chahal, Nariman Yousefi, Nathalie Tufenkji

Contributions: SC conceptualized the project, conducted the experiments, analyzed the data, made figures, wrote the manuscript. NY conceptualized the project and conducted Raman spectroscopy. NT supervised the project. All authors revised the manuscript.

Chapter 4: A comparison of carbon dot and CdTe quantum dot toxicity in *Drosophila melanogaster*

Citation: To be submitted

Authors: Shawninder Chahal, Jun-Ray Macairan, Rafik Naccache, Nathalie Tufenkji

Contributions: SC conceptualized the project, conducted the experiments, analyzed the data, made figures, wrote the manuscript. JRM characterized the nanoparticles, imaged the flies, and wrote the first draft of the related sections in the manuscript. RN and NT conceptualized the project. All authors revised the manuscript.

Chapter 5: Multigenerational effects of weathered polyethylene microplastics on *Drosophila melanogaster*

Citation: To be submitted

Authors: Shawninder Chahal, Jun-Ray Macairan, Laura M. Hernandez, Nathalie Tufenkji

Contributions: SC conceptualized the project, conducted the experiments, analyzed the data, made figures, wrote the manuscript. JRM performed FTIR on the microplastics, imaged the flies, and wrote the first draft of the related sections in the manuscript. LHM performed SEM imaging of the microplastics and wrote the first draft of the related sections in the manuscript. NT conceptualized the project. All authors revised the manuscript.

Chapter 6: Effect of emerging contaminants on soil microbial community composition, soil enzyme activity, and strawberry plant growth in polyethylene microplastic-containing soils

Citation: To be submitted

Authors: Shawninder Chahal, Peiying Wang, Vinicius Bueno, Hemanshu Anand, Stéphane Bayen, Subhasis Ghoshal, Valérie Gravel, Nathalie Tufenkji

Contributions: SC, PW, SB, SG, VG, and NT conceptualized the project. SC, PW, VB, and HA conducted experiments. SC analyzed the data, made figures, and wrote the manuscript. PW wrote the first draft of the methods section for experiments related to plant growth and chemical contaminant detection. VB wrote the first draft of the methods section for microbial community composition. PW, SB, and VG were essential in the planning and coordination of field availability and allocation of resources at Macdonald campus. All authors revised the manuscript.

1.5 Background on microplastics toxicity in terrestrial environments

For decades, the focus of microplastic pollution has been in the context of aquatic environments. Images of what should otherwise be crystal clear bodies of water filled with floating pieces of plastic quickly convey a sense of urgency towards tackling plastic pollution. However, in recent years, studies have revealed that most microplastic pollution is found in terrestrial environments.² Following these findings, research on the toxicity of microplastics in terrestrial environments has been gaining traction. This section consists of a literature review of studies that evaluated the toxicity of microplastics in terrestrial animal and plant organisms.

A variety of microplastics have shown varying forms of toxicity in animals. For instance, Song *et al.* exposed *Achatina fulica*, a type of terrestrial snail, to 710 mg/kg polyethylene terephthalate microplastic fibers with a mean length of 1258 μm and mean diameter of 76.3 μm .¹⁹ They found that the microplastics induced a variety of toxic effects on the snails such as a 34.9 % decrease in food intake, a 69.7 % decrease in excretion, and gastrointestinal tract damage in 40 % of snails.¹⁹ Another study evaluated the toxicity of nylon and PVC microplastics (<150 μm) on the terrestrial worm *Enchytraeus crypticus*.²⁰ The study found that the microplastics were not lethal at a concentration of 90 000 mg per kg soil.²⁰ Moreover, the nylon microplastics exposure resulted in a dose-dependent reduction in reproduction, whereas the PVC microplastics did not impact reproduction.²⁰ The effect of polystyrene microplastics with a mean diameter of 3.3 μm , derived from artificial plastic plants found in an urban setting for five years, on the bird, *Coturnix japonica*, was also evaluated.²¹ It was found that these microplastics induced oxidative stress in various organs and that the microplastics accumulated in the liver.²¹ Wang *et al.* conducted a study exposing mice to small (1 – 10 μm) and large (50 – 100 μm) polystyrene microplastics at a concentration of 10 mg per L drinking water.²² They found that the microplastics induced

inflammation and necroptosis in the bladder, whereby the larger microplastics induced greater inflammation and the smaller ones induced greater necroptosis.²²

Studies have also been performed investigating the impact of microplastics on plant life. For instance, one study examined the effect of 1000 mg/kg biodegradable polylactic acid microplastics (0.6 – 363 µm) on *Lolium perenne* (perennial ryegrass).²³ It was found that the polylactic acid reduced the shoot height by 19 % and germination rate by 6 %.²³ Wu *et al.* performed a study exposing rice (*Oryza sativa* L.) to polystyrene microplastics (8.5 – 30.7 µm).²⁴ They found that a 500 mg/L exposure of microplastics decreased the shoot length by 27 % and shoot biomass by 40.3 %.²⁴ Moreover, these microplastics reduced the enzyme activity of superoxide dismutase and peroxidase, and reduced malonaldehyde content in the leaves.²⁴ Another study evaluated the effect of HDPE microplastics (3 µm) on maize (*Zea mays* L.).²⁵ An exposure concentration of 100 mg/L resulted in a 37 % decrease in root dry biomass, 57 % decrease in shoot dry biomass, 70 % decrease in leaf area, and a 51 % decrease in the plant height growth rate.²⁵ Qi *et al.* exposed wheat (*Triticum aestivum*) to low-density polyethylene microplastics and biodegradable microplastics with a size range of 50 – 1000 µm at a concentration of 10 000 mg/kg.²⁶ They found that the biodegradable microplastics reduced the plant height while the polyethylene microplastics did not during the day 14 – 40 period.²⁶ By the 4-month harvest time point, there were no differences between any of the treatments and the control.²⁶ Another study investigated the effects of polypropylene, polyethylene, and polyvinylchloride microplastics (< 125 µm) at a concentration of 184 mg/kg on garden cress (*Lepidium sativum*) for 21 days.²⁷ It was found that there were no significant differences in the number of leaves and the shoot height, however the polyethylene microplastics inhibited the germination of 7.1 % of seeds, whereas the polypropylene microplastics inhibited the germination of 14.3 % of seeds.²⁷

A comprehensive literature review of carbon dots is found in Chapter 2.

1.6 References

- (1) Yang, S.-T.; Wang, X.; Wang, H.; Lu, F.; Luo, P. G.; Cao, L.; Mezirani, M. J.; Liu, J.-H.; Liu, Y.; Chen, M.; et al. Carbon Dots as Nontoxic and High-Performance Fluorescence Imaging Agents. *The Journal of Physical Chemistry C* **2009**, *113* (42), 18110-18114. DOI: 10.1021/jp9085969.
- (2) Horton, A. A.; Walton, A.; Spurgeon, D. J.; Lahive, E.; Svendsen, C. Microplastics in freshwater and terrestrial environments: Evaluating the current understanding to identify the knowledge gaps and future research priorities. *Science of The Total Environment* **2017**, *586*, 127-141. DOI: 10.1016/j.scitotenv.2017.01.190.
- (3) Liu, W.; Zhang, S.; Wang, L.; Qu, C.; Zhang, C.; Hong, L.; Yuan, L.; Huang, Z.; Wang, Z.; Liu, S.; et al. CdSe Quantum Dot (QD)-Induced Morphological and Functional Impairments to Liver in Mice. *PLOS ONE* **2011**, *6* (9), e24406. DOI: 10.1371/journal.pone.0024406.
- (4) Li, H.; Ye, S.; Guo, J.; Wang, H.; Yan, W.; Song, J.; Qu, J. Biocompatible carbon dots with low-saturation-intensity and high-photobleaching-resistance for STED nanoscopy imaging of the nucleolus and tunneling nanotubes in living cells. *Nano Research* **2019**, *12* (12), 3075-3084. DOI: 10.1007/s12274-019-2554-x.
- (5) Wei, X.; Li, L.; Liu, J.; Yu, L.; Li, H.; Cheng, F.; Yi, X.; He, J.; Li, B. Green Synthesis of Fluorescent Carbon Dots from *Gynostemma* for Bioimaging and Antioxidant in Zebrafish. *ACS Applied Materials & Interfaces* **2019**, *11* (10), 9832-9840. DOI: 10.1021/acsami.9b00074.
- (6) Radhakrishnan, K.; Panneerselvam, P. Green synthesis of surface-passivated carbon dots from the prickly pear cactus as a fluorescent probe for the dual detection of arsenic(iii) and

- hypochlorite ions from drinking water. *RSC Advances* **2018**, 8 (53), 30455-30467. DOI: 10.1039/C8RA05861J.
- (7) Shen, X.; Jia, J.; Lin, Y.; Zhou, X. Enhanced performance of CdTe quantum dot sensitized solar cell via anion exchanges. *Journal of Power Sources* **2015**, 277, 215-221. DOI: 10.1016/j.jpowsour.2014.12.022.
- (8) Hochreiner, A.; Schwarzl, T.; Eibelhuber, M.; Heiss, W.; Springholz, G.; Kolkovsky, V.; Karczewski, G.; Wojtowicz, T. Midinfrared electroluminescence from PbTe/CdTe quantum dot light-emitting diodes. *Applied Physics Letters* **2011**, 98 (2), 021106. DOI: 10.1063/1.3531760 (accessed 2022/08/02).
- (9) Qin, X.; Lu, W.; Asiri, A. M.; Al-Youbi, A. O.; Sun, X. Green, low-cost synthesis of photoluminescent carbon dots by hydrothermal treatment of willow bark and their application as an effective photocatalyst for fabricating Au nanoparticles-reduced graphene oxide nanocomposites for glucose detection. *Catalysis Science & Technology* **2013**, 3 (4), 1027-1035. DOI: 10.1039/C2CY20635H.
- (10) Habeebu, S. S. M.; Liu, J.; Klaassen, C. D. Cadmium-Induced Apoptosis in Mouse Liver. *Toxicology and Applied Pharmacology* **1998**, 149 (2), 203-209. DOI: 10.1006/taap.1997.8334.
- (11) Environment: EU ban on hazardous substances in electrical and electronic products takes effect. European Commission: 2006.
- (12) Bano, D.; Kumar, V.; Singh, V. K.; Hasan, S. H. Green synthesis of fluorescent carbon quantum dots for the detection of mercury(ii) and glutathione. *New Journal of Chemistry* **2018**, 42 (8), 5814-5821. DOI: 10.1039/C8NJ00432C.

- (13) Geyer, R.; Jambeck, J. R.; Law, K. L. Production, use, and fate of all plastics ever made. *Science Advances* **2017**, *3* (7), e1700782. DOI: 10.1126/sciadv.1700782.
- (14) Zhang, K.; Hamidian, A. H.; Tubić, A.; Zhang, Y.; Fang, J. K. H.; Wu, C.; Lam, P. K. S. Understanding plastic degradation and microplastic formation in the environment: A review. *Environmental Pollution* **2021**, *274*, 116554. DOI: 10.1016/j.envpol.2021.116554.
- (15) Hale, R. C.; Seeley, M. E.; La Guardia, M. J.; Mai, L.; Zeng, E. Y. A Global Perspective on Microplastics. *Journal of Geophysical Research: Oceans* **2020**, *125* (1), e2018JC014719. DOI: 10.1029/2018JC014719.
- (16) Carr, S. A.; Liu, J.; Tesoro, A. G. Transport and fate of microplastic particles in wastewater treatment plants. *Water Research* **2016**, *91*, 174-182. DOI: 10.1016/j.watres.2016.01.002.
- (17) Corradini, F.; Meza, P.; Eguiluz, R.; Casado, F.; Huerta-Lwanga, E.; Geissen, V. Evidence of microplastic accumulation in agricultural soils from sewage sludge disposal. *Science of The Total Environment* **2019**, *671*, 411-420. DOI: 10.1016/j.scitotenv.2019.03.368.
- (18) Liao, J.; Cheng, Z.; Zhou, L. Nitrogen-Doping Enhanced Fluorescent Carbon Dots: Green Synthesis and Their Applications for Bioimaging and Label-Free Detection of Au³⁺ Ions. *ACS Sustainable Chemistry & Engineering* **2016**, *4* (6), 3053-3061. DOI: 10.1021/acssuschemeng.6b00018.
- (19) Song, Y.; Cao, C.; Qiu, R.; Hu, J.; Liu, M.; Lu, S.; Shi, H.; Raley-Susman, K. M.; He, D. Uptake and adverse effects of polyethylene terephthalate microplastics fibers on terrestrial snails (*Achatina fulica*) after soil exposure. *Environmental Pollution* **2019**, *250*, 447-455. DOI: 10.1016/j.envpol.2019.04.066.

- (20) Lahive, E.; Walton, A.; Horton, A. A.; Spurgeon, D. J.; Svendsen, C. Microplastic particles reduce reproduction in the terrestrial worm *Enchytraeus crypticus* in a soil exposure. *Environmental Pollution* **2019**, *255*, 113174. DOI: 10.1016/j.envpol.2019.113174.
- (21) de Souza, S. S.; Freitas, Í. N.; Gonçalves, S. d. O.; Luz, T. M. d.; Araújo, A. P. d. C.; Rajagopal, R.; Balasubramani, G.; Rahman, M. M.; Malafaia, G. Toxicity induced via ingestion of naturally-aged polystyrene microplastics by a small-sized terrestrial bird and its potential role as vectors for the dispersion of these pollutants. *Journal of Hazardous Materials* **2022**, *434*, 128814. DOI: 10.1016/j.jhazmat.2022.128814.
- (22) Wang, Y.; Wang, S.; Xu, T.; Cui, W.; Shi, X.; Xu, S. A new discovery of polystyrene microplastics toxicity: The injury difference on bladder epithelium of mice is correlated with the size of exposed particles. *Science of The Total Environment* **2022**, *821*, 153413. DOI: 10.1016/j.scitotenv.2022.153413.
- (23) Boots, B.; Russell, C. W.; Green, D. S. Effects of Microplastics in Soil Ecosystems: Above and Below Ground. *Environmental Science & Technology* **2019**, *53* (19), 11496-11506. DOI: 10.1021/acs.est.9b03304.
- (24) Wu, X.; Liu, Y.; Yin, S.; Xiao, K.; Xiong, Q.; Bian, S.; Liang, S.; Hou, H.; Hu, J.; Yang, J. Metabolomics revealing the response of rice (*Oryza sativa* L.) exposed to polystyrene microplastics. *Environmental Pollution* **2020**, *266*, 115159. DOI: 10.1016/j.envpol.2020.115159.
- (25) Urbina, M. A.; Correa, F.; Aburto, F.; Ferrio, J. P. Adsorption of polyethylene microbeads and physiological effects on hydroponic maize. *Science of The Total Environment* **2020**, *741*, 140216. DOI: 10.1016/j.scitotenv.2020.140216.

- (26) Qi, Y.; Yang, X.; Pelaez, A. M.; Huerta Lwanga, E.; Beriot, N.; Gertsen, H.; Garbeva, P.; Geissen, V. Macro- and micro- plastics in soil-plant system: Effects of plastic mulch film residues on wheat (*Triticum aestivum*) growth. *Science of The Total Environment* **2018**, *645*, 1048-1056. DOI: 10.1016/j.scitotenv.2018.07.229.
- (27) Pignattelli, S.; Broccoli, A.; Renzi, M. Physiological responses of garden cress (*L. sativum*) to different types of microplastics. *Science of The Total Environment* **2020**, *727*, 138609. DOI: 10.1016/j.scitotenv.2020.138609.

Preamble to Chapter 2

Chapter 2 consists of a thorough literature review of CDs made using green synthesis methods and their applications. The goal was to gain a better understanding of the synthesis pipeline used in various green syntheses reported in the literature. The distribution of the precursors, synthesis methods, and purification methods used were plotted, as well as the size, quantum yield, peak excitation and emission wavelengths, and oxygen-to-carbon and nitrogen-to-carbon ratios of the resulting CDs to easily visualize which properties are lacking in the green-synthesized CD literature. The applications that these CDs were used in are also described and discussed. We then made suggestions on where future research should be guided to diversify the type of CDs that are being synthesized via green synthesis methods so that their performance can match that found in CDs synthesized by traditional methods.

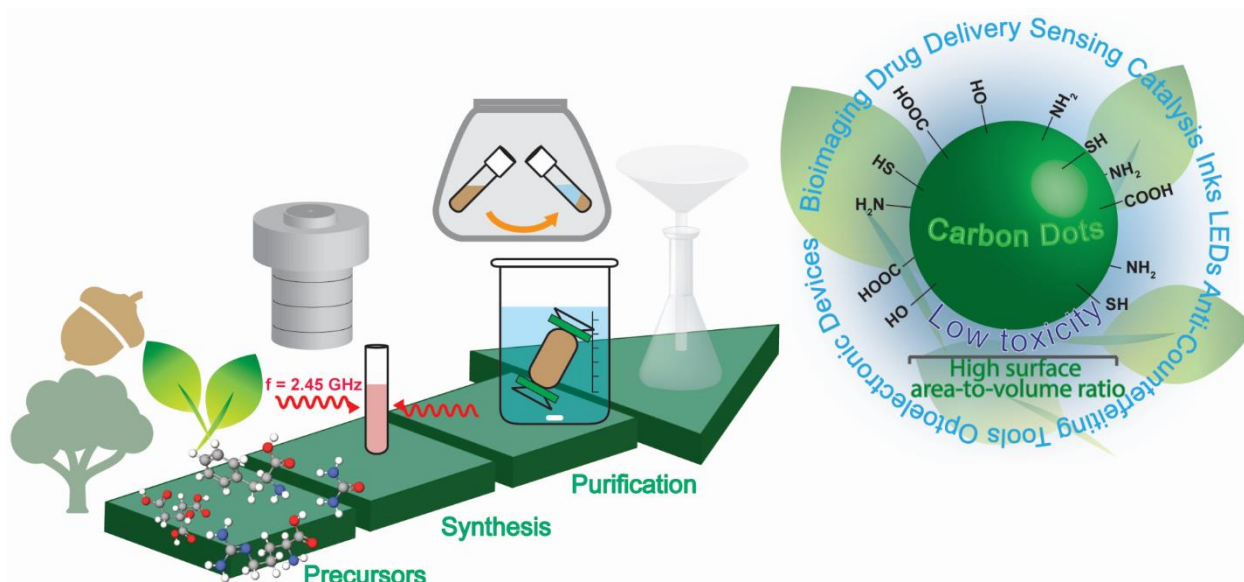
This chapter has been reprinted (adapted) from the open access (CC BY-NC 3.0) article *RSC Adv.*, 2021, 11, 25354. Copyright 2021 The Authors. Published by the Royal Society of Chemistry. The publisher does not require permission to be obtained for the reproduction of this publication in the author's thesis. The only modifications are in the enumeration of the header, figure, and table numbers whereby they have all been prefixed with "2." to reflect their placement in Chapter 2 of this thesis. The format of the references may also differ and the abbreviation "Fig." is written in full as "Figure" to maintain consistency throughout the rest of the thesis. This chapter contains figures from third-party publications for which the appropriate permissions have been obtained and acknowledgement can be found in their respective figure captions. Figures 2.3a-e and 2.5 were also published by the Royal Society of Chemistry, and therefore their figure captions do not contain the words "with permission" since they were not needed during publication. However, appropriate permissions have been obtained for this thesis.

Chapter 2: Green synthesis of carbon dots and their applications

Abstract

Carbon dots (CDs) are nanoparticles with tunable physicochemical and optical properties. Their resistance to photobleaching and relatively low toxicity render them attractive alternatives to fluorescent dyes and heavy metal-based quantum dots in the fields of bioimaging, sensing, catalysis, solar cells, and light-emitting diodes, among others. Moreover, they have garnered considerable attention as they lend themselves to green synthesis methods. Increasingly, one-pot syntheses comprising exclusively of renewable raw materials or renewable refined compounds are gaining favor over traditional approaches that rely on harsh chemicals and energy intensive conditions. The field of green CD synthesis is developing rapidly; however, challenges persist in ensuring the consistency of their properties (e.g., fluorescence quantum yield) relative to conventional preparation methods. This has mostly limited their use to sensing and bioimaging, leaving opportunities for development in optoelectronic applications. Herein, we discuss the most common green CD synthesis and purification methods reported in the literature and the renewable precursors used. The physical, chemical, and optical properties of the resulting green-synthesized CDs are critically reviewed, followed by a detailed description of their applications in sensing, bioimaging, biomedicine, inks, and catalysis. We conclude with an outlook on the future of green CD synthesis. Future research efforts should address the broad knowledge gap between CDs synthesized from renewable versus non-renewable precursors, focusing on discrepancies in their physical, chemical, and optical properties. The development of cost effective, safe, and sustainable green CDs with tunable properties will broaden their implementation in largely untapped applications, which include drug delivery, photovoltaics, catalysis, and more.

Abstract Graphic



Abstract graphic 2.1. A visual depiction of the abstract for Chapter 2.

2.1 Introduction

Carbon dots (CDs) are a class of fluorescent nanomaterials, typically less than $\sim 10 \text{ nm}$ in diameter, that can exhibit quantum dot-like behaviour. Since their initial discovery by Xu *et al.*,¹ CDs are now seen as potential alternatives to traditional fluorescent dyes owing to their versatile optical properties and resistance to photobleaching.² They also exhibit lower toxicity (both cyto- and chemical toxicity) in comparison to certain heavy metal-based quantum dots,³ speaking to their potential for integration in biomedical applications.

Early CD syntheses employed top-down approaches whereby graphite was processed through multiple steps using harsh chemicals to transform it into the more usable graphite oxide⁴ before it was broken down into nano-sized CDs.⁵ Bottom-up synthesis methods, whereby smaller molecules polymerize and carbonize to form CDs, are increasingly attractive due to their ease of implementation and tunability. Recent efforts exploit renewable raw materials (*e.g.*, plants⁶), or

renewable refined compounds (*e.g.*, citric acid, amino acids⁷) to synthesize CDs. The ability to tune and tailor the properties of CDs, prepared using sustainable materials and approaches, permits diverse application development in areas such as sensing,⁸ bioimaging,⁹ antibacterials,¹⁰ fluorescent patterning inks,¹¹ and photocatalysis,¹² to name a few.

This review will first define the scope of green CD synthesis, followed by a discussion of the advantages and limitations of the various preparation methods, carbon sources, and purification protocols used. We will then discuss the size, chemical composition, and optical properties of green-synthesized CDs with an overview of their applications. We conclude with an outlook on the future of green CD synthesis and the knowledge gaps that remain to be addressed.

2.2 Synthesis

2.2.1 What makes a synthesis green?

To answer this question, we will adopt aspects of the 12 Principles of Green Chemistry by Anastas and Warner,¹³ specifically: (3) less hazardous chemical synthesis; (4) designing safer chemicals; (5) safer solvents and auxiliaries; (6) design for energy efficiency; (7) use of renewable feedstocks; and (12) inherently safer chemistry for accident prevention. These principles can be summarized as using non-toxic renewable precursors and solvents in a CD synthesis that is safe to perform. The synthesized CD itself should also be non-toxic and chemically stable. Although CD synthesis is generally an energy-intensive process, lower energy synthesis methods should be prioritized. Moreover, given the possibility of the formation of several side products and intermediates, one must consider their safety profile to ensure their proper disposal. These principles will guide us in the following subsections discussing previously reported green CD syntheses.

2.2.2 Green synthesis methods

Owing to its low cost and ease of implementation, hydrothermal synthesis is the most common green CD preparation method. This thermal-mediated approach requires pressurized autoclave vessels, reaction temperatures ranging from 120 – 240 °C, and reaction times of 3 – 12 h in a typical synthesis (Table 2.1). The definition of green synthesis stipulates using water (hydrothermal), or benign organic solvents (solvothermal) such as ethanol. The solvent can also be a renewable substance serving a dual purpose by acting as a carbon source in the synthesis (*e.g.*, walnut oil).¹⁴ Solvent-free synthesis (*i.e.*, dry heating) is usually performed at temperatures as high as 300 °C under ambient pressure conditions (Table 2.1). Although simple to implement, these approaches require high temperatures and long reaction times. These reaction parameters can be readily optimized to maximize product yield and application-specific performance while minimizing energy requirements.

Table 2.1. Processing parameters and properties of CDs synthesized by green methods.

Carbon source	Method	Conditions	Size [nm]	N:C	O:C	Excitation [nm]	Emission [nm]	QY	Ref.
<i>Eleocharis dulcis</i>	hydrothermal	120 °C, 5 h	3.0	0.05	0.33	380	458	11%	15
<i>Azadirachta indica</i>	hydrothermal	150 °C, 4 h	3.2	0.09	0.12	340	467	27%	16
maize	hydrothermal	160 °C, 10 h	5.2	0.02	0.35	420	500	8%	17
rose-heart radish	hydrothermal	180 °C, 3 h	3.6	0.13	0.43	330	420	14%	18
<i>Ocimum sanctum</i>	hydrothermal	180 °C, 4 h	2.4	0.18	0.35	450	500	9%	8
scallion	hydrothermal	180 °C, 12 h	3.5	0.12	0.27	320	418	3%	19
strawberry	hydrothermal	180 °C, 12 h	5.2	0.10	0.35	344	427	6%	20
pomelo	hydrothermal	200 °C, 3 h	2.9	0.06	0.35	365	444	7%	21
willow	hydrothermal	200 °C, 3 h	1.6	0.43	0.39	360	444	6%	12
tulsi	hydrothermal	200 °C, 4 h	5.0	0.10	0.89	360	435	3%	11
citric acid, glutathione	hydrothermal	200 °C, 4 h	6.1	0.20	0.26	340	432	75%	22
citric acid, L-phenylalanine	hydrothermal	200 °C, 8 h	11.9	0.14	0.36	350	413	65%	7
citric acid, L-arginine	hydrothermal	200 °C, 8 h	2.7	0.11	0.17	350	440	39%	23
ginkgo	hydrothermal	200 °C, 10 h	3.0	0.06	0.35	350	436	23%	6
<i>Tamarindus indica</i>	hydrothermal	210 °C, 5 h	3.4	0.28	0.68	320	417	47%	24
<i>Allium fistulosum</i>	hydrothermal	220 °C, 3 h	4.2	0.37	0.38	412	503	10%	25
<i>Abelmoschus manihot</i>	hydrothermal	220 °C, 4 h	9.0	0.25	0.07	330	410	31%	9
<i>Osmanthus fragrans</i>	hydrothermal	240 °C, 5 h	2.2	0.04	0.38	340	411	19%	26
walnut	solvothermal	220 °C, 24 h	12.3	0.05	1.12	360	430	15%	14
watermelon	dry heating	220 °C, 2 h	2.0	0.02	0.31	470	537	7%	27
peanut	dry heating	250 °C, 2 h	1.6	0.04	0.49	320	440	10%	28
bamboo	dry heating	300 °C, 3 h	11.0	0.06	1.00	313	419	5%	29
glycine, urea	microwave	800 W, 3 min	3.2	0.40	0.42	320	380	13%	30
lotus	microwave	800 W, 6 min	9.4	0.09	0.53	360	435	19%	31

QY = Quantum yield

Microwave synthesis is advantageous as it enables direct heating of reaction mixtures, typically using ~800 W of microwave power for only a few minutes (Table 2.1). Despite these benefits, the entry point of microwave synthesis can be considerably more expensive as specialized equipment is needed. However, regular household microwaves have been used^{30, 31} with the trade-off of having less control over the synthesis parameters. Liu *et al.*³⁰ conducted a rapid, low-energy microwave synthesis at 800 W for 3 min; this rapid reaction time (60 – 240× faster than hydrothermal synthesis) highlights the increased heating efficiency of microwaves. Unlike hydrothermal synthesis that relies on conductive heat transfer, microwaves allow for direct and selective heating *via* resonance with the vibrational frequencies of molecules. Therefore, a microwave reaction is often complete before an appreciable change in temperature of an equivalent hydrothermal synthesis is attained.

2.2.3 Carbon source

Diverse plant types are used as renewable carbon feedstocks for green CD synthesis (Figure 2.1a). The most commonly used parts of the plant are the leaves,⁶ flowers,^{32, 33} or roots.³⁴ Other forms of plant biomass include shells,²⁸ kernels,³⁵ bark,¹² stalk,¹⁷ and peels.^{21, 27} Such feedstocks require preprocessing to reduce particle size and remove excess water. Drying the feedstock under direct sunlight^{35, 36} reduces energy requirements relative to conventional dehydration routes. The use of fruit juice²⁰ can be convenient as it provides a “ready-to-use” solution for hydrothermal synthesis, avoiding the need to redisperse dried plant matter in water. However, this benefit comes at the cost of the carbon diversity found in the dry feedstock.

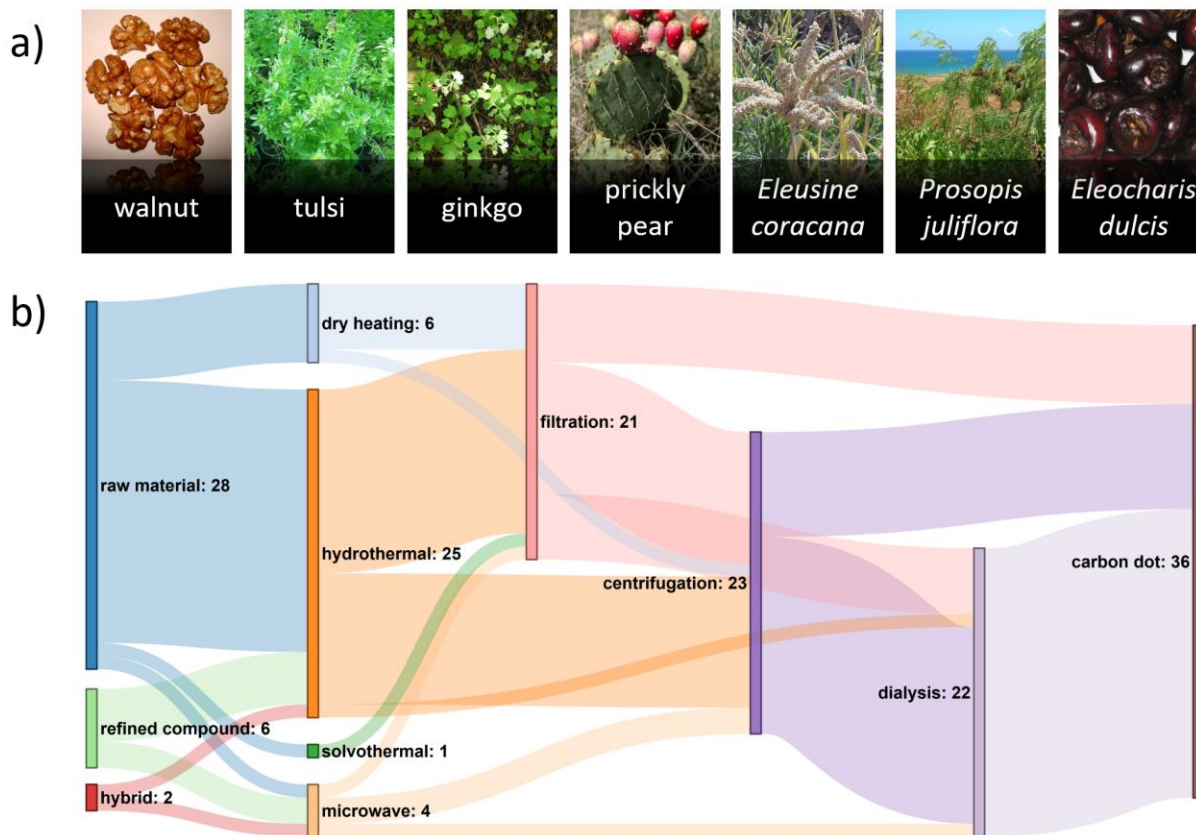


Figure 2.1. a) A diverse set of locally sourced renewable precursors can be used for the green synthesis of CDs. A reference list of these images can be found in Table S2.1 of the Electronic Supplementary Information (ESI). b) Sankey diagram showing the number of green-synthesized CD publications reporting various pathways from carbon source to CD. For this diagram, it is assumed that the purification steps followed the order: 1) filtration, 2) centrifugation, 3) dialysis, although this was not always the case, and this assumption was made for illustrative purposes only. A hybrid precursor indicates that both a renewable raw material and renewable refined compound were used. The most common synthesis route uses a renewable raw material in a hydrothermal synthesis followed by one or more purification steps. A reference list can be found in Table S2.2 of the ESI.

Renewable refined compounds (*i.e.*, compounds that can be synthesized through naturally occurring bioprocesses) have also been used in CD synthesis. For instance, Zhang *et al.* performed a hydrothermal CD synthesis from citric acid and the amino acid L-arginine,²³ whereas Liu *et al.* used urea and the amino acid glycine in a microwave synthesis of CDs.³⁰ While renewable refined compounds may not be as strictly green as the direct use of renewable raw materials, their synthesis can remain sustainable. For instance, Lotfy *et al.* prepared citric acid with an 88% yield from the fungus *Aspergillus niger* by using beet molasses, corn steep liquor, and salts as a feedstock.³⁷ Citric acid is also abundant in Nature, most notably in *Citrus* fruits, where the dry fruit mass consists of up to 8% citric acid.³⁸ Moreover, hybrid green syntheses have also been performed through the mixture of renewable raw materials and renewable refined compounds, such as the use of celery leaves and L-glutathione in a hydrothermal CD synthesis.³⁹

2.2.4 Purification

The purification of the post-synthesis CD reaction mixture is a crucial step in the production of carbon dots as it contains a myriad of side-products and unreacted precursors with varying solubilities and sizes. Indeed, the removal of side-products that possess different size and dispersibility profiles relative to the CDs, would suggest that a multi-step purification process is typically required. Extensive purification procedures are carried out with the aim of obtaining CDs with uniform physical and optical properties.⁴⁰ Poor purification can impact CDs' potential use in certain applications. For instance, Essner *et al.* demonstrated that inadequate purification steps can greatly impact the sensing performance of CDs due to the presence of fluorescent impurities.⁴¹

Carbon dot purification typically relies on a combination of multiple methods. Large insoluble matter is typically removed through centrifugation and/or filtration.²⁶ In the former, insoluble impurities will be found at the bottom of the tube after centrifugation – thus enabling

easy separation from the supernatant, which typically contains the CDs. In the latter, impurities larger than the pore size of the filter will be excluded from the filtrate. Dialysis is another purification method which is typically performed over a 24 – 72 h period to remove any remaining small soluble impurities.^{6, 31} These three methods are evenly implemented (Figure 2.1b) (although in varying order) in green CD syntheses with the goal of minimizing the presence of any impurities.

2.3 Properties

2.3.1 Size

Typically, green-synthesized CDs can be prepared with a diameter of 2 – 12 nm,^{14, 28} as measured using transmission electron microscopy (TEM). A size distribution of green-synthesized CDs found in the literature is shown in Figure 2.2d and reveals that the majority of these CDs fall within the lower end of this size range. Tailoring the size of these semiconductor-like dots can enable them to confine photons *via* modulation of their bandgap.⁴² Figure 2.2a shows a typical high-resolution TEM image of a CD (synthesized from black pepper) with crystallographic information obtained from its lattice order and spacing.⁴³ Conversely, amorphous CDs lack a periodic crystal lattice,²³ cannot diffract electrons,⁴⁴ and may show an X-ray diffraction pattern with a broad reflection (amorphous halo) that has a peak in the $2\theta = 23.4 - 24.6^\circ$ region.⁴⁵

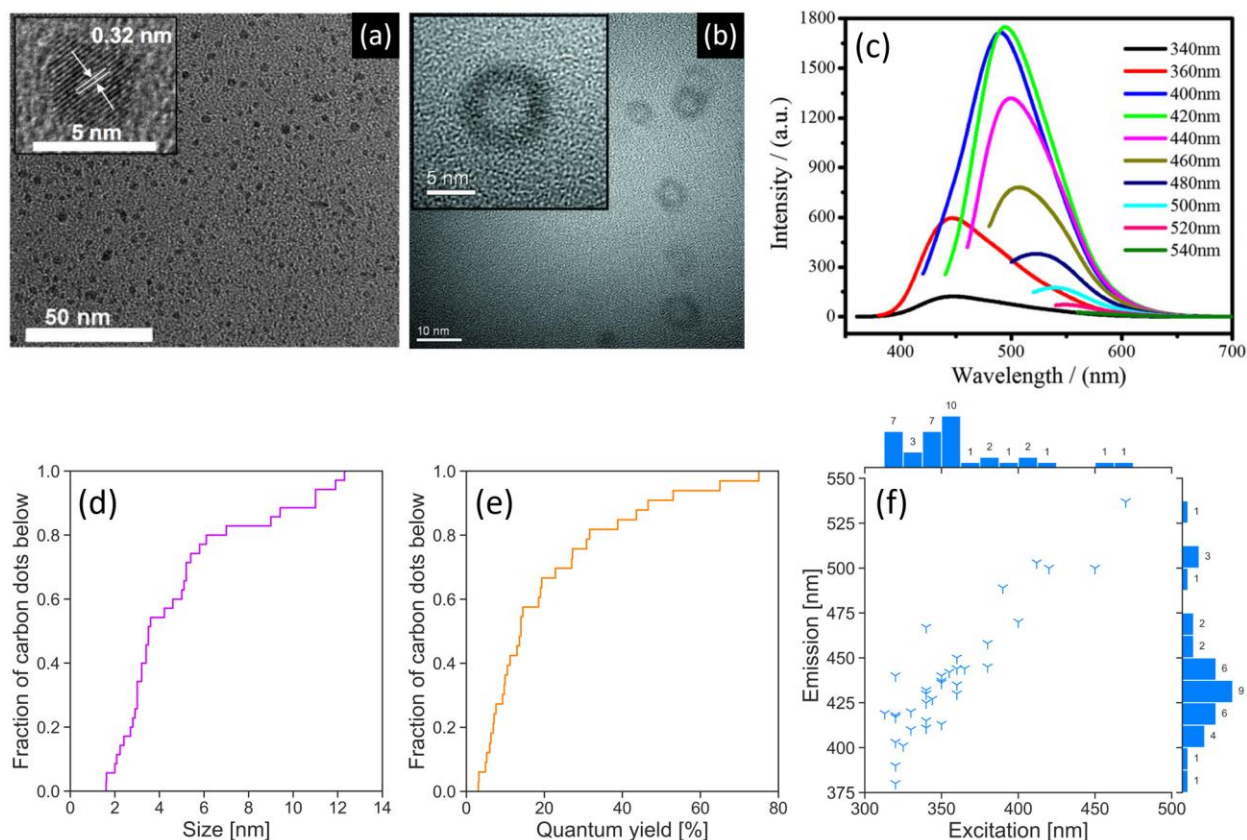


Figure 2.2. (a) HR-TEM images of CDs synthesized from black pepper (inset: lattice spacing). Adapted from Open Access ref ⁴³. Copyright 2018 Vasimalai *et al.*; licensee Beilstein-Institut. (b) HR-TEM images of hollow CDs synthesized from bovine serum albumin. The hollow design allows for this CD to be used in drug delivery applications. Adapted with permission from ref ⁴⁶. Copyright 2013 Elsevier Ltd. (c) Fluorescence spectra of a CD synthesized from maize at different excitation wavelengths. These CDs displayed green colour at their peak fluorescence emission. Adapted with permission from ref ¹⁷. Copyright 2017 Springer Science Business Media Dordrecht. Empirical cumulative distribution function plots of (d) CD size as measured by TEM and (e) fluorescence quantum yield. (f) Peak excitation and emission wavelengths of green-synthesized CDs. Counts are shown next to their respective bins and indicate the number of publications reporting CDs with properties in that bin's range. Peak emission and excitation generally move in the same direction. A reference list can be found in Table S2.2 of the ESI.

A challenging aspect of TEM imaging of CDs, especially those that are amorphous, is that their composition closely resembles that of the formvar-coated TEM grids they are typically imaged on. Moreover, deposition on the TEM grid must be done with care to minimize aggregation that could lead to sizing artefacts.⁴⁷ Atomic force microscopy (AFM) can also be used for size measurements, providing length, width, and height information of the CDs.⁷ This method avoids the contrast issues that may arise with electron microscopy of carbon nanomaterials. Ideally, both AFM and TEM should be used in conjunction to obtain both size and topographic information. In what concerns biological applications of CDs, dynamic light scattering measurements are critical as they provide a hydrodynamic radius.⁴⁶ This measurement is directly related to the diffusivity of the CDs in biological environments. Independent of size, CDs can form in quasi-spherical morphologies, including hollow CDs (Figure 2.2b) with an architecture that facilitates their use as a drug delivery agent.⁴⁶

2.3.2 Optical properties

A characteristic property of CDs is their ability to fluoresce under UV irradiation. However, the CD fluorescence mechanism remains a topic of debate and is suspected to vary according to the synthesis parameters. The CD surface properties (*e.g.*, degree of oxidation, decoration with functional groups), size-dependant quantum confinement effect, and the incorporation of fluorescent molecules at the CD core or surface can all impact the mechanism.⁴² Figure 2.2f summarizes the excitation/emission wavelength relationship for green-synthesized CDs extracted from 36 studies. Half of these CDs (1st – 3rd quartile) have peak excitations between 330 – 360 nm. The CDs in this peak excitation range have corresponding emissions ranging from 410 – 467 nm. Figure 2.2c shows the fluorescence spectra of a CD with a green colour fluorescence emission at

500 nm upon excitation at 420 nm,¹⁷ which is higher than the typical range. We note a general trend of increasing peak emission wavelength with increasing peak excitation wavelength.

The ability to tailor the peak emission wavelength as a function of the excitation wavelength is a desirable feature in bioimaging as it can minimize autofluorescence of cells and tissues by selecting an excitation wavelength that generates fluorescence of the CD, but not of the sample to be imaged. For instance, Zhou *et al.* synthesized CDs from watermelon peel with a maximum fluorescence intensity at an excitation/emission wavelength of 470/535 nm corresponding to a blue/green excitation/emission.²⁷ This can be useful for imaging biological samples with a high degree of autofluorescence under UV excitation, but with minimal autofluorescence under blue excitation.

Carbon dot fluorescence typically involves high-energy photon absorbance and lower energy emission; however, some CDs can undergo multiphoton excitation whereby they can upconvert longer wavelengths of light to emit higher energy photons. This phenomenon is desirable in applications such as bioimaging by enabling the use of lower energy excitation wavelengths that can reduce the risk of cell damage while simultaneously enhancing penetration depth.⁴⁸ Liang *et al.* synthesized CDs from gelatin which, in addition to exhibiting conventional fluorescence ($\lambda_{\text{ex}} = 350$, $\lambda_{\text{em}} = 430$ nm), also underwent photon upconversion following 750 nm excitation with an emission at 450 nm.⁴⁹

The fluorescence quantum yield (QY) of a CD, *i.e.*, the ratio of the number of photons emitted to the number of photons absorbed,⁵⁰ is a useful metric as it is theoretically independent of concentration and instrumentation, allowing for direct comparison of QYs across the literature. Green-synthesized CDs reportedly have QYs ranging from 3 – 75%, with a median QY of 14% (Figure 2.2e). We have thus far praised the various benefits of using green synthesis methods to

produce CDs. Yet, achieving high QYs using green synthesis methods lags relative to conventional preparation approaches. For instance, one of the highest QYs achieved by a CD synthesized from renewable raw materials is 47% using *Tamarindus indica* leaves.²⁴ To our knowledge, one of the highest QYs achieved by a CD synthesized from renewable refined compounds is 75% using citric acid and glutathione.²² However, a QY of 99% has been achieved using citric acid and the non-renewable tris(hydroxymethyl)aminomethane.⁵¹ The observed discrepancies in QY measurements can arise from two principal factors. Firstly, we must consider the heterogeneity of plant-based carbon sources that often comprise a mixture of carbohydrates, lipids, proteins, and nucleic acids. With more efficient extraction methods, it would be possible to isolate the desired starting materials *in lieu* of using the whole plant. Secondly, the absolute QY values are intimately tied to the purification protocols that serve to remove unreacted starting materials and fluorophores.⁴⁰ Indeed, purification of CDs is a step in the synthesis process that has not been standardized.

2.3.3 Chemical composition

Doping CDs with a heteroatom such as nitrogen is common practice since it is known to enhance QY by modifying the electronic properties and surface chemistry of the CDs.⁵² Moreover, while the presence of oxygen in green-synthesized CDs is common due to the abundance of oxygen in renewable raw materials and also many organic compounds, they can also impact the QY by affecting the degree of oxidation of the CDs.⁷ Renewable raw materials are a source of heteroatoms such as nitrogen, sulfur, and phosphorus. X-ray photoelectron spectroscopy (XPS) is commonly used to measure the CD elemental composition on an atomic basis. In the green CD literature, CDs have an oxygen-to-carbon (O:C) ratio of 0.07 – 1.12, and a nitrogen-to-carbon (N:C) ratio of 0.02 – 0.43 (Figure 2.3f). CDs synthesized from *Allium fistulosum* exhibit a sulfur-to-carbon (S:C) ratio

of 0.11 (Figure 2.3a),²⁵ while those prepared from *Eleocharis dulcis* contained traces of phosphorus resulting in a phosphorus-to-carbon (P:C) ratio of 0.004.¹⁵ The elemental diversity of renewable raw materials can be advantageous when synthesizing hetero-doped CDs, but complicate our ability to tune the chemical composition of the CDs. In such cases, renewable refined compounds should be used. Figure 2.3b, c, d, e shows a typical XPS spectra for a CD's different elements.

Despite being synthesized from a wide variety of precursors, half of the CDs in Figure 2.3f have an O:C ratio in the narrow 0.31 – 0.39 region. Cellulose is a major plant component, but has an O:C ratio of 0.83, well above the range indicated. Thermal reduction has been observed in complex compounds similar to CDs. For example, Chen *et al.* were able to thermally reduce graphene oxide with an O:C ratio of 0.48 to partially reduced graphene oxide with an O:C ratio of 0.18, as measured by XPS, using microwave irradiation.⁵³ Therefore, it is possible that the cellulose in plants, along with other biomolecules, is thermally reduced to a similar extent in reported studies, leading to similar O:C ratios in the resulting CDs. Another possible explanation for this convergence to a common O:C ratio could be that the CD is more likely to form a chemically stable structure in this region.

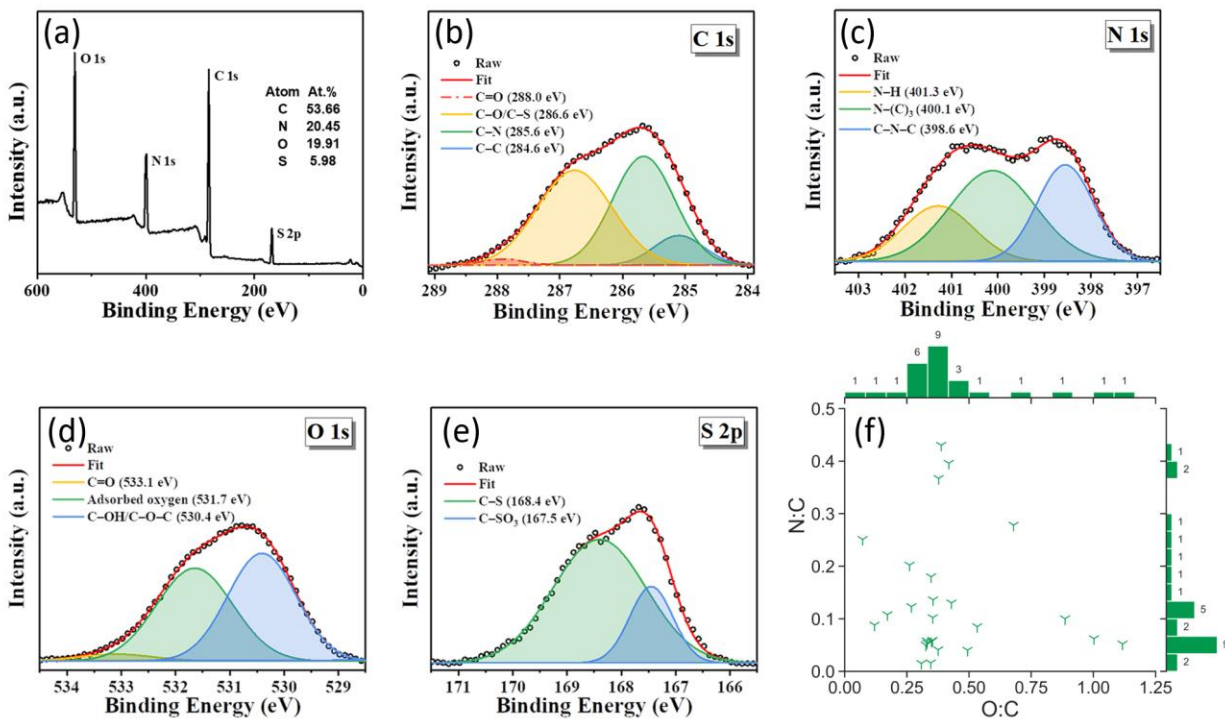


Figure 2.3. (a, b, c, d, e) XPS spectra of CDs showing nitrogen and sulfur doping. The use of *Allium fistulosum* in synthesis gave access to an abundant and diverse set of biomolecules contained within the plant resulting in an elementally diverse CD with a high sulfur content. Reproduced from RSC ref ²⁵. Copyright 2019 the Centre National de la Recherche Scientifique (CNRS) and The Royal Society of Chemistry. (f) Plot showing the diverse range of the O:C and N:C ratios of green-synthesized CDs reported in the literature. Counts are shown next to their respective bins and indicate the number of publications reporting CDs with properties in that bin's range. N:C and O:C are atomic ratios. XPS data from publications were assumed to be in atomic percent whereas elemental data from other types of instrumentation were either explicitly stated as atomic ratios or converted from their mass ratios. A reference list can be found in Table S2.2 of the ESI.

2.4 Applications

2.4.1 Chemical sensing

There is growing interest in CDs as inexpensive and sensitive chemical nanosensors (Table 2.2). Chemical sensing is typically performed by monitoring changes in CD fluorescence or absorbance in the presence of a target analyte. The presence of heteroatoms can potentially improve sensing performance and be tailored to interact with specific analytes. For instance, N/P-doped CDs synthesized from *Eleocharis dulcis* juice exhibit high selectivity towards Fe^{3+} relative to other metals.¹⁵ The high affinity of these CDs towards Fe^{3+} stems from the presence of nitrogen and oxygen groups that allow for rapid chelation.¹⁵ A static fluorescence quenching mechanism is usually operative, indicating the formation of a non-radiative complex between the CD and the metal ion.⁷ Amin *et al.* synthesized CDs from date kernels, which were used to detect zoledronic acid – an anticancer agent.³⁵ Initially, Fe^{3+} quenches the fluorescence of the CDs *via* the formation of a complex.³⁵ Subsequently, Fe^{3+} is chelated from the CD surface by zoledronic acid thereby restoring CD fluorescence with a 40 nM detection limit.³⁵ This CD sensor was successfully used in human serum, which increases its utility for routine zoledronic acid monitoring.³⁵ Similarly, Ramezani *et al.* used quince to synthesize CDs which, when coupled with MnO_4^- , can detect As^{3+} .⁵⁴ The CDs make use of the fact that MnO_4^- oxidizes both CDs and As^{3+} , therefore the presence of As^{3+} in an MnO_4^- solution will result in fewer CDs being oxidized, and in turn less fluorescence quenching.⁵⁴ Future research in green CD sensing may consider these unique approaches to sensing analytes as opposed to the traditional methods which rely on direct CD-analyte interactions. Doing so, along with gaining a deeper understanding of the role of the physical, chemical, and optical properties of the CDs, can help improve the detection limits of future green-synthesized CDs. Note that in Table 2.2, a fluorescence increase (FI) may originate

from the recovery of fluorescence from a previously quenched CD or from the actual increase of fluorescence intensity of the original CD.

Table 2.2. Summary of the sensing properties of green-synthesized CDs.

Analyte	Method of detection	Limit of detection	Linear range	Ref.
As ³⁺	FQ	2.3 nM	2 – 12 nM	55
ClO ⁻	FQ	16 nM	10 – 90 μM	55
Cr ⁶⁺	FQ	4.5 ppb	1.6 – 50 μM	11
Cu ²⁺	FQ	10 nM	0 – 100 μM	56
Fe ²⁺	FQ	180 nM	0 – 18 μM	17
Fe ³⁺	FQ	5 nM	0.01 – 50 μM	26
H ₂ O ₂	AI	35 μM	100 – 500 μM	16
Hg ²⁺	FQ	0.23 nM	0.5 – 10 nM	21
2,4,6-trinitrophenol	FQ	5 nM	0.025 – 40 μM	9
adenosine triphosphate	FI	5 nM	0.01 – 450 μM	33
ascorbic acid	AI	1.773 μM	5 – 40 μM	16
dimercaptosuccinic acid	FI	1.4 ng/mL	2.5 – 22.5 ng/mL	57
chlortetracycline	FQ	0.078 μg/mL	0.85 – 20.38 μg/mL	23
cysteamine	FQ	75.6 nM	10 – 210 μM	58
doxorubicin	FQ	0.4 ng/mL	1 – 400 ng/mL	59
glutathione	FI	1.7 μM	0 – 20 μM	24
glyphosate	FI	12 ng/mL	0.025 – 2.5 μg/mL	60
imipramine	FQ	0.6 ng/mL	1.0 – 200.0 ng/mL	34
methotrexate	FQ	7 nM	0.02 – 18.0 μM	10
morin	FQ	0.12 μM	0.4 – 60 μM	30
penicillamine	FQ	0.02 μg/mL	0.05 – 13.0 μg/mL	61
prilocaine	FQ	1.8 nM	2.3 – 400 nM	62
pyridine	FI	210 nM	0.5 – 4.1 μM	63
salazosulfapyridine	FQ	40 nM	0.1 – 80 μM	6
sulfasalazine	FQ	0.032 μg/mL	0.34 – 6.76 μg/mL	23
trifluralin	FQ	0.5 nM	0.050 – 200 μM	64
zoledronic acid	FI	40 nM	0.1 – 10 μM	35

FQ = fluorescence quenching, FI = fluorescence increase, AI = absorbance increase

2.4.2 Bioimaging

Bioimaging is one of the most studied applications of CDs due to their generally low cytotoxicity³ and resistance to photobleaching.² CDs have been used as bioimaging probes both *in vitro* (e.g., in A549²⁶ and HeLa cells⁹) and *in vivo* (e.g., zebrafish⁶⁵). CDs synthesized from watermelon peels were used to image HeLa cells, demonstrating that CDs can be good candidates for bioimaging due to their stability in aqueous solutions, small size, and strong fluorescence.²⁷ Some CDs exhibit excitation-dependent fluorescence allowing for their use in multicolour fluorescence imaging. This feature can be useful when imaging cells, tissues, or organisms which exhibit autofluorescence by allowing the user to easily switch between fluorescence wavelengths while using a single type of CD. In doing so, the user may quickly identify a wavelength that does not interfere with the natural fluorescence of their sample. For example, CDs derived from peanut shells were used to image HepG2 cells using excitation wavelengths of 405, 488, and 514 nm which resulted in blue, green, and red emission, respectively.²⁸ Similarly, CDs synthesized from *Allium fistulosum* were used to image MCF-7 and K562 cells using excitation wavelengths of 405, 488, and 561 nm which resulted in blue, green, and red emission, respectively.²⁵ CD surfaces can also be passivated with functional groups and heteroatoms that can impact their cytotoxicity and potential localization in cells. Dehvari *et al.* synthesized CDs from crab shells and functionalized the CDs with folic acid for targeted imaging of HeLa cells that possess significantly more folate-receptors than healthy cells.⁶⁶ These CDs showed enhanced uptake in cancer cells relative to their non-cancerous counterpart.⁶⁶

CDs synthesized using green approaches have also been used for *in vivo* imaging. Zebrafish embryos exhibited a ~93% survival rate (at 96 hours since fertilization) after 94 h of exposure to ≤ 200 $\mu\text{g/mL}$ CDs synthesized from gynostemma, compared to a ~97% survival rate in the control,

showing that these CDs can be safely used for bioimaging (Figure 2.4). However, the survival rate decreased to ~88% when the CD concentration increased to 400 $\mu\text{g/mL}$.⁶⁵ These CDs also showed antioxidant properties, effectively reducing the oxidative stress in the zebrafish, which may be partially responsible for their low toxicity.⁶⁵ Altogether, their study shows the importance of finding an optimal CD concentration which provides adequate imaging power while also minimizing toxicity to the organism or cells to be imaged.

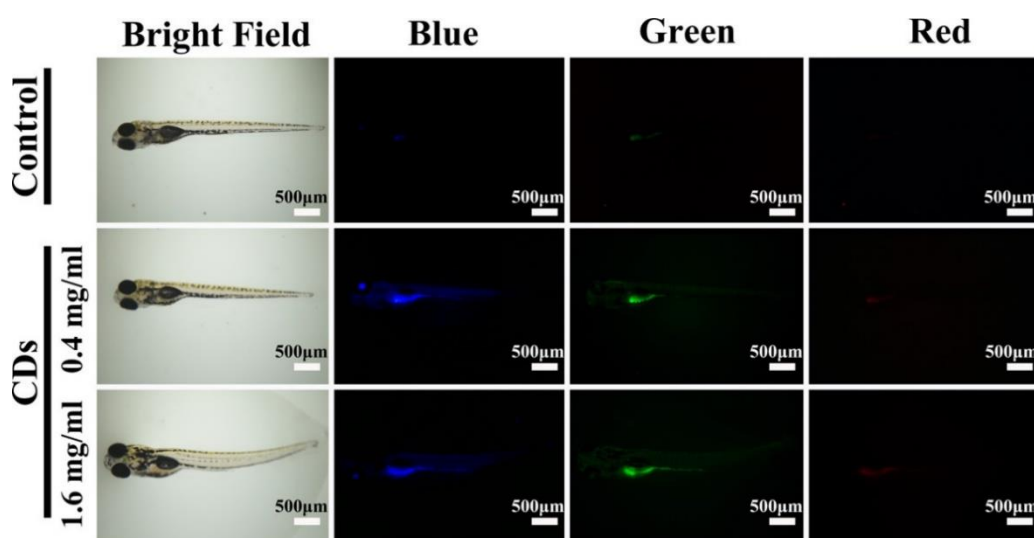


Figure 2.4. Zebrafish imaging using CDs synthesized from gynostemma. It is demonstrated that the probes localize in the digestive system. The CDs exhibit blue, green, or red fluorescence depending on the excitation source used. Reprinted with permission from ref ⁶⁵. Copyright 2019 American Chemical Society.

Most CD bioimaging probes localize in the cytoplasm and accumulate just outside the nucleus,^{43, 58} while some have been reported to also enter the nucleus itself.⁸ While these features are sufficient for general purpose bioimaging of cells, targeting specific organelles may also be of interest. The green synthesis of selectively localizing CDs is one area which merits further research to expand CD bioimaging applicability.

2.4.3 Biomedicine

CDs show promise in biomedical applications, in part due to the myriad of functional groups that decorate their surface, which allows for active targeting. For instance, Wang *et al.* used bovine serum albumin to develop a 6.8 nm hollow CD (HCD) loaded with doxorubicin.⁴⁶ After 90 minutes of incubation with the doxorubicin-HCD complex, red fluorescence stemming from the drug was observed in the nucleus of A549 cells.⁴⁶ The authors proposed a mechanism whereby the doxorubicin-HCD complex enters the cell through endocytosis and upon entering the lower pH lysosome, the complex releases the doxorubicin which then enters the nucleus.⁴⁶ Shao *et al.* have also synthesized CDs from mulberry leaves which were subsequently loaded with the anti-cancer drug lycorine.⁶⁷ Their lycorine-CD platform showed enhanced cell death in the cancerous HepG2 cell line when compared to lycorine alone.⁶⁷ CDs have also been used in antimicrobial applications. For instance, CDs synthesized from henna leaves were found to be much more effective antimicrobial agents than the bulk henna leaves against both Gram-positive *Staphylococcus aureus* and Gram-negative *Escherichia coli*.¹⁰

2.4.4 Ink

Inexpensive fluorescent inks for anti-counterfeiting applications (*e.g.*, invisible security inks) have been developed using green-synthesized CDs. For instance, CDs synthesized from oriental plane leaves were used as fluorescent inks to print patterns that were invisible under daylight and became visible under UV light (Figure 2.5).⁶⁸ Similarly, Wang *et al.* have synthesized CDs from milk which were used as fluorescent inks.⁶⁹ They were able to refill regular commercial inkjet cartridges with their CDs which were then used to produce fluorescent patterns on commercial paper.⁶⁹ The printed patterns exhibited green and red fluorescence under 455 and 523

nm excitation, respectively.⁶⁹ In another green synthesis, Qu *et al.* used citric acid and urea to produce CDs with fluorescent patterning capabilities.⁷⁰ They also showed that their CDs had no observable toxicity in bean sprouts and mice.⁷⁰ As a testament to their low toxicity, they applied their CDs on human skin and showed their use as a low-toxicity method of obtaining fingerprints.⁷⁰ Interestingly, CDs can exhibit excellent stability in printed patterns and can retain their fluorescent properties for up to 3 months.¹¹ However, in high-security applications, it is important that this fluorescence remains stable for several years. Therefore, more work is required to study and extend the long-term stability of green-synthesized CDs.

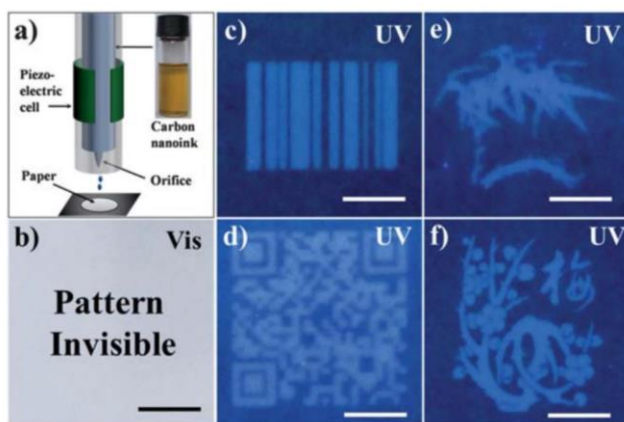


Figure 2.5. (a) Inkjet printing using CDs synthesized from oriental plane leaves. (b) Invisible pattern made from CD ink under visible light. (c, d, e, f) Fluorescent patterns made from CD ink under UV light. Scale bar = 1 cm. Reproduced from RSC ref ⁶⁸. Copyright 2013 The Royal Society of Chemistry.

2.4.5 Catalysis

With their high surface area-to-volume ratio and their versatile functional groups, CDs find application in catalysis. CDs synthesized from willow bark were used as a photocatalyst for the fabrication of a Au nanoparticle/reduced graphene oxide nanocomposite, demonstrating that the CDs effectively reduced both materials.¹² The resulting nanocomposite was used in a system that

catalyzes the reaction of glucose and oxygen into H_2O_2 allowing it to be an indirect method of glucose sensing *via* the detection of H_2O_2 .¹² In another study, Essner *et al.* synthesized CDs from citric acid.⁷¹ They first used their CDs to reduce HAuCl_4 to Au nanoparticle/CD hybrids at room temperature.⁷¹ They also showed that the CDs can reduce AgNO_3 to Ag nanoparticle/CD hybrids, albeit at elevated temperatures and with NaOH .⁷¹ They further demonstrated the performance of this Ag nanoparticle/CD hybrid as a catalyst to reduce 4-nitrophenol into 4-aminophenol in the presence of NaBH_4 .⁷¹ The use of waste products in green synthesis is often desirable to reduce the overall environmental impact of the synthesis process. For instance, Shih *et al.* synthesized CDs from used coffee grounds.⁷² The resulting CDs were used to synthesize $\text{Cu}_{2-x}\text{S}/\text{CD}$ hybrid nanomaterials which were integrated into a modified rotating disk electrode with a higher oxygen reduction reaction activity than its commercial Pt/C-modified counterpart.⁷² These studies highlight the diverse catalytic applications of CDs, particularly towards the synthesis of novel hybrid nanomaterials.

2.5 Conclusions and outlook

We have established what constitutes a green CD synthesis by considering some of the 12 Principles of Green Chemistry regarding the use of non-hazardous renewable materials, safe synthesis methods, and where possible, lowered energy requirements.¹³ The green synthesis of CDs is mainly performed using hydrothermal (or solvothermal), microwave, and dry heating methods. Plants are the most common feedstock for CD synthesis, although renewable refined compounds such as citric acid and amino acids have also been used. Purification of CDs is typically done using a combination of filtration, centrifugation, and/or dialysis.

Despite considerable advances in the green CD literature, several challenges need to be addressed to improve their range of application. Demand for sensors with increasing sensitivity requires the exploration of novel green CD detection platforms that go beyond the traditional approach of CD-analyte interactions. For instance, a third intermediary compound can often be used in conjunction with a CD to measure the concentration of an analyte that the CD or intermediary alone may fail to detect. In the field of bioimaging, the need for a wide variety of fluorescence wavelengths requires further research into the green synthesis of CDs with higher peak excitation/emission wavelengths. Moreover, while sensing and bioimaging are the most examined applications of green-synthesized CDs, their potential in other applications, such as catalysis and optoelectronics, remains largely untapped.

CDs are a diverse category of nanomaterials with endless production pathways. Closing the knowledge gap between CDs produced from green synthesis methods and those manufactured by traditional methods requires a deeper understanding of the relationship between the CD precursor, the synthesis and purification methods employed, the resulting CD's physicochemical properties, and the effect of these parameters on the performance of the CDs in various applications. The establishment of correlations between the physical (*e.g.*, size, shape) and chemical (*e.g.*, N:C, O:C) properties of a CD and the resulting optical properties (*e.g.*, peak excitation/emission wavelength, QY) and performance towards various applications will be essential to advance the field.

Conflicts of interest

There are no conflicts to declare.

Acknowledgements

The authors acknowledge funding from the Natural Sciences and Engineering Research Council of Canada, Canada Research Chairs Program, Killam Research Fellowship, Fonds de recherche du Québec – Nature et technologies and the Quebec Center for Advanced Materials. S. Chahal acknowledges NSERC for a PGS D scholarship, McGill University for a MEDA, and the EUL fund in the Department of Chemical Engineering. J.-R. Macairan is grateful for a FAS fellowship from Concordia University.

References

- (1) Xu, X.; Ray, R.; Gu, Y.; Ploehn, H. J.; Gearheart, L.; Raker, K.; Scrivens, W. A. Electrophoretic Analysis and Purification of Fluorescent Single-Walled Carbon Nanotube Fragments. *J. Am. Chem. Soc.* **2004**, *126* (40), 12736-12737. DOI: 10.1021/ja040082h.
- (2) Li, H.; Ye, S.; Guo, J.; Wang, H.; Yan, W.; Song, J.; Qu, J. Biocompatible carbon dots with low-saturation-intensity and high-photobleaching-resistance for STED nanoscopy imaging of the nucleolus and tunneling nanotubes in living cells. *Nano Research* **2019**, *12* (12), 3075-3084. DOI: 10.1007/s12274-019-2554-x.
- (3) Yang, S.-T.; Wang, X.; Wang, H.; Lu, F.; Luo, P. G.; Cao, L.; Meziani, M. J.; Liu, J.-H.; Liu, Y.; Chen, M.; et al. Carbon Dots as Nontoxic and High-Performance Fluorescence Imaging Agents. *The Journal of Physical Chemistry C* **2009**, *113* (42), 18110-18114. DOI: 10.1021/jp9085969.
- (4) Hummers, W. S.; Offeman, R. E. Preparation of Graphitic Oxide. *J. Am. Chem. Soc.* **1958**, *80* (6), 1339-1339. DOI: 10.1021/ja01539a017.
- (5) Wang, Q.; Zheng, H.; Long, Y.; Zhang, L.; Gao, M.; Bai, W. Microwave–hydrothermal synthesis of fluorescent carbon dots from graphite oxide. *Carbon* **2011**, *49* (9), 3134-3140. DOI: 10.1016/j.carbon.2011.03.041.
- (6) Jiang, X.; Qin, D.; Mo, G.; Feng, J.; Yu, C.; Mo, W.; Deng, B. Ginkgo leaf-based synthesis of nitrogen-doped carbon quantum dots for highly sensitive detection of salazosulfapyridine in mouse plasma. *J. Pharm. Biomed. Anal.* **2019**, *164*, 514-519. DOI: 10.1016/j.jpba.2018.11.025.
- (7) Chahal, S.; Yousefi, N.; Tufenkji, N. Green Synthesis of High Quantum Yield Carbon Dots from Phenylalanine and Citric Acid: Role of Stoichiometry and Nitrogen Doping. *ACS*

Sustainable Chemistry & Engineering **2020**, 8 (14), 5566-5575. DOI:

10.1021/acssuschemeng.9b07463.

- (8) Kumar, A.; Chowdhuri, A. R.; Laha, D.; Mahto, T. K.; Karmakar, P.; Sahu, S. K. Green synthesis of carbon dots from *Ocimum sanctum* for effective fluorescent sensing of Pb²⁺ ions and live cell imaging. *Sens. Actuators, B* **2017**, 242, 679-686. DOI: 10.1016/j.snb.2016.11.109.
- (9) Wan, Y.; Wang, M.; Zhang, K.; Fu, Q.; Gao, M.; Wang, L.; Xia, Z.; Gao, D. Facile and green synthesis of fluorescent carbon dots from the flowers of *Abelmoschus manihot* (Linn.) Medicus for sensitive detection of 2,4,6-trinitrophenol and cellular imaging. *Microchem. J.* **2019**, 148, 385-396. DOI: 10.1016/j.microc.2019.05.026.
- (10) Shahshahanipour, M.; Rezaei, B.; Ensafi, A. A.; Etemadifar, Z. An ancient plant for the synthesis of a novel carbon dot and its applications as an antibacterial agent and probe for sensing of an anti-cancer drug. *Mater. Sci. Eng., C* **2019**, 98, 826-833. DOI: 10.1016/j.msec.2019.01.041.
- (11) Bhatt, S.; Bhatt, M.; Kumar, A.; Vyas, G.; Gajaria, T.; Paul, P. Green route for synthesis of multifunctional fluorescent carbon dots from Tulsi leaves and its application as Cr(VI) sensors, bio-imaging and patterning agents. *Colloids Surf., B* **2018**, 167, 126-133. DOI: 10.1016/j.colsurfb.2018.04.008.
- (12) Qin, X.; Lu, W.; Asiri, A. M.; Al-Youbi, A. O.; Sun, X. Green, low-cost synthesis of photoluminescent carbon dots by hydrothermal treatment of willow bark and their application as an effective photocatalyst for fabricating Au nanoparticles-reduced graphene oxide nanocomposites for glucose detection. *Catalysis Science & Technology* **2013**, 3 (4), 1027-1035. DOI: 10.1039/C2CY20635H.

- (13) Anastas, P. T.; Warner, J. C. *Green Chemistry: Theory and Practice*; Oxford University Press, 1998.
- (14) Arkan, E.; Barati, A.; Rahmanpanah, M.; Hosseinzadeh, L.; Moradi, S.; Hajialyani, M. Green Synthesis of Carbon Dots Derived from Walnut Oil and an Investigation of Their Cytotoxic and Apoptogenic Activities toward Cancer Cells. *Adv. Pharm. Bull.* **2018**, *8* (1), 149-155. DOI: 10.15171/apb.2018.018.
- (15) Bao, R.; Chen, Z.; Zhao, Z.; Sun, X.; Zhang, J.; Hou, L.; Yuan, C. Green and Facile Synthesis of Nitrogen and Phosphorus Co-Doped Carbon Quantum Dots towards Fluorescent Ink and Sensing Applications. *Nanomater.* **2018**, *8* (6), 386. DOI: 10.3390/nano8060386.
- (16) Yadav, P. K.; Singh, V. K.; Chandra, S.; Bano, D.; Kumar, V.; Talat, M.; Hasan, S. H. Green Synthesis of Fluorescent Carbon Quantum Dots from *Azadirachta indica* Leaves and Their Peroxidase-Mimetic Activity for the Detection of H₂O₂ and Ascorbic Acid in Common Fresh Fruits. *ACS Biomater. Sci. Eng.* **2019**, *5* (2), 623-632. DOI: 10.1021/acsbomaterials.8b01528.
- (17) Shi, J.; Ni, G.; Tu, J.; Jin, X.; Peng, J. Green synthesis of fluorescent carbon dots for sensitive detection of Fe²⁺ and hydrogen peroxide. *J. Nanoparticle Res.* **2017**, *19* (6), 209. DOI: 10.1007/s11051-017-3888-5.
- (18) Liu, W.; Diao, H.; Chang, H.; Wang, H.; Li, T.; Wei, W. Green synthesis of carbon dots from rose-heart radish and application for Fe³⁺ detection and cell imaging. *Sens. Actuators, B* **2017**, *241*, 190-198. DOI: 10.1016/j.snb.2016.10.068.
- (19) Zhang, Z.; Hu, B.; Zhuang, Q.; Wang, Y.; Luo, X.; Xie, Y.; Zhou, D. Green Synthesis of Fluorescent Nitrogen–Sulfur Co-Doped Carbon Dots from Scallion Leaves for Hemin

Sensing. *Analytical Letters* **2020**, *53* (11), 1704-1718. DOI:

10.1080/00032719.2020.1716782.

- (20) Huang, H.; Lv, J.-J.; Zhou, D.-L.; Bao, N.; Xu, Y.; Wang, A.-J.; Feng, J.-J. One-pot green synthesis of nitrogen-doped carbon nanoparticles as fluorescent probes for mercury ions. *RSC Adv.* **2013**, *3* (44), 21691-21696. DOI: 10.1039/C3RA43452D.
- (21) Lu, W.; Qin, X.; Liu, S.; Chang, G.; Zhang, Y.; Luo, Y.; Asiri, A. M.; Al-Youbi, A. O.; Sun, X. Economical, Green Synthesis of Fluorescent Carbon Nanoparticles and Their Use as Probes for Sensitive and Selective Detection of Mercury(II) Ions. *Anal. Chem.* **2012**, *84* (12), 5351-5357. DOI: 10.1021/ac3007939.
- (22) Zuo, P.; Liu, J.; Guo, H.; Wang, C.; Liu, H.; Zhang, Z.; Liu, Q. Multifunctional N,S co-doped carbon dots for sensitive probing of temperature, ferric ion, and methotrexate. *Anal. Bioanal. Chem.* **2019**, *411* (8), 1647-1657. DOI: 10.1007/s00216-019-01617-4.
- (23) Zhang, Z.; Chen, J.; Duan, Y.; Liu, W.; Li, D.; Yan, Z.; Yang, K. Highly luminescent nitrogen-doped carbon dots for simultaneous determination of chlortetracycline and sulfasalazine. *Lumin.* **2018**, *33* (2), 318-325. DOI: 10.1002/bio.3416.
- (24) Bano, D.; Kumar, V.; Singh, V. K.; Hasan, S. H. Green synthesis of fluorescent carbon quantum dots for the detection of mercury(ii) and glutathione. *New Journal of Chemistry* **2018**, *42* (8), 5814-5821. DOI: 10.1039/C8NJ00432C.
- (25) Wei, Z.; Wang, B.; Liu, Y.; Liu, Z.; Zhang, H.; Zhang, S.; Chang, J.; Lu, S. Green synthesis of nitrogen and sulfur co-doped carbon dots from *Allium fistulosum* for cell imaging. *New J. Chem.* **2019**, *43* (2), 718-723. DOI: 10.1039/C8NJ05783D.
- (26) Wang, M.; Wan, Y.; Zhang, K.; Fu, Q.; Wang, L.; Zeng, J.; Xia, Z.; Gao, D. Green synthesis of carbon dots using the flowers of *Osmanthus fragrans* (Thunb.) Lour. as

- precursors: application in Fe³⁺ and ascorbic acid determination and cell imaging. *Anal. Bioanal. Chem.* **2019**, *411* (12), 2715-2727. DOI: 10.1007/s00216-019-01712-6.
- (27) Zhou, J.; Sheng, Z.; Han, H.; Zou, M.; Li, C. Facile synthesis of fluorescent carbon dots using watermelon peel as a carbon source. *Materials Letters* **2012**, *66* (1), 222-224. DOI: 10.1016/j.matlet.2011.08.081.
- (28) Xue, M.; Zhan, Z.; Zou, M.; Zhang, L.; Zhao, S. Green synthesis of stable and biocompatible fluorescent carbon dots from peanut shells for multicolor living cell imaging. *New J. Chem.* **2016**, *40* (2), 1698-1703. DOI: 10.1039/C5NJ02181B.
- (29) Yang, X.; Wang, D.; Luo, N.; Feng, M.; Peng, X.; Liao, X. Green synthesis of fluorescent N,S-carbon dots from bamboo leaf and the interaction with nitrophenol compounds. *Spectrochim. Acta, Part A* **2020**, *239*, 118462. DOI: 10.1016/j.saa.2020.118462.
- (30) Liu, L.; Mi, Z.; Hu, Q.; Li, C.; Li, X.; Feng, F. Green synthesis of fluorescent carbon dots as an effective fluorescence probe for morin detection. *Anal. Methods* **2019**, *11* (3), 353-358. DOI: 10.1039/C8AY02361A.
- (31) Gu, D.; Shang, S.; Yu, Q.; Shen, J. Green synthesis of nitrogen-doped carbon dots from lotus root for Hg(II) ions detection and cell imaging. *Appl. Surf. Sci.* **2016**, *390*, 38-42. DOI: 10.1016/j.apsusc.2016.08.012.
- (32) Murugan, N.; Sundramoorthy, A. K. Green synthesis of fluorescent carbon dots from *Borassus flabellifer* flowers for label-free highly selective and sensitive detection of Fe³⁺ ions. *New J. Chem.* **2018**, *42* (16), 13297-13307. DOI: 10.1039/C8NJ01894D.
- (33) Huang, Q.; Li, Q.; Chen, Y.; Tong, L.; Lin, X.; Zhu, J.; Tong, Q. High quantum yield nitrogen-doped carbon dots: green synthesis and application as “off-on” fluorescent

sensors for the determination of Fe³⁺ and adenosine triphosphate in biological samples.

Sens. Actuators, B **2018**, 276, 82-88. DOI: 10.1016/j.snb.2018.08.089.

- (34) Sobhani, R.; Rezaei, B.; Shahshahanipour, M.; Ensafi, A. A.; Mohammadnezhad, G. Simple and green synthesis of carbon dots (CDs) from valerian root and application of modified mesoporous boehmite (AlOOH) with CDs as a fluorescence probe for determination of imipramine. *Anal. Bioanal. Chem.* **2019**, 411 (14), 3115-3124. DOI: 10.1007/s00216-019-01779-1.
- (35) Amin, N.; Afkhami, A.; Hosseinzadeh, L.; Madrakian, T. Green and cost-effective synthesis of carbon dots from date kernel and their application as a novel switchable fluorescence probe for sensitive assay of Zoledronic acid drug in human serum and cellular imaging. *Anal. Chim. Acta* **2018**, 1030, 183-193. DOI: 10.1016/j.aca.2018.05.014.
- (36) Rooj, B.; Dutta, A.; Islam, S.; Mandal, U. Green Synthesized Carbon Quantum Dots from *Polianthes tuberosa* L. Petals for Copper (II) and Iron (II) Detection. *J. Fluoresc.* **2018**, 28 (5), 1261-1267. DOI: 10.1007/s10895-018-2292-6.
- (37) Lotfy, W. A.; Ghanem, K. M.; El-Helow, E. R. Citric acid production by a novel *Aspergillus niger* isolate: II. Optimization of process parameters through statistical experimental designs. *Bioresour. Technol.* **2007**, 98 (18), 3470-3477. DOI: 10.1016/j.biortech.2006.11.032.
- (38) Penniston, K. L.; Nakada, S. Y.; Holmes, R. P.; Assimos, D. G. Quantitative assessment of citric acid in lemon juice, lime juice, and commercially-available fruit juice products. *J. Endourol.* **2008**, 22 (3), 567-570. DOI: 10.1089/end.2007.0304 PubMed.

- (39) Qu, Y.; Yu, L.; Zhu, B.; Chai, F.; Su, Z. Green synthesis of carbon dots by celery leaves for use as fluorescent paper sensors for the detection of nitrophenols. *New J. Chem.* **2020**, *44* (4), 1500-1507. DOI: 10.1039/C9NJ05285B.
- (40) Noun, F.; Manioudakis, J.; Naccache, R. Toward Uniform Optical Properties of Carbon Dots. *Part. Part. Syst. Charact.* **2020**, *37* (8), 2000119. DOI: 10.1002/ppsc.202000119.
- (41) Essner, J. B.; Kist, J. A.; Polo-Parada, L.; Baker, G. A. Artifacts and Errors Associated with the Ubiquitous Presence of Fluorescent Impurities in Carbon Nanodots. *Chem. Mater.* **2018**, *30* (6), 1878-1887. DOI: 10.1021/acs.chemmater.7b04446.
- (42) Liu, M. L.; Chen, B. B.; Li, C. M.; Huang, C. Z. Carbon dots: synthesis, formation mechanism, fluorescence origin and sensing applications. *Green Chem.* **2019**, *21* (3), 449-471. DOI: 10.1039/C8GC02736F.
- (43) Vasimalai, N.; Vilas-Boas, V.; Gallo, J.; Cerqueira, M. d. F.; Menéndez-Miranda, M.; Costa-Fernández, J. M.; Diéguez, L.; Espiña, B.; Fernández-Argüelles, M. T. Green synthesis of fluorescent carbon dots from spices for in vitro imaging and tumour cell growth inhibition. *Beilstein J. Nanotechnol.* **2018**, *9*, 530-544. DOI: 10.3762/bjnano.9.51.
- (44) Chandra, S.; Laha, D.; Pramanik, A.; Ray Chowdhuri, A.; Karmakar, P.; Sahu, S. K. Synthesis of highly fluorescent nitrogen and phosphorus doped carbon dots for the detection of Fe³⁺ ions in cancer cells. *Lumin.* **2016**, *31* (1), 81-87. DOI: 10.1002/bio.2927.
- (45) Wu, G.; Feng, M.; Zhan, H. Generation of nitrogen-doped photoluminescent carbonaceous nanodots via the hydrothermal treatment of fish scales for the detection of hypochlorite. *RSC Adv.* **2015**, *5* (55), 44636-44641. DOI: 10.1039/C5RA04989J.

- (46) Wang, Q.; Huang, X.; Long, Y.; Wang, X.; Zhang, H.; Zhu, R.; Liang, L.; Teng, P.; Zheng, H. Hollow luminescent carbon dots for drug delivery. *Carbon* **2013**, *59*, 192-199. DOI: 10.1016/j.carbon.2013.03.009.
- (47) Domingos, R. F.; Baalousha, M. A.; Ju-Nam, Y.; Reid, M. M.; Tufenkji, N.; Lead, J. R.; Leppard, G. G.; Wilkinson, K. J. Characterizing Manufactured Nanoparticles in the Environment: Multimethod Determination of Particle Sizes. *Environ. Sci. Technol.* **2009**, *43* (19), 7277-7284. DOI: 10.1021/es900249m.
- (48) Sun, Q.-C.; Ding, Y. C.; Sagar, D. M.; Nagpal, P. Photon upconversion towards applications in energy conversion and bioimaging. *Prog. Surf. Sci.* **2017**, *92* (4), 281-316. DOI: 10.1016/j.progsurf.2017.09.003.
- (49) Liang, Q.; Ma, W.; Shi, Y.; Li, Z.; Yang, X. Easy synthesis of highly fluorescent carbon quantum dots from gelatin and their luminescent properties and applications. *Carbon* **2013**, *60*, 421-428. DOI: 10.1016/j.carbon.2013.04.055.
- (50) Williams, A. T. R.; Winfield, S. A.; Miller, J. N. Relative fluorescence quantum yields using a computer-controlled luminescence spectrometer. *Anal.* **1983**, *108* (1290), 1067-1071. DOI: 10.1039/AN9830801067.
- (51) Zhang, Y.; Liu, X.; Fan, Y.; Guo, X.; Zhou, L.; Lv, Y.; Lin, J. One-step microwave synthesis of N-doped hydroxyl-functionalized carbon dots with ultra-high fluorescence quantum yields. *Nanoscale* **2016**, *8* (33), 15281-15287. DOI: 10.1039/C6NR03125K.
- (52) Liao, J.; Cheng, Z.; Zhou, L. Nitrogen-Doping Enhanced Fluorescent Carbon Dots: Green Synthesis and Their Applications for Bioimaging and Label-Free Detection of Au³⁺ Ions. *ACS Sustainable Chemistry & Engineering* **2016**, *4* (6), 3053-3061. DOI: 10.1021/acssuschemeng.6b00018.

- (53) Chen, W.; Yan, L.; Bangal, P. R. Preparation of graphene by the rapid and mild thermal reduction of graphene oxide induced by microwaves. *Carbon* **2010**, *48* (4), 1146-1152. DOI: 10.1016/j.carbon.2009.11.037.
- (54) Ramezani, Z.; Qorbanpour, M.; Rahbar, N. Green synthesis of carbon quantum dots using quince fruit (*Cydonia oblonga*) powder as carbon precursor: Application in cell imaging and As³⁺ determination. *Colloids Surf., A* **2018**, *549*, 58-66. DOI: 10.1016/j.colsurfa.2018.04.006.
- (55) Radhakrishnan, K.; Panneerselvam, P. Green synthesis of surface-passivated carbon dots from the prickly pear cactus as a fluorescent probe for the dual detection of arsenic(iii) and hypochlorite ions from drinking water. *RSC Advances* **2018**, *8* (53), 30455-30467. DOI: 10.1039/C8RA05861J.
- (56) Murugan, N.; Prakash, M.; Jayakumar, M.; Sundaramurthy, A.; Sundramoorthy, A. K. Green synthesis of fluorescent carbon quantum dots from *Eleusine coracana* and their application as a fluorescence 'turn-off' sensor probe for selective detection of Cu²⁺. *Appl. Surf. Sci.* **2019**, *476*, 468-480. DOI: 10.1016/j.apsusc.2019.01.090.
- (57) Pourreza, N.; Ghomi, M. Green synthesized carbon quantum dots from *Prosopis juliflora* leaves as a dual off-on fluorescence probe for sensing mercury (II) and chemet drug. *Mater. Sci. Eng., C* **2019**, *98*, 887-896. DOI: 10.1016/j.msec.2018.12.141.
- (58) Konar, S.; Kumar, B. N. P.; Mahto, M. K.; Samanta, D.; Shaik, M. A. S.; Shaw, M.; Mandal, M.; Pathak, A. N-doped carbon dot as fluorescent probe for detection of cysteamine and multicolor cell imaging. *Sens. Actuators, B* **2019**, *286*, 77-85. DOI: 10.1016/j.snb.2019.01.117.

- (59) Rezaei, B.; Hassani, Z.; Shahshahanipour, M.; Ensafi, A. A.; Mohammadnezhad, G. Application of modified mesoporous boehmite (γ -AlOOH) with green synthesis carbon quantum dots for a fabrication biosensor to determine trace amounts of doxorubicin. *Lumin.* **2018**, *33* (8), 1377-1386. DOI: 10.1002/bio.3558.
- (60) Wang, L.; Bi, Y.; Hou, J.; Li, H.; Xu, Y.; Wang, B.; Ding, H.; Ding, L. Facile, green and clean one-step synthesis of carbon dots from wool: Application as a sensor for glyphosate detection based on the inner filter effect. *Talanta* **2016**, *160*, 268-275. DOI: 10.1016/j.talanta.2016.07.020.
- (61) Ensafi, A. A.; Sefat, S. H.; Kazemifard, N.; Rezaei, B. An optical sensor based on inner filter effect using green synthesized carbon dots and Cu(II) for selective and sensitive penicillamine determination. *J. Iran. Chem. Soc.* **2019**, *16* (2), 355-363. DOI: 10.1007/s13738-018-1518-5.
- (62) Ensafi, A. A.; Hghighat Sefat, S.; Kazemifard, N.; Rezaei, B.; Moradi, F. A novel one-step and green synthesis of highly fluorescent carbon dots from saffron for cell imaging and sensing of prilocaine. *Sens. Actuators, B* **2017**, *253*, 451-460. DOI: 10.1016/j.snb.2017.06.163.
- (63) Ahmed, H. M.; Ghali, M.; Zahra, W. K.; Ayad, M. Optical sensing of pyridine based on green synthesis of passivated carbon dots. *Materials Today: Proceedings* **2020**, *33*, 1845-1848. DOI: 10.1016/j.matpr.2020.05.185.
- (64) Lai, Z.; Guo, X.; Cheng, Z.; Ruan, G.; Du, F. Green Synthesis of Fluorescent Carbon Dots from Cherry Tomatoes for Highly Effective Detection of Trifluralin Herbicide in Soil Samples. *ChemistrySelect* **2020**, *5* (6), 1956-1960. DOI: 10.1002/slct.201904517.

- (65) Wei, X.; Li, L.; Liu, J.; Yu, L.; Li, H.; Cheng, F.; Yi, X.; He, J.; Li, B. Green Synthesis of Fluorescent Carbon Dots from *Gynostemma* for Bioimaging and Antioxidant in Zebrafish. *ACS Applied Materials & Interfaces* **2019**, *11* (10), 9832-9840. DOI: 10.1021/acsami.9b00074.
- (66) Dehvari, K.; Liu, K. Y.; Tseng, P.-J.; Gedda, G.; Girma, W. M.; Chang, J.-Y. Sonochemical-assisted green synthesis of nitrogen-doped carbon dots from crab shell as targeted nanoprobe for cell imaging. *J. Taiwan Inst. Chem. Eng.* **2019**, *95*, 495-503. DOI: 10.1016/j.jtice.2018.08.037.
- (67) Shao, Y.; Zhu, C.; Fu, Z.; Lin, K.; Wang, Y.; Chang, Y.; Han, L.; Yu, H.; Tian, F. Green synthesis of multifunctional fluorescent carbon dots from mulberry leaves (*Morus alba* L.) residues for simultaneous intracellular imaging and drug delivery. *J. Nanoparticle Res.* **2020**, *22* (8), 229. DOI: 10.1007/s11051-020-04917-4.
- (68) Zhu, L.; Yin, Y.; Wang, C.-F.; Chen, S. Plant leaf-derived fluorescent carbon dots for sensing, patterning and coding. *J. Mater. Chem. C* **2013**, *1* (32), 4925-4932. DOI: 10.1039/C3TC30701H.
- (69) Wang, J.; Peng, F.; Lu, Y.; Zhong, Y.; Wang, S.; Xu, M.; Ji, X.; Su, Y.; Liao, L.; He, Y. Large-Scale Green Synthesis of Fluorescent Carbon Nanodots and Their Use in Optics Applications. *Adv. Opt. Mater.* **2015**, *3* (1), 103-111. DOI: 10.1002/adom.201400307.
- (70) Qu, S.; Wang, X.; Lu, Q.; Liu, X.; Wang, L. A Biocompatible Fluorescent Ink Based on Water-Soluble Luminescent Carbon Nanodots. *Angew. Chem., Int. Ed.* **2012**, *51* (49), 12215-12218. DOI: 10.1002/anie.201206791.

- (71) Essner, J. B.; Laber, C. H.; Baker, G. A. Carbon dot reduced bimetallic nanoparticles: size and surface plasmon resonance tunability for enhanced catalytic applications. *J. Mater. Chem. A* **2015**, *3* (31), 16354-16360. DOI: 10.1039/C5TA02949J.
- (72) Shih, Z.-Y.; Periasamy, A. P.; Hsu, P.-C.; Chang, H.-T. Synthesis and catalysis of copper sulfide/carbon nanodots for oxygen reduction in direct methanol fuel cells. *Applied Catalysis B: Environmental* **2013**, *132-133*, 363-369. DOI: 10.1016/j.apcatb.2012.12.004.

Electronic supplementary information

Table S2.1. References for images in Figure 2.1. All images are in the public domain.

Image	Source
walnut	https://commons.wikimedia.org/wiki/File:Walnuts_no_shell.jpg
tulsi	https://commons.wikimedia.org/wiki/File:Basil-raihan.jpg
ginkgo	https://commons.wikimedia.org/wiki/File:GinkgoSaplings.jpg
prickly pear	https://commons.wikimedia.org/wiki/File:Prickly_Pear_Closeup.jpg
<i>Eleusine coracana</i>	https://commons.wikimedia.org/wiki/File:Finger_millet_3_11-21-02.jpg
<i>Prosopis juliflora</i>	https://commons.wikimedia.org/wiki/File:Prosopis_juliflora.jpg
<i>Eleocharis dulcis</i>	https://commons.wikimedia.org/wiki/File:Wasserkastanien.jpg

Table S2.2. References for data shown in Figures 2.1b, 2.2d, 2.2e, 2.2f, 2.3f.

Carbon source	Reagents type	Reaction medium	Synthesis conditions	Synthesis method	Filtration	Centrifugation	Dialysis	Size [nm]	N:C	O:C	Excitation [nm]	Emission [nm]	QY [%]	Ref
glycine, urea	refined compound	water	800 W, 3 min	microwave	no	no	yes	3.2	0.396	0.419	320	380	13	1
mulberry	raw material	water	200 °C, 6 h	hydrothermal	yes	no	yes	3	0.058	0.330	320	390	-	2
L-ascorbic acid, β-alanine	refined compound	water	180 °C, 1 h	microwave	no	yes	yes	-	0.054	0.332	325	401	14	3
<i>Borassus flabellifer</i>	raw material	air	300 °C, 2 h	dry heating	yes	no	no	5.1	-	-	320	403	13.97	4
<i>Abelmoschus manihot</i>	raw material	water	220 °C, 4 h	hydrothermal	yes	yes	no	9	0.251	0.072	330	410	30.8	5
<i>Osmanthus fragrans</i>	raw material	water	240 °C, 5 h	hydrothermal	yes	yes	yes	2.23	0.041	0.376	340	411	18.53	6
citric acid, L-phenylalanine	refined compound	water	200 °C, 8 h	hydrothermal	yes	no	yes	11.9	0.136	0.355	350	413	65	7
celery, L-glutathione	hybrid	water	200 °C, 4 h	hydrothermal	yes	no	no	2.08	-	-	340	415	53	8
<i>Tamarindus indica</i>	raw material	water	210 °C, 5 h	hydrothermal	no	yes	yes	3.4	0.278	0.679	320	417	46.6	9
scallion	raw material	water	180 °C, 12 h	hydrothermal	no	yes	no	3.5	0.123	0.268	320	418	3.2	10
bamboo	raw material	air	300 °C, 3 h	dry heating	yes	no	no	11	0.062	1.002	313	419	5.18	11
rose-heart radish	raw material	water	180 °C, 3 h	hydrothermal	yes	yes	yes	3.6	0.130	0.429	330	420	13.6	12
<i>Eleusine coracana</i>	raw material	air	300 °C, 3 h	dry heating	yes	no	no	5.4	-	-	340	425	-	13
strawberry	raw material	water	180 °C, 12 h	hydrothermal	yes	no	no	5.2	0.102	0.354	344	427	6.3	14
walnut	raw material	walnut oil	220 °C, 24 h	solvothermal	yes	yes	no	12.3	0.052	1.117	360	430	14.5	15
cherry tomato	raw material	water	180 °C, 6 h	hydrothermal	yes	yes	yes	7	-	-	340	430	9.7	16
citric acid, glutathione	refined compound	water	200 °C, 4 h	hydrothermal	no	yes	yes	6.1	0.202	0.261	340	432	75	17
tulsi	raw material	water	200 °C, 4 h	hydrothermal	yes	no	no	5	0.100	0.886	360	435	3.06	18
lotus	raw material	water	800 W, 6 min	microwave	yes	yes	yes	9.41	0.085	0.533	360	435	19	19
ginkgo	raw material	water	200 °C, 10 h	hydrothermal	yes	yes	yes	3	0.059	0.353	350	436	22.8	20
<i>Prosopis juliflora</i>	raw material	air	200 °C, 1 h	dry heating	no	yes	no	5.8	-	-	350	437	4.9	21
peanut	raw material	air	250 °C, 2 h	dry heating	yes	no	no	1.62	0.040	0.494	320	440	9.91	22
citric acid, L-arginine	refined compound	water	200 °C, 8 h	hydrothermal	no	no	yes	2.7	0.108	0.172	350	440	38.8	23
<i>Bauhinia</i>	hybrid	ethanol/water	1000 W, 10 min	microwave	no	yes	yes	3.4	-	-	355	442	27	24
willow	raw material	water	200 °C, 3 h	hydrothermal	no	yes	yes	1.6	0.430	0.388	360	444	6	25
pomelo	raw material	water	200 °C, 3 h	hydrothermal	no	yes	no	2.9	0.057	0.349	365	444	6.9	26
folic acid	refined compound	water	180 °C, 3 h	hydrothermal	no	yes	no	2.8	-	-	380	445	31.59	27
pepper	raw material	water	180 °C, 5 h	hydrothermal	no	yes	yes	4.6	-	-	360	450	19.3	28
<i>Eleocharis dulcis</i>	raw material	water	120 °C, 5 h	hydrothermal	yes	yes	yes	3	0.050	0.326	380	458	11.2	29
<i>Azadirachta indica</i>	raw material	water	150 °C, 4 h	hydrothermal	no	yes	yes	3.2	0.088	0.120	340	467	27.2	30
potato	raw material	water	220 °C, 3 h	hydrothermal	no	yes	no	11	-	-	400	470	-	31
black pepper	raw material	water	200 °C, 12 h	hydrothermal	yes	no	yes	3.5	-	-	390	489	43.6	32
maize	raw material	water	160 °C, 10 h	hydrothermal	yes	no	yes	5.2	0.016	0.346	420	500	7.6	33
<i>Ocimum sanctum</i>	raw material	water	180 °C, 4 h	hydrothermal	yes	no	yes	2.4	0.180	0.347	450	500	9.3	34
<i>Allium fistulosum</i>	raw material	water	220 °C, 3 h	hydrothermal	no	yes	yes	4.22	0.367	0.378	412	503	10.48	35
watermelon	raw material	air	220 °C, 2 h	dry heating	yes	yes	yes	2	0.015	0.308	470	537	7.1	36

QY = Quantum yield

References

- (1) Liu, L.; Mi, Z.; Hu, Q.; Li, C.; Li, X.; Feng, F. Green synthesis of fluorescent carbon dots as an effective fluorescence probe for morin detection. *Anal. Methods* **2019**, *11* (3), 353-358. DOI: 10.1039/C8AY02361A.
- (2) Shao, Y.; Zhu, C.; Fu, Z.; Lin, K.; Wang, Y.; Chang, Y.; Han, L.; Yu, H.; Tian, F. Green synthesis of multifunctional fluorescent carbon dots from mulberry leaves (*Morus alba* L.) residues for simultaneous intracellular imaging and drug delivery. *J. Nanoparticle Res.* **2020**, *22* (8), 229. DOI: 10.1007/s11051-020-04917-4.
- (3) Edison, T. N. J. I.; Atchudan, R.; Sethuraman, M. G.; Shim, J.-J.; Lee, Y. R. Microwave assisted green synthesis of fluorescent N-doped carbon dots: Cytotoxicity and bio-imaging applications. *J. Photochem. Photobiol., B* **2016**, *161*, 154-161. DOI: 10.1016/j.jphotobiol.2016.05.017.
- (4) Murugan, N.; Sundramoorthy, A. K. Green synthesis of fluorescent carbon dots from *Borassus flabellifer* flowers for label-free highly selective and sensitive detection of Fe³⁺ ions. *New J. Chem.* **2018**, *42* (16), 13297-13307. DOI: 10.1039/C8NJ01894D.
- (5) Wan, Y.; Wang, M.; Zhang, K.; Fu, Q.; Gao, M.; Wang, L.; Xia, Z.; Gao, D. Facile and green synthesis of fluorescent carbon dots from the flowers of *Abelmoschus manihot* (Linn.) Medicus for sensitive detection of 2,4,6-trinitrophenol and cellular imaging. *Microchem. J.* **2019**, *148*, 385-396. DOI: 10.1016/j.microc.2019.05.026.
- (6) Wang, M.; Wan, Y.; Zhang, K.; Fu, Q.; Wang, L.; Zeng, J.; Xia, Z.; Gao, D. Green synthesis of carbon dots using the flowers of *Osmanthus fragrans* (Thunb.) Lour. as precursors: application in Fe³⁺ and ascorbic acid determination and cell imaging. *Anal. Bioanal. Chem.* **2019**, *411* (12), 2715-2727. DOI: 10.1007/s00216-019-01712-6.

- (7) Chahal, S.; Yousefi, N.; Tufenkji, N. Green Synthesis of High Quantum Yield Carbon Dots from Phenylalanine and Citric Acid: Role of Stoichiometry and Nitrogen Doping. *ACS Sustainable Chemistry & Engineering* **2020**, *8* (14), 5566-5575. DOI: 10.1021/acssuschemeng.9b07463.
- (8) Qu, Y.; Yu, L.; Zhu, B.; Chai, F.; Su, Z. Green synthesis of carbon dots by celery leaves for use as fluorescent paper sensors for the detection of nitrophenols. *New J. Chem.* **2020**, *44* (4), 1500-1507. DOI: 10.1039/C9NJ05285B.
- (9) Bano, D.; Kumar, V.; Singh, V. K.; Hasan, S. H. Green synthesis of fluorescent carbon quantum dots for the detection of mercury(ii) and glutathione. *New Journal of Chemistry* **2018**, *42* (8), 5814-5821. DOI: 10.1039/C8NJ00432C.
- (10) Zhang, Z.; Hu, B.; Zhuang, Q.; Wang, Y.; Luo, X.; Xie, Y.; Zhou, D. Green Synthesis of Fluorescent Nitrogen–Sulfur Co-Doped Carbon Dots from Scallion Leaves for Hemin Sensing. *Analytical Letters* **2020**, *53* (11), 1704-1718. DOI: 10.1080/00032719.2020.1716782.
- (11) Yang, X.; Wang, D.; Luo, N.; Feng, M.; Peng, X.; Liao, X. Green synthesis of fluorescent N,S-carbon dots from bamboo leaf and the interaction with nitrophenol compounds. *Spectrochim. Acta, Part A* **2020**, *239*, 118462. DOI: 10.1016/j.saa.2020.118462.
- (12) Liu, W.; Diao, H.; Chang, H.; Wang, H.; Li, T.; Wei, W. Green synthesis of carbon dots from rose-heart radish and application for Fe³⁺ detection and cell imaging. *Sens. Actuators, B* **2017**, *241*, 190-198. DOI: 10.1016/j.snb.2016.10.068.
- (13) Murugan, N.; Prakash, M.; Jayakumar, M.; Sundaramurthy, A.; Sundramoorthy, A. K. Green synthesis of fluorescent carbon quantum dots from *Eleusine coracana* and their

- application as a fluorescence ‘turn-off’ sensor probe for selective detection of Cu²⁺. *Appl. Surf. Sci.* **2019**, *476*, 468-480. DOI: 10.1016/j.apsusc.2019.01.090.
- (14) Huang, H.; Lv, J.-J.; Zhou, D.-L.; Bao, N.; Xu, Y.; Wang, A.-J.; Feng, J.-J. One-pot green synthesis of nitrogen-doped carbon nanoparticles as fluorescent probes for mercury ions. *RSC Adv.* **2013**, *3* (44), 21691-21696. DOI: 10.1039/C3RA43452D.
- (15) Arkan, E.; Barati, A.; Rahmanpanah, M.; Hosseinzadeh, L.; Moradi, S.; Hajialyani, M. Green Synthesis of Carbon Dots Derived from Walnut Oil and an Investigation of Their Cytotoxic and Apoptogenic Activities toward Cancer Cells. *Adv. Pharm. Bull.* **2018**, *8* (1), 149-155. DOI: 10.15171/apb.2018.018.
- (16) Lai, Z.; Guo, X.; Cheng, Z.; Ruan, G.; Du, F. Green Synthesis of Fluorescent Carbon Dots from Cherry Tomatoes for Highly Effective Detection of Trifluralin Herbicide in Soil Samples. *ChemistrySelect* **2020**, *5* (6), 1956-1960. DOI: 10.1002/slct.201904517.
- (17) Zuo, P.; Liu, J.; Guo, H.; Wang, C.; Liu, H.; Zhang, Z.; Liu, Q. Multifunctional N,S co-doped carbon dots for sensitive probing of temperature, ferric ion, and methotrexate. *Anal. Bioanal. Chem.* **2019**, *411* (8), 1647-1657. DOI: 10.1007/s00216-019-01617-4.
- (18) Bhatt, S.; Bhatt, M.; Kumar, A.; Vyas, G.; Gajaria, T.; Paul, P. Green route for synthesis of multifunctional fluorescent carbon dots from Tulsi leaves and its application as Cr(VI) sensors, bio-imaging and patterning agents. *Colloids Surf., B* **2018**, *167*, 126-133. DOI: 10.1016/j.colsurfb.2018.04.008.
- (19) Gu, D.; Shang, S.; Yu, Q.; Shen, J. Green synthesis of nitrogen-doped carbon dots from lotus root for Hg(II) ions detection and cell imaging. *Appl. Surf. Sci.* **2016**, *390*, 38-42. DOI: 10.1016/j.apsusc.2016.08.012.

- (20) Jiang, X.; Qin, D.; Mo, G.; Feng, J.; Yu, C.; Mo, W.; Deng, B. Ginkgo leaf-based synthesis of nitrogen-doped carbon quantum dots for highly sensitive detection of salazosulfapyridine in mouse plasma. *J. Pharm. Biomed. Anal.* **2019**, *164*, 514-519. DOI: 10.1016/j.jpba.2018.11.025.
- (21) Pourreza, N.; Ghomi, M. Green synthesized carbon quantum dots from *Prosopis juliflora* leaves as a dual off-on fluorescence probe for sensing mercury (II) and chemet drug. *Mater. Sci. Eng., C* **2019**, *98*, 887-896. DOI: 10.1016/j.msec.2018.12.141.
- (22) Xue, M.; Zhan, Z.; Zou, M.; Zhang, L.; Zhao, S. Green synthesis of stable and biocompatible fluorescent carbon dots from peanut shells for multicolor living cell imaging. *New J. Chem.* **2016**, *40* (2), 1698-1703. DOI: 10.1039/C5NJ02181B.
- (23) Zhang, Z.; Chen, J.; Duan, Y.; Liu, W.; Li, D.; Yan, Z.; Yang, K. Highly luminescent nitrogen-doped carbon dots for simultaneous determination of chlortetracycline and sulfasalazine. *Lumin.* **2018**, *33* (2), 318-325. DOI: 10.1002/bio.3416.
- (24) Huang, Q.; Li, Q.; Chen, Y.; Tong, L.; Lin, X.; Zhu, J.; Tong, Q. High quantum yield nitrogen-doped carbon dots: green synthesis and application as “off-on” fluorescent sensors for the determination of Fe³⁺ and adenosine triphosphate in biological samples. *Sens. Actuators, B* **2018**, *276*, 82-88. DOI: 10.1016/j.snb.2018.08.089.
- (25) Qin, X.; Lu, W.; Asiri, A. M.; Al-Youbi, A. O.; Sun, X. Green, low-cost synthesis of photoluminescent carbon dots by hydrothermal treatment of willow bark and their application as an effective photocatalyst for fabricating Au nanoparticles-reduced graphene oxide nanocomposites for glucose detection. *Catalysis Science & Technology* **2013**, *3* (4), 1027-1035. DOI: 10.1039/C2CY20635H.

- (26) Lu, W.; Qin, X.; Liu, S.; Chang, G.; Zhang, Y.; Luo, Y.; Asiri, A. M.; Al-Youbi, A. O.; Sun, X. Economical, Green Synthesis of Fluorescent Carbon Nanoparticles and Their Use as Probes for Sensitive and Selective Detection of Mercury(II) Ions. *Anal. Chem.* **2012**, *84* (12), 5351-5357. DOI: 10.1021/ac3007939.
- (27) Zheng, Y.; Yang, D.; Wu, X.; Yan, H.; Zhao, Y.; Feng, B.; Duan, K.; Weng, J.; Wang, J. A facile approach for the synthesis of highly luminescent carbon dots using vitamin-based small organic molecules with benzene ring structure as precursors. *RSC Adv.* **2015**, *5* (110), 90245-90254. DOI: 10.1039/C5RA14720D.
- (28) Yin, B.; Deng, J.; Peng, X.; Long, Q.; Zhao, J.; Lu, Q.; Chen, Q.; Li, H.; Tang, H.; Zhang, Y.; et al. Green synthesis of carbon dots with down- and up-conversion fluorescent properties for sensitive detection of hypochlorite with a dual-readout assay. *Anal.* **2013**, *138* (21), 6551-6557. DOI: 10.1039/C3AN01003A.
- (29) Bao, R.; Chen, Z.; Zhao, Z.; Sun, X.; Zhang, J.; Hou, L.; Yuan, C. Green and Facile Synthesis of Nitrogen and Phosphorus Co-Doped Carbon Quantum Dots towards Fluorescent Ink and Sensing Applications. *Nanomater.* **2018**, *8* (6), 386. DOI: 10.3390/nano8060386.
- (30) Yadav, P. K.; Singh, V. K.; Chandra, S.; Bano, D.; Kumar, V.; Talat, M.; Hasan, S. H. Green Synthesis of Fluorescent Carbon Quantum Dots from *Azadirachta indica* Leaves and Their Peroxidase-Mimetic Activity for the Detection of H₂O₂ and Ascorbic Acid in Common Fresh Fruits. *ACS Biomater. Sci. Eng.* **2019**, *5* (2), 623-632. DOI: 10.1021/acsbiomaterials.8b01528.

- (31) Ahmed, H. M.; Ghali, M.; Zahra, W. K.; Ayad, M. Optical sensing of pyridine based on green synthesis of passivated carbon dots. *Materials Today: Proceedings* **2020**, *33*, 1845-1848. DOI: 10.1016/j.matpr.2020.05.185.
- (32) Vasimalai, N.; Vilas-Boas, V.; Gallo, J.; Cerqueira, M. d. F.; Menéndez-Miranda, M.; Costa-Fernández, J. M.; Diéguez, L.; Espiña, B.; Fernández-Argüelles, M. T. Green synthesis of fluorescent carbon dots from spices for in vitro imaging and tumour cell growth inhibition. *Beilstein J. Nanotechnol.* **2018**, *9*, 530-544. DOI: 10.3762/bjnano.9.51.
- (33) Shi, J.; Ni, G.; Tu, J.; Jin, X.; Peng, J. Green synthesis of fluorescent carbon dots for sensitive detection of Fe²⁺ and hydrogen peroxide. *J. Nanoparticle Res.* **2017**, *19* (6), 209. DOI: 10.1007/s11051-017-3888-5.
- (34) Kumar, A.; Chowdhuri, A. R.; Laha, D.; Mahto, T. K.; Karmakar, P.; Sahu, S. K. Green synthesis of carbon dots from *Ocimum sanctum* for effective fluorescent sensing of Pb²⁺ ions and live cell imaging. *Sens. Actuators, B* **2017**, *242*, 679-686. DOI: 10.1016/j.snb.2016.11.109.
- (35) Wei, Z.; Wang, B.; Liu, Y.; Liu, Z.; Zhang, H.; Zhang, S.; Chang, J.; Lu, S. Green synthesis of nitrogen and sulfur co-doped carbon dots from *Allium fistulosum* for cell imaging. *New J. Chem.* **2019**, *43* (2), 718-723. DOI: 10.1039/C8NJ05783D.
- (36) Zhou, J.; Sheng, Z.; Han, H.; Zou, M.; Li, C. Facile synthesis of fluorescent carbon dots using watermelon peel as a carbon source. *Materials Letters* **2012**, *66* (1), 222-224. DOI: 10.1016/j.matlet.2011.08.081.

Preamble to Chapter 3

In Chapter 2, we identified the need for a better understanding of how the precursor and synthesis conditions affect the physical and chemical properties of the CD. We further discussed the importance of understanding how the resulting physicochemical properties of a CD can affect their optical properties. Chapter 3 aims to close some of these knowledge gaps by determining the role of stoichiometry in determining the chemical composition of the CD, and how the chemical structure affects quantum yield. Chapter 2 revealed that the majority of green synthesis methods used raw materials such as plants. We hypothesized that this may have contributed to the homogeneity of the resulting CDs across the literature, with many plants having similar components. In Chapter 3, we instead opted for refined chemicals that are found abundantly in the natural environment. A hydrothermal synthesis was performed since it is a well-established method for performing low-cost one-pot syntheses. By using citric acid and the amino acid phenylalanine as pure compounds rather than as part of a raw material, we were afforded greater control over the synthesis with more predictable results. By synthesizing CDs with nine ratios of citric acid to phenylalanine, we were able to obtain nine CDs with different chemical structures and quantum yields, synthesized under identical conditions. This allowed us to isolate the effect of stoichiometry in determining the N:C ratio of the resulting CDs. From here, we were able to develop a model that correlates certain chemical properties and functional groups to the fluorescence quantum yield of the CD. A stoichiometric ratio for the synthesis was also determined by considering the point where the N:C ratio in the reactants would be equivalent to the N:C ratio in the resulting CD. Finally, the CDs were also shown to act as Fe³⁺ sensors.

This chapter has been reprinted (adapted) with permission from *ACS Sustainable Chem. Eng.*, 2020, 8, 14, 5566–5575. Copyright 2020 American Chemical Society. The only

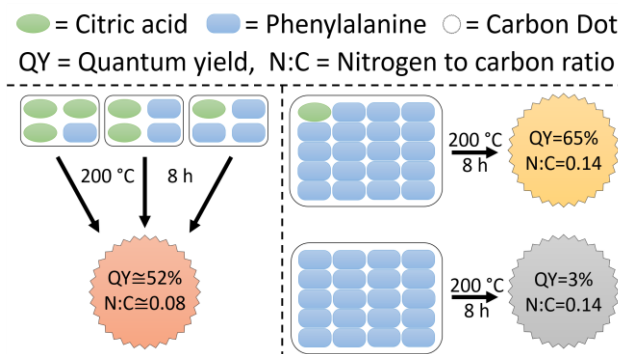
modifications are in the enumeration of the header, figure, table, equation, and scheme numbers whereby they have all been prefixed with “3.” to reflect their placement in Chapter 3 of this thesis. The format of the references may also differ so that they are consistent with the format of the rest of the thesis.

Chapter 3: Green synthesis of high quantum yield carbon dots from phenylalanine and citric acid: Role of stoichiometry and nitrogen doping

Abstract

Despite a growing interest in carbon dots (CDs), notably for their potential as a more sustainable, less toxic alternative to inorganic quantum dots, the critical factors affecting their physical, chemical, and optical properties are relatively unknown, limiting their widespread use. Herein, a one-pot hydrothermal method was used to synthesize CDs from citric acid and phenylalanine. CDs were synthesized over a range of reactant ratios; from pure citric acid to pure phenylalanine and seven mixed ratios in between, achieving a quantum yield (QY) as high as 65% with a peak excitation/emission of 350/413 nm. The goal was to determine the role of stoichiometry on the chemical and structural composition of CDs, particularly its impact on nitrogen doping, and in turn its effect on QY. We showed that a wide range of reactant ratios tend towards reacting in a stoichiometric 2:1 molar ratio of phenylalanine to citric acid whereby the resulting CDs have similar chemical composition and QY. Using this ratio may lead to a more efficient and sustainable mass production process by reducing and reusing reactant waste. The QY of the CDs was found to be more dependant on the oxygen-to-carbon ratio and the relative amount of carboxyl oxygen in the CD, than it was on the nitrogen-to-carbon ratio. The resulting CDs also showed Fe³⁺ sensing capabilities through static fluorescence quenching with a limit of detection of 3.5 μM. This study provides new insights which may be useful for the optimization of the green synthesis of CDs for more widespread applications.

Abstract Graphic



Abstract graphic 3.1. A visual depiction of the abstract for Chapter 3.

Synopsis

This work reveals a stoichiometric ratio for producing high quantum yield carbon dots that can be useful for reducing reactant waste during large-scale production.

Keywords

Fluorescence, green chemistry, hydrothermal synthesis, nitrogen doping, regression analysis, static quenching, quantum dots, nanomaterials.

3.1 Introduction

Interest in carbon dots (CDs), a type of fluorescent carbon nanoparticle, has been steadily increasing since their discovery by Xu *et al.*¹ One advantage of using CDs over traditional fluorescent dyes is that while dyes may experience considerable photobleaching after only a few seconds of photon excitation, some CDs can remain fluorescent for several hours while losing little to no fluorescence intensity.²⁻⁴ CD synthesis methods such as hydrothermal,⁵ microwave,⁶ and dry heating (*e.g.* pyrolysis or calcination),⁷ can be made sustainable by using non-toxic, renewable,

organic compounds found in Nature and consequently have often been shown to exhibit lower cytotoxicity than other quantum dots.⁸⁻¹¹ This reduced cytotoxicity is best taken advantage of in the fields of bioimaging,¹² drug delivery,¹³ and other forms of biomedical treatment.¹⁴ In addition to biological applications, CDs can also be used in chemical sensing,¹⁵ inks,¹⁶ films,¹⁷ light-emitting diodes,¹⁸ catalysts,¹⁹ and solar cells.²⁰

Several bottom-up CD synthesis methods such as hydrothermal,⁵ microwave,⁶ and dry heating (*e.g.* pyrolysis or calcination),⁷ are popular in green CD synthesis since they are generally easy to implement, inexpensive, and can be performed as a one-pot synthesis. Citric acid is a common source of carbon in bottom-up CD synthesis, likely due to the presence of three carboxyl groups and a hydroxyl group allowing it to react with itself and other organic compounds. Citric acid can also be synthesized by the fungus *Aspergillus niger*, allowing for its production through bioprocesses.²¹ Fluorescence quantum yield (QY) is an important metric that quantifies the ability of a particle to release absorbed electromagnetic radiation as photons. A nitrogen doping agent is commonly added in the CD synthesis process, since it has been well documented that N-doped CDs have enhanced QY when compared to non-doped CDs.²² L-phenylalanine – a naturally occurring amino acid and one of the key components of the popular sweetener aspartame^{23, 24} – contains a phenyl group, making it easier to produce graphene-like structures, and carboxyl and amine groups, which can polymerize through addition-elimination reactions, making its chemical structure advantageous for CD synthesis. It also contains nitrogen which can be used for doping CDs to increase QY. Previously, Yang *et al.* performed a hydrothermal synthesis of CDs using phenylalanine alone.²⁵ Lijuan *et al.* performed pyrolysis of phenylalanine and citric acid to synthesize graphene quantum dots for use in the anode material of lithium ion batteries.²⁶ Shen and Xia synthesized CDs hydrothermally from phenylalanine and NaOH.²⁷ Pandey *et al.* used

microwaves to synthesize CDs from phenylalanine, ethanol, and NaOH for the application of haloperidol delivery.¹³ Wang *et al.* synthesized CDs hydrothermally from tryptophan, phenylalanine, and HCl for the bioimaging of cancer cells and achieved a quantum yield of 21%.²⁸

Significant knowledge gaps prevent CDs from replacing inorganic quantum dots in many applications. For example, nitrogen doping is known to increase the QY of CDs by tuning their electronic and surface properties, but the exact mechanism by which it does this is unknown.²² Moreover, there are many possible starting reagents that CDs may be synthesized from; however, they lead to a range of properties and QYs. In this work, two types of CDs with the same atomic ratio of nitrogen to carbon, but with remarkably different QYs, were synthesized with the intent of gaining insight into the role of CD chemical composition and nitrogen doping on QY. We also created an array of CDs, by varying the citric acid to phenylalanine reactant ratio, from which we can determine the role of stoichiometry on the chemical composition of the synthesized CDs. Gaining insight into the stoichiometry of CD synthesis and its impact on QY would help in the development of more economical and sustainable synthesis routes, particularly for mass production, by minimizing reactant waste. The synthesized CDs also displayed Fe³⁺ sensing capabilities.

3.2 Experimental

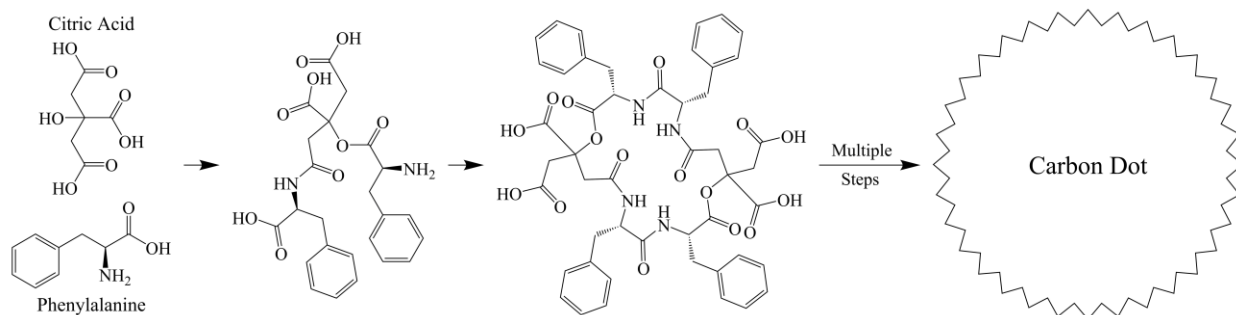
3.2.1 Chemicals

Citric acid, L-phenylalanine, quinine hemisulfate salt monohydrate, AgNO₃, HAuCl₄·3H₂O, BaCl₂·2H₂O, CaCl₂·2H₂O, CdCl₂, CoCl₂·6H₂O, CsCl, CuCl₂, FeCl₃, LiCl, MgCl₂, MnCl₂·4H₂O, NaCl, NaNO₃, Pd(CH₃COO)₂, and ZnCl₂ were purchased from Sigma-Aldrich. FeCl₂·4H₂O, HCl, KCl, KBr, KI, NaCH₃COO·3H₂O, NaClO₄ were purchased from Thermo Fisher

Scientific. Sulfuric acid was purchased from VWR. Reverse osmosis water (produced from a Mar Cor Purification reverse osmosis water purification unit) was used across all the experiments.

3.2.2 Synthesis of Carbon Dots

Citric acid (from 0 to 270 mM) and phenylalanine (from 0 to 180 mM) were dissolved in 15 mL of water and placed in a glass vial which was then placed in a Teflon-lined autoclave chamber (Hydrion Scientific, 50 mL) and heated to 200 °C for 8 h. A complete list of synthesis concentrations can be found in Table S3.1. The resulting suspension was left to cool naturally to room temperature. The suspension was then filtered using a 0.1 μm PVDF syringe filter unit (Millex-VV, EMD Millipore) to remove any large particles. Approximately 10 mL of the sample was then dialyzed in 1 L of water using a 3.5 kDa molecular weight cut-off regenerated cellulose membrane (Spectrum Labs) for 24 h with two changes of the dialysis water to remove any unreacted citric acid and phenylalanine, as well as any small fluorophores that may have been generated. CDs are named based on the phenylalanine mole percent in the reactants, *e.g.* P₉₅-CDs were made using 95 mol% phenylalanine and 5 mol% citric acid in water. A proposed mechanism of the initial synthesis steps is shown in Scheme 3.1.



Scheme 3.1 Proposed mechanism of the initial synthesis steps for the reaction of citric acid and phenylalanine.

3.2.3 Characterization

Fluorescence measurements were performed using a Horiba FluoroMax-4. UV-Vis absorbance measurements were taken using a Thermo Fisher Scientific BioMate 3S UV-Visible spectrophotometer. Fluorescence lifetime measurements were taken using a Horiba EasyLife X (368 nm excitation). X-ray photoelectron spectroscopy (XPS) measurements were taken using a Thermo Fisher Scientific K-Alpha X-Ray Photoelectron Spectrometer System. Fourier-transform infrared (FTIR) spectroscopy measurements were performed using a PerkinElmer Spectrum Two FTIR spectrometer with a single reflection diamond ATR. Atomic force microscopy (AFM) was done in tapping mode using a Bruker MultiMode 8 AFM equipped with a Nanoscope V controller using a Bruker ScanAsyst-air silicon nitride probe (nominal frequency: 70 kHz, spring constant: 0.4 N/m, tip radius: 2 nm). Transmission electron microscopy (TEM) images were obtained using an FEI Tecnai G2 F20 TEM located at the Facility for Electron Microscopy Research at McGill University. Raman spectroscopy was performed using a Bruker SENTERRA II compact Raman microscope with a He-Ne laser at a 532 nm wavelength.

3.2.4 Quantum Yield

Quantum yields were measured using the relative approach reported by Williams *et al.*²⁹ All samples had an absorbance of 0.1 or lower. Equation 3.1 was then used to determine the quantum yield:

$$QY_S = QY_R \frac{F_S A_R \eta_S^2}{F_R A_S \eta_R^2} \quad (3.1)$$

where QY is the quantum yield, F is the integral of the fluorescence emission scan, A is the absorbance, η is the index of refraction of the solvent, S denotes the type of sample to be analysed

(i.e. CDs), and R denotes the reference material. The reference material was quinine sulfate in 0.1 M H_2SO_4 , which has a QY of 54.6%.³⁰ QY fluorescence measurements were performed using an excitation and emission slit width of 1 nm. An excitation wavelength of 350 nm was used unless otherwise specified.

3.2.5 Ion Sensing

P₉₅-CDs were mixed with individual salts such that the resulting mixture in water had a CD and ion concentration of $\sim 15 \text{ mg L}^{-1}$ and $1000 \text{ }\mu\text{M}$, respectively. The mixture was then incubated for 1 hr at room temperature. An excitation wavelength of 350 nm was used, and the fluorescence intensity was measured at an emission wavelength of 400 nm.

A linear Fe^{3+} calibration curve was generated in a similar manner with slight variations. P₉₅-CDs were mixed with $FeCl_3$ such that the resulting mixture had a CD and Fe^{3+} concentration of $\sim 140 \text{ mg L}^{-1}$ and up to $50 \text{ }\mu\text{M}$, respectively. The mixture was then incubated for 1 hr at room temperature. An excitation wavelength of 350 nm was used, and fluorescence intensity was measured at an emission wavelength of 376 nm, which provided the best limit of detection (LOD) using Equation 3.2.³¹

$$LOD = 3.3 \left(\frac{S_y}{S} \right) \quad (3.2)$$

where S_y is the standard deviation of the response of the linear calibration curve, and S is the slope of the linear regression.

All ion sensing fluorescence measurements were done using an excitation and emission slit width of 2 nm.

3.2.6 Statistical Analysis

Data is reported as the mean \pm 2 standard errors of the mean. Statistical significance was measured using the Student's *t*-test, with $p < 0.05$ considered as significant. Comparisons made between two types of CDs (*e.g.* P₉₅-CDs vs P₁₀₀-CDs) were done using an unpaired homoscedastic *t*-test. Comparisons made on a CD before and after a treatment (*e.g.* addition of Fe³⁺) were done using a paired *t*-test.

3.3 Results and Discussion

3.3.1 Nitrogen Doping and Quantum Yield

It has been argued that nitrogen doping of CDs can greatly increase their QY.²² Figure 3.1a shows that the QY increased as the phenylalanine mole fraction (x_p) in the reactants increased from 0.00 to 0.95. However, this is only true so long as citric acid is present, whereas using only phenylalanine ($x_p=1.00$) in water results in a low QY. Interestingly, there is no significant difference ($p > 0.05$) between the QY of undoped P₀-CDs ($2.0 \pm 0.9\%$) and N-doped P₁₀₀-CDs ($3.4 \pm 2.5\%$) indicating that citric acid and phenylalanine create higher QY CDs when together than either reactant alone. Citric acid plays two major roles in the synthesis of CDs. It contains three carboxyl groups and one hydroxyl group which gives it several sites to react with phenylalanine and other citric acid molecules. Citric acid also keeps the pH of the reacting mixture low which acts as a catalyst for addition-elimination reactions such as Fischer esterification.³² Therefore, the absence of citric acid in the P₁₀₀-CD reaction may have caused those CDs to synthesize poorly and could partially explain why the QY of P₉₅-CDs ($65 \pm 7.2\%$) is 19 times higher ($p < 0.01$) than P₁₀₀-CDs ($3.4 \pm 2.5\%$). This places the QY of P₉₅-CDs on the higher end of CDs synthesized using renewable nitrogen doping agents,³³⁻³⁵ but on the lower end of those synthesized from synthetic

nitrogen doping agents.³⁶⁻⁴⁰ The post-dialysis pH of the suspensions of CDs synthesized from citric acid (*i.e.* all the CDs except P₁₀₀-CDs) ranges from 3.4–3.7, while the suspension of P₁₀₀-CDs has a pH of 4.6. To determine if this difference in pH could explain the vast difference in QY between P₉₅-CDs and P₁₀₀-CDs, the post-dialysis pH of the P₉₅-CD and P₁₀₀-CD suspensions were adjusted to 2.4 using HCl; however, the QY of P₉₅-CDs was still 11 times greater than that of P₁₀₀-CDs ($p < 0.01$), confirming that the post-dialysis pH is not the primary cause for the discrepancy in QY. In addition, the QY remains mostly unchanged in P₂₅-CDs, P₅₀-CDs, and P₇₅-CDs, revealing that continuously increasing the concentration of the nitrogen doping agent does not necessarily increase the QY at the same rate. For instance, tripling x_p from 0.25 to 0.75 only increases ($p < 0.05$) the QY from $49 \pm 1.1\%$ to $52 \pm 1.6\%$.

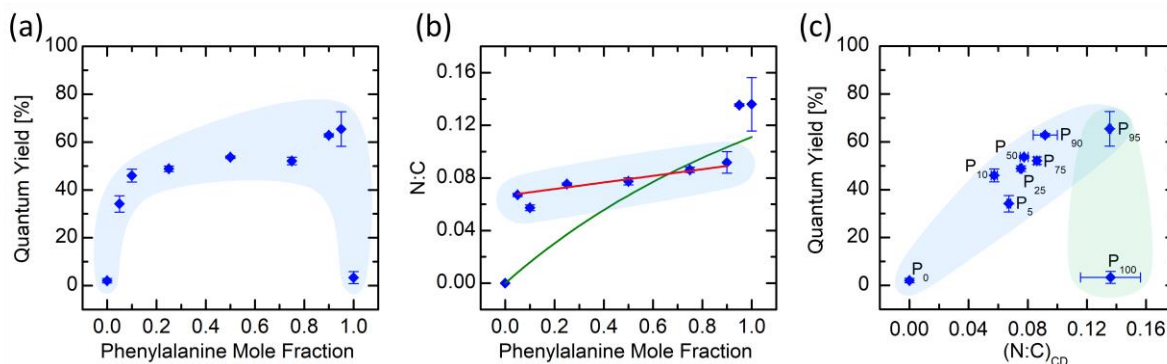


Figure 3.1. (a) Quantum yield of CDs vs phenylalanine mole fraction (balance is citric acid) in water at an excitation wavelength of 350 nm. (b) Nitrogen to carbon ratios for various phenylalanine mole fractions. Blue diamonds represent (N:C)_{CD}. Green curved line represents (N:C)_R. Red line shows a linear trend for $0.05 \leq x_p \leq 0.90$. (c) Quantum Yield vs (N:C)_{CD} as determined by XPS. Error bars represent 2 standard errors of the mean (N=3).

Figure 3.1b shows that there is a linear trend for $0.05 \leq x_p \leq 0.90$, over which the nitrogen to carbon atomic ratio in the CDs ((N:C)_{CD}), as determined using XPS, shows little change despite

large changes in the nitrogen to carbon atomic ratio of the reactants ((N:C)_R) and x_p . Specifically, when $0.05 \leq x_p \leq 0.90$, (N:C)_{CD} follows the fitted function (Equation 3.3, red line in Figure 3.1b):

$$(N:C)_{CD} = 0.025x_p + \frac{1}{15} \quad (3.3)$$

The intercept of Equation 3.3 (*i.e.* $\frac{1}{15}$) is equal to the (N:C)_R when phenylalanine and citric acid are in a 1:1 molar ratio (*i.e.* $x_p = 0.5$), revealing that when there is a small amount of phenylalanine relative to citric acid (*i.e.* x_p approaches 0), then phenylalanine and citric acid will react in a 1:1 molar ratio. This shows that excess citric acid is wasted or produces low QY CDs when x_p approaches 0. Conversely, the (N:C)_{CD} and the (N:C)_R are equal to each other when $x_p = \frac{2}{3}$, and can be visualized by the intersection of the two functions in Figure 3.1b, indicating that a 2:1 molar ratio of phenylalanine to citric acid is the stoichiometric ratio. Oxygen and hydrogen are not considered in this stoichiometry, since they may be added to and removed from the CD during synthesis in the form of water molecules. These results show that the reaction tends to proceed at a phenylalanine to citric acid molar ratio of 2:1 when $0.25 \leq x_p \leq 0.75$, and 1:1 as x_p approaches 0.

Figure 3.1c shows the relationship between the measured QY and (N:C)_{CD}. Over the range, $0 \leq x_p \leq 0.95$, the QY generally increases with (N:C)_{CD}. As mentioned previously, P₂₅-CDs, P₅₀-CDs, and P₇₅-CDs have similar QYs and (N:C)_{CD}, but their x_p , and in turn, (N:C)_R, varies considerably. Figure 3.1c shows these three CDs clustered together despite covering a wide range of x_p . This further supports the mechanism proposed previously; that having $0.25 \leq x_p \leq 0.75$ during synthesis does not change the composition or properties of the resulting CDs considerably and that

phenylalanine and citric acid will tend towards a stoichiometric ratio at $x_p = \frac{2}{3}$. Conversely, there is a great difference in QY between P₉₅-CDs and P₁₀₀-CDs despite having similar (N:C)_{CD}.

There is little work in the literature with specific focus on the role of nitrogen doping in enhancing the QY of CDs, particularly with regards to stoichiometry. Permatasari *et al.* synthesized graphene quantum dots from citric acid and urea.⁴¹ They reported that graphene quantum dots with a larger ratio of pyridinic nitrogen to pyrrolic nitrogen exhibited more fluorescence; however, the effect on QY was not measured. By examining the optical, chemical, and physical properties of the CDs synthesized in this work, we hope to gain new insight into the role of stoichiometry and nitrogen doping on QY.

3.3.2 Chemistry of CDs

Analysis of the XPS spectra reveals peaks indicating the presence of carbon, nitrogen, and oxygen at binding energies of ~285 eV, ~400 eV, and ~532 eV, respectively. A charge correction is applied, where needed, in the form of a binding energy region shift to account for any charge accumulation. When considering only C, N, and O, all the CDs have a composition of approximately 50–70% C, 0–10% N, and 20–50% O on an atomic basis (Table S3.2). A representative example of the deconvolution of C_{1s}, N_{1s}, and O_{1s} peaks for P₂₅-CDs, P₅₀-CDs, and P₇₅-CDs is shown in Figure S3.1 and P₉₅-CDs and P₁₀₀-CDs is shown in Figure S3.2.

The C_{1s} spectra is deconvoluted using five peaks representing sp² (~284.2 eV),⁴² sp³ (~284.9 eV),⁴³ C–N/C–O (~286.0 eV),^{44, 45} C=N/C=O (~287.8 eV),⁴⁶ and O–C=O (~288.8 eV)⁴⁷ carbon. The N_{1s} spectra is deconvoluted using three peaks representing C–NH–C (2° amine) and/or pyridinic N (~399.6 eV), C–N(C)–C/N–C=O (3° amine and/or amide) and/or pyrrolic N (~400.4 eV), and –NH₃⁺/graphitic N (~401.6 eV).^{48, 49} The O_{1s} spectra is deconvoluted using four peaks

representing COOH (~531.1 eV), C=O (~531.9 eV), C–O (~532.7 eV), and C–OH (~533.5 eV).⁵⁰ A detailed breakdown and analysis of the relative amounts of these bonds can be found in Table S3.3 and the XPS Analysis section of the Supporting Information (SI).

The chemical similarity of P₂₅-CDs, P₅₀-CDs, and P₇₅-CDs is evident in their FTIR spectra (Figure 3.2a), which further indicates that there is little difference between these CDs. A comparison of the FTIR spectra of P₉₅-CDs and P₁₀₀-CDs (Figure 3.2b) shows four regions of interest. Regions 1–3 are considerably more pronounced in P₉₅-CDs. P₉₅-CDs and P₁₀₀-CDs both show a prominent peak in Region 4, *i.e.* 1260 – 890 cm⁻¹, with prominence at 1084 cm⁻¹ originating from C–N and C–O stretching, indicating the presence of amines and alkoxy groups. Only this last region has similar prominence among P₉₅-CDs and P₁₀₀-CDs, but when considered relative to the magnitude of the other peaks (Figure S3.3), P₁₀₀-CDs appear to have a greater relative amount of the bonds associated with this peak (*i.e.* C–N/C–O) than P₉₅-CDs, which is consistent with the results from XPS (Table S3.3). A detailed analysis can be found in the FTIR Analysis section of the SI. Figure S3.4 shows the FTIR spectra for all the synthesized CDs as well as the reactants, citric acid and phenylalanine.

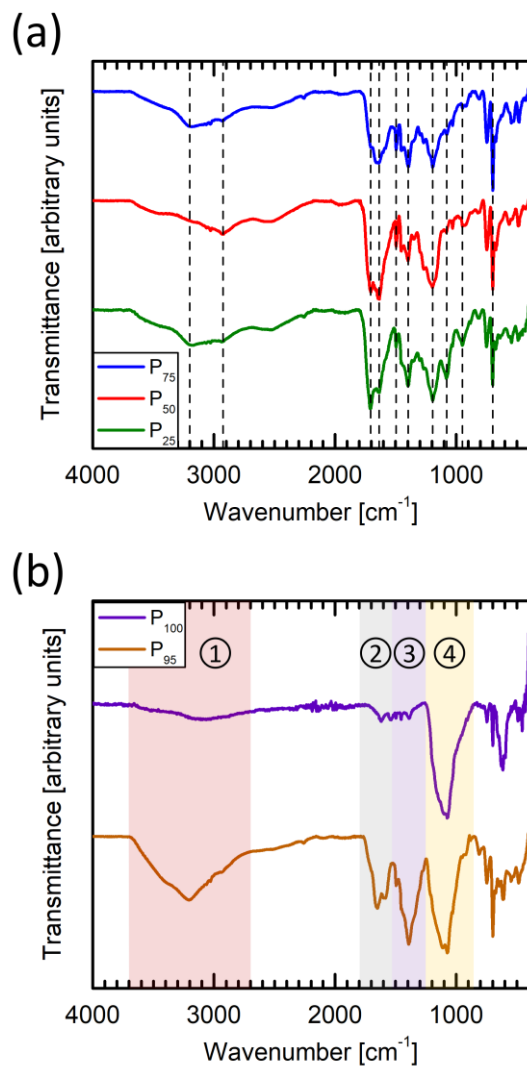


Figure 3.2. FTIR spectra of (a) P₂₅-CDs, P₅₀-CDs, and P₇₅-CDs and (b) P₉₅-CDs and P₁₀₀-CDs. Dashed lines in (a) are to show alignment of peaks between CD types. Shaded regions in (b) are to highlight similarities and differences in certain regions.

A shortcoming of FTIR and XPS analyses is that peaks can often be associated with more than one type of bond. For instance, it is difficult to assess how much of the N is in the form of a protonated amine ($-\text{NH}_3^+$) versus a graphitic form, since these two peaks are generally found at the same location (~ 401.6 eV).^{48, 51} From FTIR, the strong presence of C–N, but minimal N–H in P₁₀₀-CDs suggests that nitrogen is incorporated inside the CDs in the form of a tertiary amine,

pyridinic N, or graphitic N, as opposed to its presence on the surface as a primary or secondary amine or a pyrrolic N. This suggests that the increase in -NH_3^+ /graphitic N in P₁₀₀-CDs when compared to P₉₅-CDs could be due to an increase in graphitic N, instead of -NH_3^+ as this is supported by the FTIR spectra for the two CDs. In general, there is agreement between the FTIR and XPS analyses in terms of the types of bonds identified. Both techniques confirm that nitrogen doping occurs and indicate the presence of sp^2 and sp^3 carbon, as well as the presence of alkoxy, hydroxyl, carboxyl, and carbonyl groups.

The difference in QY between P₉₅-CDs and P₁₀₀-CDs may be best explained by examining the oxygen containing groups. Zhang *et al.* synthesized graphene quantum dots that were not nitrogen-doped, and found that reducing them using NaBH_4 increased their QY from 2.6% to 10.1%.⁵² In this study, P₉₅-CDs have 33% less ($p < 0.05$) relative COOH oxygen and a 22% lower ($p < 0.05$) oxygen to carbon ratio $(\text{O:C})_{\text{CD}}$ than P₁₀₀-CDs, indicating that P₉₅-CDs are overall more reduced than P₁₀₀-CDs.

Furthermore, to illustrate the uniqueness of P₁₀₀-CDs chemical composition relative to the other CDs synthesized in this work, a principal component analysis (PCA) was performed on the 14-dimensional XPS data (*i.e.* $(\text{N:C})_{\text{CD}}$, $(\text{O:C})_{\text{CD}}$, and the relative amount of each bond type in the 5 C_{1s} features, 3 N_{1s} features, and 4 O_{1s} features) which captured 75% of the variance in two principal components (Figure S3.5). From the PCA plot, P₀-CDs are distinct from the rest of the CDs, as expected, due to its lack of nitrogen. Interestingly, P₁₀₀-CDs are shown to be overall, quite dissimilar as well from the rest of the N-doped carbon dots. A multiple linear regression analysis was performed, correlating the chemical composition of the CDs based on XPS spectra to the QY. To determine the most important of the 14 features, we aimed to maximize the coefficient of determination, R^2 , with the least number of features possible. Our analysis revealed that an

$R^2=0.934$ (Figure 3.3) was achievable using only 2 features, the $(O:C)_{CD}$ and the relative amount of COOH oxygen (from O_{1s} spectra), in the form of Equation 3.4:

$$QY = 0.271 - 0.500z_1 - 0.238z_2 - 0.192z_1z_2 \quad (3.4)$$

where z_1 and z_2 are the standard score of the $(O:C)_{CD}$ and the relative amount of COOH oxygen (from O_{1s} spectra), respectively.

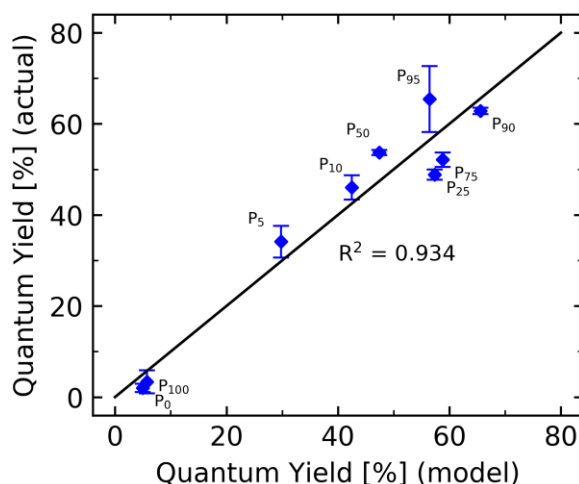


Figure 3.3. Comparison of the actual QY (blue diamonds) to the QY calculated from Equation 3.4 (black line).

All of the coefficients in Equation 3.4 were negative, suggesting that an increase in either the $(O:C)_{CD}$ or the relative amount of COOH oxygen would decrease the quantum yield. The interaction term suggests a compounding effect when the two features move in the same direction. Interestingly, if we replace the interaction term with a 3rd feature, the $(N:C)_{CD}$, the regression model would only have an $R^2=0.838$ (Table S3.4), suggesting that the role of nitrogen comes second to the role of oxygen in determining the QY of this set of CDs. It is worth clarifying here that the purpose of developing this multiple linear regression was to be qualitative, as opposed to

quantitative. It is entirely possible that the QY of a CD is dependant on features beyond the 14 features assessed here from XPS, but we still consider it interesting that the (O:C)_{CD} and the relative amount of COOH oxygen on their own can account for a large portion of the variance observed in QY. The parameters and R²-values of the different permutations of the features used to make the multiple linear regression are found in Table S3.4. Similarly, the means and standard deviations of the features considered are found in Table S3.5.

3.3.3 Fluorescence and UV-Vis Spectroscopy

Fluorescence and absorbance measurements were performed on CD suspensions in water. In addition to being used to calculate the QY, the fluorescence data provides the peak excitation and emission wavelengths for a CD, while the absorbance data provides peak absorbance wavelengths. Figure 3.4a,b compares the fluorescence intensity of P₉₅-CDs with P₁₀₀-CDs. A clear difference in the peak fluorescence between the two CDs is observed. P₉₅-CDs display a peak fluorescence at an excitation/emission wavelength of 350/413 nm, while P₁₀₀-CDs peak at 315/395 nm. Although the fluorescence intensity of P₁₀₀-CDs is higher when an excitation wavelength of 315 nm is used, this is due to an increase in absorbance, and therefore the QY of the P₁₀₀-CDs shows no significant difference ($p > 0.05$) at an excitation wavelength of 315 nm when compared to an excitation wavelength of 350 nm. Therefore, the shift in the peak excitation and emission wavelengths do not explain the difference in QY. Fluorescence heat maps for P₂₅-CDs, P₅₀-CDs, and P₇₅-CDs (Figure S3.6) reveal that their peak intensities occur in the same general excitation/emission region, specifically at, 345/402 nm, 345/408 nm, and 350/421 nm, respectively. The relatively circular appearances of the heat maps demonstrate that the emission spectra of the CDs are not strongly dependant on their excitation wavelength in the regions

surrounding their peak excitation and emission wavelengths. For instance, over the excitation range of 300–365 nm, P₉₅-CD's peak emission occurs between 411–415 nm. Only excitation wavelengths of 370–400 nm begin showing excitation-dependant emission; however, the fluorescence intensity begins to weaken as well.

The UV-Vis absorbance spectra reveal differences between P₉₅-CDs and P₁₀₀-CDs (Figure 3.4c). The ratio between the absorbance of the peak at 217 nm to the peak at 237 nm is 2.2× higher in P₉₅-CDs relative to the ratio in P₁₀₀-CDs. A more broad-spectrum absorbance is also observed in the 300–400 nm region. Figure 3.4d shows the similarities in the UV-Vis spectra of P₂₅-CDs, P₅₀-CDs, and P₇₅-CDs. They all share their most prominent peak at 220 nm, a second peak at 237 nm, and a small peak at 334 nm.

A partial explanation for the lower QY in P₁₀₀-CDs is self-quenching. The ratio of the absorbance at 430 nm to the absorbance at 350 nm is 0.27 for P₉₅-CDs, but 0.62 for P₁₀₀-CDs. This means that a larger proportion of the fluorescence that may have been generated by P₁₀₀-CDs is reabsorbed by itself, effectively lowering its QY.

Individual fluorescence lifetimes of P₉₅-CDs were significantly different ($p < 0.05$) from P₁₀₀-CDs. Both CDs exhibited a biexponential decay with two fluorescence lifetimes (Figure S3.7a). P₉₅-CDs had a lifetime of 5.12 ± 0.70 ns and 36.5 ± 1.0 ns, while P₁₀₀-CDs had a lifetime of 2.51 ± 1.38 ns and 47.7 ± 6.8 ns.

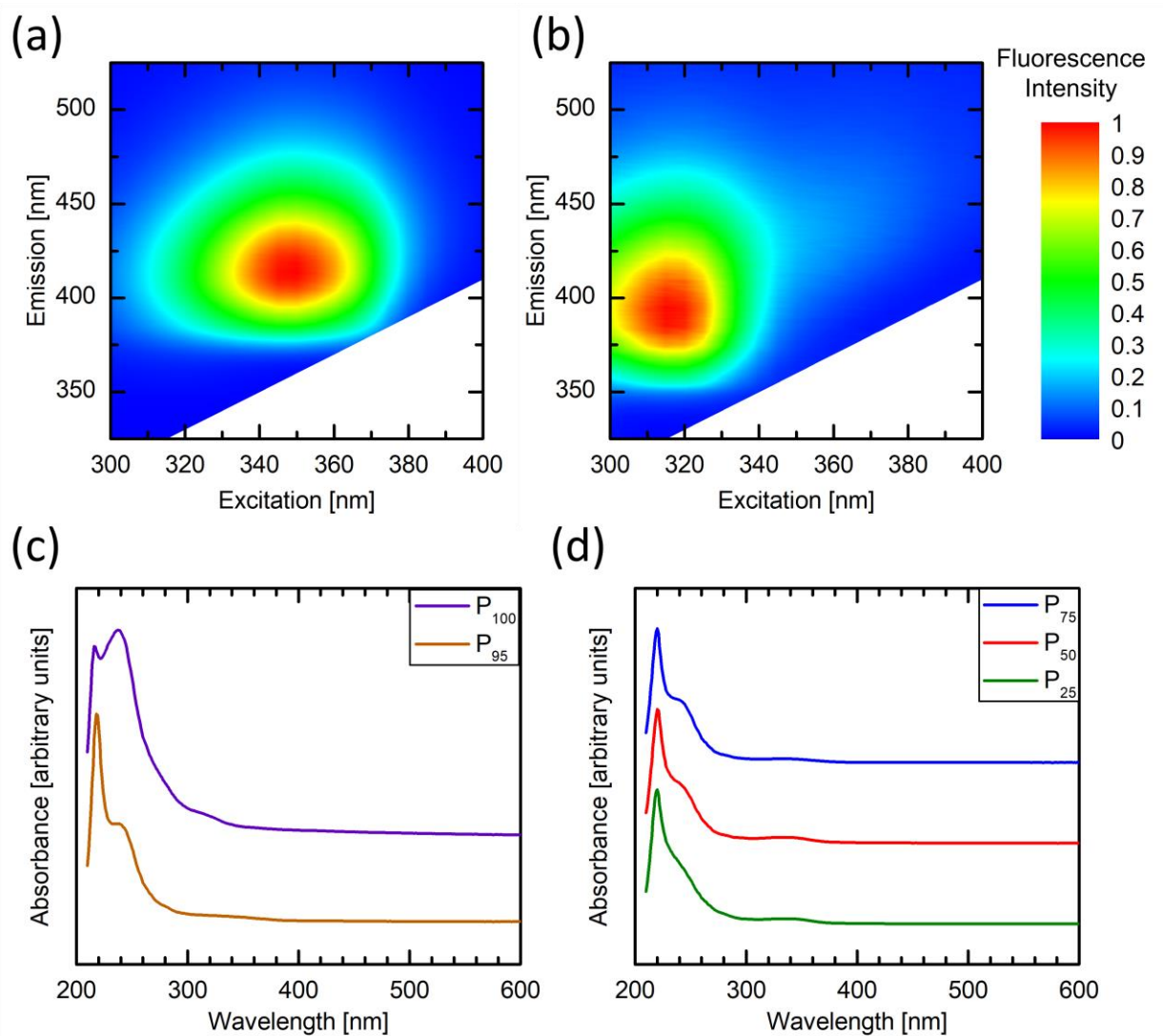


Figure 3.4. Fluorescence heat maps of (a) P₉₅-CDs and (b) P₁₀₀-CDs over a range of excitation and emission wavelengths using an excitation and emission slit width of 3 nm. Absorbance spectra of (c) P₉₅-CDs and P₁₀₀-CDs, and (d) P₂₅-CDs, P₅₀-CDs, and P₇₅-CDs. Fluorescence heat maps and absorbance spectra were normalized to their respective maximum peaks.

3.3.4 Structural Characterization of CDs

AFM imaging (Figure 3.5a,b) indicates that P₉₅-CDs have a thickness of 1.8 ± 0.2 nm and a diameter of 12.8 ± 0.6 nm. The P₁₀₀-CDs are larger, with a thickness of 3.7 ± 0.5 nm and a diameter of 17.0 ± 1.7 nm. TEM data suggests smaller diameters than those obtained by AFM. TEM imaging (Figure 3.5c,d) shows that P₉₅-CDs have a mean diameter of 11.9 ± 0.6 nm, while P₁₀₀-CDs have a mean diameter of 7.2 ± 0.4 nm. Figure S3.8 shows the histogram of the size distribution for P₉₅-CDs and P₁₀₀-CDs based on TEM imaging. Possible explanations for the size discrepancy between AFM and TEM results are provided in the Size Analysis section of the SI. Additionally, the AFM and TEM images (Figure 3.5) indicate that our processing and purification methods did not result in any noticeable aggregation of the CDs in water.

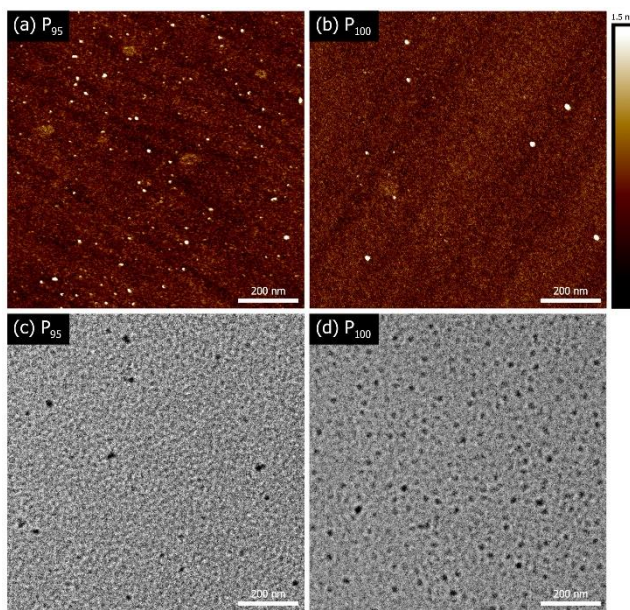


Figure 3.5. AFM images of (a) P₉₅-CDs and (b) P₁₀₀-CDs. TEM images of (c) P₉₅-CDs and (d) P₁₀₀-CDs. TEM images have been cropped to match the scale of AFM images. Uncropped images can be found in Figure S3.9.

Although there are differences in size and thickness between P₉₅-CDs and P₁₀₀-CDs, it is difficult to determine if this factor played a role in the vast difference between their QYs. Chandra *et al.* synthesized CDs from citric acid and (NH₄)₂HPO₄ with a size of 1.5–4 nm, as measured by TEM, and a QY of 59%.⁵³ This shows that it is possible to have high QYs with small CDs, making it unlikely that size is the primary explanation for the difference in QY since other researchers have reported smaller sizes while still having a comparable QY to P₉₅-CDs.^{54, 55}

To study the structure of the CDs, Raman spectroscopy was attempted; however, the high fluorescence from the CDs obscured the Raman signal (Figure S3.10).⁵⁶⁻⁵⁸

3.3.5 Ion Sensing

P₉₅-CDs displayed metal cation sensing capabilities. Other researchers have used CDs to detect Al³⁺,⁵⁹ As³⁺,⁶⁰ Au³⁺,⁶¹ Cr⁶⁺,¹⁶ Cu²⁺,⁶² Fe²⁺,⁶³ Fe³⁺,⁶⁴ and Hg²⁺.⁶⁵ Fluorescence quenching capabilities were tested for 1000 μM concentrations of Li⁺, Na⁺, K⁺, Cs⁺, Mg²⁺, Ca²⁺, Ba²⁺, Mn²⁺, Fe²⁺, Fe³⁺, Co²⁺, Pd²⁺, Cu²⁺, Ag⁺, Au³⁺, Zn²⁺, Cd²⁺, Cl⁻, Br⁻, I⁻, CH₃COO⁻, ClO₄⁻, and NO₃⁻ and the results are summarized in Figure 3.6a. Fluorescence quenching is observed by Fe²⁺, Fe³⁺, Co²⁺, Pd²⁺, Cu²⁺, Ag⁺, and Au³⁺ at 1000 μM; however, only Fe³⁺ and Pd²⁺ are able to completely quench the CD fluorescence at this concentration. Fe³⁺ plays an important role in several biological functions and an imbalance in its concentration in the body can lead to various diseases.⁶⁶ Similarly, Pd²⁺ has shown toxicity.⁶⁷ Of the ions tested, Fe³⁺ shows the greatest fluorescence quenching capability (see Figure S3.11 for a comparison with Pd²⁺ at concentrations below 1000 μM). The fluorescence intensity of the P₉₅-CD emission spectrum decreases with increasing Fe³⁺ concentration (Figure S3.12a). Examining the fluorescence quenching capabilities of Fe³⁺ reveals

a linear trend (Figure 3.6b) at Fe^{3+} concentrations below 50 μM . The limit of detection for Fe^{3+} is 3.5 μM .

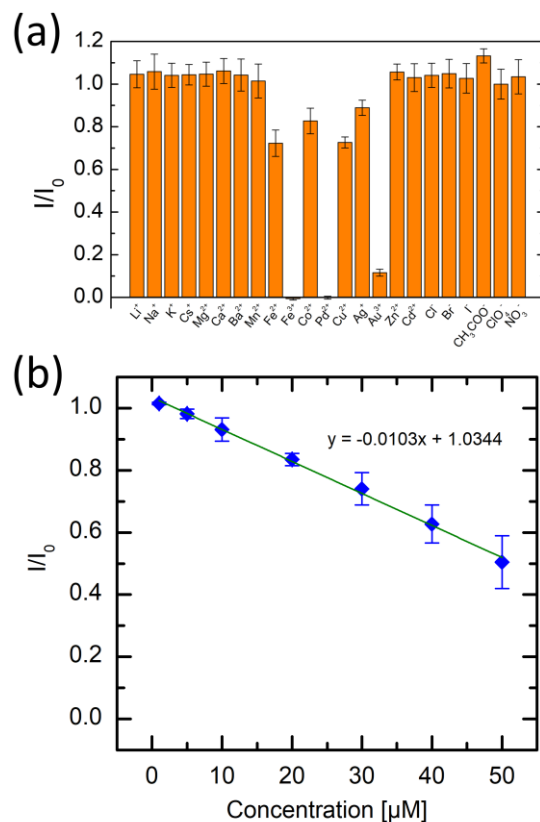


Figure 3.6. Relative fluorescence of P₉₅-CDs exposed to a) 1000 μM of various ions and b) Fe^{3+} at various concentrations. Error bars show 2 standard errors of the mean (N=3).

A new absorbance peak forms at 220 nm when P₉₅-CDs are mixed with Fe^{3+} ions (Figure S3.12b). Moreover, the peak absorbance of the Fe^{3+} solution does not overlap with the peak emission spectra of P₉₅-CDs (Figure S3.13). Furthermore, the fluorescence lifetime of P₉₅-CDs remains unchanged after the addition of 50 μM Fe^{3+} (Figure S3.7b). These observations suggest that a static fluorescence quenching mechanism is in effect, whereby Fe^{3+} ions form a complex with the P₉₅-CDs.⁶¹ Zhang *et al.* suggested that the presence of phenolic hydroxyl groups may explain the fluorescence quenching of Fe^{3+} .⁶⁸ The fact that Fe^{2+} did not quench fluorescence while

Fe³⁺ did, has been used creatively by other researchers to detect other oxidizing agents. For example, Qian *et al.* prepared a mixture of CDs with Fe²⁺, which upon exposure to H₂O₂, would get oxidized into Fe³⁺ and quench fluorescence, effectively creating an H₂O₂ sensor.⁶⁹ Consequently, Fe³⁺ sensing CDs can find application by either detecting the presence of Fe³⁺ directly, or through the oxidation of Fe²⁺ to the fluorescence quenching Fe³⁺.

3.4 Conclusions

Carbon dots were synthesized from citric acid and phenylalanine over a range of reactant ratios achieving a QY as high as 65% with a peak excitation/emission of 350/413 nm. The initial addition of phenylalanine to citric acid resulted in a great increase in QY, whereas adding more phenylalanine increased QY at a more gradual rate. Phenylalanine reacts with citric acid in a 1:1 molar ratio as the phenylalanine mole fraction approaches zero. P₂₅-CDs, P₅₀-CDs, and P₇₅-CDs had comparable QYs, (N:C)_{CD}, and FTIR, fluorescence, and UV-Vis spectra despite being synthesized over a large range of reactant ratios. This information could be useful for the optimization of large-scale CD synthesis, *e.g.* synthesis at, or near, the stoichiometric 2:1 phenylalanine to citric acid ratio could allow for the recycling of the dialysis buffer to produce more CDs. It was found that the QY of CDs was correlated to the (O:C)_{CD} and the relative amount of COOH oxygen, whereby a reduction in these components resulted in an increase in QY. This phenomenon explained why P₉₅-CDs had a considerably larger QY than P₁₀₀-CDs, despite both CDs having the same (N:C)_{CD}, revealing that nitrogen doping alone is insufficient to increase QY. Fe³⁺ ions exhibited static fluorescence quenching of P₉₅-CDs leading to a limit of detection of 3.5 μM.

Acknowledgements

The authors acknowledge funding from the Natural Sciences and Engineering Research Council of Canada, the Canada Research Chairs Program, and the Canada Foundation for Innovation. S. Chahal acknowledges NSERC for a PGS D scholarship, McGill University for a MEDA fellowship, and the support of the EUL fund in the Department of Chemical Engineering. N. Yousefi acknowledges McGill University for a MEDA fellowship, and the support of the EUL fund in the Department of Chemical Engineering. We also thank M. Ramkaran for her help in acquiring AFM images, as well as D. Liu and S. K. Sears for their help in acquiring TEM images.

Supporting Information Content

List of synthesis conditions. Elemental composition of CDs from XPS. Detailed breakdown of XPS peak deconvolutions. Parameters for multiple linear regression analysis. Graphical representations of XPS peak deconvolutions. Different normalization of FTIR spectra. Complete FTIR data of CDs and reactants. Principal component analysis of XPS data of CDs. Fluorescence heat maps of P₂₅-CDs, P₅₀-CDs, and P₇₅-CDs. Fluorescence lifetime decay of P₉₅-CDs (with and without Fe³⁺) and P₁₀₀-CDs. Histograms of CD size distributions from TEM. Uncropped TEM images. Raman spectroscopy showing fluorescence interference from CDs. Fluorescence quenching of Fe³⁺ and Pd²⁺. Fluorescence and UV-Vis absorbance spectra regarding Fe³⁺ sensing. Detailed XPS, FTIR, and size analyses.

References

- (1) Xu, X.; Ray, R.; Gu, Y.; Ploehn, H. J.; Gearheart, L.; Raker, K.; Scrivens, W. A. Electrophoretic Analysis and Purification of Fluorescent Single-Walled Carbon Nanotube Fragments. *J. Am. Chem. Soc.* **2004**, *126* (40), 12736-12737. DOI: 10.1021/ja040082h.
- (2) Peng, H.; Travas-Sejdic, J. Simple Aqueous Solution Route to Luminescent Carbogenic Dots from Carbohydrates. *Chem. Mater.* **2009**, *21* (23), 5563-5565. DOI: 10.1021/cm901593y.
- (3) Zhang, X.; Wang, H.; Wang, H.; Zhang, Q.; Xie, J.; Tian, Y.; Wang, J.; Xie, Y. Single-Layered Graphitic-C₃N₄ Quantum Dots for Two-Photon Fluorescence Imaging of Cellular Nucleus. *Adv. Mater.* **2014**, *26* (26), 4438-4443. DOI: 10.1002/adma.201400111.
- (4) Zhao, Q.-L.; Zhang, Z.-L.; Huang, B.-H.; Peng, J.; Zhang, M.; Pang, D.-W. Facile preparation of low cytotoxicity fluorescent carbon nanocrystals by electrooxidation of graphite. *Chem. Commun.* **2008**, (41), 5116-5118. DOI: 10.1039/B812420E.
- (5) Yadav, P. K.; Singh, V. K.; Chandra, S.; Bano, D.; Kumar, V.; Talat, M.; Hasan, S. H. Green Synthesis of Fluorescent Carbon Quantum Dots from *Azadirachta indica* Leaves and Their Peroxidase-Mimetic Activity for the Detection of H₂O₂ and Ascorbic Acid in Common Fresh Fruits. *ACS Biomater. Sci. Eng.* **2019**, *5* (2), 623-632. DOI: 10.1021/acsbomaterials.8b01528.
- (6) Zhi, B.; Cui, Y.; Wang, S.; Frank, B. P.; Williams, D. N.; Brown, R. P.; Melby, E. S.; Hamers, R. J.; Rosenzweig, Z.; Fairbrother, D. H.; et al. Malic Acid Carbon Dots: From Super-resolution Live-Cell Imaging to Highly Efficient Separation. *ACS Nano* **2018**, *12* (6), 5741-5752. DOI: 10.1021/acsnano.8b01619.
- (7) Wei, X.; Li, L.; Liu, J.; Yu, L.; Li, H.; Cheng, F.; Yi, X.; He, J.; Li, B. Green Synthesis of Fluorescent Carbon Dots from *Gynostemma* for Bioimaging and Antioxidant in Zebrafish.

- ACS Applied Materials & Interfaces* **2019**, *11* (10), 9832-9840. DOI: 10.1021/acsami.9b00074.
- (8) Derfus, A. M.; Chan, W. C. W.; Bhatia, S. N. Probing the Cytotoxicity of Semiconductor Quantum Dots. *Nano Lett.* **2004**, *4* (1), 11-18. DOI: 10.1021/nl0347334.
- (9) Geys, J.; Nemmar, A.; Verbeken, E.; Smolders, E.; Ratoi, M.; Hoylaerts, M. F.; Nemery, B.; Hoet, P. H. M. Acute Toxicity and Prothrombotic Effects of Quantum Dots: Impact of Surface Charge. *Environ. Health Perspect.* **2008**, *116* (12), 1607-1613. DOI: 10.1289/ehp.11566.
- (10) Kirchner, C.; Liedl, T.; Kudera, S.; Pellegrino, T.; Muñoz Javier, A.; Gaub, H. E.; Stölzle, S.; Fertig, N.; Parak, W. J. Cytotoxicity of Colloidal CdSe and CdSe/ZnS Nanoparticles. *Nano Lett.* **2005**, *5* (2), 331-338. DOI: 10.1021/nl047996m.
- (11) Yang, S.-T.; Wang, X.; Wang, H.; Lu, F.; Luo, P. G.; Cao, L.; Meziani, M. J.; Liu, J.-H.; Liu, Y.; Chen, M.; et al. Carbon Dots as Nontoxic and High-Performance Fluorescence Imaging Agents. *The Journal of Physical Chemistry C* **2009**, *113* (42), 18110-18114. DOI: 10.1021/jp9085969.
- (12) Wei, Z.; Wang, B.; Liu, Y.; Liu, Z.; Zhang, H.; Zhang, S.; Chang, J.; Lu, S. Green synthesis of nitrogen and sulfur co-doped carbon dots from *Allium fistulosum* for cell imaging. *New J. Chem.* **2019**, *43* (2), 718-723. DOI: 10.1039/C8NJ05783D.
- (13) Pandey, S.; Mewada, A.; Thakur, M.; Tank, A.; Sharon, M. Cysteamine hydrochloride protected carbon dots as a vehicle for the efficient release of the anti-schizophrenic drug haloperidol. *RSC Adv.* **2013**, *3* (48), 26290-26296. DOI: 10.1039/C3RA42139B.
- (14) Gong, N.; Ma, X.; Ye, X.; Zhou, Q.; Chen, X.; Tan, X.; Yao, S.; Huo, S.; Zhang, T.; Chen, S.; et al. Carbon-dot-supported atomically dispersed gold as a mitochondrial oxidative

- stress amplifier for cancer treatment. *Nat. Nanotechnol.* **2019**, *14* (4), 379-387. DOI: 10.1038/s41565-019-0373-6.
- (15) Ensafi, A. A.; Sefat, S. H.; Kazemifard, N.; Rezaei, B. An optical sensor based on inner filter effect using green synthesized carbon dots and Cu(II) for selective and sensitive penicillamine determination. *J. Iran. Chem. Soc.* **2019**, *16* (2), 355-363. DOI: 10.1007/s13738-018-1518-5.
- (16) Bhatt, S.; Bhatt, M.; Kumar, A.; Vyas, G.; Gajaria, T.; Paul, P. Green route for synthesis of multifunctional fluorescent carbon dots from Tulsi leaves and its application as Cr(VI) sensors, bio-imaging and patterning agents. *Colloids Surf., B* **2018**, *167*, 126-133. DOI: 10.1016/j.colsurfb.2018.04.008.
- (17) Bhunia, S. K.; Nandi, S.; Shikler, R.; Jelinek, R. Tuneable light-emitting carbon-dot/polymer flexible films prepared through one-pot synthesis. *Nanoscale* **2016**, *8* (6), 3400-3406. DOI: 10.1039/C5NR08400H.
- (18) Xu, J.; Miao, Y.; Zheng, J.; Yang, Y.; Liu, X. Ultrahigh Brightness Carbon Dot-Based Blue Electroluminescent LEDs by Host-Guest Energy Transfer Emission Mechanism. *Adv. Opt. Mater.* **2018**, *6* (14), 1800181 (1800181-1800185). DOI: 10.1002/adom.201800181.
- (19) Jayanthi, M.; Megarajan, S.; Subramaniyan, S. B.; Kamlekar, R. K.; Veerappan, A. A convenient green method to synthesize luminescent carbon dots from edible carrot and its application in bioimaging and preparation of nanocatalyst. *J. Mol. Liq.* **2019**, *278*, 175-182. DOI: 10.1016/j.molliq.2019.01.070.
- (20) Dao, V.-D.; Kim, P.; Baek, S.; Larina, L. L.; Yong, K.; Ryoo, R.; Ko, S. H.; Choi, H.-S. Facile synthesis of carbon dot-Au nanoraspberries and their application as high-

- performance counter electrodes in quantum dot-sensitized solar cells. *Carbon* **2016**, *96*, 139-144. DOI: 10.1016/j.carbon.2015.09.023.
- (21) Kumar, D.; Jain, V. K.; Shanker, G.; Srivastava, A. Citric acid production by solid state fermentation using sugarcane bagasse. *Process Biochemistry* **2003**, *38* (12), 1731-1738. DOI: 10.1016/S0032-9592(02)00252-2.
- (22) Liao, J.; Cheng, Z.; Zhou, L. Nitrogen-Doping Enhanced Fluorescent Carbon Dots: Green Synthesis and Their Applications for Bioimaging and Label-Free Detection of Au³⁺ Ions. *ACS Sustainable Chemistry & Engineering* **2016**, *4* (6), 3053-3061. DOI: 10.1021/acssuschemeng.6b00018.
- (23) Ding, D.; Liu, Y.; Xu, Y.; Zheng, P.; Li, H.; Zhang, D.; Sun, J. Improving the Production of L-Phenylalanine by Identifying Key Enzymes Through Multi-Enzyme Reaction System *in Vitro. Sci. Rep.* **2016**, *6*, 32208 (32201-32211). DOI: 10.1038/srep32208.
- (24) Gerigk, M.; Bujnicki, R.; Ganpo-Nkwenkwa, E.; Bongaerts, J.; Sprenger, G.; Takors, R. Process control for enhanced L-phenylalanine production using different recombinant *Escherichia coli* strains. *Biotechnol. Bioeng.* **2002**, *80* (7), 746-754. DOI: 10.1002/bit.10428.
- (25) Yang, J.; Chen, W.; Liu, X.; Zhang, Y.; Bai, Y. Hydrothermal synthesis and photoluminescent mechanistic investigation of highly fluorescent nitrogen doped carbon dots from amino acids. *Mater. Res. Bull.* **2017**, *89*, 26-32. DOI: 10.1016/j.materresbull.2017.01.013.
- (26) Lijuan, K.; Yongqiang, Y.; Ruiyi, L.; Zaijun, L. Phenylalanine-functionalized graphene quantum dot-silicon nanoparticle composite as an anode material for lithium ion batteries

- with largely enhanced electrochemical performance. *Electrochim. Acta* **2016**, *198*, 144-155. DOI: 10.1016/j.electacta.2016.03.034.
- (27) Shen, P.; Xia, Y. Synthesis-Modification Integration: One-Step Fabrication of Boronic Acid Functionalized Carbon Dots for Fluorescent Blood Sugar Sensing. *Anal. Chem.* **2014**, *86* (11), 5323-5329. DOI: 10.1021/ac5001338.
- (28) Wang, Z.; Fu, B.; Zou, S.; Duan, B.; Chang, C.; Yang, B.; Zhou, X.; Zhang, L. Facile construction of carbon dots via acid catalytic hydrothermal method and their application for target imaging of cancer cells. *Nano Res.* **2016**, *9* (1), 214-223. DOI: 10.1007/s12274-016-0992-2.
- (29) Williams, A. T. R.; Winfield, S. A.; Miller, J. N. Relative fluorescence quantum yields using a computer-controlled luminescence spectrometer. *Anal.* **1983**, *108* (1290), 1067-1071. DOI: 10.1039/AN9830801067.
- (30) Brouwer, A. M. Standards for photoluminescence quantum yield measurements in solution (IUPAC Technical Report). *Pure Appl. Chem.* **2011**, *83* (12), 2213-2228. DOI: 10.1351/PAC-REP-10-09-31.
- (31) Yarur, F.; Macairan, J.-R.; Naccache, R. Ratiometric detection of heavy metal ions using fluorescent carbon dots. *Environ. Sci.: Nano* **2019**, *6* (4), 1121-1130. DOI: 10.1039/C8EN01418C.
- (32) Solomons, T. W. G.; Fryhle, C. B. *Organic Chemistry*; John Wiley & Sons, Inc., 2011.
- (33) Zhang, Z.; Chen, J.; Duan, Y.; Liu, W.; Li, D.; Yan, Z.; Yang, K. Highly luminescent nitrogen-doped carbon dots for simultaneous determination of chlortetracycline and sulfasalazine. *Lumin.* **2018**, *33* (2), 318-325. DOI: 10.1002/bio.3416.

- (34) Miao, X.; Qu, D.; Yang, D.; Nie, B.; Zhao, Y.; Fan, H.; Sun, Z. Synthesis of Carbon Dots with Multiple Color Emission by Controlled Graphitization and Surface Functionalization. *Adv. Mater.* **2018**, *30* (1), 1704740 (1704741-1704748). DOI: 10.1002/adma.201704740.
- (35) Ogi, T.; Aishima, K.; Permatasari, F. A.; Iskandar, F.; Tanabe, E.; Okuyama, K. Kinetics of nitrogen-doped carbon dot formation via hydrothermal synthesis. *New J. Chem.* **2016**, *40* (6), 5555-5561. DOI: 10.1039/C6NJ00009F.
- (36) Hou, J.; Wang, W.; Zhou, T.; Wang, B.; Li, H.; Ding, L. Synthesis and formation mechanistic investigation of nitrogen-doped carbon dots with high quantum yields and yellowish-green fluorescence. *Nanoscale* **2016**, *8* (21), 11185-11193. DOI: 10.1039/C6NR02701F.
- (37) Zheng, C.; An, X.; Gong, J. Novel pH sensitive N-doped carbon dots with both long fluorescence lifetime and high quantum yield. *RSC Adv.* **2015**, *5* (41), 32319-32322. DOI: 10.1039/C5RA01986A.
- (38) Qu, D.; Zheng, M.; Zhang, L.; Zhao, H.; Xie, Z.; Jing, X.; Haddad, R. E.; Fan, H.; Sun, Z. Formation mechanism and optimization of highly luminescent N-doped graphene quantum dots. *Sci. Rep.* **2014**, *4*, 5294 (5291-5299). DOI: 10.1038/srep05294 PMC.
- (39) Zhu, S.; Meng, Q.; Wang, L.; Zhang, J.; Song, Y.; Jin, H.; Zhang, K.; Sun, H.; Wang, H.; Yang, B. Highly Photoluminescent Carbon Dots for Multicolor Patterning, Sensors, and Bioimaging. *Angew. Chem., Int. Ed.* **2013**, *52* (14), 3953-3957. DOI: 10.1002/anie.201300519.
- (40) Guo, Y.; Wang, Z.; Shao, H.; Jiang, X. Hydrothermal synthesis of highly fluorescent carbon nanoparticles from sodium citrate and their use for the detection of mercury ions. *Carbon* **2013**, *52*, 583-589. DOI: 10.1016/j.carbon.2012.10.028.

- (41) Permatasari, F. A.; Aimon, A. H.; Iskandar, F.; Ogi, T.; Okuyama, K. Role of C–N Configurations in the Photoluminescence of Graphene Quantum Dots Synthesized by a Hydrothermal Route. *Sci. Rep.* **2016**, *6*, 21042 (21041-21048). DOI: 10.1038/srep21042.
- (42) Tyagi, A.; Tripathi, K. M.; Singh, N.; Choudhary, S.; Gupta, R. K. Green synthesis of carbon quantum dots from lemon peel waste: applications in sensing and photocatalysis. *RSC Adv.* **2016**, *6* (76), 72423-72432. DOI: 10.1039/C6RA10488F.
- (43) Bandi, R.; Gangapuram, B. R.; Dadigala, R.; Eslavath, R.; Singh, S. S.; Guttena, V. Facile and green synthesis of fluorescent carbon dots from onion waste and their potential applications as sensor and multicolour imaging agents. *RSC Adv.* **2016**, *6* (34), 28633-28639. DOI: 10.1039/C6RA01669C.
- (44) Atchudan, R.; Edison, T. N. J. I.; Sethuraman, M. G.; Lee, Y. R. Efficient synthesis of highly fluorescent nitrogen-doped carbon dots for cell imaging using unripe fruit extract of *Prunus mume*. *Appl. Surf. Sci.* **2016**, *384*, 432-441. DOI: 10.1016/j.apsusc.2016.05.054.
- (45) Huang, H.; Lv, J.-J.; Zhou, D.-L.; Bao, N.; Xu, Y.; Wang, A.-J.; Feng, J.-J. One-pot green synthesis of nitrogen-doped carbon nanoparticles as fluorescent probes for mercury ions. *RSC Adv.* **2013**, *3* (44), 21691-21696. DOI: 10.1039/C3RA43452D.
- (46) Zhu, C.; Zhai, J.; Dong, S. Bifunctional fluorescent carbon nanodots: green synthesis via soy milk and application as metal-free electrocatalysts for oxygen reduction. *Chem. Commun.* **2012**, *48* (75), 9367-9369. DOI: 10.1039/C2CC33844K.
- (47) Li, Q.; Chen, B.; Xing, B. Aggregation Kinetics and Self-Assembly Mechanisms of Graphene Quantum Dots in Aqueous Solutions: Cooperative Effects of pH and Electrolytes. *Environ. Sci. Technol.* **2017**, *51* (3), 1364-1376. DOI: 10.1021/acs.est.6b04178.

- (48) Hsiao, M.-C.; Liao, S.-H.; Lin, Y.-F.; Wang, C.-A.; Pu, N.-W.; Tsai, H.-M.; Ma, C.-C. M. Preparation and characterization of polypropylene-graft-thermally reduced graphite oxide with an improved compatibility with polypropylene-based nanocomposite. *Nanoscale* **2011**, *3* (4), 1516-1522. DOI: 10.1039/C0NR00981D.
- (49) Samantara, A. K.; Chandra Sahu, S.; Ghosh, A.; Jena, B. K. Sandwiched graphene with nitrogen, sulphur co-doped CQDs: an efficient metal-free material for energy storage and conversion applications. *J. Mater. Chem. A* **2015**, *3* (33), 16961-16970. DOI: 10.1039/C5TA03376D.
- (50) Oh, Y. J.; Yoo, J. J.; Kim, Y. I.; Yoon, J. K.; Yoon, H. N.; Kim, J.-H.; Park, S. B. Oxygen functional groups and electrochemical capacitive behavior of incompletely reduced graphene oxides as a thin-film electrode of supercapacitor. *Electrochim. Acta* **2014**, *116*, 118-128. DOI: 10.1016/j.electacta.2013.11.040.
- (51) Błoński, P.; Tuček, J.; Sofer, Z.; Mazánek, V.; Petr, M.; Pumera, M.; Otyepka, M.; Zbořil, R. Doping with Graphitic Nitrogen Triggers Ferromagnetism in Graphene. *J. Am. Chem. Soc.* **2017**, *139* (8), 3171-3180. DOI: 10.1021/jacs.6b12934.
- (52) Zhang, W.; Liu, Y.; Meng, X.; Ding, T.; Xu, Y.; Xu, H.; Ren, Y.; Liu, B.; Huang, J.; Yang, J.; et al. Graphenol defects induced blue emission enhancement in chemically reduced graphene quantum dots. *Phys. Chem. Chem. Phys.* **2015**, *17* (34), 22361-22366. DOI: 10.1039/C5CP03434E.
- (53) Chandra, S.; Laha, D.; Pramanik, A.; Ray Chowdhuri, A.; Karmakar, P.; Sahu, S. K. Synthesis of highly fluorescent nitrogen and phosphorus doped carbon dots for the detection of Fe³⁺ ions in cancer cells. *Lumin.* **2016**, *31* (1), 81-87. DOI: 10.1002/bio.2927.

- (54) Dong, Y.; Wang, R.; Li, H.; Shao, J.; Chi, Y.; Lin, X.; Chen, G. Polyamine-functionalized carbon quantum dots for chemical sensing. *Carbon* **2012**, *50* (8), 2810-2815. DOI: 10.1016/j.carbon.2012.02.046.
- (55) Yang, Y.; Cui, J.; Zheng, M.; Hu, C.; Tan, S.; Xiao, Y.; Yang, Q.; Liu, Y. One-step synthesis of amino-functionalized fluorescent carbon nanoparticles by hydrothermal carbonization of chitosan. *Chem. Commun.* **2012**, *48* (3), 380-382. DOI: 10.1039/C1CC15678K.
- (56) Yang, Z.; Xu, M.; Liu, Y.; He, F.; Gao, F.; Su, Y.; Wei, H.; Zhang, Y. Nitrogen-doped, carbon-rich, highly photoluminescent carbon dots from ammonium citrate. *Nanoscale* **2014**, *6* (3), 1890-1895. DOI: 10.1039/C3NR05380F.
- (57) Xu, M.; He, G.; Li, Z.; He, F.; Gao, F.; Su, Y.; Zhang, L.; Yang, Z.; Zhang, Y. A green heterogeneous synthesis of N-doped carbon dots and their photoluminescence applications in solid and aqueous states. *Nanoscale* **2014**, *6* (17), 10307-10315. DOI: 10.1039/C4NR02792B.
- (58) Bourlinos, A. B.; Stassinopoulos, A.; Angelos, D.; Zboril, R.; Karakassides, M.; Giannelis, E. P. Surface Functionalized Carbogenic Quantum Dots. *Small* **2008**, *4* (4), 455-458. DOI: 10.1002/smll.200700578.
- (59) Bhamore, J. R.; Jha, S.; Singhal, R. K.; Park, T. J.; Kailasa, S. K. Facile green synthesis of carbon dots from *Pyrus pyrifolia* fruit for assaying of Al³⁺ ion via chelation enhanced fluorescence mechanism. *J. Mol. Liq.* **2018**, *264*, 9-16. DOI: 10.1016/j.molliq.2018.05.041.
- (60) Radhakrishnan, K.; Panneerselvam, P. Green synthesis of surface-passivated carbon dots from the prickly pear cactus as a fluorescent probe for the dual detection of arsenic(iii) and

- hypochlorite ions from drinking water. *RSC Advances* **2018**, 8 (53), 30455-30467. DOI: 10.1039/C8RA05861J.
- (61) Ramanan, V.; Siddaiah, B.; Raji, K.; Ramamurthy, P. Green Synthesis of Multifunctionalized, Nitrogen-Doped, Highly Fluorescent Carbon Dots from Waste Expanded Polystyrene and Its Application in the Fluorimetric Detection of Au³⁺ Ions in Aqueous Media. *ACS Sustainable Chem. Eng.* **2018**, 6 (2), 1627-1638. DOI: 10.1021/acssuschemeng.7b02852.
- (62) Murugan, N.; Prakash, M.; Jayakumar, M.; Sundaramurthy, A.; Sundramoorthy, A. K. Green synthesis of fluorescent carbon quantum dots from *Eleusine coracana* and their application as a fluorescence ‘turn-off’ sensor probe for selective detection of Cu²⁺. *Appl. Surf. Sci.* **2019**, 476, 468-480. DOI: 10.1016/j.apsusc.2019.01.090.
- (63) Rooj, B.; Dutta, A.; Islam, S.; Mandal, U. Green Synthesized Carbon Quantum Dots from *Polianthes tuberosa* L. Petals for Copper (II) and Iron (II) Detection. *J. Fluoresc.* **2018**, 28 (5), 1261-1267. DOI: 10.1007/s10895-018-2292-6.
- (64) Ramanan, V.; Subray, S. H.; Ramamurthy, P. A green synthesis of highly luminescent carbon dots from itaconic acid and their application as an efficient sensor for Fe³⁺ ions in aqueous medium. *New J. Chem.* **2018**, 42 (11), 8933-8942. DOI: 10.1039/C8NJ00813B.
- (65) Pourreza, N.; Ghomi, M. Green synthesized carbon quantum dots from *Prosopis juliflora* leaves as a dual off-on fluorescence probe for sensing mercury (II) and chemet drug. *Mater. Sci. Eng., C* **2019**, 98, 887-896. DOI: 10.1016/j.msec.2018.12.141.
- (66) Hu, Y.; Zhao, F.; Hu, S.; Dong, Y.; Li, D.; Su, Z. A novel turn-on colorimetric and fluorescent sensor for Fe³⁺ and its application in living cells. *J. Photochem. Photobiol., A* **2017**, 332, 351-356. DOI: 10.1016/j.jphotochem.2016.09.006.

- (67) Wataha, J. C.; Hanks, C. T. Biological effects of palladium and risk of using palladium in dental casting alloys. *J. Oral Rehabil.* **1996**, *23* (5), 309-320. DOI: 10.1111/j.1365-2842.1996.tb00858.x.
- (68) Zhang, Y.-L.; Wang, L.; Zhang, H.-C.; Liu, Y.; Wang, H.-Y.; Kang, Z.-H.; Lee, S.-T. Graphitic carbon quantum dots as a fluorescent sensing platform for highly efficient detection of Fe³⁺ ions. *RSC Adv.* **2013**, *3* (11), 3733-3738. DOI: 10.1039/C3RA23410J.
- (69) Qian, Z.; Ma, J.; Shan, X.; Feng, H.; Shao, L.; Chen, J. Highly Luminescent N-Doped Carbon Quantum Dots as an Effective Multifunctional Fluorescence Sensing Platform. *Chem.: Eur. J.* **2014**, *20* (8), 2254-2263. DOI: 10.1002/chem.201304374.

Supporting Information

Table S3.1. Synthesis concentrations at various phenylalanine mole fractions.

Phenylalanine mole fraction	0.00	0.05	0.10	0.25	0.50	0.75	0.90	0.95	1.00
Name	P ₀	P ₅	P ₁₀	P ₂₅	P ₅₀	P ₇₅	P ₉₀	P ₉₅	P ₁₀₀
Phenylalanine [mM]	0	13	26	60	108	147	168	174	180
Citric acid [mM]	270	250	231	180	108	49	19	9	0
Carbon [mM]	1620	1620	1620	1620	1620	1620	1620	1620	1620
Nitrogen [mM]	0	13	26	60	108	147	168	174	180
(N:C) _R	0.000	0.008	0.016	0.037	0.067	0.091	0.103	0.107	0.111

Table S3.2. Summary of the elemental composition of CDs, on the basis of carbon (C), nitrogen (N), and oxygen

(O). Uncertainties show 2 standard errors of the mean (N = 3).

CD	C [at%]	N [at%]	O [at%]
P ₀	50.4 ± 3.1	0.0 ± 0.0	49.6 ± 2.5
P ₅	58.4 ± 0.9	3.9 ± 0.1	37.7 ± 0.9
P ₁₀	60.7 ± 4.6	3.5 ± 0.1	35.8 ± 1.8
P ₂₅	69.0 ± 1.0	5.2 ± 0.1	25.8 ± 0.1
P ₅₀	69.8 ± 6.9	5.4 ± 0.6	24.8 ± 1.4
P ₇₅	70.1 ± 0.2	6.0 ± 0.1	23.8 ± 0.3
P ₉₀	69.9 ± 0.2	6.4 ± 0.6	23.7 ± 0.5
P ₉₅	67.1 ± 1.5	9.1 ± 0.1	23.8 ± 2.0
P ₁₀₀	63.0 ± 3.1	8.5 ± 0.9	28.4 ± 2.3

Table S3.3. XPS data. Relative amount of sp^2 , sp^3 , C-N/C-O, C=N/C=O, and O-C=O groups from the deconvolution of C_{1s} peaks. Relative amount of C-NH-C/pyridinic N, C-N(C)-C/N-C=O/pyrrolic N, and -NH₃⁺/graphitic N groups from the deconvolution of N_{1s} peaks. Relative amount of COOH, C=O, C-O, and C-OH groups from the deconvolution of O_{1s} peaks. Uncertainties show 2 standard errors of the mean (N = 3).

CD	Carbon [%C _{1s}]					Nitrogen [%N _{1s}]			Oxygen [%O _{1s}]			
	sp^2	sp^3	C-N/C-O	C=N/C=O	O-C=O	C-NH-C/ pyridinic N	C-N(C)-C/ N-C=O/ pyrrolic N	-NH ₃ ⁺ / graphitic N	COOH	C=O	C-O	C-OH
	~284.2 eV	~284.9 eV	~286.0 eV	~287.8 eV	~288.8 eV	~399.6 eV	~400.4 eV	~401.6 eV	~531.1 eV	~531.9 eV	~532.7 eV	~533.5 eV
P ₀	9 ± 7	34 ± 6	25 ± 2	4 ± 0	29 ± 1	0 ± 0	0 ± 0	0 ± 0	8 ± 1	47 ± 5	30 ± 4	15 ± 1
P ₅	27 ± 3	32 ± 3	13 ± 0	7 ± 0	20 ± 1	45 ± 4	22 ± 2	33 ± 3	13 ± 2	40 ± 2	26 ± 1	22 ± 3
P ₁₀	24 ± 8	35 ± 7	17 ± 1	5 ± 2	19 ± 2	34 ± 6	39 ± 2	28 ± 5	11 ± 3	43 ± 1	29 ± 3	17 ± 1
P ₂₅	45 ± 2	22 ± 1	16 ± 2	9 ± 0	8 ± 0	69 ± 6	24 ± 6	7 ± 1	26 ± 1	39 ± 2	21 ± 1	14 ± 2
P ₅₀	47 ± 1	22 ± 1	15 ± 1	7 ± 1	9 ± 1	55 ± 5	32 ± 3	13 ± 1	44 ± 2	24 ± 1	21 ± 2	11 ± 3
P ₇₅	51 ± 5	19 ± 4	18 ± 2	6 ± 0	6 ± 0	54 ± 2	18 ± 2	27 ± 1	35 ± 2	37 ± 2	16 ± 2	11 ± 0
P ₉₀	42 ± 4	23 ± 4	22 ± 3	7 ± 0	5 ± 0	50 ± 8	24 ± 5	26 ± 4	26 ± 8	40 ± 2	22 ± 6	12 ± 2
P ₉₅	46 ± 6	31 ± 4	13 ± 0	7 ± 1	2 ± 2	31 ± 10	37 ± 12	32 ± 3	33 ± 2	42 ± 2	16 ± 0	8 ± 1
P ₁₀₀	42 ± 9	28 ± 11	25 ± 2	4 ± 1	1 ± 0	22 ± 8	25 ± 2	53 ± 8	49 ± 12	30 ± 11	15 ± 1	5 ± 2

Table S3.4. Table of parameters and corresponding coefficient of determination (R^2) of the function: $QY = \beta_0 + \beta_1 z_1 + \beta_2 z_2 + \beta_3 z_3 + \beta_4 z_1 z_2$ where z_i is the standard score of: (i=1) (O:C)_{CD}, (i=2) relative amount of COOH oxygen (from O_{1s} spectra), and (i=3) (N:C)_{CD}.

β_0	β_1	β_2	β_3	β_4	R^2
0.271	-0.500	-0.238	0	-0.192	0.934
0.409	-0.309	-0.159	-0.045	0	0.838
0.409	-0.287	-0.178	0	0	0.825
0.409	-0.256	0	-0.124	0	0.640
0.409	-0.159	0	0	0	0.516
0.409	0	-0.065	0.125	0	0.152
0.409	0	0	0.075	0	0.115
0.409	0	0.029	0	0	0.017

Table S3.5. Table of means (μ_i) and standard deviations (σ_i) for the features: (i=1) (O:C)_{CD}, (i=2) relative amount of COOH oxygen (from O_{1s} spectra), and (i=3) (N:C)_{CD}. Values are used to calculate the standard score (z_i) as follows: $z_i = \frac{x_i - \mu_i}{\sigma_i}$ where x_i is the real value of: (i=1) (O:C)_{CD}, (i=2) relative amount of COOH oxygen (from O_{1s} spectra), and (i=3) (N:C)_{CD}.

μ_1	μ_2	μ_3
0.492	0.272	0.081
σ_1	σ_2	σ_3
0.204	0.139	0.039

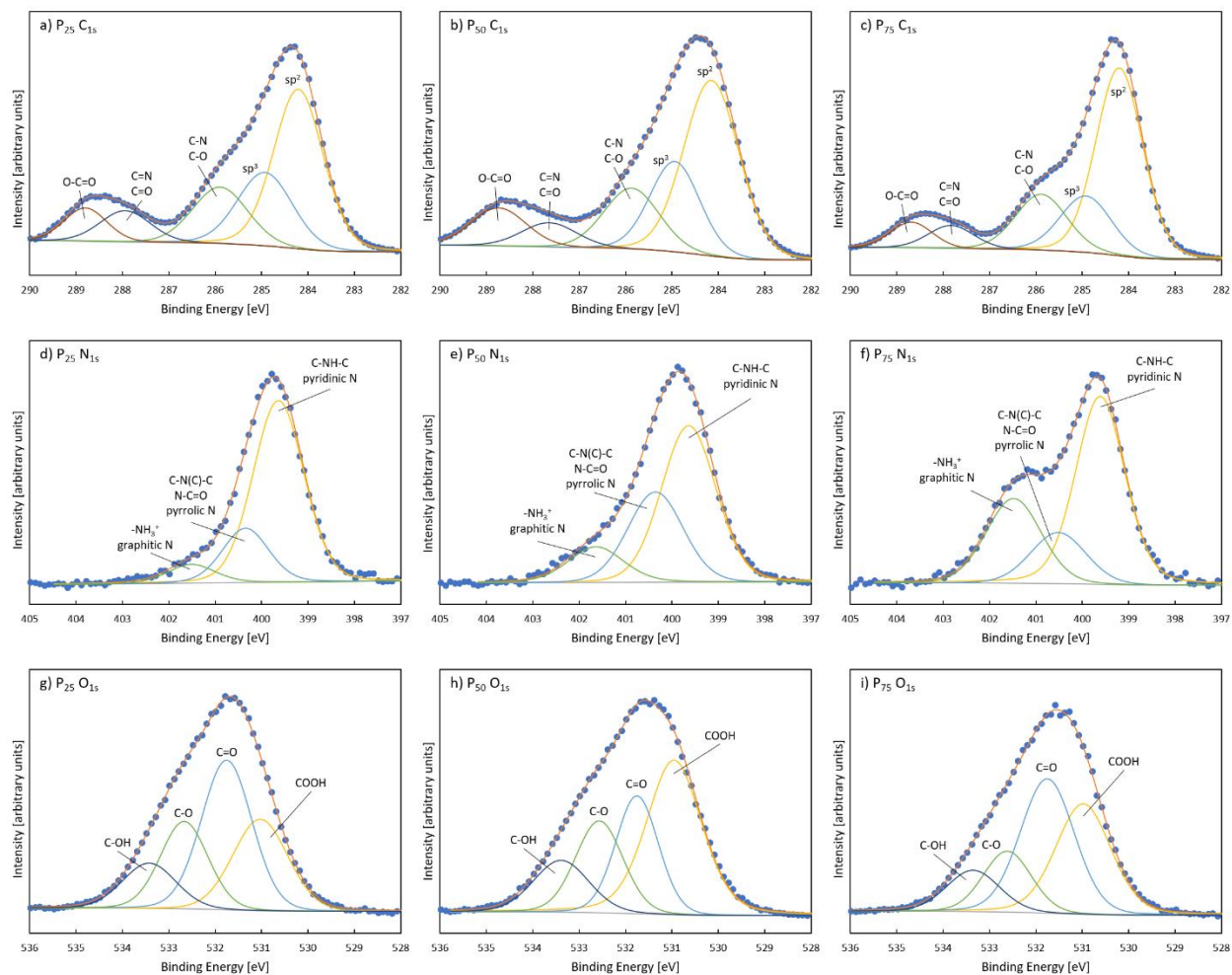


Figure S3.1. C_{1s}, N_{1s}, and O_{1s} XPS peak deconvolution for a), d), g) P₂₅-CDs, b), e), h) P₅₀-CDs, and c), f), i) P₇₅-CDs, respectively.

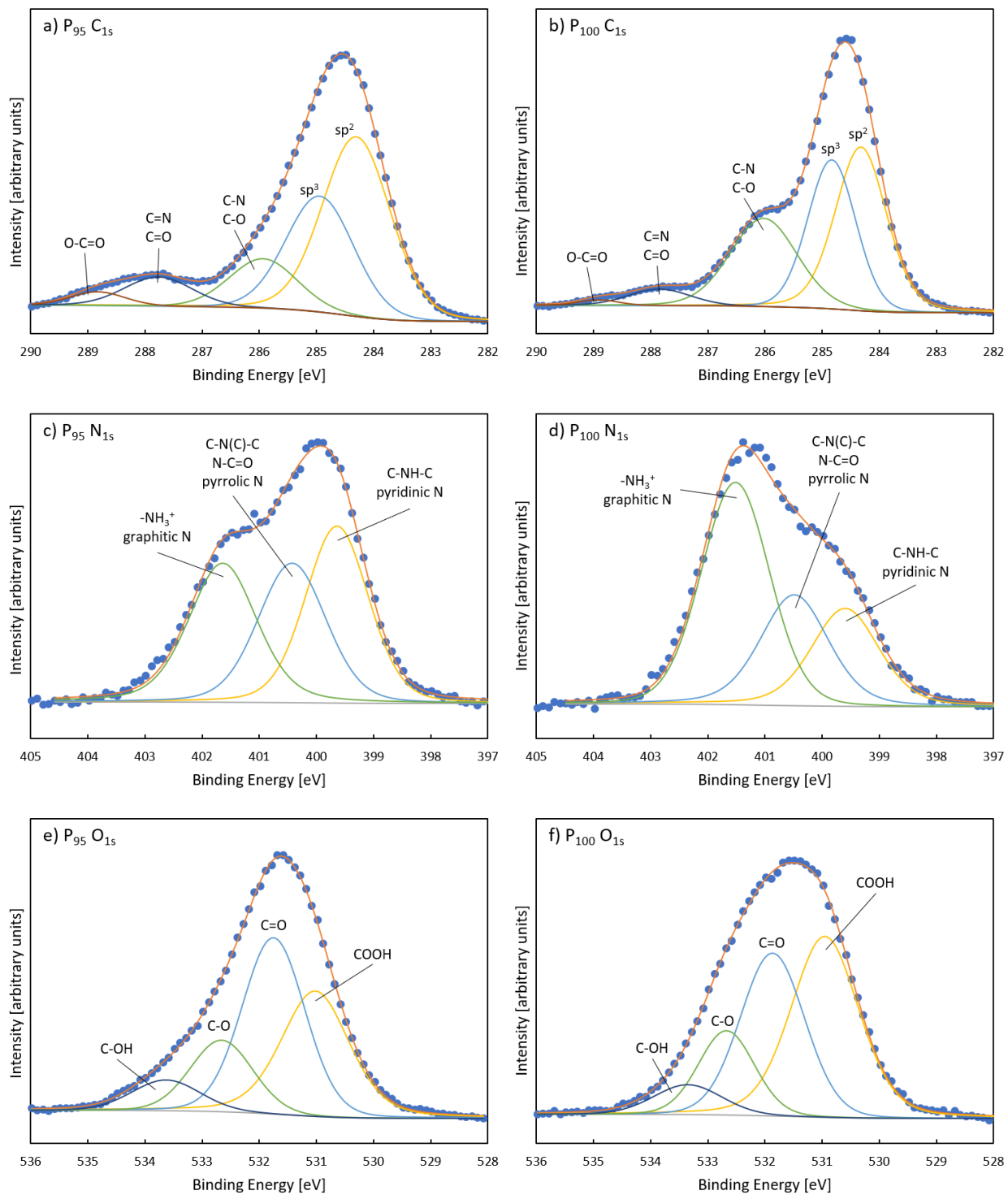


Figure S3.2. C_{1s} , N_{1s} , and O_{1s} XPS peak deconvolution for a), c), e) P_{95} -CDs and b), d), f) P_{100} -CDs, respectively.

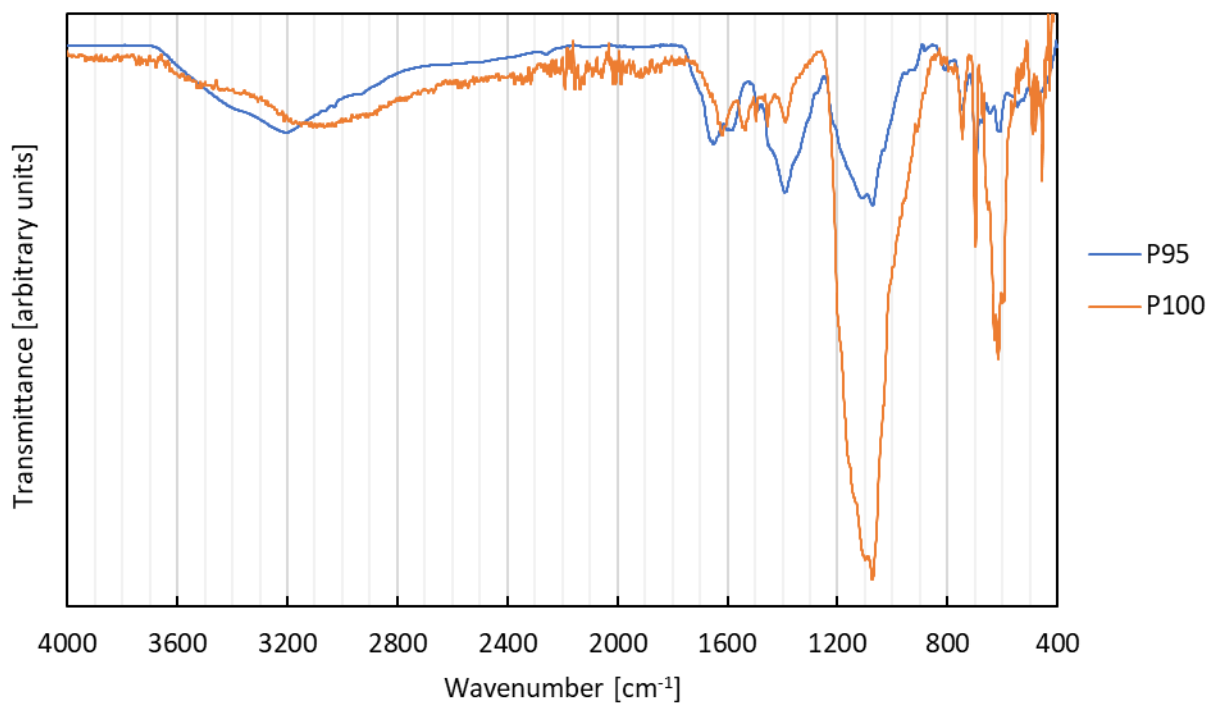


Figure S3.3. FTIR spectra of P₉₅-CDs and P₁₀₀-CDs. This figure shows the same data as Figure 3.2b, but the P₁₀₀-CD spectra has been normalized to match the peaks between the two CDs at ~3200 cm⁻¹ instead of at ~1100 cm⁻¹.

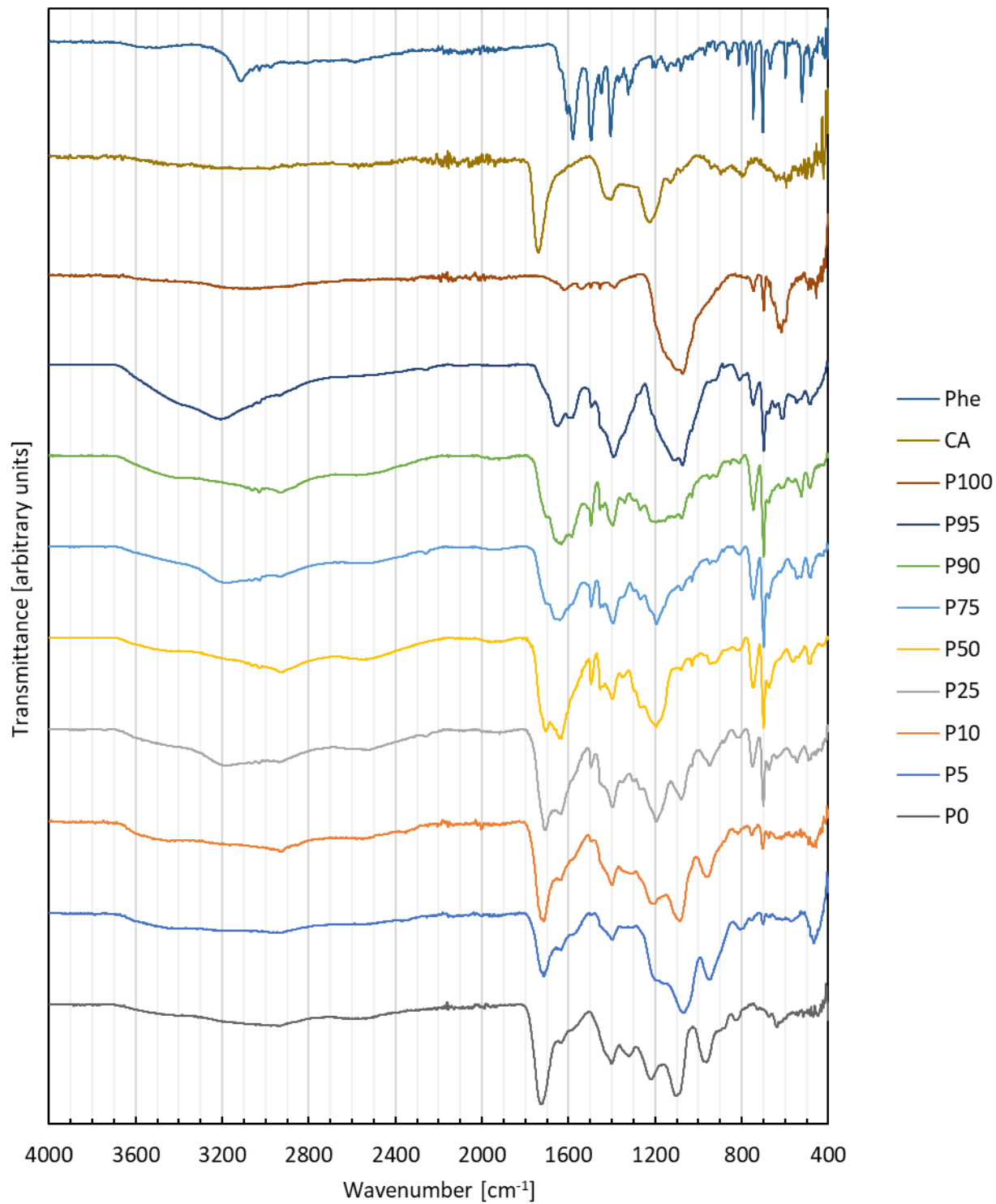


Figure S3.4. FTIR spectra of CDs, citric acid (CA), and phenylalanine (Phe). Normalized to each spectrum's most prominent peak.

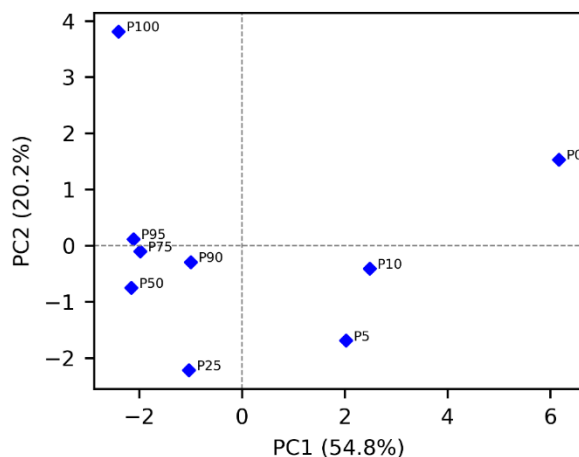


Figure S3.5. Principal component analysis (PCA) of the 14-dimensional XPS data (*i.e.* (N:C)_{CD} and (O:C)_{CD}, and the relative amount of each bond type in the 5 C_{1s} features, 3 N_{1s} features, and 4 O_{1s} features) on the first two principal components (PCs). Percentage of total variance explained by each PC is indicated in brackets.

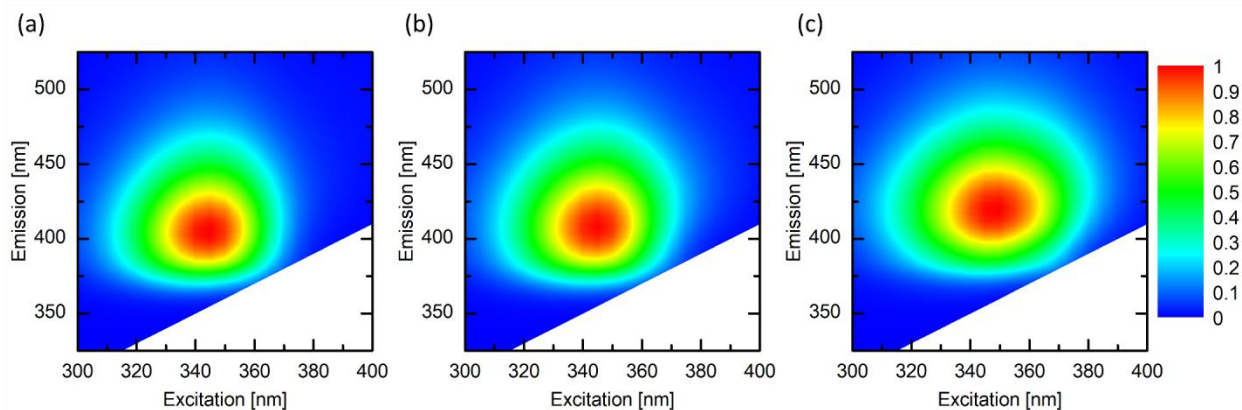


Figure S3.6. Fluorescence heat maps of (a) P₂₅-CDs, (b) P₅₀-CDs, and (c) P₇₅-CDs, over a range of excitation and emission wavelengths using an excitation and emission slit width of 3 nm. Fluorescence heat maps were normalized to their respective maximum peaks.

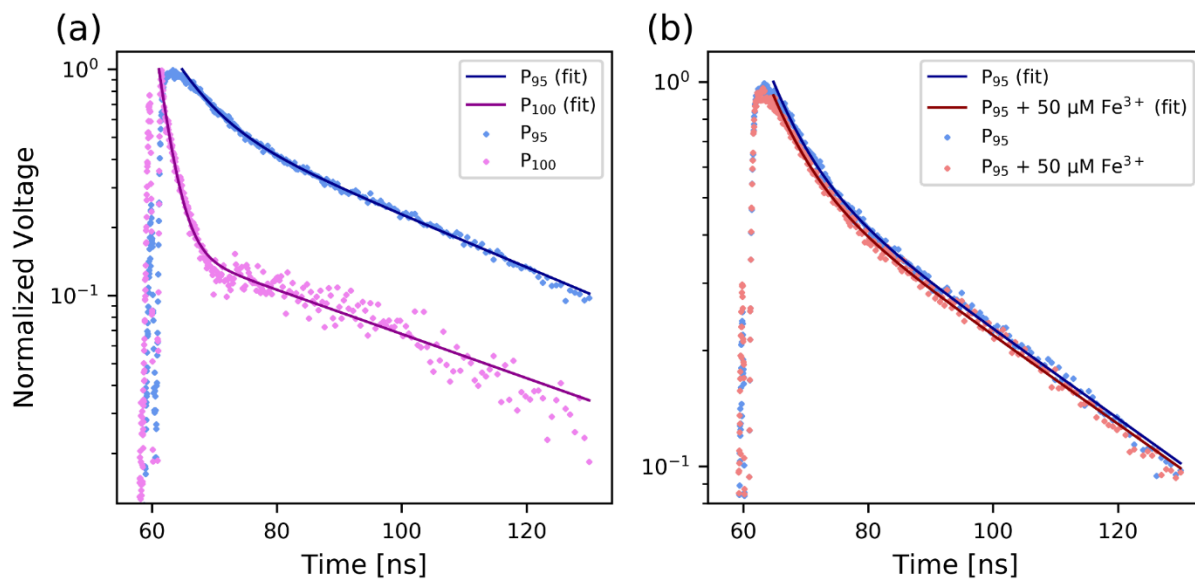


Figure S3.7. Fluorescence lifetime decay fit to a biexponential function of a) P₉₅-CD and P₁₀₀-CD and b) P₉₅-CD with and without 50 μM Fe³⁺.

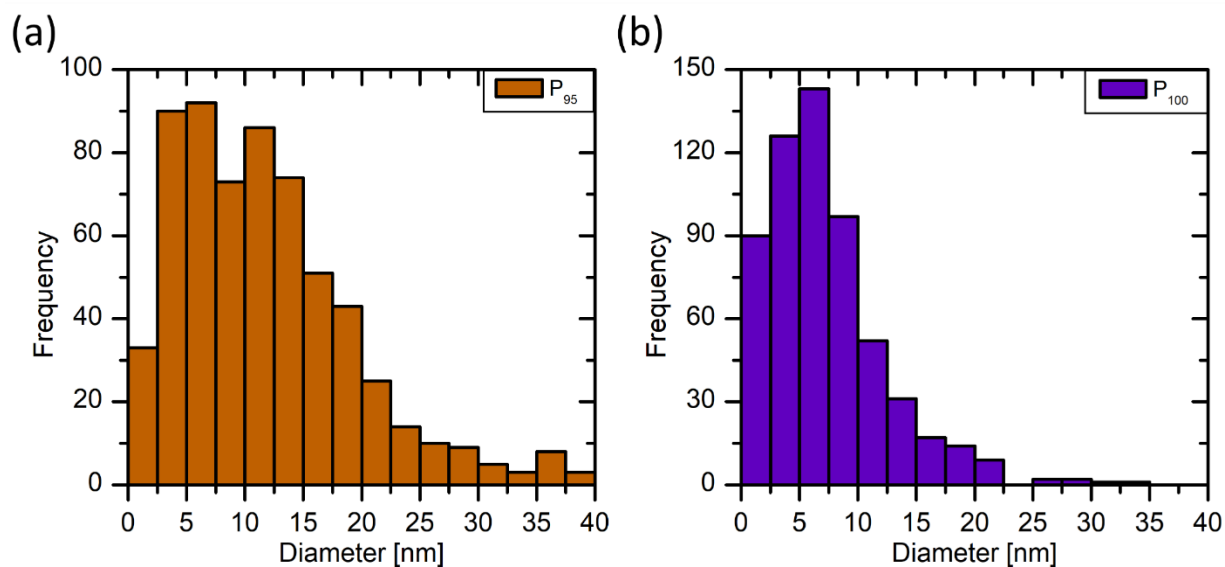


Figure S3.8. Histogram of (a) P₉₅-CD and (b) P₁₀₀-CD size distribution from TEM.

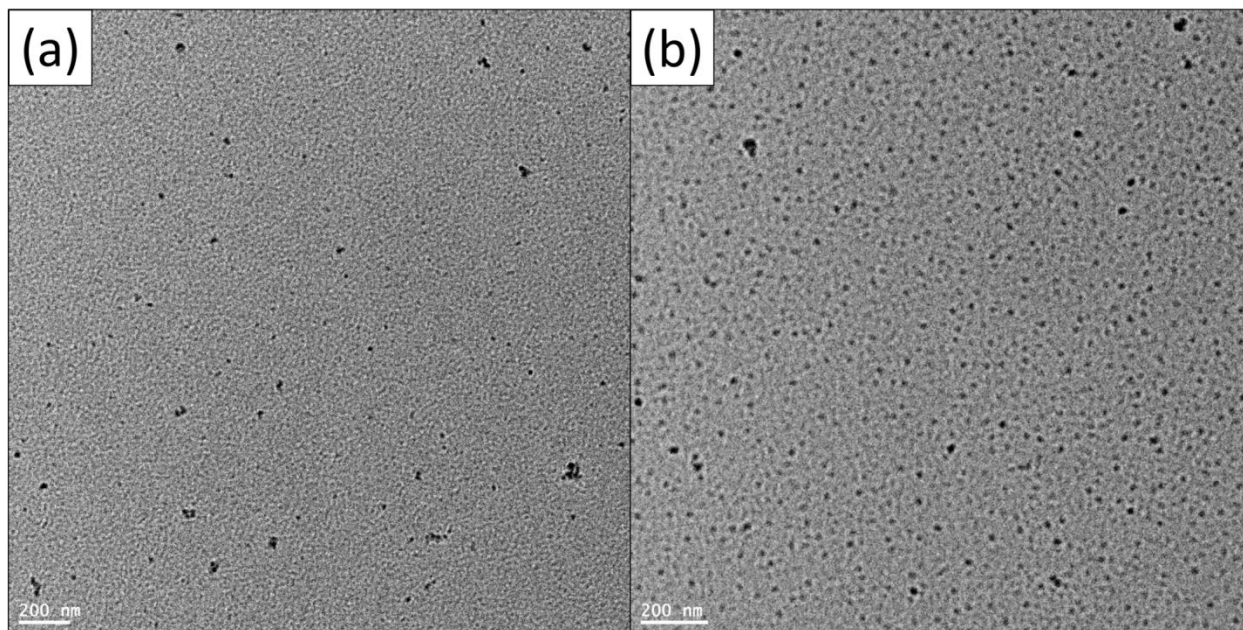


Figure S3.9. Original TEM images of (a) P₉₅-CDs and (b) P₁₀₀-CDs as shown in Figure 3.5c,d.

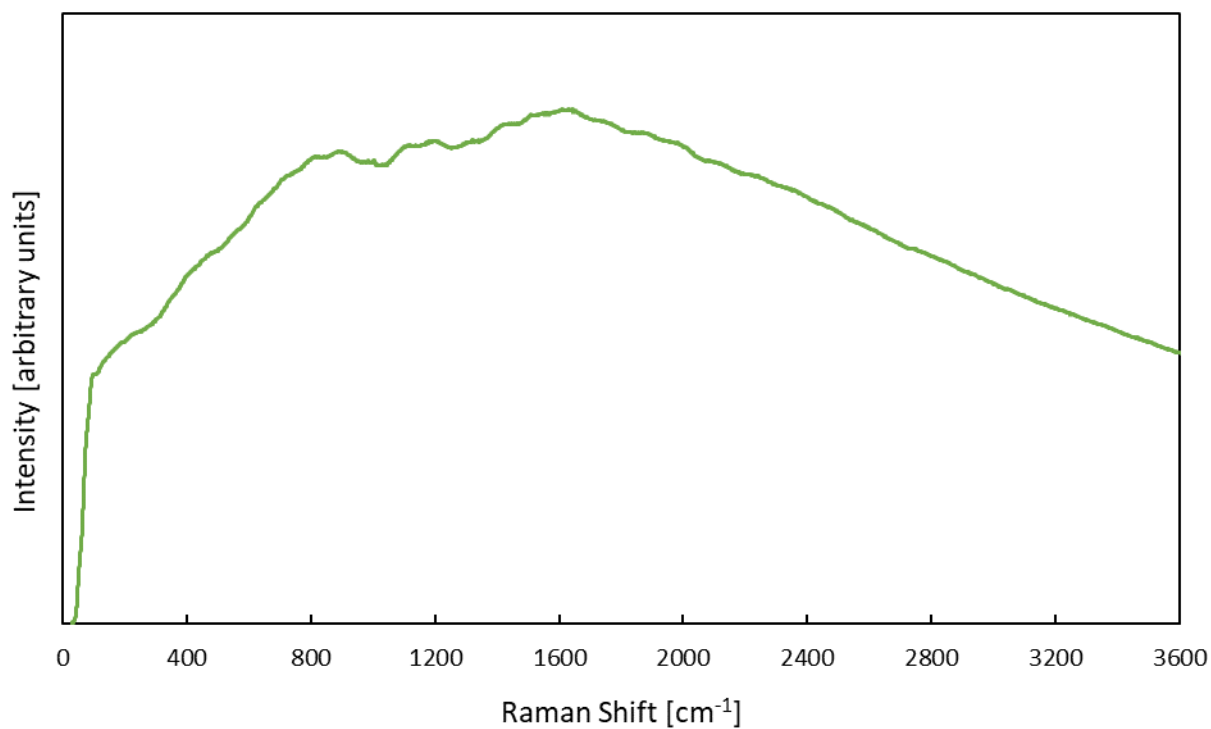


Figure S3.10. Raman spectrum of P₉₅-CDs. The fluorescence from the CDs is obscuring the Raman signal.

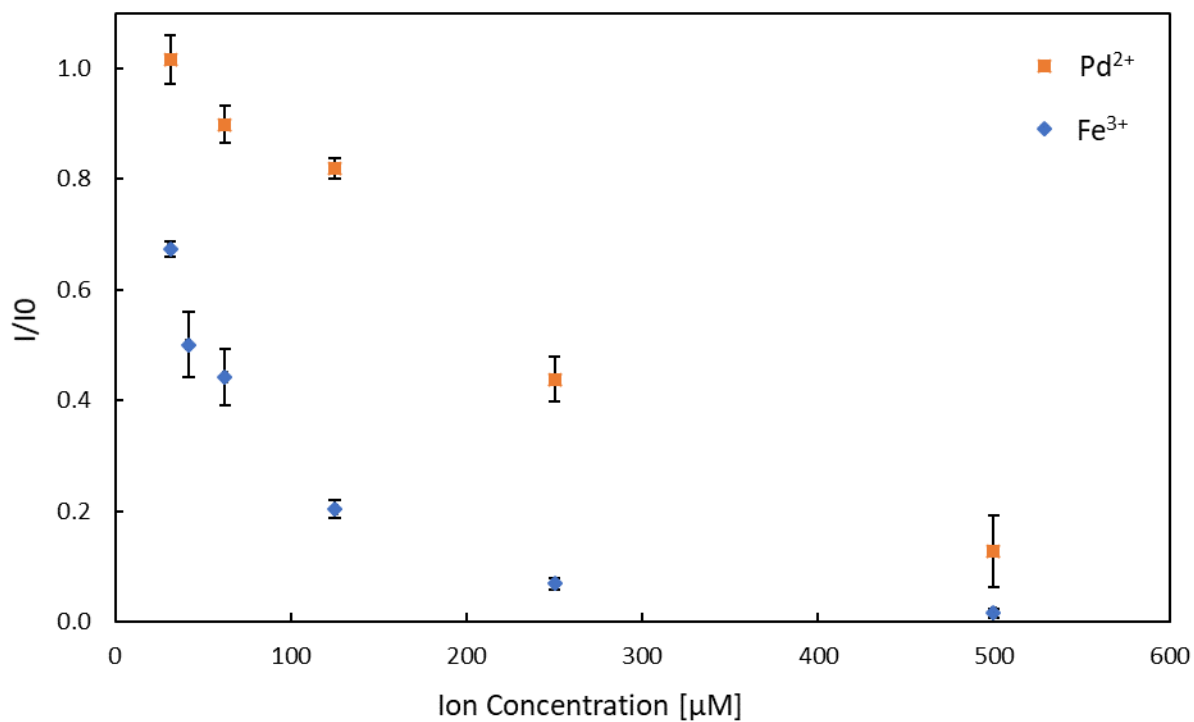


Figure S3.11. Relative fluorescence of P₉₅-CDs exposed to Fe³⁺ and Pd²⁺.

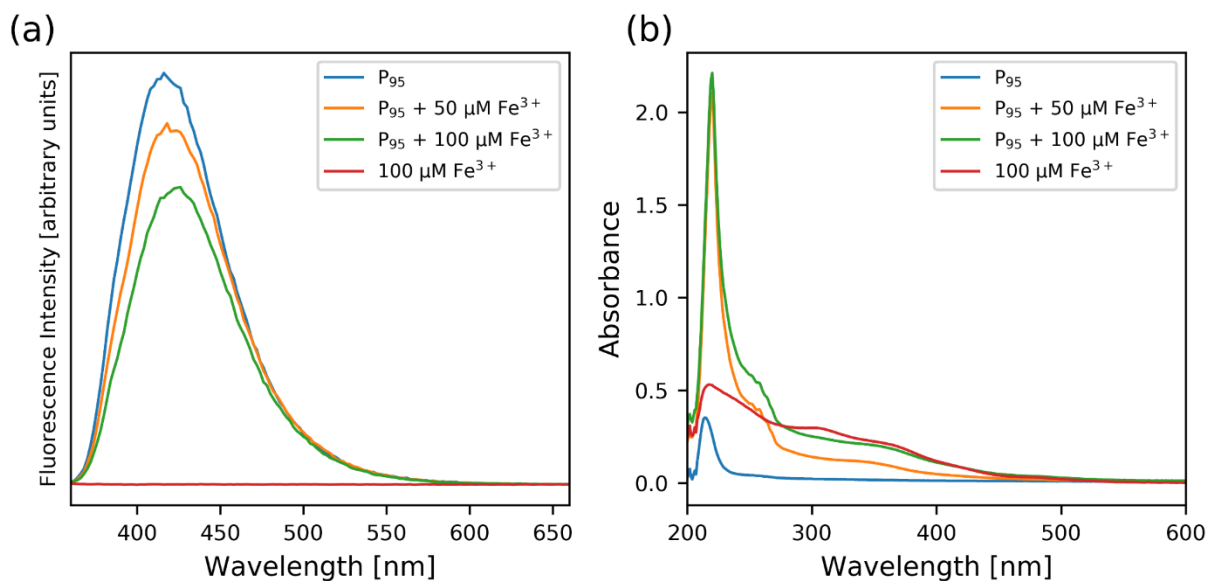


Figure S3.12. Fe³⁺ sensing data in the form of a) fluorescence emission spectra at an excitation wavelength of 350 nm and b) absorbance spectra.

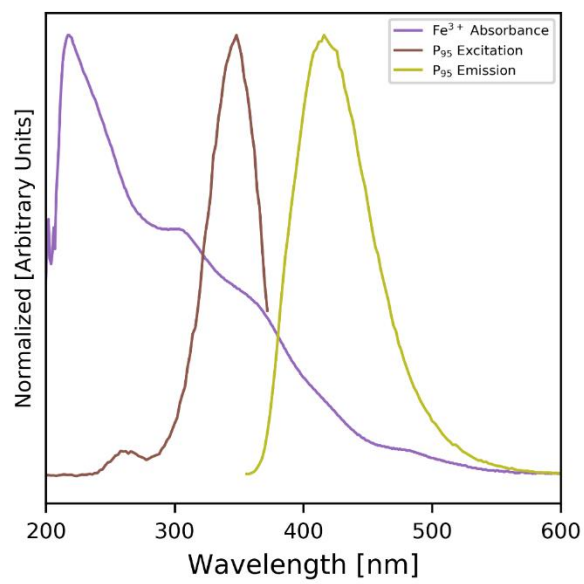


Figure S3.13. Absorbance of Fe³⁺ and fluorescence of P₉₅-CDs. All spectra are normalized to their respective maximum. P₉₅-CD excitation spectra was performed at an emission wavelength of 376 nm. P₉₅-CD emission spectra was performed at an excitation wavelength of 350 nm.

XPS Analysis

Here, we discuss those statistically significant results ($p < 0.05$) with a considerable difference in magnitude ($1.4\times$) between CD types. Regarding the deconvolution of the C_{1s} spectra, P₅₀-CDs have 45% more ($p < 0.01$) O-C=O carbon than P₇₅-CDs. Interestingly, P₁₀₀-CDs have 92% more ($p < 0.01$) C-N/C-O carbon and 44% less ($p < 0.01$) C=N/C=O carbon than P₉₅-CDs.

Concerning the deconvolution of the N_{1s} spectra, P₅₀-CDs and P₇₅-CDs have 89% more ($p < 0.01$) and 301% more ($p < 0.01$) $-NH_3^+$ /graphitic N than P₂₅-CDs, respectively, however there is no clear trend correlating these great variations with QY. P₁₀₀-CDs also have 68% more ($p < 0.01$) $-NH_3^+$ /graphitic N than P₉₅-CDs. The overall trend indicates that for $0.25 \leq x_p \leq 1.00$, there is an increase in $-NH_3^+$ /graphitic N and a decrease in C-NH-C/pyridinic N as x_p increased.

Finally, the deconvolution of the O_{1s} spectra shows that P₅₀-CDs have 70% more ($p < 0.01$) COOH oxygen than P₂₅-CDs. P₂₅-CDs and P₇₅-CDs have 58% more ($p < 0.01$) and 52% more ($p < 0.01$) C=O oxygen than P₅₀-CDs, respectively. P₁₀₀-CDs have 49% more ($p < 0.05$) COOH oxygen and 35% less ($p < 0.05$) C-OH oxygen than P₉₅-CDs, respectively.

FTIR Analysis

The FTIR spectra of P₂₅-CDs, P₅₀-CDs, and P₇₅-CDs have many common features such as a peak at 3190 and 2920 cm⁻¹ representing O-H and C-H stretching, respectively, suggesting the presence of alcohols, carboxylic acids, and alkanes. N-H stretching is also found in the 3400 – 3100 cm⁻¹ region. Further evidence of carboxylic acids and aliphatic ketones appears at the 1706 cm⁻¹ peak representing C=O stretching. The peak at 1637 cm⁻¹ could be due to a mix of C=C and C=N stretching and N-H bending suggesting the presence of conjugated or cyclic alkenes, and amines. A peak at 1395 cm⁻¹ from O-H bending indicates the presence of alcohols. Similarly, C-O stretching appears at 1195 cm⁻¹ suggesting the presence of tertiary alcohols or esters. Amines are shown by C-N stretching at 1080 cm⁻¹ and may also include alkoxy C-O. Alkenes are shown by C=C bending at 700 cm⁻¹.

A comparison of the FTIR spectra of P₉₅-CDs and P₁₀₀-CDs (Figure 3.2b) shows four regions of interest. Region 1 shows a broad peak at 3710 – 2710 cm⁻¹ representing O-H stretching from alcohols and carboxylic acids. This region is also host to various types of amines by possible N-H stretching from 3450 – 3250 cm⁻¹. A small peak at 2920 cm⁻¹ indicates the presence of C-H stretching from alkanes. Region 2 shows a set of peaks in the 1800 – 1520 cm⁻¹ region. The peak at 1710 cm⁻¹ results from C=O stretching indicating the presence of aliphatic ketones or carboxylic acids, while the peak at 1630 cm⁻¹ arises from C=C stretching and N-H bending suggesting the presence of conjugated and cyclic alkenes and amines, respectively. Region 3 shows a peak in the 1520 – 1260 cm⁻¹ region for P₉₅-CDs with prominence at 1385 cm⁻¹ originating from C-H bending suggesting the presence of aldehydes and alkanes. P₉₅-CDs and P₁₀₀-CDs both show a prominent peak in Region 4, *i.e.* 1260 – 890 cm⁻¹, with prominence at 1084 cm⁻¹ originating from C-N and C-O stretching indicating the presence of amines and alkoxy groups.

Size Analysis

Different substrates are used between the two methods, with a carbon grid used for TEM and silicon for AFM. These different substrates may cause differences in the way the CDs deposit, potentially resulting in varying degrees of aggregation. Another consequence of the different substrates used is background noise. While the silicon substrate is very smooth, the carbon substrate used for TEM, while generally pristine, is not as smooth as silicon and has approximately the same thickness as the CDs, which results in more background noise. For this reason, particles less than 1.5 nm in diameter are not included when calculating the mean diameter of the CDs from TEM images. Overall, the TEM and AFM size analysis agree for P₉₅-CDs, but not for P₁₀₀-CDs, suggesting that P₁₀₀-CDs may be more susceptible to aggregation on silicon.

Preamble to Chapter 4

In Chapter 3, we showed how CDs can be synthesized from compounds that occur abundantly in nature. While there is still much room for improvement regarding the green synthesis of CDs as discussed in Chapter 2, our work resulted in a sustainably synthesized CD with a high QY while simultaneously allowing us to determine which chemical features affect the fluorescence capabilities of CDs. In addition, we also determined a stoichiometric reaction ratio of citric acid to phenylalanine and showed the CD's application as an Fe^{3+} sensor. While using greener CD synthesis methods is important, this is only part of the journey towards advancing the overall sustainability of CDs. In Chapter 4, we evaluate the health effects that these CDs can have in the model organism *Drosophila melanogaster*, the common fruit fly. Moreover, we compare these health effects in parallel with exposure to CdTeQDs, which have become popular due to the ease with which their size and peak fluorescence wavelengths can be tuned. Cadmium is known to be toxic and as a result CdTeQDs have limited use outside of labs or other controlled environments, making CDs an attractive alternative. We use the same precursors as in Chapter 3, but now in a microwave synthesis to produce nitrogen-doped CDs. The microwave synthesis allows us to also show that the same precursors can be used in a more energy efficient and rapid synthesis, resulting in the production of a greater quantity of CDs in less time. In addition, we use a previously reported method to synthesize nitrogen/sulfur-codoped CDs. Therefore, the direct comparison of two chemically diverse CDs with CdTeQDs in measuring their developmental toxicity and ability to impact the reproductive performance, climbing ability, mass, larvae crawling, and locomotor activity of flies will provide more insight into the relative toxicity of these three particles without having to compare data from different publications which often use different organisms, routes of exposure, and concentrations.

Chapter 4: A comparison of carbon dot and CdTe quantum dot toxicity in *Drosophila melanogaster*

Abstract

Carbon dots (CDs) are carbon nanoparticles typically less than 10 nm in size, which feature many similar properties to quantum dots (QDs). CdTeQDs are among some of the most commonly studied QDs due to the high degree of precision with which their size can be controlled during synthesis allowing for the fine tuning of their band gap. However, cadmium is also known to be highly toxic, and therefore the use of cadmium in consumer goods is typically limited or outright banned in many jurisdictions. While many studies have examined the toxicity of CDs and CdTeQDs, few have compared both nanoparticles directly to each other under the same conditions. Herein, we provide a direct comparison of the toxicity of nitrogen-doped CDs (NCDs), nitrogen, sulfur co-doped CDs (SCDs), and CdTeQDs in the model organism *Drosophila melanogaster* (fruit fly). We found no impact on the development of larvae into adult flies from NCDs or SCDs in the 10 – 100 mg/kg food range measured, whereas an EC₅₀ of 46 mg/kg CdTeQD in food was observed. Moreover, a strong positive correlation was found between CdTeQD concentration in food and the mean pupation and eclosion time indicating severe developmental delays as CdTeQD concentration increased. Further sublethal experiments conducted at 100 mg/kg NCD, 100 mg/kg SCD, and 5 mg/kg CdTeQD revealed no significant difference between any of the treatments when evaluating reproductive performance, larval crawling, and fly climbing ability. This work demonstrates that both NCDs and SCDs are considerably less toxic than CdTeQDs in the 10 – 100 mg/kg food range.

4.1 Introduction

Quantum dots (QDs) are semiconductor nanoparticles that exhibit unique properties when compared to their bulk counterparts. Notably, QDs exhibit the quantum confinement effect, a phenomenon that links a QD's bandgap and fluorescence spectra (within the UV, visible, and near-infrared range) to its size.¹ This property, along with their reduced photobleaching compared to organic dyes,¹ has enabled the use of QDs in a variety of applications such as: bioimaging,² solar cells,³ light-emitting diodes,⁴ and chemical sensing⁵ to name a few.

Initial QDs included CdS, CdSe, and CdTe nanocrystallites that were synthesized through the injection of organometals into a high-temperature solvent.⁶ However, cadmium is an element with known toxicity, and this has translated into cadmium-derived QD toxicity as well. For instance, Liu *et al.* found that CdSeQDs can accumulate in the liver of mice, inducing morphological changes to their hepatic lobules and increased oxidative stress.⁷ Of particular concern is the fact that these QDs were found to be more toxic than cadmium ions, suggesting that QD toxicity is not caused by cadmium alone. Even after coating CdSe with a less toxic compound such as ZnS, the resulting CdSe/ZnS-QDs can still nick DNA due to free radical generation.⁸ Similarly, CdTeQDs have also shown similar toxic effects in mouse liver and AML12 cells causing increased oxidative stress and apoptosis.⁹ CdTeQDs have also shown toxicity in zebrafish,¹⁰ *Hydra vulgaris*,¹¹ and *Bombyx mori*.¹²

Carbon dots (CDs), a type of carbon nanoparticle with quantum dot-like properties, have emerged as a potentially safer alternative to metallic QDs. They are also being increasingly synthesized from renewable raw materials and compounds, further increasing the sustainability of CD use over QDs.¹³ While the outlook on CDs is promising, much work remains before their performance can be comparable to that of QDs, especially in optoelectronic fields, which has led

to the bulk of CD studies exploring applications in bioimaging and chemical sensing whereby their less toxic nature can give them an advantage over cadmium-derived QDs.¹³

Drosophila melanogaster, more commonly known as the fruit fly, has proven to be an interesting model organism for the study of nanoparticle toxicity.¹⁴ For instance, it has been found that 77 % of human disease genes have a highly similar related gene in flies.¹⁵ Moreover, a single mating pair can produce hundreds of offspring in under two weeks whereas mammalian models produce considerably fewer offspring on the order of months.¹⁶ Flies also have several structures that play a similar role to the mammalian heart, lung, kidney, gut, and reproductive tract.¹⁶ In addition, the effect of several central nervous system drugs on flies has been shown to be similar to their effect on mammals.¹⁶ Common routes by which nanoparticles may result in toxicity include ingestion, inhalation, and surface contact, leading to oxidative stress, which can in turn impact the lifespan and fecundity of the flies and result in genotoxicity and metabolic defects.¹⁴ Specifically, CdSeQDs are known to be toxic to flies by penetrating the intestine of larvae and eventually interacting with hemocytes, causing genotoxicity and elevated reactive oxygen species production.¹⁷ The release of Cd²⁺ from the QDs is thought to play a major role in the observed toxicity.¹⁷

Few studies directly compared CD toxicity with that of Cd-derived QDs. For instance, the toxicity of CDs and CdTeQDs has previously been evaluated in the microalgae *Chlorella pyrenoidosa*.¹⁸ Herein, we evaluate and compare the toxicity of CDs and CdTeQDs in a model animal organism *Drosophila melanogaster*. Moreover, we assessed the toxicity of two types of CDs, nitrogen-doped CDs (NCDs) and sulfur, nitrogen co-doped CDs (SCDs), to determine if their toxicity profile would differ as a result of their unique chemical functional groups.

4.2 Experimental

4.2.1 Synthesis of NCDs

Synthesis of NCDs was done according to previously reported methods, with some modification.¹⁹ Briefly, 7.2 g of L-phenylalanine (Sigma-Aldrich, P2126) and 2.1 g of citric acid (Sigma-Aldrich, 251275) were added to 20 mL of MilliQ water in a glass microwave reaction vial. The reaction mixture was placed into the microwave reactor and initially heated at 100 °C for 5 min to completely dissolve the reagents in water. Afterwards, the reaction mixture was allowed to heat to a temperature of 200 °C for 12 min. The resulting suspension was left to cool naturally to room temperature. The purification process is described in Section 4.2.3.

4.2.2 Synthesis of SCDs

Synthesis of SCDs was done according to previously reported methods, with some modification.²⁰ Briefly, 0.689 g of L-glutathione (Sigma-Aldrich, G4251) was mixed into 20 mL of formamide (Sigma-Aldrich, F7503). The mixture was sonicated for 15 min until it became clear. The reaction medium was then poured into a glass microwave reactor vial and heated to 180 °C for 5 min. The resulting suspension was left to cool naturally to room temperature. The purification process is described in Section 4.2.3.

4.2.3 Purification of carbon and quantum dots

Purification of CDs and QDs was done according to previous methods with some modifications.²⁰ The CdTeQDs (PlasmaChem, PL-QDN-610) were suspended in water (concentration: 1.4 mg/mL). The CD suspension (post-synthesis mixture) or QD suspension was filtered using a 0.2 µm nylon filter (Millipore, SLGN033) to remove any large particles. The CD

or QD dispersions were then dialyzed using a cellulose ester dialysis membrane with a molecular weight cut-off of 3.5 – 5.0 kDa (Repligen, 132725) to remove unreacted materials and intermediates from the CD suspensions, and to ensure similar sample preparation in the QD suspensions. The samples were dialyzed in 1 L of Type 1 water over 5 days with the water changed twice a day. Following this, the nanoparticles were filtered using a 0.2 µm nylon filter to remove any aggregates. For the control treatment, water alone was processed in the same manner and was later added to the fly food, to ensure that all treatments were treated as similarly as possible. At this point, the CdTeQDs remained in suspension and were diluted as needed for further use.

The SCD suspensions were washed twice with ethanol and then twice with acetone to remove any remaining impurities (*i.e.*, until the supernatant was colourless). On the other hand, due to their enhanced dispersibility in ethanol, the NCD suspensions were washed four times with acetone. The first wash consisted of a 1:10 (suspension:solvent) volume ratio. The precipitate was collected by centrifugation at 10 000 g for 10 min and resuspended in fresh solvent for the next wash step. The resulting material was dried overnight in an oven at 70 °C and resuspended in water at the desired concentration.

4.2.4 Characterization of carbon dots and quantum dots

X-ray photoelectron spectroscopy (XPS) measurements were taken using a Thermo Fisher Scientific K-Alpha X-Ray Photoelectron Spectrometer System. Fourier-transform infrared (FTIR) spectroscopy was performed using a Nicolet iS5 FTIR spectrometer. Transmission electron microscopy (TEM) images were obtained using a DeLong LVEM5 benchtop electron microscope (from the McGill Institute for Advanced Materials). Quantum yields were measured using a

FLS920 fluorescence spectrometer (Edinburgh Instruments). Fluorescence spectroscopy and UV-vis measurements were performed using a Horiba Fluorolog-QM.

4.2.5 *Drosophila melanogaster* husbandry

Fruit flies were reared according to methods described previously, with some modification.²¹ *Drosophila melanogaster* (Oregon-R strain) were reared in a food mixture consisting of: 84.6 wt% reverse osmosis (RO) water (Type II, >1 M Ω), 14.9 wt% Nutri-Fly Bloomington Formulation powder (Diamed, GEN66-112), and 0.5 wt% sodium propionate (Genesee Scientific, 20-271) in a *Drosophila* culture bottle (Carolina, 173135). These culture bottles were kept in a Versatile Environmental Test Chamber (Panasonic, MLR-352H-PA) operating under a day/night cycle at 60 % relative humidity at 25 °C. Days consisted of illumination at ~1500 lx for 12 h. Nights consisted of complete darkness for 12 h.

4.2.6 Larvae collection

When a larger quantity of flies was needed, embryo collection cages (Diamed, GEN59-101) were set up according to methods described previously, with some modification.²² Briefly, one packet of FlyStuff grape agar premix (Diamed, GEN47-102) was mixed into 500 mL of RO water and autoclaved. The contents were then poured into multiple 100-mm Petri dishes (Fisher Scientific, FB0875713). Next, 15 g of inactive dry yeast nutritional flake (Diamed, GEN62-106) was mixed with 15 mL of RO water to create a yeast paste which was then spread onto the center of the grape agar plate. Flies were transferred to the embryo collection cage, which was placed on top of the grape agar plate where the flies then laid eggs. This moment is referred to as day 0. The grape agar plate containing eggs was removed from the cage after 4 hours. Approximately 24 h

later, the eggs that had transformed into larvae were then used for subsequent experiments as described in the following sections unless stated otherwise.

4.2.7 Carbon dioxide anesthesia

When a specific selection of flies was required (*e.g.*, obtaining an equal amount of female and male flies), flies were anesthetized with CO₂ on a Flystuff Flypad (Genesee Scientific, 59-114) and sorted as needed. Total anesthesia time was restricted to less than 10 min to minimize undesirable physiological effects on the flies.²³

4.2.8 Developmental toxicity

Developmental toxicity was measured according to previous methods with some modifications.²² Briefly, NCDs, SCDs, or CdTeQDs were mixed into fly food such that the final concentration in food was 0, 10, 40, 70, or 100 mg/kg. Thereafter, 10 mL of the treated or control (CTRL) fly food was added into a 50-mL glass test tube and capped with a cotton plug. Approximately twenty larvae were then transferred from grape agar plates into the test tube. The number of pupae and adult flies were counted every 2 days until day 14. The CdTeQD treatments were counted until day 16 to account for the severe developmental delays caused by the quantum dots. We note that during the counting process, if any flies were present in the test tube, they were removed from the test tube for counting and not returned. This allowed for accurate counting of the flies over time by ensuring that any flies counted must have emerged during the previous 48 h. Each treatment or control was replicated with 1 – 3 test tubes simultaneously. The entire experiment was performed in three experimental blocks for a final count of N = 6.

4.2.9 Sublethal toxicity assays

The results from the developmental toxicity study allowed us to determine a sublethal concentration of NCDs, SCDs, and CdTeQDs in food at which to measure other endpoints. The use of a sublethal dose minimizes survivorship bias, allowing for a more reliable measure of the sublethal toxic effects of NCDs, SCDs, and CdTeQDs. Briefly, NCDs, SCDs, or CdTeQDs were mixed into fly food such that the final concentration was either 100 mg/kg NCD, 100 mg/kg SCD, or 5 mg/kg CdTeQD. A control was also made. Thereafter, 10 mL of the treated or control fly food was added into a 50-mL glass test tube and capped with a cotton plug. Each assay began with approximately 20 first instar larvae being transferred from a grape agar plate into the test tube. The test tube was closed with a cotton plug.

4.2.9.1 Reproductive performance assay

The reproductive performance of flies was measured according to previous methods with some modification.²⁴ On day 9, any adult flies present in the treated or control test tubes were removed. Approximately 4 h later, newly emerged flies were placed under CO₂ anesthesia. One female and one male fly were transferred into a new test tube with control fly food (*i.e.*, that does not contain NCDs, SCDs, or CdTeQDs). The mating pair was transferred to a new test tube every two days for 10 days. The number of pupae and adult flies that emerged from each test tube that the mating pair laid eggs in was recorded 14 days after the parents first entered the test tube. Each treatment or control was replicated with 3 – 6 test tubes simultaneously. The entire experiment was performed in two experimental blocks for a final replicate count of $8 \leq N \leq 12$.

4.2.9.2 Larval crawling assay

The peristalsis of larvae was measured as done previously with some modifications.²² On day 4, three larvae were removed from the treated or control test tube and, one at a time, placed on a 100-mm Petri dish containing grape agar. The larva was allowed 30 s to adjust to their new environment and the Petri dish was then video recorded under an Olympus SZX16 stereo microscope for 60 s. The larva was then removed from the dish and the next larva was placed on the grape agar plate and the cycle started again. Each treatment group had its own dish, to avoid cross-contamination from larvae exposed to different nanoparticles. The average number of peristaltic contractions per min of the three larvae from a single test tube was taken and represents a single data point. Each treatment or control was replicated with three test tubes in parallel. The entire experiment was performed in two experimental blocks for a final replicate count of $N = 6$.

4.2.9.3 Climbing and fly mass assay

A climbing assay was performed according to methods described previously, with some modification.²⁵ On day 11, the flies were transferred from the treated or control test tube to a 100-mL graduated cylinder marked at a height of 10 cm that was then capped with a cotton plug. The cylinder was tapped to move the flies to the bottom. The flies were then left to ascend. After 10 s, the number of flies that crossed the 10 cm mark was video recorded and divided by the total number of flies in the graduated cylinder. This process was performed five times. The average of these five trials was taken and represents a single replicate of data.

The flies from the climbing assay were then placed under CO₂ anesthesia and separated into male and female groups. The collective mass of each sex of flies was measured and divided by their respective number of flies and represents a single replicate of data.

Each treatment or control was replicated with 2 – 3 test tubes simultaneously. The entire experiment was performed in two experimental blocks for a final replicate count of $5 \leq N \leq 6$.

4.2.9.4 Locomotor activity monitoring

Locomotor activity monitoring was done according to previously reported methods with some modifications.²⁶ On day 11, one male fly (from a treated or control test tube) was placed in a glass tube (outside diameter \times length: 5 mm \times 65 mm) with control fly food (*i.e.*, that does not contain NCDs, SCDs, or CdTeQDs) at one end and a cotton plug at the other end. A *Drosophila* Activity Monitor (DAM2, TriKinetics) was used with 32 tubes fitted in it (8 control, 8 NCD, 8 SCD, and 8 CdTeQD). The activity monitor counted the number of times per minute that the fly would interrupt a beam of infrared light at the middle of the tube. The flies were given 24 – 48 h to adjust to their new environment and then flies went through 3 days of a light-dark cycle consisting of 12 h light, 12 h dark. The experiment started at the beginning of the first 12 h light phase. If any tube showed zero counts in the final 24 h, then the fly was presumed dead, and removed from the analysis. Two DAM2 units ran in parallel (*i.e.*, 16 tubes per treatment or control simultaneously). The entire experiment was performed in two experimental blocks for a final replicate count of $31 \leq N \leq 32$ after the removal of dead flies.

4.2.10 Lightsheet imaging

Lightsheet imaging was performed on female flies taken at day 11 to determine if there was any uptake of the NCDs, SCDs, or CdTeQDs. Flies were stored in refrigerated (4 °C) 10 % neutral-buffered formalin for 24-48 h.

Flies were mounted in a 1-mL syringe containing ScaleS4 with 2.0 % low melting point agarose as developed by Hama et al.²⁷ The index of refraction of the mounting media was adjusted with glycerol or water until it reached a value of 1.44. The chamber of the Zeiss lightsheet Z.1 microscope was filled with ScaleS4 to ensure a consistent index of refraction with the sample. A 5× 0.1 NA objective was used for illumination and a 5× 0.16 NA objective was used for detection.

4.2.11 Statistical analysis

Data was first tested for normality of the residuals using the Shapiro-Wilk test. The data was then tested for equal variance among groups using Bartlett's test. If both these tests validated the assumption of normality and equal variance, then statistical significance was measured using an n -way analysis of variance (n -way ANOVA). If the ANOVA showed a significant difference among treatments, then a Tukey-Kramer test was performed for sublethal toxicity assays. However, if the data did not pass the test of normality or equal variance, then n Kruskal-Wallis H tests were performed, followed by a Mann-Whitney U test with Bonferroni correction where significant differences were observed for sublethal toxicity assays. For developmental toxicity when significant differences were observed between concentrations for a given treatment and the number of pupae or flies was monotonically decreasing with concentration, then a Hill equation (Equation 4.1) was fit to the data to obtain a half maximal effective concentration (EC_{50}) value. Similarly, when significant differences in emergence time were observed between concentrations for a given treatment, a linear regression was performed. Throughout all statistical tests, $p < 0.05$ was considered as significant. Data analysis and visualization was performed in Python 3.9.12 using numpy 1.21.5,²⁸ pandas 1.4.2,²⁹ scipy 1.7.3,³⁰ statsmodels 0.13.2,³¹ and matplotlib 3.5.1.³²

The Hill equation takes the form of:

$$\frac{x - \mu_{CTRL}}{\mu_{MAX} - \mu_{CTRL}} = \frac{1}{1 + \left(\frac{EC_{50}}{[NP]}\right)^n} \quad (4.1)$$

Where x is the number of pupae or flies after 14 days; μ_{CTRL} is the mean number of pupae or flies after 14 days in the control; μ_{MAX} is the maximum response (*i.e.*, 0 pupae or flies), EC_{50} is the half maximal effective concentration, $[NP]$ is the concentration of NCDs, SCDs, or CdTeQDs in food; and n is the Hill coefficient.

4.3 Results and discussion

4.3.1 Characterization of carbon and quantum dots

The size of NCDs and SCDs was measured using TEM. The NCDs had a mean size of 7.4 nm (Figure S4.1a) and the SCDs had a mean size of 7.0 nm (Figure S4.1b). The CdTeQDs were ~3.5 nm according to the manufacturer's specifications.

The FTIR spectra for the NCDs, SCDs, and CdTeQDs can be found in Figure S4.2. From the NCDs, the peak at 1703 cm^{-1} is indicative of C=O stretching stemming from the presence of carboxylic acids and aliphatic ketones, while the presence of C-N is confirmed with the peak at 1389 cm^{-1} . The SCDs showed a broad peak centered at 3330 cm^{-1} stemming from the symmetric and asymmetric stretching of N-H and -OH groups, while stretching of C=O (from amide), C-OH, and C-N groups were observed at 1665, 1596, and 1384 cm^{-1} , respectively. The CdTeQDs had a broad peak centered around 3400 cm^{-1} originating from O-H stretching. The peak at 1543 cm^{-1} corresponds to C=O stretching, whereas the peak at 1405 cm^{-1} corresponds to the C-O-H in-plane

bending. The XPS spectra of the NCDs confirms that nitrogen-doping occurred (C: 52 %, O: 38 %, N: 10 %) (Figure S4.3), and the spectra for SCDs indicates that both nitrogen and sulfur doping occurred (C: 51%, O: 27 %, N: 19 %, S: 2.9%) (Figure S4.4).

The quantum yield of the CdTeQDs, NCDs, and SCDs were 21.9 %, 17.2 %, and 7.3 %, respectively. The fluorescence spectra of the CdTeQDs, NCDs, and SCDs is shown in Figure S4.5 with peaks at 615 nm, 482 nm, and 681 nm, respectively. For both quantum yield and fluorescence measurements, an excitation wavelength of 561 nm was used for CdTeQDs and 405 nm for NCDs and SCDs to match their respective excitation wavelengths used for lightsheet imaging. The UV-Vis spectra of NCDs, SCDs, and CdTeQDs is shown in Figure S4.6. NCDs had a local peak at 340 nm and SCDs showed local peaks at 418 nm, 629 nm, and 670 nm. While the UV-Vis spectrum of CdTeQDs is mostly monotonically decreasing, it briefly inverts at 558 – 560 nm before continuing to decrease. This range is close to the lightsheet imaging excitation wavelength used (*i.e.*, 561 nm).

4.3.2 Developmental toxicity

The toxicity of the SCDs in HeLa cells was previously studied and was shown to have a half maximal inhibitory concentration (IC₅₀) of 148 mg/L.²⁰ We note, however, that mechanisms involved in *in vitro* toxicity may differ considerably from *in vivo*, and the original work demonstrated that 100 mg/L was a sufficient and safe concentration for bioimaging purposes.²⁰ Moreover, our preliminary screening of CdTeQDs indicated that the 10 – 100 mg/kg CdTeQD concentration range would be adequate for the development of a dose-response curve. The results of this preliminary screening are not discussed further in this study since they were performed under different conditions with a different CdTeQD. As a result, we wanted to examine a CD

concentration range that may be used in practice, and that also matches the relevant range over which CdTeQD toxicity manifests. Therefore, the developmental toxicity of the NCDs, SCDs, and CdTeQDs on 1st instar larvae's development into pupae and adult flies was measured over the concentration range of 10 – 100 mg/kg food. No significant difference was observed in the total number of pupae and flies emerging from the larvae exposed to NCDs or SCDs across concentrations ($p > 0.05$) (Figure 4.1a, b). We note that significant differences were observed between experimental blocks in the NCD treatments (pupae: $p = 1.9 \times 10^{-2}$; flies: $p = 2.3 \times 10^{-2}$). While several studies have examined the toxicity of CDs, few have compared them directly to quantum dots that may be used in similar applications. We found that there was a significant difference in the total number of pupae ($p = 2.3 \times 10^{-4}$) and flies ($p = 7.6 \times 10^{-5}$) emerging from the larvae exposed to CdTeQDs (Figure 4.1a, b) at different concentrations. No significant differences were observed between experimental blocks for both pupae and flies. Fitting data to the Hill equation revealed that the EC_{50} of the CdTeQDs on larval development into pupae was 74 ± 6.0 mg/kg food, and into flies was 46 ± 4.7 mg/kg food (mean \pm standard error). These curve fits are shown in Figure S4.7. This discrepancy between the EC_{50} values for the larval development into pupae and flies becomes clear when examining the eclosion fraction, *i.e.*, the fraction of pupae that successfully eclose into flies. No significant dose-response was observed in the eclosion fraction of pupae exposed to NCDs or SCDs (Figure S4.8). Conversely, significant differences in the eclosion fraction of pupae were found between CdTeQD treatment concentrations ($p = 2.5 \times 10^{-4}$) (Figure S4.8). However, since the data did not fit the shape of the Hill equation, no curve fitting was performed on the eclosion fraction. Moreover, we note that there were no significant differences between experimental blocks for any of the treatments when measuring the eclosion fraction.

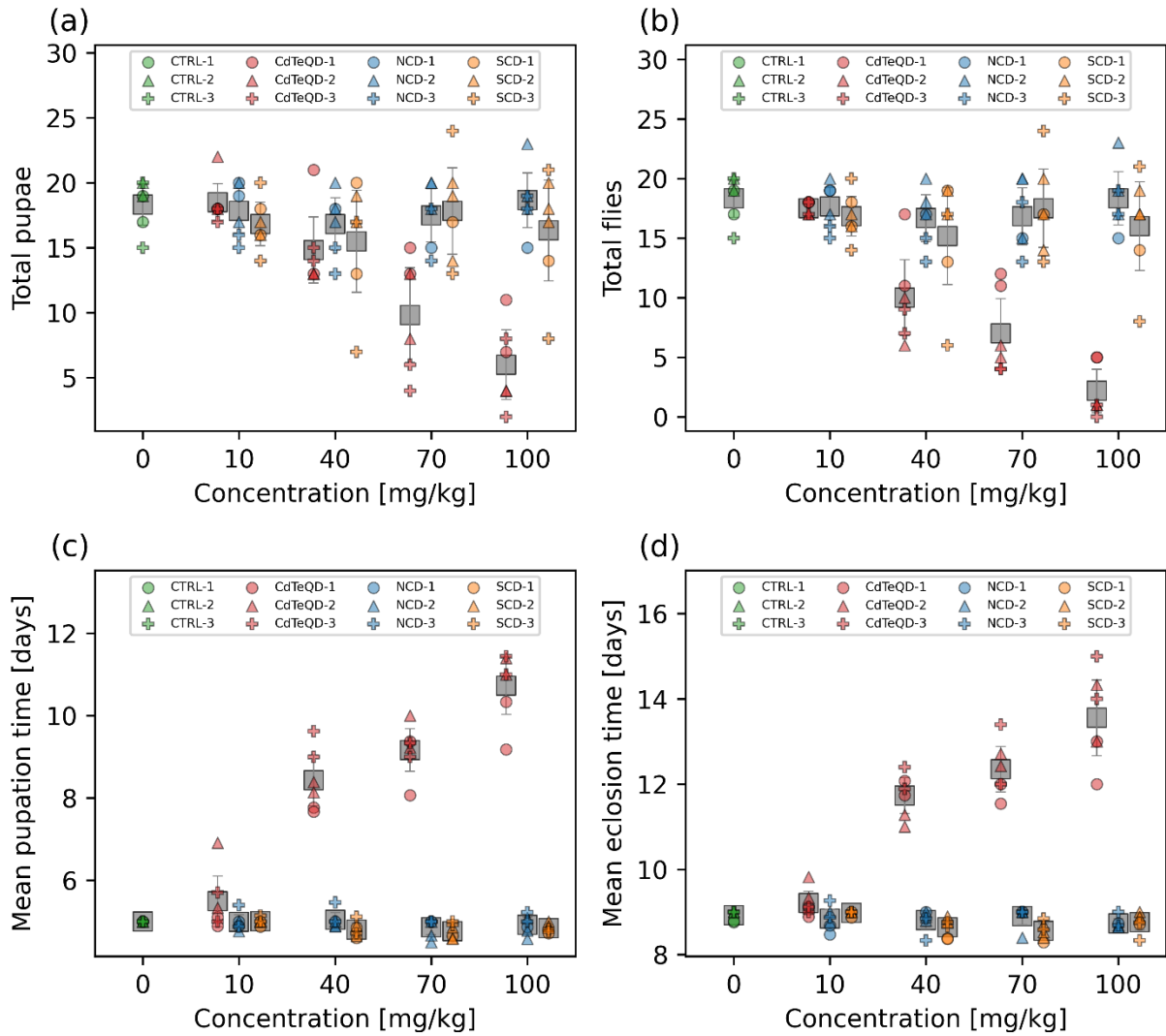


Figure 4.1. Number of (a) pupae and (b) flies that emerged from approximately twenty first instar larvae raised on 0, 10, 40, 70, or 100 mg/kg NCD, SCD, or CdTeQD treated food by day 14. The mean (c) pupation and (d) eclosion time of the pupae and flies in (a) and (b), respectively. Grey squares represent the mean of data points in that column and error bars represent $2 \times$ the standard error of the mean. Legend labels have the format X-Y where X is the treatment and Y is the experimental block ID.

Another important metric in evaluating developmental toxicity is the time it takes for larvae to develop into pupae and adult flies. Delays in development time can be lost when screening just for mortality. No dose-response was observed in the mean pupation or eclosion time of larvae exposed to NCDs (Figure 4.1c, d). We remark that significant differences were observed between experimental blocks ($p=0.037$) in the mean pupation time of NCD-exposed larvae. While a significant difference on the basis of concentration was observed from the SCDs on the mean pupation ($p=0.012$) and eclosion ($p=2.1 \times 10^{-3}$) time (Figure 4.1c, d), a linear regression revealed that both showed a weak negative correlation (pupation: $r=-0.49$, eclosion: $r=-0.46$) (Figure S4.9). The CdTeQDs also showed a significant difference in the mean pupation ($p=4.6 \times 10^{-5}$) and eclosion time ($p=5.5 \times 10^{-5}$) (Figure 4.1c, d) across different concentrations. In this case, a linear regression revealed a strong positive correlation for both mean pupation ($r=0.94$) and eclosion ($r=0.93$) time (Figure S4.9). The slopes of the regressions indicated that increasing the CdTeQD concentration in the food by 1 mg/kg would delay pupation by 83 min and eclosion by 68 min at concentrations below 100 mg/kg. No significant differences were observed between experimental blocks in the mean pupation or eclosion time of larvae exposed to SCD or CdTeQDs.

Interestingly, Chousidis *et al.* also investigated the toxicity of undoped, N-doped, and N,S co-doped CDs in zebrafish, finding that they had an LD₅₀ of 584 mg/L, 400 mg/L, and 150 mg/L, respectively.³³ These results are all well above the highest concentration we examined (100 mg/kg), however, Chousidis *et al.* did report an LD₂₅ of 63 mg/L for the N,S co-doped CD, whereas our SCDs did not show any developmental toxicity near this concentration.³³ This further emphasizes the importance of conducting toxicity studies in a multitude of environments and organisms, especially when comparing results from aquatic and terrestrial organisms. While both organisms must consume nanoparticles through their diet, the aquatic organism must also be

submerged in it for the entirety of the exposure, allowing for the nanoparticle to enter the organism via more routes of exposure. Moreover, Chousidis *et al.* synthesized their N,S co-doped CDs from citric acid and thiourea,³³ whereas we synthesized ours from glutathione and formamide, therefore it is likely that there are chemical differences between the two CDs. Liu *et al.* exposed zebrafish embryos to CDs over the 1.5 – 96 h postfertilization period, and found no significant differences in mortality in the 50 – 200 mg/L range, however, a dose-response was observed at higher concentrations resulting in an LC₅₀ of 257 mg/L.³⁴ Yang *et al.* exposed mice to CDs via a single inhalation and found that a concentration of 5 mg/kg resulted in the survival of 80 % of mice after 15 days, whereas 100 % survival was measured in the control.³⁵ The single dose toxicity of CDs on mice via intravenous exposure was examined by Zheng *et al.*, finding that the LD₅₀ in female mice was 392 mg/kg and for male mice was 358 mg/kg.³⁶ Ambrosone *et al.* exposed *Hydra vulgaris* to thioglycolic acid coated CdTeQDs for 72 h monitored daily.¹¹ They found that after 24 hr of exposure the LC₅₀ was 1.4 mg/L Cd equivalent, and that this dropped to 0.72 mg/L Cd equivalent after 72 h.¹¹ Another study found that exposing *Biomphalaria glabrata* embryos to 5 nM (~0.25 mg/L) CdTeQDs for 24 h resulted in 100 % of embryos being deemed unviable.³⁷ Adult *Biomphalaria glabrata* had a higher tolerance, with 100 % mortality observed 48 h after a 24-h exposure to 400 nM (~ 20 mg/L) CdTeQDs.³⁷ Our results, show similar trends to those found in literature, which indicate that CdTeQDs exhibit considerably more toxicity than CDs.

4.3.3 Reproductive performance

Our developmental toxicity assay showed clear toxicity stemming from the exposure of *Drosophila melanogaster* to CdTeQDs with an EC₅₀ of 46 mg/kg food. Conversely, no toxicity was observed from the NCDs or SCDs in the 10 – 100 mg/kg range evaluated. However, there are

many forms in which toxicity can manifest in an organism that do not necessarily lead to death. To ensure a comprehensive evaluation of carbon dot toxicity, we measured the impact of these particles on the reproductive performance of flies. Since no toxicity was observed in the NCDs and SCDs, further experiments were conducted at 100 mg/kg since this concentration is known not to induce toxicity. However, this same concentration could not be used when evaluating CdTeQD toxicity, since we have already shown that it exhibits severe lethality and developmental delays (Figure 4.1). Instead, we conducted further sublethal assessment of CdTeQDs at 5 mg/kg, a concentration approximately equal to the EC₁ or the concentration that would result in the failure of 1 % of larvae to successfully develop into adult flies. No significant differences between treatments or experimental blocks were observed in the number of pupae or flies that emerged from the eggs laid over the span of ten days (Figure 4.2). The time-series data (Figure S4.10) showed that reproductive performance typically increased or remained approximately constant during the 2 – 10 day period. These results indicate a lack of reproductive toxicity from these particles at a sublethal concentration.

Han *et al.* examined the effect of CDs on the reproduction of *Bursaphelenchus xylophilus*, and found that a 6000 mg/L concentration reduced the number of eggs laid.³⁸ A study examining the effects of thioglycolic acid coated CdTeQDs on the reproduction of *Hydra vulgaris* found that exposure to CdTeQD concentrations as low as 1 mg/L Cd for 14 days reduced their budding rate by 42 % relative to the control.¹¹ Another study also examined the toxicity of CdTeQDs on the reproductive performance of *Drosophila melanogaster* and found a dose-dependent decline in fecundity, fertility, and hatchability in the 1 – 100 μM (approximately 100 – 10 000 mg/L) range.³⁹ The toxicity of CdTeQDs in *Caenorhabditis elegans* was investigated by Qu *et al.*⁴⁰ They found no significant difference in the egg-laying rate at 5 – 25 mg/L relative to the control, but observed

a dose-dependent decrease at 50 – 100 mg/L.⁴⁰ Similarly, our results are mostly consistent with literature showing that toxicity can vary between organisms and nanoparticles.

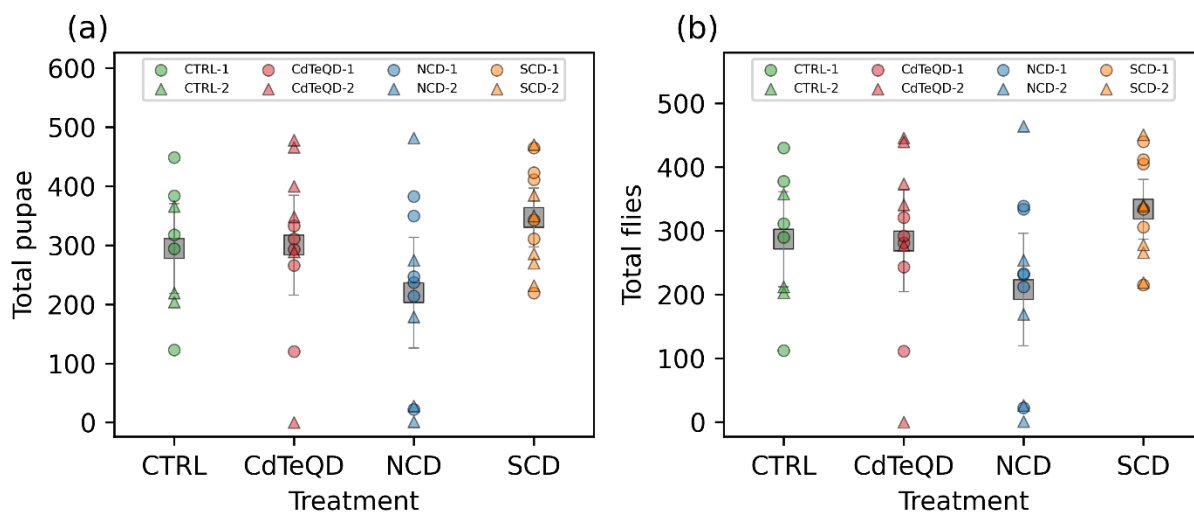


Figure 4.2. Number of (a) pupae and (b) flies that emerged after allowing one female and one male fly that were raised on CTRL (0 mg/kg), NCD (100 mg/kg), SCD (100 mg/kg), or CdTeQD (5 mg/kg) treated food to mate for 10 days. Grey squares represent the mean of data points in that column and error bars represent $2 \times$ the standard error of the mean. Legend labels have the format X-Y where X is the treatment and Y is the experimental block ID.

4.3.4 Fly mass assay

When given a fixed food source, the mass of a particular healthy organism is typically stable and predictable. The flies in each treatment were raised on identical food sources, with the only difference being the presence of NCDs (100 mg/kg), SCDs (100 mg/kg), or CdTeQDs (5 mg/kg). Considering that the highest of these concentrations (*i.e.*, 100 mg/kg) is equivalent to 0.01 wt% food, we can assume that food displacement is unlikely to be a contributing factor to any changes in mass observed. No significant differences between treatments were found in the mass

of female flies, however the difference between experimental blocks was significant ($p=0.024$) (Figure 4.3a). It is worth noting that a large contribution to this difference in blocks is due to one particularly high mass measurement observed in block 2 (Figure 4.3a). Significant differences between treatments ($p=0.012$) and experimental block ($p=0.037$) were observed in the mass of male flies (Figure 4.3b). Due to the significant differences observed between blocks, we only consider significant differences between treatments if they occur within the same block. A post hoc analysis revealed that in block 2, the male flies raised on 100 mg/kg SCD had a significantly greater mass ($p<0.05$) than those raised on 100 mg/kg NCD and the CTRL food. No significant differences were observed between treatments in block 1. The implication of these results, especially when considering the results in Figure S4.9 showing a significant, but weak, correlation pointing towards larvae raised on SCDs having a slightly faster development time than the other treatments, suggest that SCDs might elicit a minor biological response in *Drosophila melanogaster* at 100 mg/kg food.

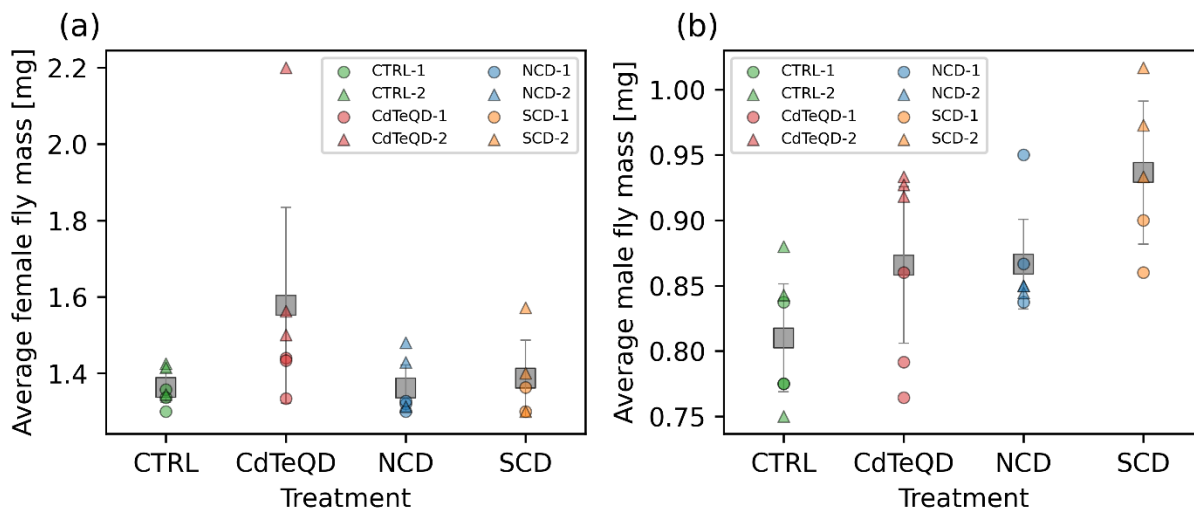


Figure 4.3. Average mass of (a) female and (b) male flies that were raised on CTRL (0 mg/kg), NCD (100 mg/kg), SCD (100 mg/kg), or CdTeQD (5 mg/kg) treated food. Grey squares represent the mean of data points in that column and error bars represent $2 \times$ the standard error of the mean. Legend labels have the format X-Y where X is the treatment and Y is the experimental block ID.

Zheng *et al.* exposed mice to a daily intravenous 100 mg/kg dose of CDs for 7 days and monitored their mass over 90 days finding no notable difference in the overall mouse mass throughout the period evaluated.³⁶ In a study by Du *et al.*, CdTeQDs functionalized with thioglycolic acid and mercapto-acetohydrazine reduced the growth rate of mice relative to the control over the 7 days following 10 mg/kg intravenous injection of the CdTeQDs.⁴¹ Interestingly, this reduction was no longer significantly different from the control when the CdTeQDs were further functionalized with polyethylene glycol.⁴¹ Another study also examined the toxicity of CdTeQDs in mice and found that there were no significant differences in mass between the control and the 4.12 – 16.5 mg/kg range measured.⁹ Similarly, our results coincide with these literature findings when considering the concentrations evaluated. While some significant differences were observed, they were not present in all experimental blocks.

4.3.5 Larvae crawling and fly climbing assays

To get a true grasp of sublethal toxicity we must look at multiple stages of development. In the reproductive performance assay, we measured the impact that parental exposure may have on their ability to produce offspring. We now focus on the activity of the larvae that were raised on CTRL (0 mg/kg), NCDs (100 mg/kg), SCDs (100 mg/kg), or CdTeQDs (5 mg/kg). No significant differences between treatments or experimental blocks were observed in the number of contractions per minute of the larvae (Figure 4.4a). Similarly, when evaluating the climbing ability of the flies, no significant differences between treatments or experimental blocks were observed in the number of flies able to climb 10 cm within 10 s (Figure 4.4b).

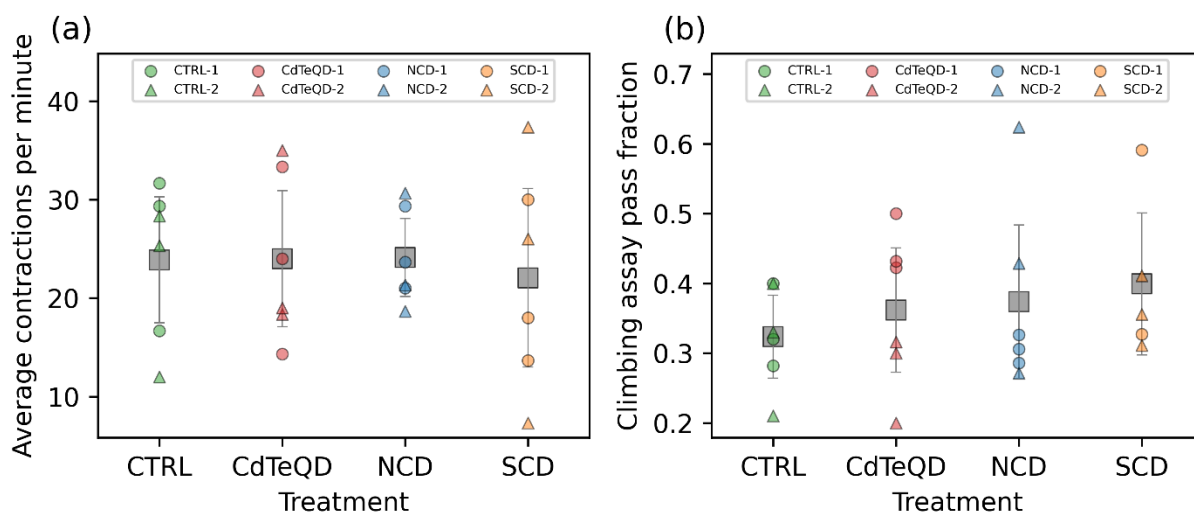


Figure 4.4. (a) Average number of larval contractions per minute and (b) fraction of flies able to climb 10 cm within 10 s. Larvae and flies were raised on CTRL (0 mg/kg), NCD (100 mg/kg), SCD (100 mg/kg), or CdTeQD (5 mg/kg) treated food. Grey squares represent the mean of data points in that column and error bars represent $2 \times$ the standard error of the mean. Legend labels have the format X-Y where X is the treatment and Y is the experimental block ID.

Liu *et al.* examined the effect of CDs on zebrafish larvae locomotion and found no significant difference in the distance travelled by larvae exposed to 50 – 150 mg/L CDs, but a dose-response was observed whereby the travel distance declined in the range 200 – 2000 mg/L.³⁴ Similarly, Han *et al.* showed a decline in the number of thrashes per minute of *Bursaphelenchus xylophilus* in the 4000 – 6000 mg/L CD range.³⁸ Paithankar *et al.* exposed *Drosophila melanogaster* to CdTeQDs in the concentration range of 0.2 – 100 μ M (approximately 20 – 10000 mg/L) and saw no significant difference in the climbing ability of flies when compared to the control.³⁹ Although the literature sometimes reports that CDs and CdTeQDs can negatively impact the locomotion or climbing ability of organisms, these effects were typically observed at concentrations higher than measured in our study.

4.3.6 Locomotor activity

The larvae crawling assay is useful for assessing the activity of *Drosophila melanogaster* during their development into adult flies. Once adults, the climbing assay is also a convenient tool for measuring the ability of flies to conduct a physically demanding task. One limitation to both these assays is the relatively short time span over which data is recorded, typically on the order of a few seconds or minutes. Using an activity monitor, we were able to monitor the movement of adult male flies in one-minute intervals over three days. Averaging the daily activity over 72 h removes any variance that may come from the time of day that the measurement was taken at. It also provides an overall measure of activity since it also includes the night cycle of the flies. Significant differences between treatments ($p=0.032$) and experimental blocks ($p=0.024$) in the number of activity counts per day (*i.e.*, infrared beam breaks per day) were observed (Figure 4.5). A post hoc analysis revealed that these significant differences stemmed from the CTRL activity in

block 1 being more than double the SCD and CdTeQD activities in block 2. However, since there were significant differences observed between blocks, a comparison of treated flies from block 2 with the CTRL in block 1, is not very meaningful even if the difference is significant. Moreover, Figure 4.5 clearly shows that three replicates from the CTRL in block 1 had unusually high activity which may have skewed the mean upward.

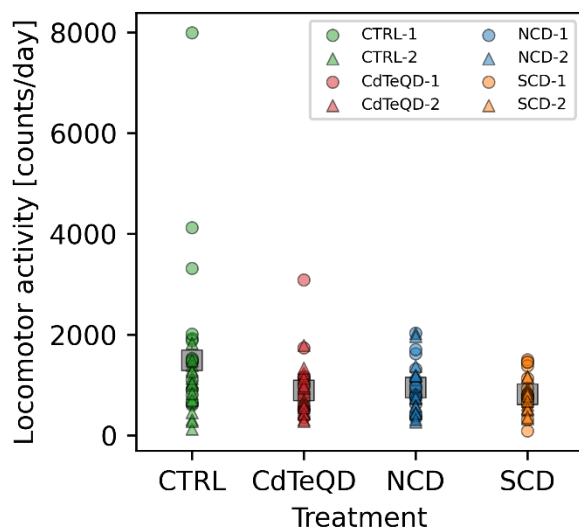


Figure 4.5. Locomotor activity measured as average number of infrared beam breaks per day of male flies raised on CTRL (0 mg/kg), NCD (100 mg/kg), SCD (100 mg/kg), or CdTeQD (5 mg/kg) treated food. Grey squares represent the mean of data points in that column and error bars represent $2 \times$ the standard error of the mean. The standard errors are relatively small due to the large sample size and may be difficult to see in the figure. Legend labels have the format X-Y where X is the treatment and Y is the experimental block ID.

4.3.7 Nanoparticle uptake analysis

Nanoparticle-exposed flies were imaged using lightsheet microscopy (Figure 4.6). Due to the difference in peak fluorescence wavelengths of the particles, different filters and excitation wavelengths were utilized. An excitation wavelength of 405 nm with a bandpass filter at 420 –

470 nm were used to illustrate the autofluorescence of the fruit fly. The fluorescence of the NCDs was not evident since its emission spectrum was similar to that of the fly's autofluorescence. On the other hand, SCDs were visualized in red by using a 640 nm long pass filter under 405 nm excitation. Signals stemming from the CdTeQDs were obtained using an excitation wavelength of 561 nm and a long pass filter at 640 nm. In the case of SCDs and CdTeQDs, it was apparent that the particles were found internally and on the surface of the organism.

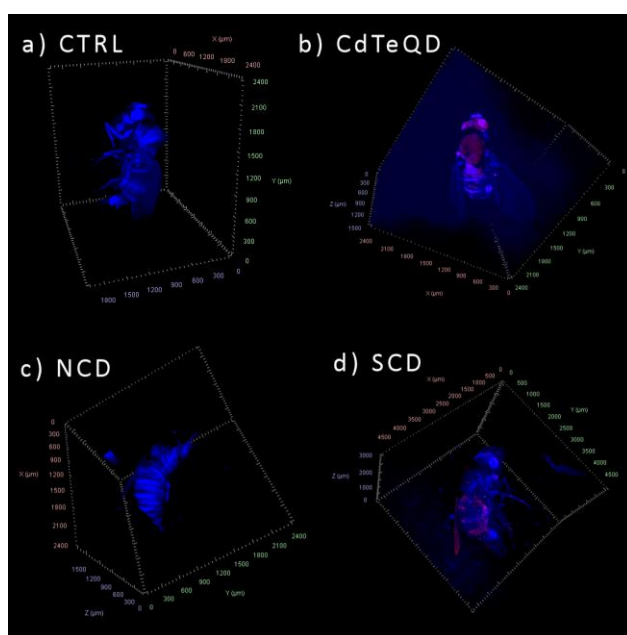


Figure 4.6. Lightsheet images of female flies from day 11 raised on a) CTRL (0 mg/kg), b) CdTeQD (5 mg/kg), c) NCD (100 mg/kg), or d) SCD (100 mg/kg) treated food. Red light shows fluorescence from SCD and CdTeQDs. Blue fluorescence is from the fly's autofluorescence. NCDs also emit blue light and are therefore not easily visible.

4.4 Conclusions

While there was no developmental toxicity from NCDs or SCDs observed, a dose-dependant toxicity was observed from the CdTeQDs with a larva-to-fly EC_{50} of 46 ± 4.7 mg/kg

food (mean \pm standard error). We also saw no correlation between NCDs concentration and emergence time but saw a weak negative correlation for SCDs and a strong positive correlation for CdTeQDs indicating that CdTeQDs can delay the development of larvae into pupae and flies. Using sublethal concentrations of 100 mg/kg for NCDs and SCDs and 5 mg/kg for CdTeQDs, further assays concluded that the SCD-exposed male flies had a significantly greater mass than those raised on CTRL and NCD food in experimental block 2, but not in block 1. Moreover, while significant differences were observed between treatments in the locomotor activity of flies, these differences occurred between blocks, and therefore were not indicative of a potential response. No significant difference between any of the treatments when evaluating reproductive performance, larval crawling, and fly climbing ability were observed.

This work shows that two chemically diverse carbon dots containing a variety of elements and functional groups were considerably less toxic than CdTeQDs in the model organism *Drosophila melanogaster*. Moreover, the fact that CdTeQDs showed no sublethal toxicity at 5 mg/kg but had an EC₅₀ of just 46 mg/kg, suggests that there is a narrow range of concentrations whereby CdTeQD toxicity rapidly increases. SCDs might induce a minor biological response in *Drosophila melanogaster* at a concentration of 100 mg/kg. Further research may be warranted on other organisms and perhaps at a higher concentration to determine the nature of this potential response. The direct comparison of CDs and CdTeQDs allows us to gain insight into the relative toxicity of the two types of nanoparticles.

Acknowledgements

The authors acknowledge financial support from the Natural Sciences and Engineering Research Council of Canada (NSERC) for the Discovery, Strategic, and PURE CREATE

programs, the Canada Research Chairs Program, the Killam Research Fellowship, the Canada Foundation for Innovation, and the FRQNT. Shawninder Chahal acknowledges NSERC for a PGS D scholarship, EcotoQ (FRQNT), and McGill University for a MEDA fellowship and the support of the EUL fund in the Department of Chemical Engineering. J.-R. M. acknowledges NSERC for a Postdoctoral Fellowship. The authors thank Sara Matthews and Eva Roubeau Dumont for helpful discussions.

References

- (1) Pu, Y.; Cai, F.; Wang, D.; Wang, J.-X.; Chen, J.-F. Colloidal Synthesis of Semiconductor Quantum Dots toward Large-Scale Production: A Review. *Industrial & Engineering Chemistry Research* **2018**, *57* (6), 1790-1802. DOI: 10.1021/acs.iecr.7b04836.
- (2) Zhang, Y.; Li, Y.; Yan, X.-P. Aqueous Layer-by-Layer Epitaxy of Type-II CdTe/CdSe Quantum Dots with Near-Infrared Fluorescence for Bioimaging Applications. *Small* **2009**, *5* (2), 185-189. DOI: 10.1002/sml.200800473.
- (3) Choi, Y.; Seol, M.; Kim, W.; Yong, K. Chemical Bath Deposition of Stoichiometric CdSe Quantum Dots for Efficient Quantum-Dot-Sensitized Solar Cell Application. *The Journal of Physical Chemistry C* **2014**, *118* (11), 5664-5670. DOI: 10.1021/jp411221q.
- (4) Bera, S.; Singh, S. B.; Ray, S. K. Green route synthesis of high quality CdSe quantum dots for applications in light emitting devices. *Journal of Solid State Chemistry* **2012**, *189*, 75-79. DOI: 10.1016/j.jssc.2011.11.048.
- (5) Yi, K.-Y. Application of CdSe quantum dots for the direct detection of TNT. *Forensic Science International* **2016**, *259*, 101-105. DOI: 10.1016/j.forsciint.2015.12.028.
- (6) Murray, C. B.; Norris, D. J.; Bawendi, M. G. Synthesis and characterization of nearly monodisperse CdE (E = sulfur, selenium, tellurium) semiconductor nanocrystallites. *Journal of the American Chemical Society* **1993**, *115* (19), 8706-8715. DOI: 10.1021/ja00072a025.
- (7) Liu, W.; Zhang, S.; Wang, L.; Qu, C.; Zhang, C.; Hong, L.; Yuan, L.; Huang, Z.; Wang, Z.; Liu, S.; et al. CdSe Quantum Dot (QD)-Induced Morphological and Functional Impairments to Liver in Mice. *PLOS ONE* **2011**, *6* (9), e24406. DOI: 10.1371/journal.pone.0024406.

- (8) Green, M.; Howman, E. Semiconductor quantum dots and free radical induced DNA nicking. *Chemical Communications* **2005**, (1), 121-123. DOI: 10.1039/B413175D.
- (9) Zhang, T.; Hu, Y.; Tang, M.; Kong, L.; Ying, J.; Wu, T.; Xue, Y.; Pu, Y. Liver Toxicity of Cadmium Telluride Quantum Dots (CdTe QDs) Due to Oxidative Stress *in Vitro* and *in Vivo*. *International Journal of Molecular Sciences* **2015**, 16 (10). DOI: 10.3390/ijms161023279.
- (10) Zhang, W.; Lin, K.; Miao, Y.; Dong, Q.; Huang, C.; Wang, H.; Guo, M.; Cui, X. Toxicity assessment of zebrafish following exposure to CdTe QDs. *Journal of Hazardous Materials* **2012**, 213-214, 413-420. DOI: 10.1016/j.jhazmat.2012.02.014.
- (11) Ambrosone, A.; Mattera, L.; Marchesano, V.; Quarta, A.; Susa, A. S.; Tino, A.; Rogach, A. L.; Tortiglione, C. Mechanisms underlying toxicity induced by CdTe quantum dots determined in an invertebrate model organism. *Biomaterials* **2012**, 33 (7), 1991-2000. DOI: 10.1016/j.biomaterials.2011.11.041.
- (12) Liu, T.; Xing, R.; Zhou, Y.-F.; Zhang, J.; Su, Y.-Y.; Zhang, K.-Q.; He, Y.; Sima, Y.-H.; Xu, S.-Q. Hematopoiesis toxicity induced by CdTe quantum dots determined in an invertebrate model organism. *Biomaterials* **2014**, 35 (9), 2942-2951. DOI: 10.1016/j.biomaterials.2013.12.007.
- (13) Chahal, S.; Macairan, J.-R.; Yousefi, N.; Tufenkji, N.; Naccache, R. Green synthesis of carbon dots and their applications. *RSC Advances* **2021**, 11 (41), 25354-25363. DOI: 10.1039/D1RA04718C.
- (14) Ong, C.; Yung, L.-Y. L.; Cai, Y.; Bay, B.-H.; Baeg, G.-H. *Drosophila melanogaster* as a model organism to study nanotoxicity. *Nanotoxicology* **2015**, 9 (3), 396-403. DOI: 10.3109/17435390.2014.940405.

- (15) Reiter, L. T.; Potocki, L.; Chien, S.; Gribskov, M.; Bier, E. A systematic analysis of human disease-associated gene sequences in *Drosophila melanogaster*. *Genome Res* **2001**, *11* (6), 1114-1125. DOI: 10.1101/gr.169101 PubMed.
- (16) Pandey, U. B.; Nichols, C. D. Human Disease Models in *Drosophila melanogaster* and the Role of the Fly in Therapeutic Drug Discovery. *Pharmacological Reviews* **2011**, *63* (2), 411. DOI: 10.1124/pr.110.003293.
- (17) Alaraby, M.; Demir, E.; Hernández, A.; Marcos, R. Assessing potential harmful effects of CdSe quantum dots by using *Drosophila melanogaster* as *in vivo* model. *Science of The Total Environment* **2015**, *530-531*, 66-75. DOI: 10.1016/j.scitotenv.2015.05.069.
- (18) Xiao, A.; Wang, C.; Chen, J.; Guo, R.; Yan, Z.; Chen, J. Carbon and Metal Quantum Dots toxicity on the microalgae *Chlorella pyrenoidosa*. *Ecotoxicology and Environmental Safety* **2016**, *133*, 211-217. DOI: 10.1016/j.ecoenv.2016.07.026.
- (19) Chahal, S.; Yousefi, N.; Tufenkji, N. Green Synthesis of High Quantum Yield Carbon Dots from Phenylalanine and Citric Acid: Role of Stoichiometry and Nitrogen Doping. *ACS Sustainable Chemistry & Engineering* **2020**, *8* (14), 5566-5575. DOI: 10.1021/acssuschemeng.9b07463.
- (20) Macairan, J.-R.; Jaunky, D. B.; Piekny, A.; Naccache, R. Intracellular ratiometric temperature sensing using fluorescent carbon dots. *Nanoscale Advances* **2019**, *1* (1), 105-113. DOI: 10.1039/C8NA00255J.
- (21) Pappus, S. A.; Ekka, B.; Sahu, S.; Sabat, D.; Dash, P.; Mishra, M. A toxicity assessment of hydroxyapatite nanoparticles on development and behaviour of *Drosophila melanogaster*. *Journal of Nanoparticle Research* **2017**, *19* (4), 136. DOI: 10.1007/s11051-017-3824-8.

- (22) Matthews, S.; Xu, E. G.; Roubeau Dumont, E.; Meola, V.; Pikuda, O.; Cheong, R. S.; Guo, M.; Tahara, R.; Larsson, H. C. E.; Tufenkji, N. Polystyrene micro- and nanoplastics affect locomotion and daily activity of *Drosophila melanogaster*. *Environmental Science: Nano* **2021**, 8 (1), 110-121. DOI: 10.1039/D0EN00942C.
- (23) Bartholomew, N. R.; Burdett, J. M.; VandenBrooks, J. M.; Quinlan, M. C.; Call, G. B. Impaired climbing and flight behaviour in *Drosophila melanogaster* following carbon dioxide anaesthesia. *Sci Rep* **2015**, 5, 15298-15298. DOI: 10.1038/srep15298 PubMed.
- (24) Pompa, P. P.; Vecchio, G.; Galeone, A.; Brunetti, V.; Sabella, S.; Maiorano, G.; Falqui, A.; Bertoni, G.; Cingolani, R. *In Vivo* toxicity assessment of gold nanoparticles in *Drosophila melanogaster*. *Nano Research* **2011**, 4 (4), 405-413. DOI: 10.1007/s12274-011-0095-z.
- (25) Feany, M. B.; Bender, W. W. A *Drosophila* model of Parkinson's disease. *Nature* **2000**, 404 (6776), 394-398. DOI: 10.1038/35006074.
- (26) Niccoli, T.; Cabecinha, M.; Tillmann, A.; Kerr, F.; Wong, Chi T.; Cardenes, D.; Vincent, Alec J.; Bettedi, L.; Li, L.; Grönke, S.; et al. Increased Glucose Transport into Neurons Rescues A β Toxicity in *Drosophila*. *Current Biology* **2016**, 26 (17), 2291-2300. DOI: 10.1016/j.cub.2016.07.017.
- (27) Hama, H.; Hioki, H.; Namiki, K.; Hoshida, T.; Kurokawa, H.; Ishidate, F.; Kaneko, T.; Akagi, T.; Saito, T.; Saido, T.; et al. ScaleS: an optical clearing palette for biological imaging. *Nature Neuroscience* **2015**, 18 (10), 1518-1529. DOI: 10.1038/nn.4107.
- (28) Harris, C. R.; Millman, K. J.; van der Walt, S. J.; Gommers, R.; Virtanen, P.; Cournapeau, D.; Wieser, E.; Taylor, J.; Berg, S.; Smith, N. J.; et al. Array programming with NumPy. *Nature* **2020**, 585 (7825), 357-362. DOI: 10.1038/s41586-020-2649-2.

- (29) McKinney, W. Data Structures for Statistical Computing in Python. In *Python in Science*, Austin, Texas, June 28 - July 3, 2010; van der Walt, S., Millman, J., Eds.; 2010; Vol. 445, pp 56 - 61. DOI: 10.25080/Majora-92bf1922-00a.
- (30) Virtanen, P.; Gommers, R.; Oliphant, T. E.; Haberland, M.; Reddy, T.; Cournapeau, D.; Burovski, E.; Peterson, P.; Weckesser, W.; Bright, J.; et al. SciPy 1.0: fundamental algorithms for scientific computing in Python. *Nature Methods* **2020**, *17* (3), 261-272. DOI: 10.1038/s41592-019-0686-2.
- (31) Seabold, S.; Perktold, J. Statsmodels: Econometric and statistical modeling with python. In *Proceedings of the 9th Python in Science Conference*, Austin, TX, 2010; Vol. 57, p 61.
- (32) Hunter, J. D. Matplotlib: A 2D Graphics Environment. *Computing in Science & Engineering* **2007**, *9* (3), 90-95. DOI: 10.1109/MCSE.2007.55.
- (33) Chousidis, I.; Stalikas, C. D.; Leonardos, I. D. Induced toxicity in early-life stage zebrafish (*Danio rerio*) and its behavioral analysis after exposure to non-doped, nitrogen-doped and nitrogen, sulfur-co doped carbon quantum dots. *Environmental Toxicology and Pharmacology* **2020**, *79*, 103426. DOI: 10.1016/j.etap.2020.103426.
- (34) Liu, W.; Huang, G.; Su, X.; Li, S.; Wang, Q.; Zhao, Y.; Liu, Y.; Luo, J.; Li, Y.; Li, C.; et al. Zebrafish: A Promising Model for Evaluating the Toxicity of Carbon Dot-Based Nanomaterials. *ACS Applied Materials & Interfaces* **2020**, *12* (43), 49012-49020. DOI: 10.1021/acsami.0c17492.
- (35) Yang, Y.; Ren, X.; Sun, Z.; Fu, C.; Liu, T.; Meng, X.; Wang, Z. Toxicity and bio-distribution of carbon dots after single inhalation exposure *in vivo*. *Chinese Chemical Letters* **2018**, *29* (6), 895-898. DOI: 10.1016/j.ccllet.2018.04.018.

- (36) Zheng, X.; Shao, D.; Li, J.; Song, Y.; Chen, Y.; Pan, Y.; Zhu, S.; Yang, B.; Chen, L. Single and repeated dose toxicity of citric acid-based carbon dots and a derivative in mice. *RSC Advances* **2015**, *5* (111), 91398-91406. DOI: 10.1039/C5RA18391J.
- (37) de Vasconcelos Lima, M.; de Andrade Pereira, M. I.; Cabral Filho, P. E.; Nascimento de Siqueira, W.; Milca Fagundes Silva, H. A.; de França, E. J.; Saegesser Santos, B.; Mendonça de Albuquerque Melo, A. M.; Fontes, A. Studies on Toxicity of Suspensions of CdTe Quantum Dots to *Biomphalaria glabrata* Mollusks. *Environmental Toxicology and Chemistry* **2019**, *38* (10), 2128-2136. DOI: 10.1002/etc.4525 (accessed 2022/07/21).
- (38) Han, Y.; Han, Y.; Du, G.; Zhang, T.; Guo, Q.; Yang, H.; Li, R.; Xu, Y. Physiological effect of colloidal carbon quantum dots on *Bursaphelenchus xylophilus*. *RSC Advances* **2021**, *11* (11), 6212-6220. DOI: 10.1039/D0RA10144C.
- (39) Paithankar, J. G.; Kushalan, S.; S, N.; Hegde, S.; Kini, S.; Sharma, A. Systematic toxicity assessment of CdTe quantum dots in *Drosophila melanogaster*. *Chemosphere* **2022**, *295*, 133836. DOI: 10.1016/j.chemosphere.2022.133836.
- (40) Qu, M.; Qiu, Y.; Lv, R.; Yue, Y.; Liu, R.; Yang, F.; Wang, D.; Li, Y. Exposure to MPA-capped CdTe quantum dots causes reproductive toxicity effects by affecting oogenesis in nematode *Caenorhabditis elegans*. *Ecotoxicology and Environmental Safety* **2019**, *173*, 54-62. DOI: 10.1016/j.ecoenv.2019.02.018.
- (41) Du, Y.; Zhong, Y.; Dong, J.; Qian, C.; Sun, S.; Gao, L.; Yang, D. The effect of PEG functionalization on the *in vivo* behavior and toxicity of CdTe quantum dots. *RSC Advances* **2019**, *9* (22), 12218-12225. DOI: 10.1039/C9RA00022D.

Supplementary information

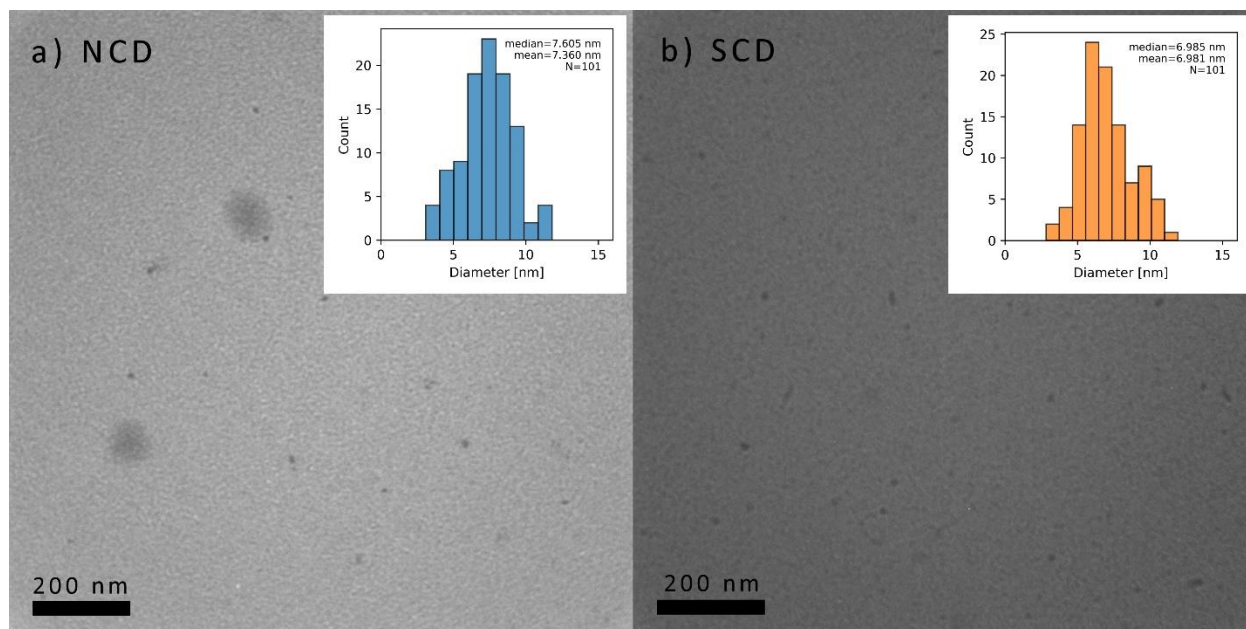


Figure S4.1. TEM images of a) NCDs and b) SCDs. Insets show their respective size distributions.

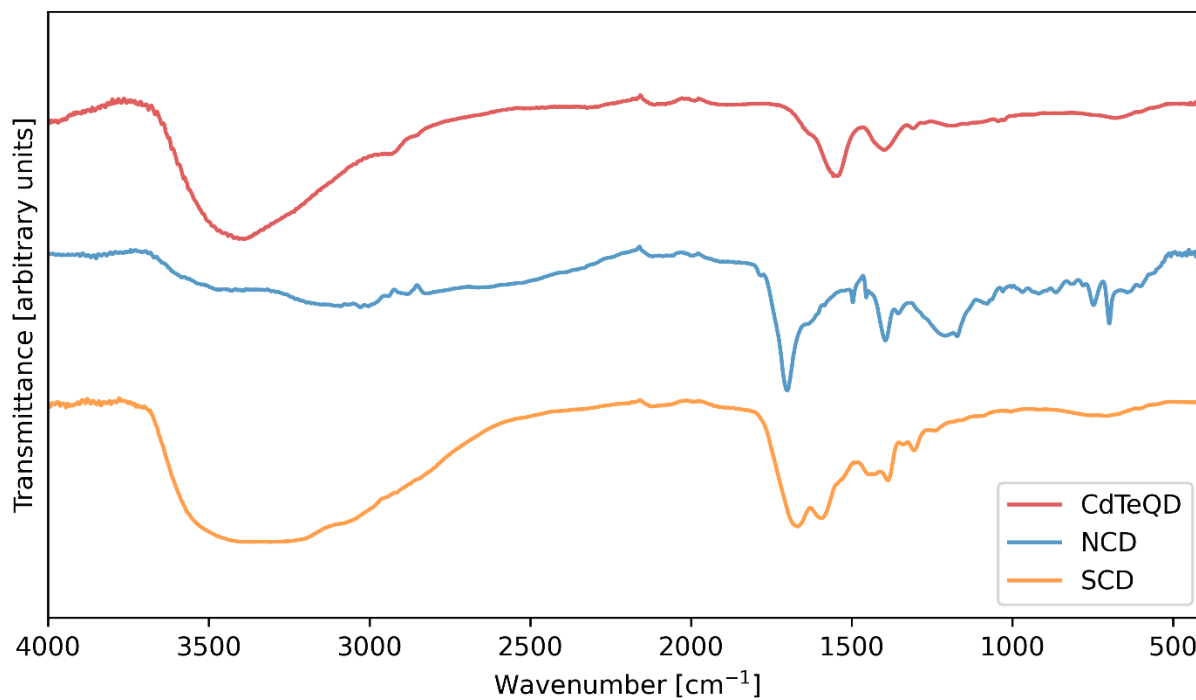


Figure S4.2. FTIR spectra of CdTeQDs, NCDs, and SCDs.

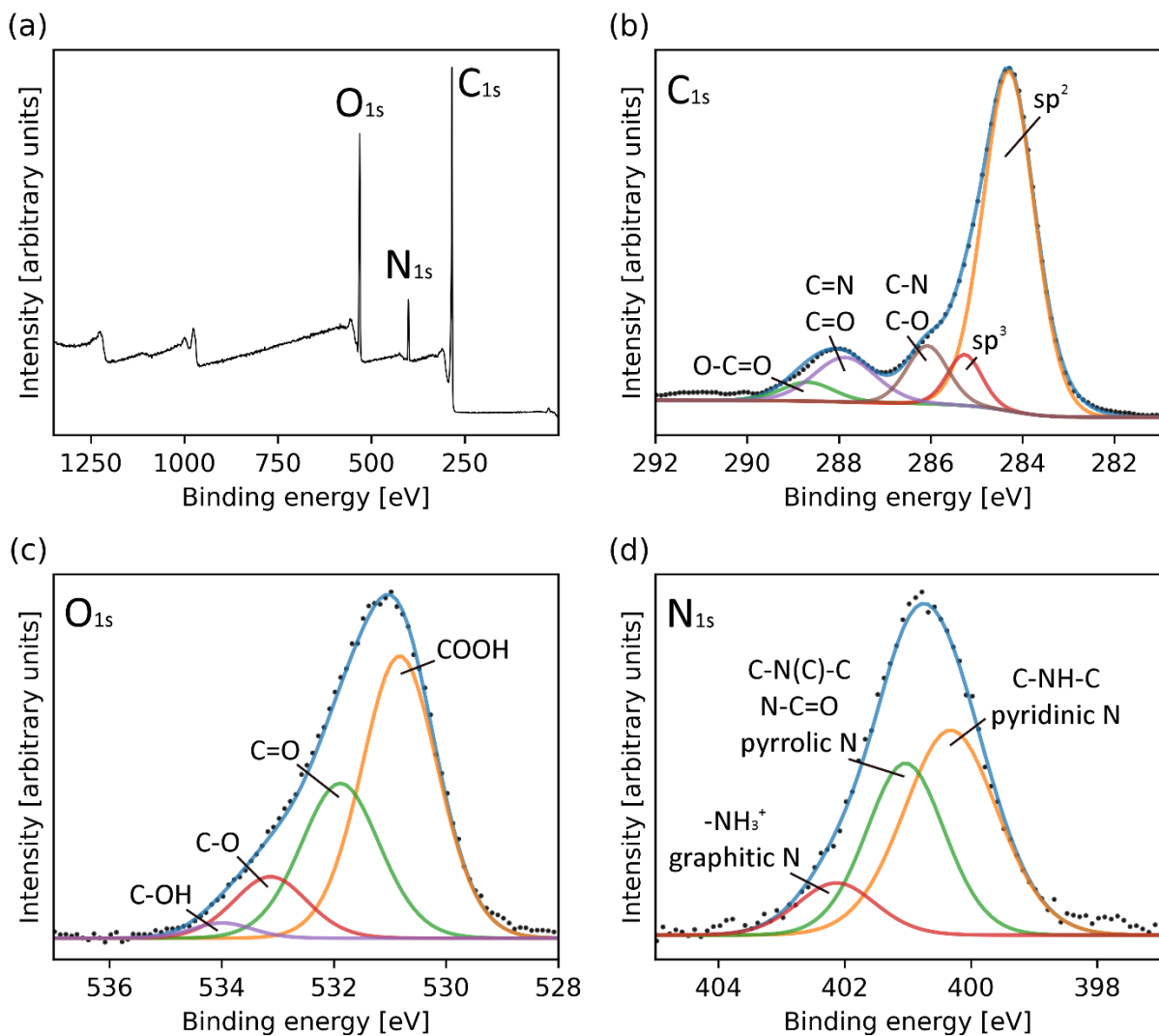


Figure S4.3. XPS spectra of NCDs showing a) survey scan, b) C_{1s} spectra, c) O_{1s} spectra, and d) N_{1s} spectra.

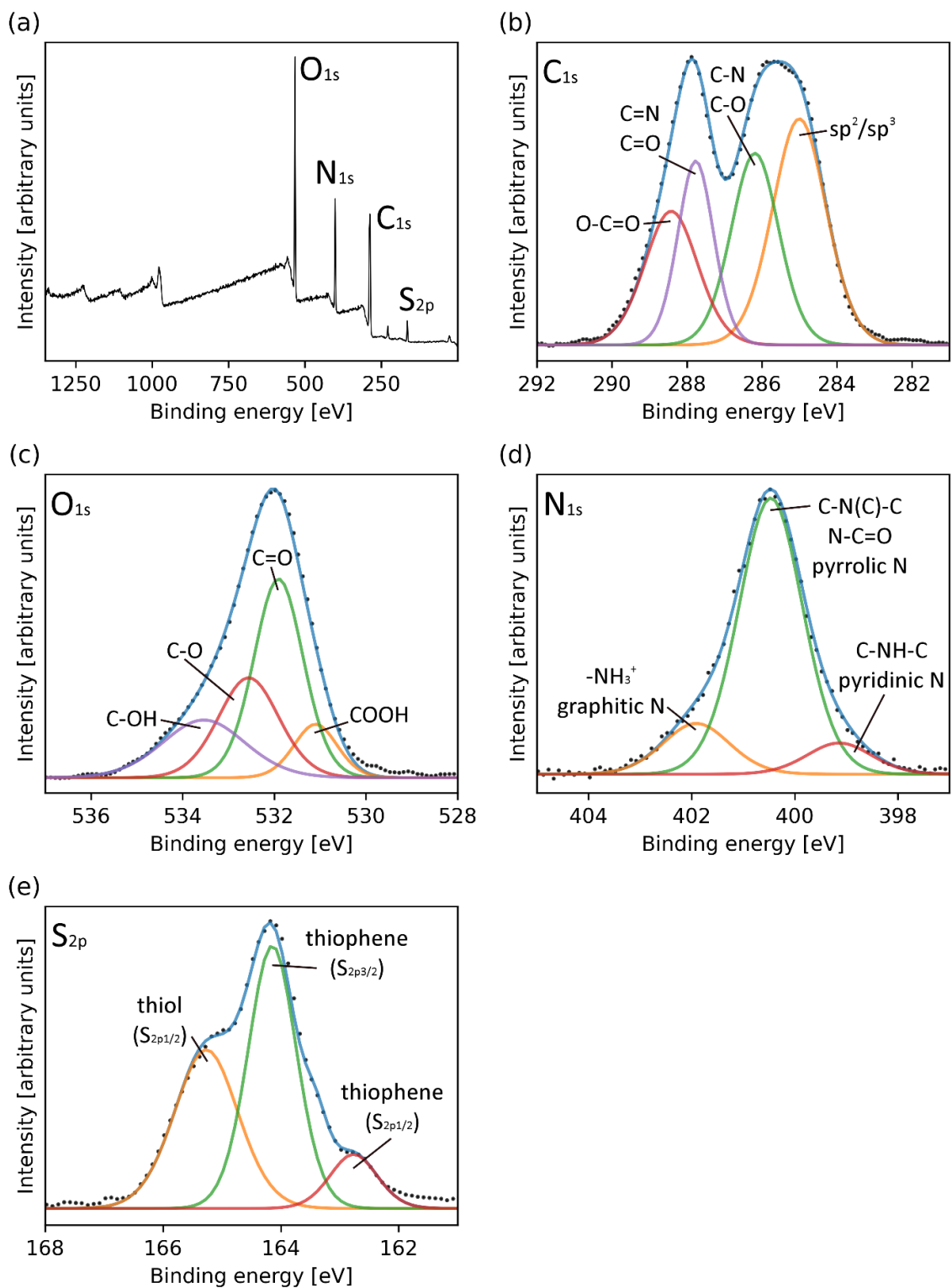


Figure S4.4. XPS spectra of SCDs showing a) survey scan, b) C_{1s} spectra, c) O_{1s} spectra, d) N_{1s} spectra, and e) S_{2p} spectra.

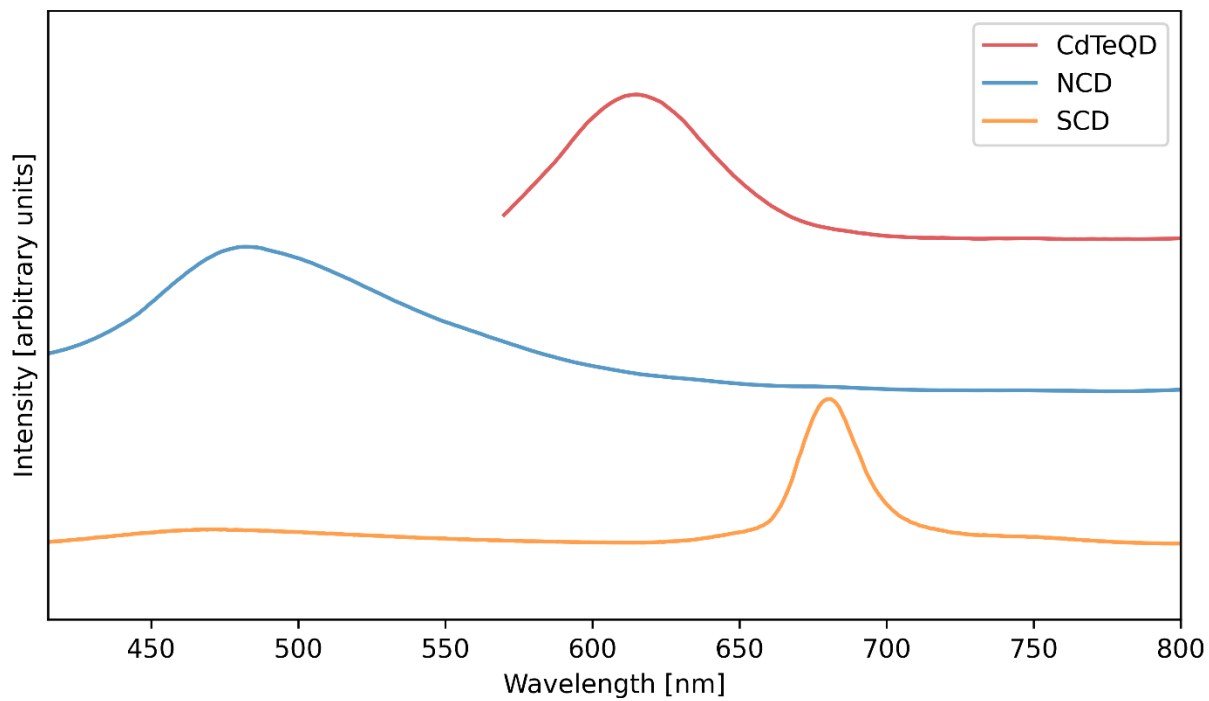


Figure S4.5. Fluorescence spectra of CdTeQDs, NCDs, and SCDs. The CdTeQDs were excited under 561 nm light, whereas the NCDs and SCDs were excited under 405 nm.

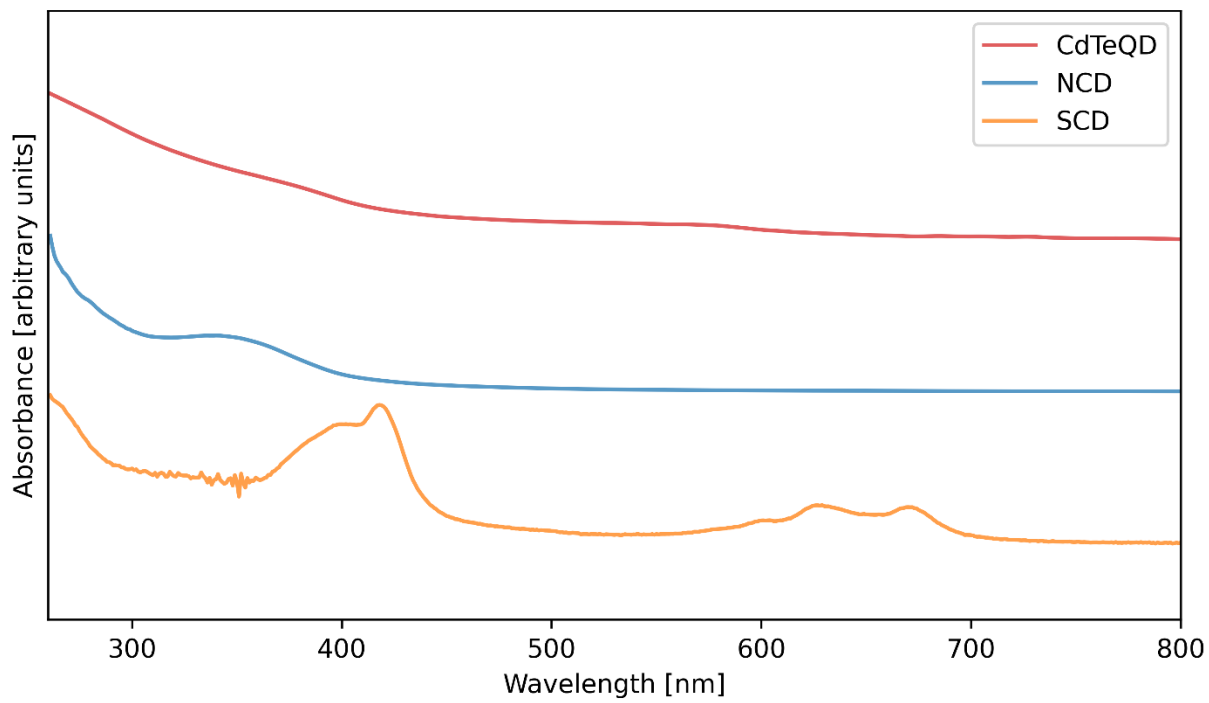


Figure S4.6. UV-Vis spectra of CdTeQDs, NCDs, and SCDs.

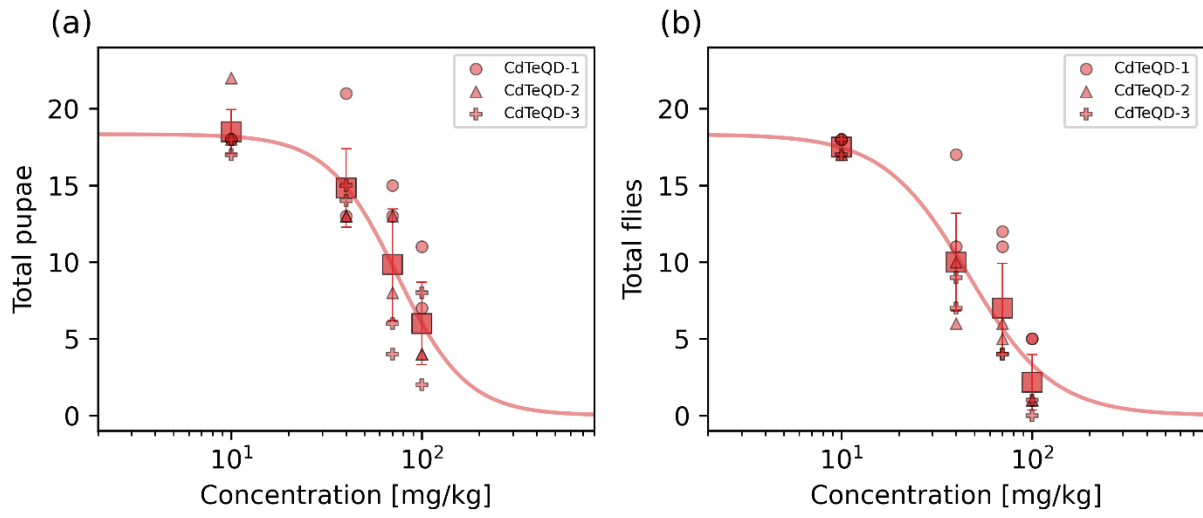


Figure S4.7. Number of (a) pupae and (b) flies that emerged from approximately twenty first instar larvae raised on 0, 10, 40, 70, or 100 mg/kg CdTeQD treated food by day 14. Squares represent the mean of data points in that column and error bars represent $2 \times$ the standard error of the mean. Legend labels have the format X-Y where X is the treatment and Y is the experimental block ID. Red curve represents the Hill equation that was fit to the corresponding data.

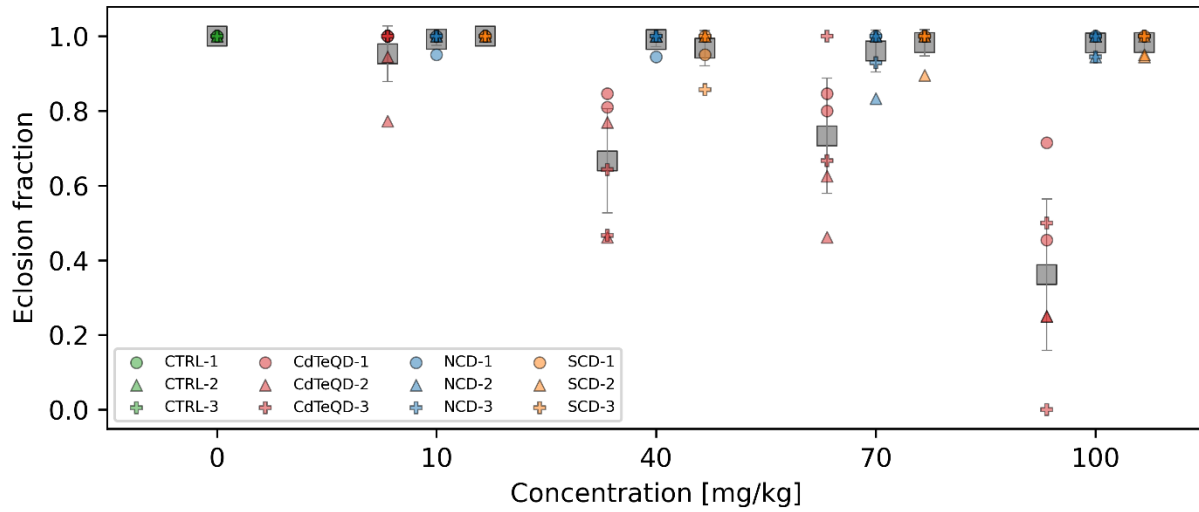


Figure S4.8. Eclosion fraction representing the fraction of pupae raised on 0, 10, 40, 70, or 100 mg/kg NCD, SCD, or CdTeQD treated food that successfully eclosed into flies by day 14. Grey squares represent the mean of data points in that column and error bars represent $2 \times$ the standard error of the mean. Legend labels have the format X-Y where X is the treatment and Y is the experimental block ID.

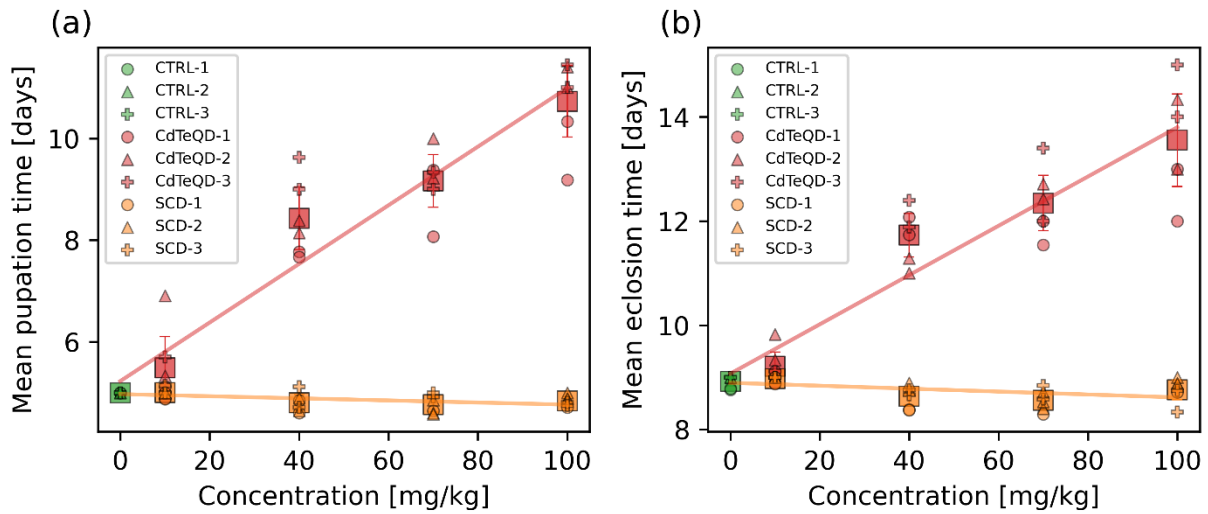


Figure S4.9. The mean (c) pupation and (d) eclosion time of the pupae and flies that emerged from approximately twenty first instar larvae raised on 0, 10, 40, 70, or 100 mg/kg SCD, or CdTeQD treated food by day 14. Squares represent the mean of data points in that column and error bars represent $2 \times$ the standard error of the mean. Legend labels have the format X-Y where X is the treatment and Y is the experimental block ID. Lines represents a linear regression that was fit to the corresponding data.

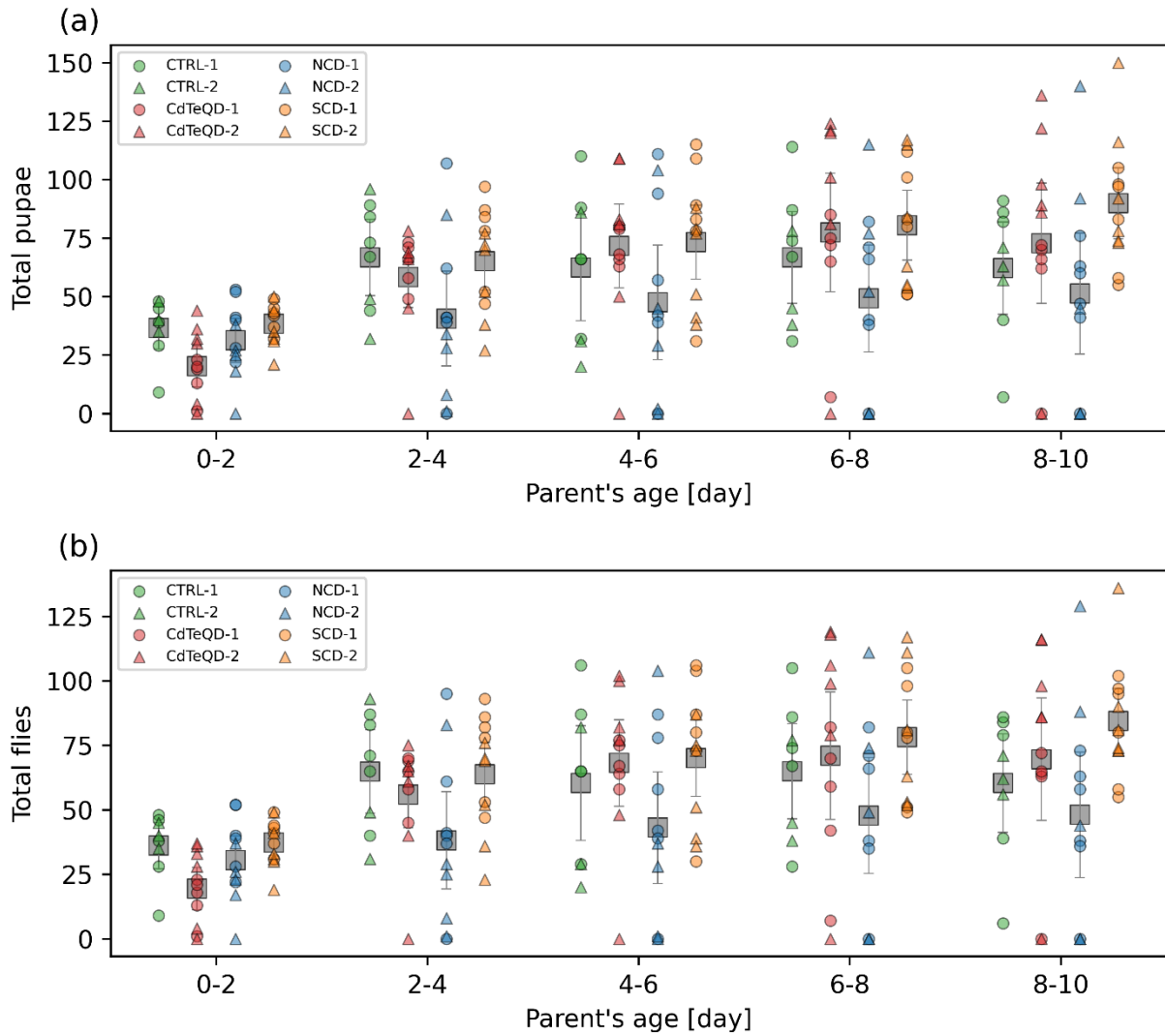


Figure S4.10. Number of (a) pupae and (b) flies that emerged after allowing one female and one male fly that were raised on CTRL (0 mg/kg), NCD (100 mg/kg), SCD (100 mg/kg), or CdTeQD (5 mg/kg) treated food to mate over 10 days. Grey squares represent the mean of data points in that column and error bars represent $2 \times$ the standard error of the mean. Legend labels have the format X-Y where X is the treatment and Y is the experimental block ID.

Preamble to Chapter 5

We have concluded that CdTeQDs are far more toxic towards *Drosophila melanogaster* than our CDs. While this is an important finding if CDs are to one day see widespread implementation in commercial products, at the moment, CDs are mostly confined to a laboratory setting. As a result, they are not an immediate environmental concern in the same sense as another class of anthropogenic carbon-based nanoparticles and microparticles. Plastics have widespread use to the point that it is difficult to imagine what life would be like today without the convenience of lightweight, easy to shape, plastic materials. Unfortunately, the majority of this plastic ends up being released into the environment or left in landfills at the end of their use. In both these scenarios the plastic may break down over time into microplastics and eventually nanoplastics. Continuing from Chapter 4 with our use of *Drosophila melanogaster* to evaluate CD and CdTeQD toxicity, we now shift focus towards examining the toxicity of one of the most widely used polymers in plastics, HDPE. Specifically, we are evaluating the toxicity of mechanically and UV-weathered HDPE microplastics less than 38 μm in size. SEM images also revealed the presence of nanoplastics with a median size of 228 nm in the particle distribution. We performed a developmental toxicity assay followed by further sublethal assays including a climbing assay, larvae crawling assay, and fly mass assay. Most notably, we evaluated the long-term effects of HDPE microplastics on reproduction over four generations of flies. The outcome of this chapter, in conjunction with Chapter 4, provides more insight into the toxicity of anthropogenic carbon-based particles in fruit flies.

Chapter 5: Multigenerational effects of weathered polyethylene microplastics on *Drosophila melanogaster*

Abstract

The vast majority of plastics are released into the environment or landfills once they are no longer of use, and as a result, microplastics are now found in every corner of the Earth. To gain a better understanding of the toxicity that may arise from such pollution, we exposed four generations of the fruit fly, *Drosophila melanogaster*, to HDPE microplastics (<38 µm) and monitored their reproductive performance. We found that the eclosion fraction of pupae was 5.73 % higher ($p < 0.05$) in the stream of flies that were fed 100 mg/kg HDPE across all generations when compared to those fed control food. However, no toxicity was observed in the number of pupae and flies that emerged from the eggs laid in each generation, or the mean pupation and eclosion time of these eggs. We also observed no toxicity in the development of larvae into adult flies (0.1 – 10 000 mg/kg HDPE), and various sublethal endpoints (100 mg/kg HDPE) such as larvae and adult fly locomotion, and the mass of female and male flies. Although no toxicity was observed from the HDPE microplastics, we believe the results are an important contribution to the literature since they were performed with a large sample size and performed in multiple blocks, allowing us to conclude with greater confidence that any toxicity in *Drosophila melanogaster* that may arise from HDPE microplastics in the concentrations evaluated is likely to be minimal.

5.1 Introduction

Upon disposal, it is estimated that 79 % of plastic is released into the environment, including landfills.¹ Over time, these plastics experience photo-oxidation from solar UV radiation, mechanical weathering through abrasions with sand and rocks initiated by ocean currents and wind, and to a lesser extent thermal degradation.² This natural weathering of plastics produces microplastics, which are loosely defined as plastic particles ranging from ~1 – 5000 μm in size.³ Due to the widespread use of plastics, microplastics are consequently found in every corner of the planet and their concentration in the environment can vary considerably. For instance, soil microplastic concentrations in industrial areas can range from 300 – 67 500 mg kg^{-1} .⁴ Conversely, a study conducted in the Tibetan Plateau found only 48 microplastic items per kg of soil, noting that 38 % were smaller than 50 μm and that polyethylene was the most abundant, comprising 44 – 49 % of the microplastics found in the soils.⁵

The toxicity of microplastics in aquatic organisms has been well documented. Some of the most commonly examined microplastics in aquatic ecotoxicology studies are those derived from polystyrene, with toxicity being reported in *Scrobicularia plana*,⁶ *Gammarus pulex*,⁷ *Dolioletta gegenbauri*,⁸ and goldfish.⁹ However, polyethylene makes up 29 % of plastic production and 32 % of plastic waste, making it by far the most widely used plastic.¹ In particular, high-density polyethylene (HDPE) comprises 13 % of total plastic waste.¹ Polyethylene has also shown toxicity in aquatic organisms such as *Crassostrea gigas*¹⁰ and zebrafish.¹¹ While there are many studies examining microplastic toxicity to a diverse set of aquatic organisms, far fewer studies exist examining the toxicity of microplastics in terrestrial organisms.

Drosophila melanogaster, commonly known as the fruit fly, has long been used as a model organism for genetics studies but is now seeing increasing use in toxicity studies.¹² Contributing

to this rising popularity is their rapid development time, typically less than two weeks, and relatively low maintenance, in terms of both time and cost, allowing for studies to be conducted with a large sample size and over multiple generations. Flies also undergo distinct development cycles starting as an egg and developing into larvae, pupae, and finally adult flies. This can allow one to isolate which stage of development an examined substance may cause toxicity in, whether toxicity is only observed after long-term exposure, or even over several generations. The study of toxicity over multiple generations of a species can reveal long-term effects that could otherwise go unnoticed in a single generation. For instance, in a study by Panacek *et al.* where fruit flies were exposed to 5 mg L⁻¹ silver nanoparticles, no difference in the number of hatched flies was observed in the first generation, but there was a sharp decline in the second generation.¹³

Herein, we present our ecotoxicology study on the effects of HDPE microplastics on the fruit fly, *Drosophila melanogaster*. We produced HDPE microplastics from bulk HDPE through accelerated mechanical and ultraviolet weathering to simulate real-world weathering of plastics to ensure our microplastics have similar properties to those found in the environment. Larvae were raised on food containing HDPE microplastics at concentrations of 0.1, 1, 10, 100, 1000, and 10 000 mg kg⁻¹, covering the wide range of microplastic concentrations found in the environment, from remote locations, industrial zones, or pollution hotspots. Further experiments were conducted at 100 mg kg⁻¹ food to measure the locomotion of larvae and adult flies, the mass of female and male flies, and the reproductive performance of the flies over 4 generations. Lightsheet fluorescence microscopy was also performed to assess the potential uptake of the HDPE microplastics in the flies. We believe the comprehensive nature of this work, namely, examining developmental toxicity over the span of 6 concentrations, as well as the multigenerational

assessment of HDPE microplastic toxicity, provides new insights into the long-term effects of HDPE microplastics exposure and provide data that can apply to various regions around the world.

5.2 Experimental

5.2.1 Preparation of weathered high-density polyethylene microplastics

HDPE sheets (48" × 96" × 1/16", McMaster-Carr 8619K112) were cut into squares of approximately 4 cm × 4 cm. The HDPE squares were first rinsed with 70 vol% ethanol to remove any oil or dust that may have accumulated on the surface through handling and storage. The HDPE squares were then rinsed with reverse osmosis water (Type II, >1 MΩ), hereafter referred to simply as water. Any residual water was left to be absorbed by a brown paper towel. The dry HDPE squares were then placed in a 2500 W, 36 000 rpm, stainless steel spice grinder (Homend) and left to run for two minutes and then turned off to allow the grinder to cool. This process was repeated by continuing to add HDPE squares and running the grinder for two minutes at a time until the grinder was approximately half full and there was no longer any visible difference in the fineness of the HDPE between runs. The granular HDPE was then passed through a 38 μm opening (US Standard Mesh No. 400) stainless steel sieve (Cole-Parmer RK-59984-24) to obtain HDPE microplastics. The HDPE microplastics (<38 μm) were then placed on an acetone-washed glass Petri dish and placed under UV irradiation (365 nm, 25 W m⁻²) for 14 days at 25 °C in an incubator (INFORS HT Multitron Pro) to induce photo-oxidation.¹⁴ The glass Petri dish was shaken every two days to ensure that the HDPE was uniformly exposed to the UV light over the 14 days.

5.2.2 Scanning electron microscopy

The resulting HDPE microplastics were then imaged using scanning electron microscopy (SEM) to gain a better understanding of their size distribution and shape. A hydrophilic polycarbonate membrane filter (Sterlitech PCT00147100, pore size 10 nm) with the shiny side facing upwards was attached to an SEM stud (Ted Pella 16084-1) using carbon tape (Ted Pella 16111). Then 0.1 mg of HDPE microplastics were dispersed in 5 mL of ethanol (Les Alcools de Commerce, UN1170). The suspension was sonicated (Fisherbrand CPXH Series Heated Ultrasonic Cleaning Bath) for 10 minutes and subsequently 100 μ L of suspension was deposited onto the polycarbonate filter. The suspension was allowed to dry in a glass Petri dish. The polycarbonate filter was then coated with a 2 nm layer of platinum (Leica Microsystems EM ACE600 Sputter Coater). SEM imaging was done using a FEI Quanta 450 environmental SEM at 5 kV and spot size 3.0. Images were taken at 100 \times (10 images), 1000 \times (15 images), and 2500 \times (15 images). To determine the particle size distribution, 2495 particles were measured from eight 2500 \times magnification images using ImageJ software. ImageJ analysis was done starting with background subtraction, then the threshold was adjusted, and finally, the automatic particle counting function was used. The maximum Feret diameter was assigned as the diameter, since this represents the largest distance between two boundary points on a particle. No large particles were imaged in the 1000 \times and 2500 \times magnification images.

5.2.3 Fourier-transform infrared spectroscopy

The HDPE microplastics, before and after UV weathering, were analyzed under Fourier-transform infrared (FTIR) spectroscopy to determine if any changes to the surface chemistry occurred during the UV weathering process. FTIR spectroscopy was performed using a Thermo

Scientific Nicolet iS5 equipped with an iD5 ATR accessory. The FTIR spectra were collected from 32 scans at a resolution of 0.4 cm^{-1} , an optical velocity of 0.4747 cm s^{-1} , a gain of 1, and an aperture setting of 100. The resulting data was processed using OMNIC 9.

To verify the chemical composition of the nano-sized HDPE observed under SEM, a 5 mg mL^{-1} suspension of weathered HDPE particles in water was prepared and sonicated (Branson CPX). It was then filtered through a $0.2\text{ }\mu\text{m}$ nylon filter. The resulting suspension was then pipetted onto the FTIR's ATR crystal and left to dry before measuring.

5.2.4 Maintenance of *Drosophila melanogaster*

Drosophila melanogaster (Oregon-R strain) was raised on food consisting of 84.6 wt% water, 14.9 wt% Nutri-Fly Bloomington Formulation powder (Diamed, GEN66-112), and 0.5 wt% sodium propionate (Genesee Scientific, 20-271) in glass vials (Carolina, 173135) in an environmental chamber (Panasonic MLR-352H-PA) operating under a day/night cycle at 60 % relative humidity at $25\text{ }^{\circ}\text{C}$. Days consisted of illumination at $\sim 1500\text{ lx}$ for 12 h. Nights consisted of complete darkness for 12 h.

To ensure that the flies for any given experiment were of similar age, egg collection cages were set up. Approximately 5 g of yeast paste (2.5 g dry yeast (Diamed, GEN62-106) mixed with 2.5 g water) was spread on the center of a grape agar (Diamed, GEN47-102) plate. A fly cage (Diamed, GEN59-101) was placed on top of the agar plate where the flies laid eggs. This moment is referred to as day 0. After 4 hours, the flies were removed from the cage and the eggs were allowed to age for an additional 24 hours. Any larvae that emerged from the eggs in the agar plate were then used for subsequent experiments unless stated otherwise.

When a specific selection of flies was required (*e.g.*, sorting of female and male flies), flies were anesthetized with CO₂ on a flypad (Genesee Scientific, 59-114) and sorted as needed. Total anesthesia time was restricted to less than 10 min to minimize undesirable physiological effects on the flies.¹⁵

5.2.5 Developmental toxicity

Developmental toxicity was measured according to previous methods with some modifications.¹³ First, 10 mL of food containing 0, 0.1, 1, 10, or 100 mg HDPE microplastics per kg total food was dispensed into a 50-mL glass test tube. The food preparation required a step where the food was first brought to a boil, simmered for 10 min, then cooled down. The HDPE microplastics were mixed into the food after the simmer phase as the temperature began to decrease to minimize any additional weathering that could have occurred at such an elevated temperature. Once the food had cooled to room temperature and had solidified, approximately 20 first instar larvae were transferred from the grape agar plates to the test tube which was then sealed with a cotton plug. For each test tube, the number of pupae and flies were counted every 2 days over 14 days. If any flies were present, they were removed from the vial, and not returned, to facilitate counting. Each treatment was done in up to four replicates (*i.e.*, four test tubes). The entire experiment was then repeated three times for a total of up to 12 replicates (*i.e.*, N≤12). This assay was performed again with food containing 0, 1000, or 10 000 mg/kg HDPE. In this case, each treatment was done in six replicates (*i.e.*, six test tubes). The entire experiment was then repeated twice for a total of 12 replicates (*i.e.*, N=12).

5.2.6 Multigenerational reproductive assay

Multigenerational toxicity was measured according to previous methods with some modifications.¹³ First, 10 mL of food containing 0 or 100 mg HDPE microplastics per kg total food was dispensed into a 50-mL glass test tube. Once the food had cooled to room temperature and had solidified, approximately 20 first instar larvae were then transferred from the grape agar plates to the test tube and the test tube was then sealed with a cotton plug. On day 9, any flies present in the test tube were released from the test tube. After 4 hours, the newly emerged flies (F0, parental flies) were separated into mating pairs (one female, one male) and placed into a new test tube containing 10 mL of food with either 0 or 100 mg HDPE microplastics per kg total food.

This step reset the clock to day 0 for the new test tube since the F0 flies had entered a new test tube in which they would begin to lay eggs. On day 4, the F0 mating pair was removed from the test tube. The eggs laid by the F0 flies gave rise to the first generation (F1) of flies. On day 12, any F1 flies present in the test tube were released from the test tube. After 4 hours, the newly emerged F1 flies were separated into mating pairs (one female, one male) and placed into a new test tube containing 10 mL of food with either 0 or 100 mg HDPE microplastics per kg total food.

The process described in the preceding paragraph was continued for the second (F2), third (F3), and fourth (F4) generation of flies. For each test tube, the number of pupae and flies were counted every two days for 16 days. If any flies were present, they were removed from the vial, and not returned, to facilitate counting. Each treatment was done in up to six replicates (*i.e.*, six test tubes). The entire experiment was then repeated twice for a total of up to 12 replicates (*i.e.*, $N \leq 12$). When transferring flies to the next generation, up to three mating pairs may have been taken from a single test tube of the previous generation. This was done to ensure that the sample size did not decrease throughout the experiment since sometimes no potential mating pair would

emerge during the 4 h eclosion period from some of the test tubes or in some cases the parent flies did not produce any offspring. Table 5.1 shows an overview of the food which was fed to each generation in each treatment stream.

Table 5.1. There are three treatment streams. This table shows the type of food, *i.e.*, control (CTRL) or 100 mg/kg HDPE, each generation was fed for each stream. For example, BF1 flies were raised on 100 mg kg⁻¹ HDPE microplastics from egg to adult.

Stream	F0	F1	F2	F3	F4
A	CTRL	CTRL	CTRL	CTRL	CTRL
B	HDPE	HDPE	HDPE	HDPE	HDPE
C	HDPE	CTRL	CTRL	CTRL	CTRL

5.2.7 Larval crawling assay

Larval crawling was measured according to previous methods with some modifications.¹⁶ First, 10 mL of food containing 0 or 100 mg HDPE microplastics per kg total food was dispensed into a 50-mL glass test tube. Once the food had cooled to room temperature and had solidified, approximately 20 first instar larvae were then transferred from the grape agar plates to the test tube which was then sealed with a cotton plug. On day 4, a larva was randomly selected from the test tube and transferred onto the center of a 100-mm grape agar Petri dish which did not contain HDPE microplastics. The larva was given 30 s to adjust to its environment and was then video recorded (Canon EOS Rebel SL2) under an Olympus SZX16 stereo microscope for 60 s. The plate was slowly moved as the larva crawled such that the larva remained near the center view of the camera. The number of peristaltic contractions performed by the larva in 60 s was recorded. This was repeated with a total of 3 larvae from each test tube. The average number of peristaltic contractions per minute from these three larvae was taken as one replicate (*i.e.*, N=1). Each treatment was done

in six replicates (*i.e.*, six test tubes). The entire experiment was performed twice for a total of 12 replicates (*i.e.*, N=12).

5.2.8 Climbing assay

A climbing assay was performed according to previous methods with some modifications.¹⁷ First, 10 mL of food containing 0 or 100 mg HDPE microplastics per kg total food was dispensed into a 50-mL glass test tube. Once the food had cooled to room temperature and had solidified, approximately 20 first instar larvae were then transferred from the grape agar plates to the test tube which was then sealed with a cotton plug. On day 11, the flies that emerged from the larvae were transferred to a 100-mL glass graduated cylinder marked at a height of 10 cm which was capped with a cotton plug. The cylinder was tapped to move the flies to the bottom. The flies were then allowed to ascend. After 10 s, the number of unique flies that crossed the 10-cm mark was recorded. This cycle was repeated five times for each test tube of flies to obtain an average value recorded as the number of flies passing the 10-cm mark divided by the total number of flies and represents one replicate (*i.e.*, N=1). This process was video recorded (Canon EOS Rebel SL2) so that counting could be done later. Each treatment was done in six replicates (*i.e.*, six test tubes). The entire experiment was performed three times for a total of 18 replicates (*i.e.*, N=18).

5.2.9 Fly mass measurements

After the flies went through the climbing assay, they were anesthetized using CO₂, separated into female and male groups, and the collective mass of each sex was divided by the number of flies for each sex from each test tube and represents one replicate (*i.e.*, N=1). Each

treatment was done in up to six replicates (*i.e.*, six test tubes). The entire experiment was performed twice for a total of up to 12 replicates (*i.e.*, $N \leq 12$).

5.2.10 Lightsheet fluorescence microscopy

The female fruit flies from the developmental toxicity study on day 10 were stored in 10 % neutral-buffered formalin for 24 hours at 4 °C. Following fixation, samples were washed with water and stained with a solution created by adding 1 part 1 mg/mL meso-tetraphenylchlorin (TPC) (Toronto Research Chemical T310540) dissolved in tetrahydrofuran followed by 3 parts water in a dropwise manner. To reduce the tissue-bound dye in an organism, the fruit flies were kept in a tissue clearing solution (adapted from Hama *et al.*¹⁸) for 7 days. The clearing solution consisted of 550 g/L urea, 225 g/L sorbitol, and 50 g/L Triton-X100 in water.

Samples were imaged using a Zeiss lightsheet Z.1 microscope. Samples were mounted in 1.5 % low melting temperature agarose gel made from ScaleS4 mounting solution (240 g/L urea, 400 g/L sorbitol, 100 g/L glycerol, 150 g/L dimethyl sulfoxide in water) as described by Hama *et al.*¹⁸ in 1-mL syringes. The refractive index of the ScaleS4 was measured with a refractometer and adjusted to 1.44 by adding glycerol or water as needed. The imaging chamber was filled with liquid ScaleS4 to minimize refractive index mismatch during imaging. All imaging was done with a 5× 0.16 NA objective for detection and 5× 0.1 NA objectives for illumination. Autofluorescence from tissue was detected using a 405 nm laser for excitation and a 420 nm to 470 nm bandpass filter for emission. The signal from TPC was detected using a 405 nm excitation laser and a 660 nm long-pass filter for emission.

5.2.11 Statistical analysis

To determine if a parametric test could be used, the data was first tested for normality of the residuals using the Shapiro-Wilk test or if there were more than 30 residuals, then a normal distribution was assumed. The data was then tested for equal variance among groups using Bartlett's test, or if any of the groups had zero variance, then it was assumed that the groups do not have equal variance. If both these tests validate the assumption of normality and equal variance, then statistical significance was measured using an n -way analysis of variance (ANOVA) without interaction terms. If the data did not pass the test of normality or equal variance, then n separate Kruskal-Wallis tests were performed. Here, n represents the number of factors for which statistical significance was being tested. If the n -way ANOVA showed a significant difference among treatments, then a Tukey-Kramer test was performed. If the Kruskal-Wallis test showed significant differences, then a Mann-Whitney U test with Bonferroni correction was performed. Throughout all statistical tests, $p < 0.05$ was considered significant. All data analysis was performed in Python 3.9.12 using numpy 1.21.5,¹⁹ pandas 1.4.2,²⁰ scipy 1.7.3,²¹ and statsmodels 0.13.2.²² Plots were made using matplotlib 3.5.1.²³

Test tubes from which no pupae or flies emerged were not used in the calculation of mean pupation or eclosion time (*e.g.*, due to sterile parents in the multigenerational assay) since there would be no time data to measure. Similarly, if no pupae emerged in a given test tube then an eclosion fraction was not calculated. In general, no outliers were removed. Any samples that were discarded were done so because of a known issue that occurred during handling, or for example if the flies died before the end of the experiment (*e.g.*, a multigenerational assay parent dying before the 4-day mating period ended). Occasionally pupae or flies would get stuck in the food and sink over time making them not visible. Therefore, irregularities such as there being more flies than

pupae, an eclosion fraction greater than 1, or the cumulative number of flies eclosed decreasing after a certain time point may occur. However, these incidences were rare, therefore we decided to keep the raw recorded values as is.

5.3 Results and discussion

5.3.1 Size and imaging of microplastics

The HDPE microplastics were imaged using SEM and darkfield microscopy. A 38 μm mesh sieve was used to isolate the smaller microplastics which were used in the exposure studies. However, this meant that only two dimensions of any particle or aggregate had to be below this size allowing for larger particles to pass through in a third dimension. Figure 5.1a shows that when the microplastics are well dispersed, many nano-sized plastic fragments are present. These nano-sized plastics had a median size of 228 nm (Figure 5.1a-inset). However, many larger microplastics were present as well. Figure 5.1b reveals that these larger particles may often be aggregates of many smaller microplastics. Figure 5.1c shows a visible-light image of the HDPE microplastics under dark-field microscopy (Olympus BX43). Using visible light allows one to see the translucence of the microplastics, facilitating the visualization and thickness of these particles as they twist and bend. These images, taken under various microscopy methods and magnifications, indicate that there is a wide distribution of sizes found in our microplastics. Several considerations need to be made from this data. For instance, on a mass basis, it is still likely that most of the microplastics have a size closer to $\sim 38 \mu\text{m}$, whereas on a number basis most may be $\sim 200 \text{ nm}$. Another consideration is that although aggregation was observed under SEM, the dispersibility of the microplastics may be considerably different during the food preparation where microplastics are added as the food mixture is cooling down from a boil. The food mixture, despite

being above room temperature at the time of HDPE addition and consisting mostly of water, has a high viscosity and it is unclear to what extent this may affect dispersion. Finally, upon consumption of microplastics by *Drosophila melanogaster*, the microplastics may further aggregate or disperse based on the unique chemical profile in the fluids contained in various portions of the gut.

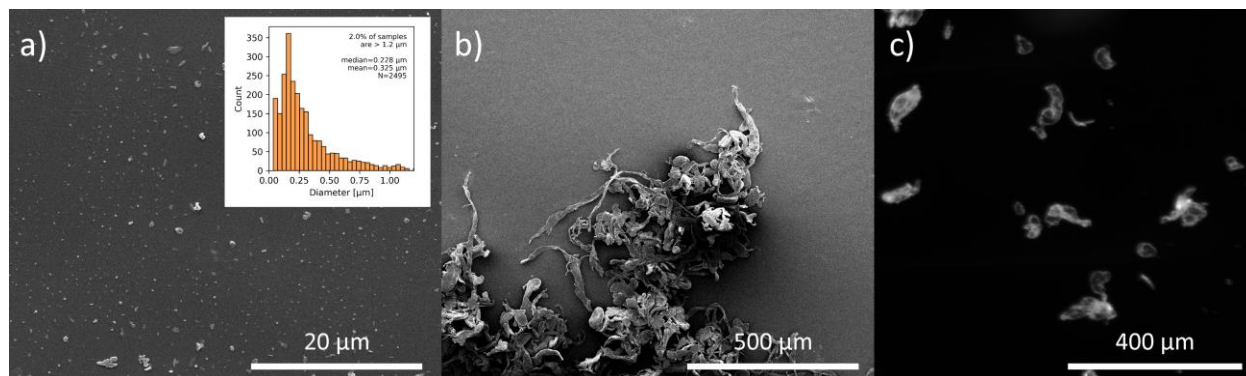


Figure 5.1. (a) SEM image showing nano-sized HDPE fragments. (a-inset) Size distribution of 2495 microplastic fragments taken from eight SEM images at 2500× magnification. The fragments likely formed during mechanical and/or UV weathering. We note that this histogram does not cover the entire distribution of the microplastics used in this study, but instead focuses on the distribution of sub-micrometer sized plastic particles. (b) SEM image showing aggregated HDPE microplastics. (c) Dark-field microscopy image of HDPE microplastics.

5.3.2 Fourier-transform infrared spectroscopy

To assess the chemical composition of the plastic samples, FTIR spectroscopy was performed. Three prominent peaks that are characteristic of HDPE were observed (Figure S5.1). Peaks associated with C-H stretching of $-\text{CH}_2-$ groups were found at 2850 and 2912 cm^{-1} , while a peak at 1470 cm^{-1} originated from C-H bending. We note that upon weathering, there were not any considerable changes to the microplastics with regards to the chemical functional groups observed. The FTIR spectra of the filtered HDPE suspension confirmed that any sub-200 nm particles found

in the HDPE suspension were, despite having a weaker signal, showing the same distinctive peaks as HDPE.

5.3.3 Developmental toxicity

Various endpoints can be measured to evaluate the toxicity of a substance on an organism. A major factor contributing to the popularity of *Drosophila melanogaster* as a model organism is its rapid development time from egg to adult. To measure the toxicity of HDPE microplastics on the development of *Drosophila melanogaster*, batches of approximately 20 first instar larvae, were transferred to test tubes containing HDPE microplastics in concentrations of 0.1, 1, 10, and 100 mg/kg food, and in a separate set of experiments, HDPE concentrations of 1000 and 10 000 mg/kg food. Both sets of experiments had their respective controls and were conducted separately from each other.

Of interest was the number of pupae and adult flies that emerged from these larvae (14 days after the laying of eggs), and the amount of time it would take for them to reach the pupal and adult stage in their development cycle. Figures 5.2a and b show that there were no significant differences in the total number of pupae or flies that emerged from the larvae in the HDPE concentration range of 0 – 100 mg/kg. The result is particularly meaningful since a two-way ANOVA revealed that no significant differences based on concentration were detected in the total pupae ($p=0.174$) or flies ($p=0.133$), even after accounting for significant differences based on experimental block in the total pupae ($p=0.011$) and flies ($p=0.006$). Similarly, at 0, 1000 and 10 000 mg/kg HDPE in food, Figures 5.3a and b showed no significant differences on the basis of concentration (total pupae: $p=0.079$; total flies: $p=0.606$) or experimental block (total pupae:

p=0.267; total flies: p=0.219). This shows that even at concentrations as high as 1 wt% HDPE microplastic in food, no toxicity was observed even with a sample size of N=12.

Another useful metric is the eclosion fraction which measures the fraction of pupae that successfully eclose into adult flies. An eclosion fraction considerably lower than 1 could indicate that the *Drosophila melanogaster* are having trouble completing their development, resulting in death at the pupal stage. Given that there were no significant differences observed in the total number of pupae and flies, it is not surprising that there were also no significant differences in the eclosion fraction (Figure S5.2) based on concentration or experimental block in the 0 – 100 mg/kg HDPE set (concentration: p=0.249; block: p=0.596) and the 0, 1000, and 10 000 mg/kg set (concentration: p=0.538; block: p=0.278). In general, the eclosion fractions were high at all concentrations with mean values in the range of 0.97 – 1.00, suggesting that the eclosion of *Drosophila melanogaster* is unaffected by HDPE microplastics at concentrations as high as 10 000 mg/kg.

The data in the developmental toxicity assay was collected every two days over 14 days, allowing for the calculation of mean emergence times. Figures 5.2c and d show that there were no significant differences in the mean pupation or eclosion time of larvae in the HDPE concentration range of 0 – 100 mg/kg on the basis of concentration (pupation: p=0.783; eclosion: p=0.070) or experimental block (pupation: p=0.091; eclosion: p=0.389). Similarly, at 0, 1000, and 10 000 mg/kg HDPE in food, Figures 5.3c and d showed no significant differences on the basis of concentration (pupation: p=0.687; eclosion: p=0.077) or experimental block (pupation: p=0.584; eclosion: p=0.462).

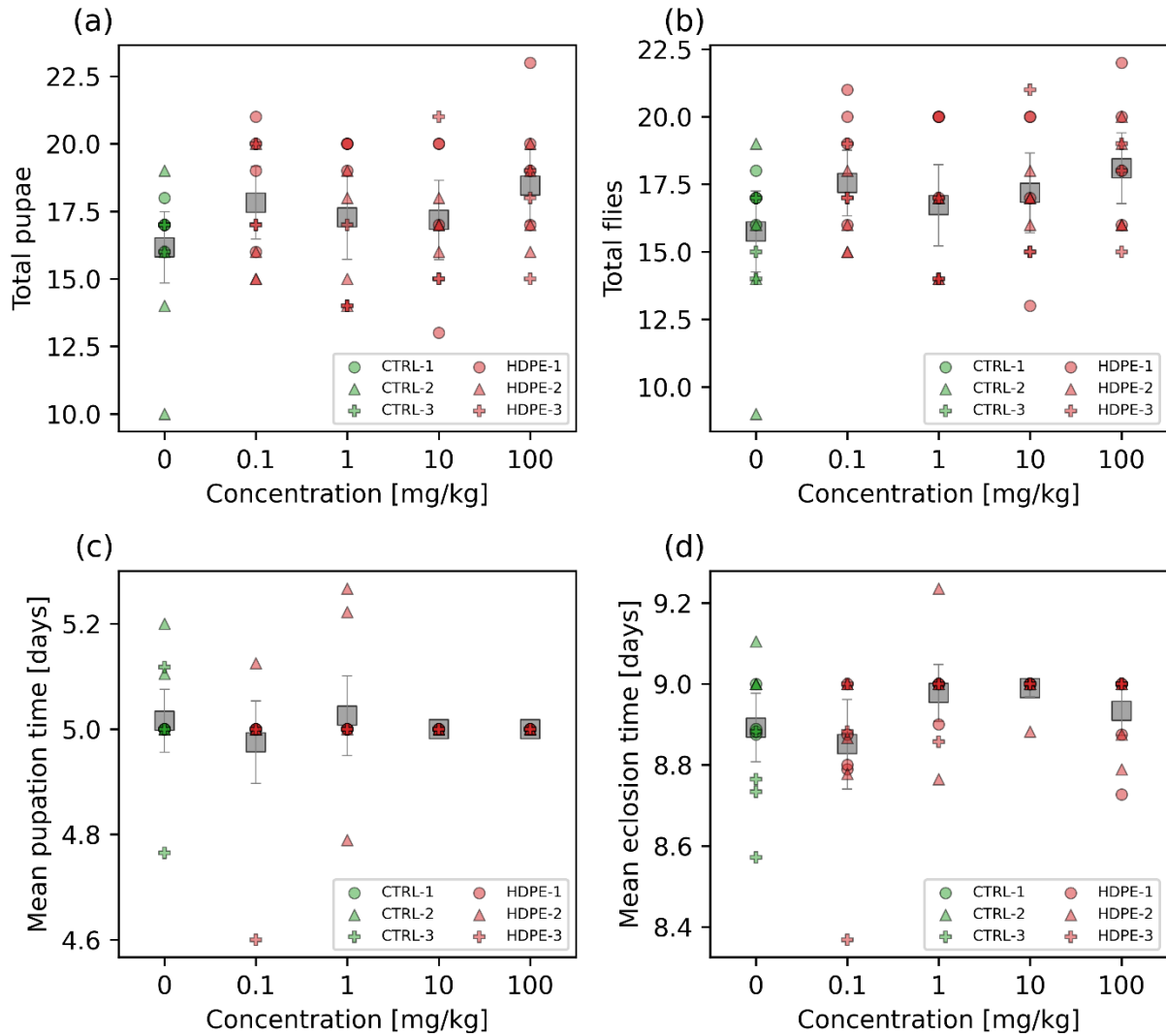


Figure 5.2. Total number of (a) pupae and (b) flies that emerged from approximately 20 *Drosophila melanogaster* 1st instar larvae raised in control (CTRL) food or food containing 0.1, 1, 10, or 100 mg HDPE microplastics per kg food. Mean (c) pupation and (d) eclosion time of the same eggs described in (a) and (b), respectively. Legend labels are formatted as X-Y, where X is the treatment, and Y is the experimental block ID. Grey squares represent the mean value of all markers that appear in that column and error bars represent 2 × the standard error of the mean.

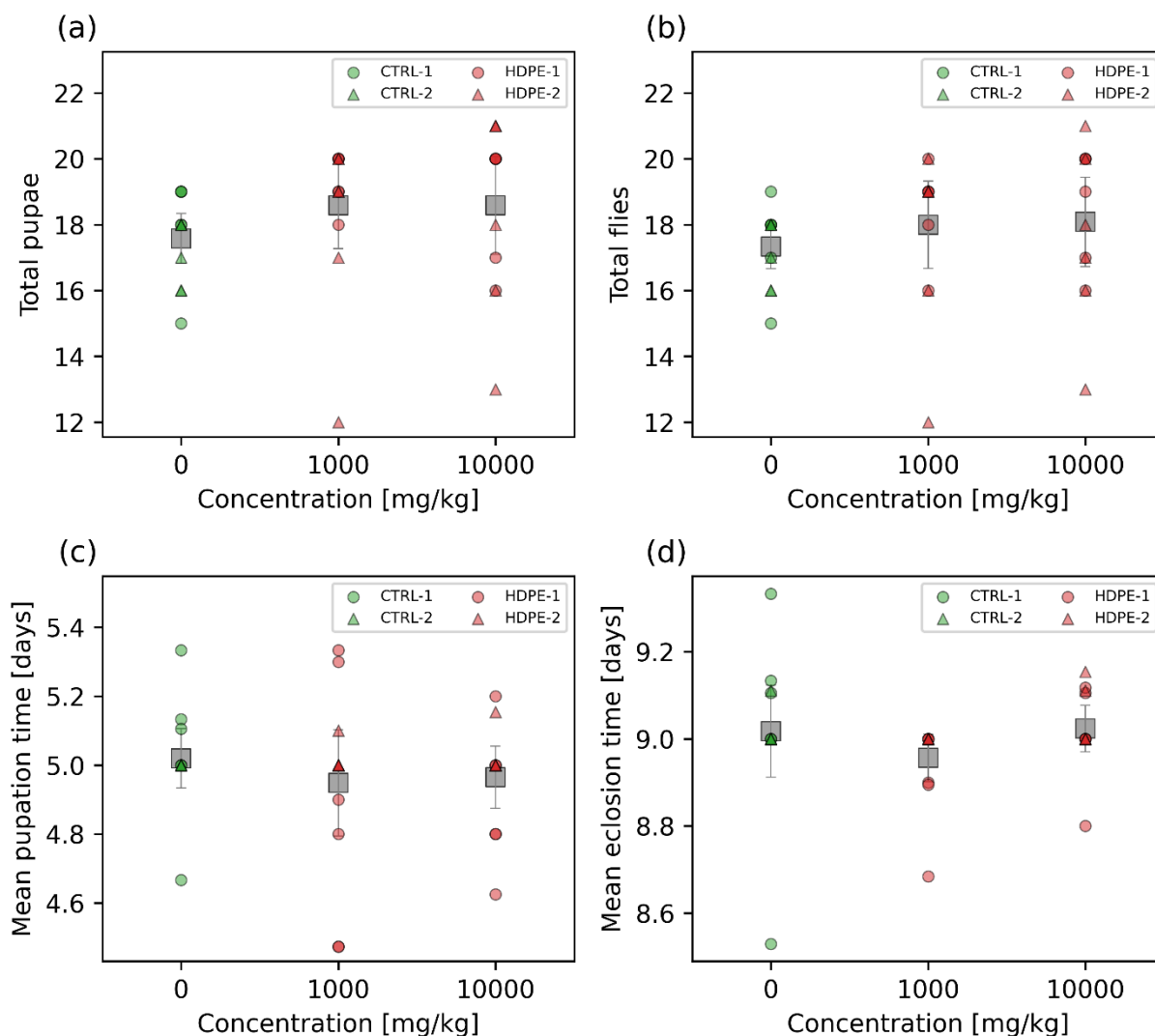


Figure 5.3. Total number of (a) pupae and (b) flies that emerged from approximately 20 *Drosophila melanogaster* 1st instar larvae raised in control (CTRL) food or food containing 1000 or 10 000 mg HDPE microplastics per kg food after 14 days. Mean (c) pupation and (d) eclosion time of the same eggs described in (a) and (b), respectively. Legend labels are formatted as X-Y, where X is the treatment, and Y is the experimental block ID. Grey squares represent the mean value of all markers that appear in that column and error bars represent $2 \times$ the standard error of the mean.

Other groups have also studied the developmental toxicity of microplastics over a variety of plastic types, sizes, and concentrations. A study whereby *Drosophila melanogaster* were raised

from egg to adult fly in 4, 10, or 20 μm polystyrene microplastics in concentrations ranging from 2.604 – 2604 mg/kg food found that the viability of the eggs decreased as concentration increased with all sizes.²⁴ At the highest concentration, the viability of the eggs dropped from 100 % in the control to 76 %, 82 %, and 87 %, when exposed to 4, 10, and 20 μm polystyrene microplastics, respectively, however, we note that the study concluded that this was nontoxic.²⁴ A study by Liu *et al.* found that exposing *Drosophila melanogaster* to 0.1 μm amino-functionalized polystyrene particles at a concentration of 50 $\mu\text{g/L}$ resulted in no significant differences in the fraction of embryos that successfully developed into pupae or flies compared to the control.²⁵ Likewise, the results of our developmental toxicity assay showed that the HDPE microplastics, at concentrations as high as 10 000 mg/kg, had no measurable impact on the mortality or development time of larvae as they transform into pupae and then adults during the first 14 days of their life.

5.3.4 Multigenerational reproductive assay

When testing a substance for toxicity, it is important to investigate long-term effects, especially when acute exposure shows no signs of toxicity. The developmental toxicity study looked at toxicity over the first 14 days after the eggs were laid. Since no mortality or developmental delays were observed, we now look over a longer time span. Multigenerational assays can sometimes detect toxicity at concentrations that are otherwise too low to show acute toxicity. For instance, Panacek *et al.* conducted a study evaluating the toxicity of silver nanoparticles on *Drosophila melanogaster*.¹³ They found that 10 mg/L silver nanoparticle exposure did not induce acute developmental toxicity.¹³ They then performed a multigenerational study using 5 mg/L silver nanoparticles and observed no toxicity in the first generation, but a sharp decline in the number of flies eclosed in generations 2 – 4, recovery in generations 5 – 6, and

finally returning to levels seen in the control by generation 7.¹³ To measure the long-term toxicity of HDPE microplastics on the reproductive performance of *Drosophila melanogaster*, mating pairs, consisting of one female and one male fly that had eclosed less than 4 hours earlier, were transferred to test tubes containing control food or 100 mg/kg HDPE in food. The offspring of this mating pair were then put through the same process. This cycle was repeated for 4 generations. Three streams of food supply were set up for this assay (Table 5.1). Stream A consisted of control food throughout all 4 generations, while Stream B consisted of HDPE food throughout. Stream C featured the initial parent flies that were used to start the experiment raised on HDPE, while subsequent generations were fed control food. This was done to see if there would be any lingering effects even after the HDPE was no longer in the food supply.

Since we are transferring mating pairs, we are now shifting focus towards measuring their reproductive performance, rather than mortality. This is because we already know that 100 mg/kg HDPE in food is not known to impact the development of *Drosophila melanogaster*, therefore any differences in the number of pupae or flies that emerge would likely be due to differences in reproductive performance between the mating pairs in different streams or another unmeasured biological factor. From each generation, the total number of pupae and adult flies that would emerge from the eggs laid by their parents after 16 days was measured. Using a three-way ANOVA with stream, generation, and experimental block as factors, Figures 5.4a and b show that there were no significant differences in the total number of pupae (stream: $p=0.712$; generation: $p=0.339$; block: $p=0.129$) or flies (stream: $p=0.493$; generation: $p=0.233$; block: $p=0.214$) that emerged throughout the assay. Interestingly, significant differences in the eclosion fraction (stream: $p=0.011$; generation: $p=0.332$; block: $p=0.052$) were observed based on stream, but not generation or experimental block (Figure S5.3). A post hoc analysis showed that stream B

(eclosion fraction=0.929) had a significantly higher eclosion fraction ($p<0.05$) than stream A (eclosion fraction=0.879) when pooling data from all generations and blocks. However, we note that the total sample size of all stream A and B samples throughout the experiment was high ($N=83$). Therefore, it is important to compare the magnitude of these differences which shows that the eclosion fraction of stream B is only 5.73 % higher than stream A. This relatively small increase in the context of seeing no significant differences in the total number of pupae and flies would suggest that changes in the eclosion fraction are unlikely to be part of a larger trend, especially when Figure S5.3 shows that most of this difference arose from Stream A – Generation 3 having a lower eclosion fraction than most treatments.

The data in the multigenerational reproductive assay was collected every two days over a period of 16 days allowing for the calculation of the mean emergence time of the pupae and flies. Significant differences in the mean pupation time (stream: $p=0.214$; generation: $p=7.55\times 10^{-5}$; block: $p=2.77\times 10^{-3}$) and mean eclosion time (stream: $p=0.104$; generation: $p=9.66\times 10^{-7}$; block: $p=7.44\times 10^{-3}$) were observed on the basis of generation and experimental block, but not stream (Figures 5.4c and d). Post hoc analysis revealed that these differences typically arose from generation 1 having a faster pupation and eclosion time than the other generations.

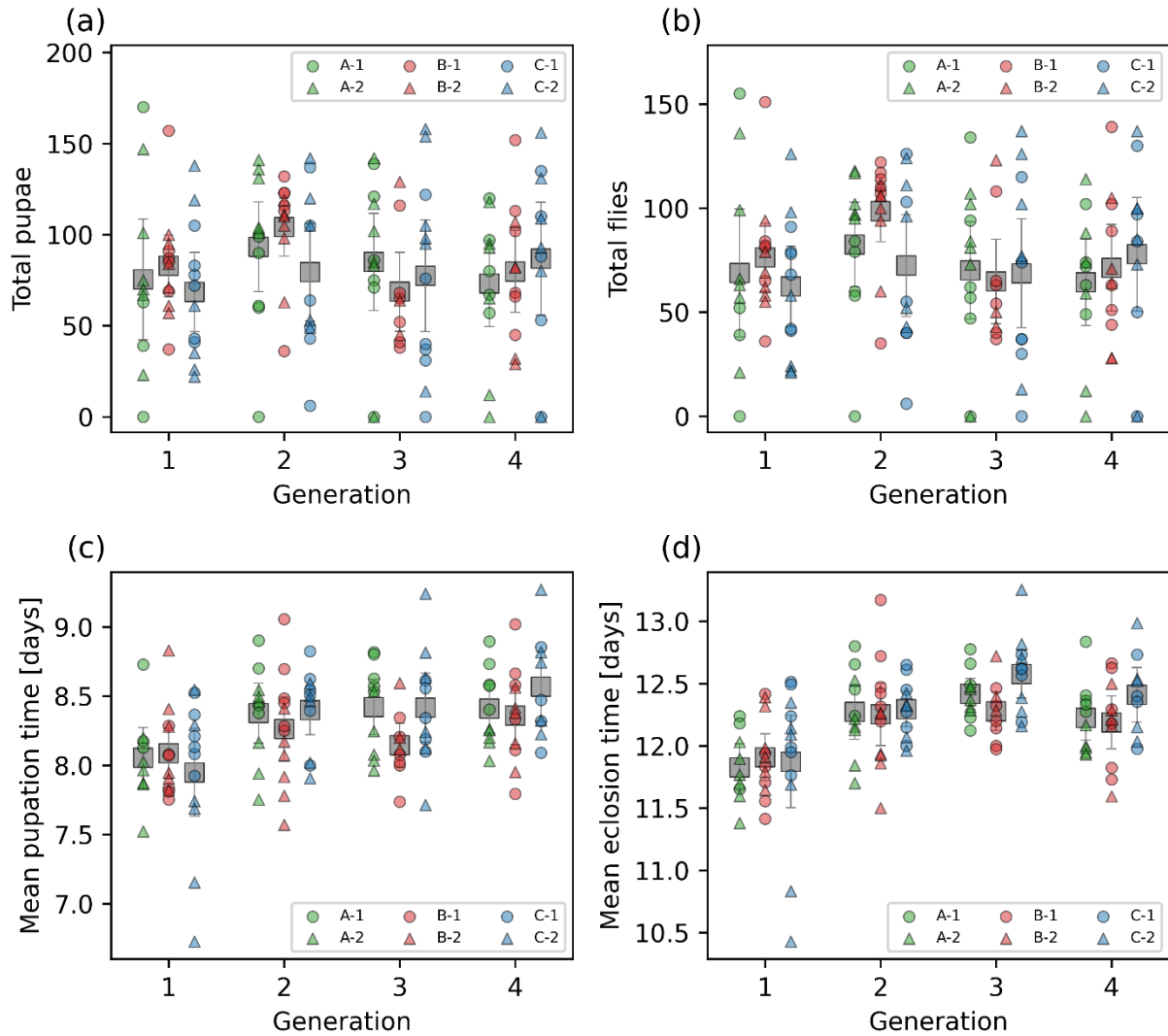


Figure 5.4. Total number of (a) pupae and (b) flies that emerged from eggs laid by a *Drosophila melanogaster* mating pair over 4 days. The eggs were laid and raised on control (CTRL) food or food containing 100 mg HDPE microplastics per kg food. The pupae and flies were monitored over 16 days starting when the mating pair was first isolated and transferred to their respective test tube. Mean (c) pupation and (d) eclosion time of the eggs described in (a) and (b), respectively. Legend labels are formatted as X-Y, where X is the stream ID as indicated in Table 5.1, and Y is the experimental block ID. Grey squares represent the mean value of all markers that appear in that column and error bars represent $2 \times$ the standard error of the mean. The flies were monitored over 4 generations.

Few studies exist examining the effect of microplastics on *Drosophila melanogaster* over multiple generations. Jimenez-Guri *et al.* exposed *Drosophila melanogaster* to control, 1 % polyethylene, and 1 % polyvinyl chloride (PVC) food during the first generation, but only control food in the second generation.²⁶ In the first generation, they observed no significant differences in the number of pupae, number of flies, eclosion fraction, mean pupation time, and mean eclosion time between treatments.²⁶ However, in the second generation, *Drosophila melanogaster*, with parents raised on polyethylene or PVC in the first generation, had significantly shorter pupal stages than those with parents raised on control food.²⁶ They also found that the number of flies in the second generation with parents raised on polyethylene was 76 % higher than those with parents raised on the control.²⁶ While their study showed a similar lack of any toxicity in the first generation, some effects were observed in the second generation. This may be due to differences in the size and concentration of the exposed particles. In our study, we use microplastics that are < 38 μm whereas Jimenez-Guri *et al.* used 23 – 500 μm particles, with 90 % being > 125 μm in size.²⁶ Likewise, they used a concentration of 1 % polyethylene corresponding to approximately 10 000 mg/kg compared to our study which used a concentration of 100 mg/kg.²⁶ Another study by Liu *et al.* found that exposing *Drosophila melanogaster* parental flies to 0.1 μm amino-functionalized polystyrene particles at a concentration of 50 $\mu\text{g/L}$ resulted in female flies laying fewer embryos.²⁵ However, no significant differences in the female or male fly mass of the offspring were observed compared to the control.²⁵ A study involving the exposure of *Drosophila melanogaster* to 2 μm polyethylene terephthalate (PET) microplastics found that a 20 g/L exposure resulted in a significant 50 % decrease in oviposition, whereas the decrease was not significant at 1 and 10 g/L.²⁷ This shows the importance of covering a wide range of sizes and concentrations when examining toxicity throughout the literature, and we believe our work adequately fills a

relevant knowledge gap on multigenerational toxicity of HDPE microplastics in *Drosophila melanogaster*.

Our results show that the HDPE microplastics are unlikely to affect the long-term reproductive performance of *Drosophila melanogaster* over multiple generations. Even when significant differences were observed, although small, it was a non-toxic response showing that pupae raised on HDPE microplastics had a higher eclosion fraction.

5.3.5 Sublethal toxicity assays

We have shown thus far that there was no observable negative impact of the HDPE microplastics at the concentrations tested on the development of larvae into pupae and flies, or the reproductive performance of the flies over 4 generations. For a comprehensive investigation of toxicity, we now turn to sublethal assays. These are assays that are designed to detect toxicity at concentrations that do not induce death (*i.e.*, sublethal) and would otherwise have been missed in assays that involve counting the total number of pupae or flies that emerge after exposure. In this work, we measured the locomotion of both larvae and adult flies and the mass of female and male flies. Figure 5.5a shows that there were no significant differences in the number of contractions per minute of larvae based on treatment ($p=0.716$) and experimental block ($p=0.795$). Here, the treatment refers to the control (CTRL) or 100 mg/kg HDPE microplastics food. There were no significant differences between CTRL and HDPE-fed flies ($p=0.056$) (Figure 5.5b) when measuring the fraction of flies which were able to climb 10 cm in 10 s or less, but there were differences between experimental blocks ($p=1.48\times 10^{-3}$). There were also no significant differences on the basis of treatment or experimental block, on the mass of female (treatment: $p=0.528$; block: $p=0.304$) (Figure 5.5c) or male (treatment: $p=0.488$, block: $p=0.359$) (Figure 5.5d) flies.

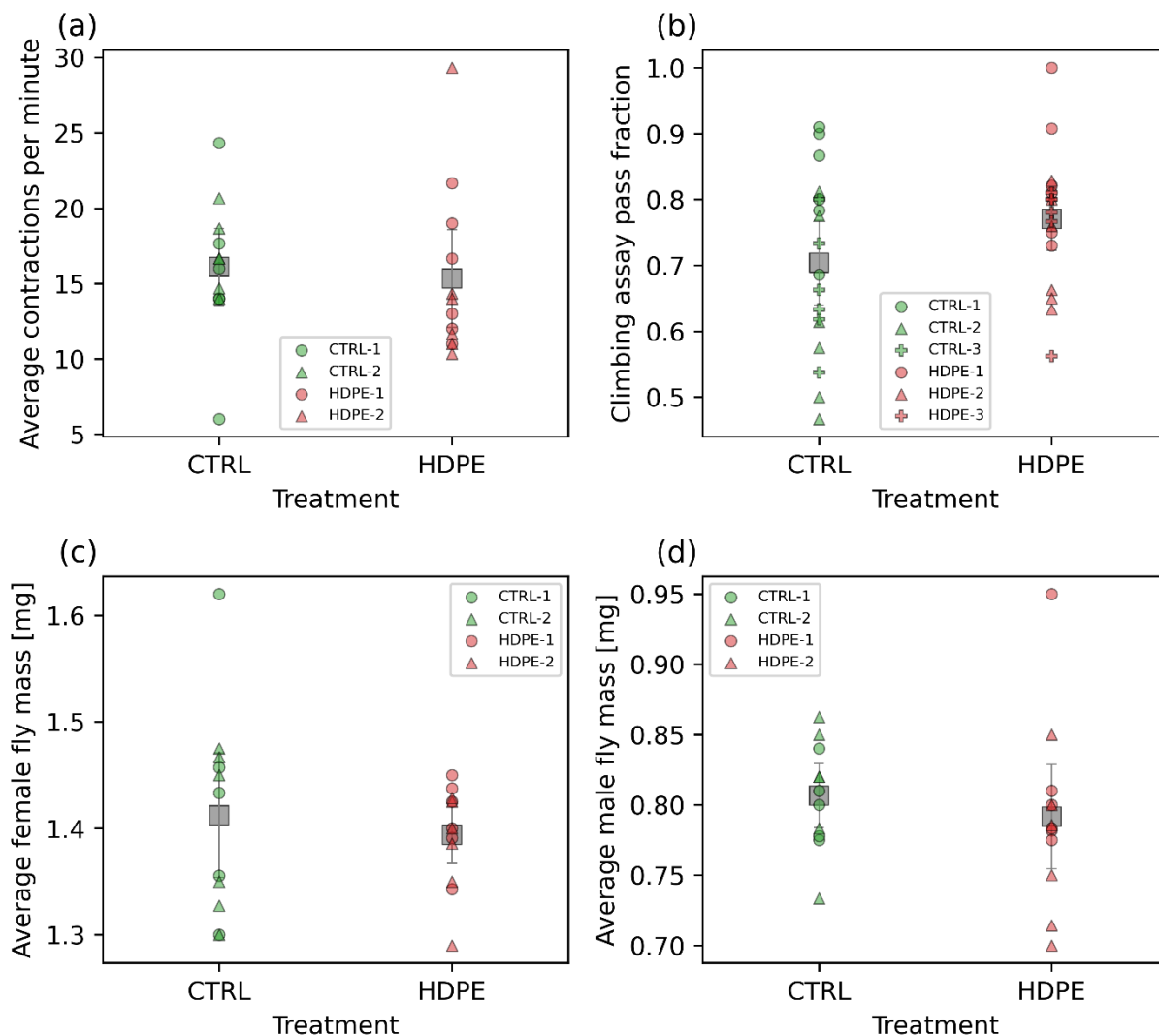


Figure 5.5. (a) Average number of contractions per minute for larvae. (b) The fraction of flies able to climb 10 cm within 10 s. The average mass of (c) female and (d) male flies. Larvae and flies were raised on control (CTRL) food or food containing 100 mg HDPE microplastics per kg food. Larvae were sampled 4 days after eggs were laid. Adult flies were sampled 11 days after eggs were laid. Legend labels are formatted as X-Y, where X is the treatment, and Y is the experimental block ID. Grey squares represent the mean value of all markers that appear in that column and error bars represent $2 \times$ the standard error of the mean.

The sublethal toxicity of microplastics in *Drosophila melanogaster* has also been documented previously in the literature. A study where *Drosophila melanogaster* were exposed to

4, 10, or 20 μm polystyrene microplastics for 7 days in concentrations ranging from 2.604 – 2604 mg/kg food found that the percentage of flies able to climb 7 cm in 10 s decreased as concentration increased with all sizes.²⁴ At the highest concentration, the climbing ability of the flies showed a significant decrease from 100 % in the control to 51 %, 56 %, and 59 %, when exposed to 4, 10, and 20 μm polystyrene microplastics, respectively.²⁴ At 1302 mg/kg, they still observed a significant decrease for all three microplastics, but the result was no longer significant at lower concentrations.²⁴ Similarly, we used < 38 μm HDPE microplastics at a lower concentration of 100 mg/kg food and saw no impact on the climbing ability of the flies. However, in another study, flies were exposed to 0.1 μm and 1 μm polystyrene plastic beads at a concentration of 200 mg/L for 7 days before evaluating their climbing ability.²⁸ Whereas 100 % of both male and female flies passed their climbing test (*i.e.*, ability to climb 9.5 cm within 120 s) in the control, only 80 % and 66 % of male and female flies, respectively, passed the test after exposure to the 0.1 μm polystyrene, and only 83 % and 68 % of male and female flies, respectively, passed the test after exposure to the 1 μm polystyrene.²⁸ The size of these plastic particles was considerably smaller than our work, as well as the concentration being approximately double the 100 mg/kg we used. Polystyrene is also chemically different from polyethylene and could have different biological effects as a result.

Overall, we saw no sublethal toxicity from the HDPE microplastics at a concentration of 100 mg/kg on the locomotion of larvae and flies, or the mass of female and male flies in our work.

5.3.6 Lightsheet fluorescence microscopy

To determine if the flies were able to uptake any HDPE microplastics, on day 10, female flies that were raised on control and 10 000 mg/kg HDPE were sampled for lightsheet imaging at

a later date. Figure 5.6 shows that there were no signs of internalization of the microplastics, whereby the majority of the red signal (representing HDPE) was found on the surface of the flies (Figure 5.6b). From Figure 5.1, it was apparent that the microplastics have many different shapes and sizes, and the varying degree to which they may aggregate creates further polydispersity. On a mass basis, most of the particles were likely large relative to the fly's mouth, meaning it may be possible for the flies to avoid ingestion of the larger particles. Conversely, on a number basis, the sub-micrometer-sized particles may form the majority, but their mass concentration may have been too low to be detected, or they might not necessarily accumulate in any internal tissues. These results are consistent with the overall lack of toxicity observed. Although surface contact of the HDPE microplastics occurred with the fruit fly, it was not a route of exposure capable of inducing observed toxicity.

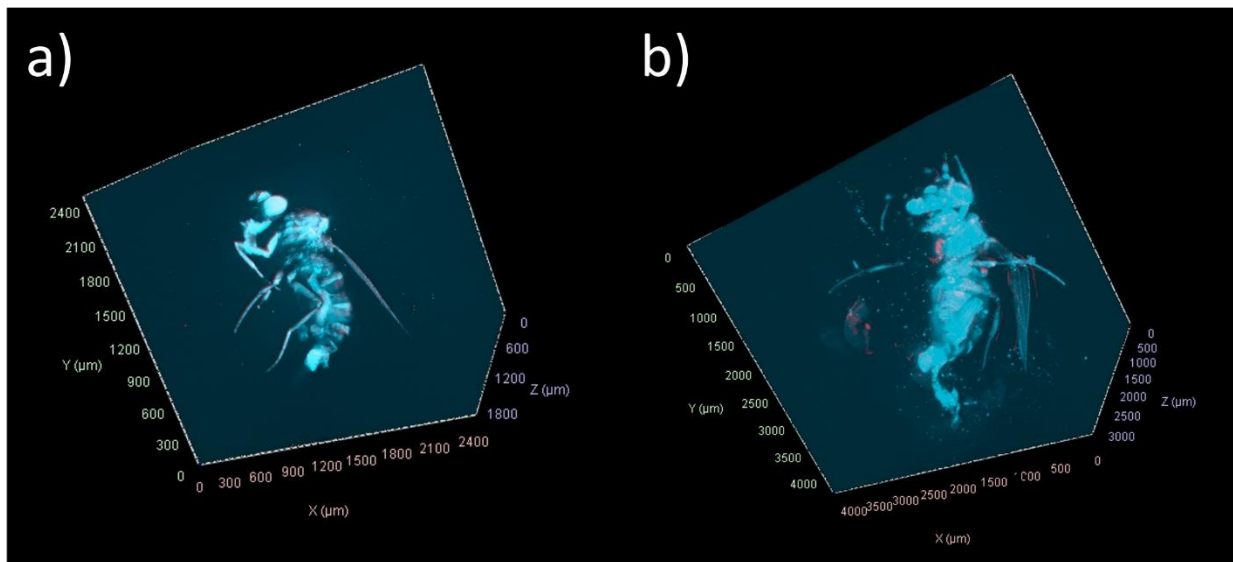


Figure 5.6. Lightsheet images of female flies (day 10) raised on (a) control and (b) 10 000 mg/kg HDPE food. The red signal represents HDPE and is found mainly on the surface of the flies.

5.4 Conclusions

Several assays were performed to measure the toxicity of HDPE microplastics (<38 μm) in the fruit fly, *Drosophila melanogaster*. The effect of the microplastics on the development of larvae into adult flies was measured in concentrations ranging from 0.1 to 10 000 mg/kg HDPE in food. No toxicity was observed in the number of pupae and flies that emerged, the eclosion fraction, or the mean pupation and eclosion time. Further assays were performed at 100 mg/kg HDPE to be more representative of HDPE concentrations found in the environment. The effects of chronic HDPE microplastic exposure on the reproductive performance of flies over four generations were evaluated. The presence of HDPE microplastics in the fly food had no effect on reproductive performance over the four generations observed in terms of the total number of pupae and flies that emerged, and the mean pupation and eclosion time. However, the eclosion fraction was 5.73 % higher ($p < 0.05$) in the stream of *Drosophila melanogaster* that were fed HDPE microplastics throughout all generations when compared to those that were always fed control food. To ensure that we did not miss certain sublethal toxic effects (*e.g.*, toxicity that is not severe enough to lead to a decline in the number of pupae and flies), the effect of the HDPE microplastics on the locomotion of larvae and adult flies and the mass of female and male flies was measured. No sublethal toxicity was observed on these endpoints after exposure to HDPE microplastics. Overall, the lack of toxicity is not unusual. For instance, Liang *et al.* exposed *Drosophila melanogaster* to 1 g/L polyethylene terephthalate microplastics (2 μm) and found that it lengthened the lifespan of male flies,²⁹ suggesting that not all microplastic effects on organisms are necessarily toxic.

We believe these results paint a comprehensive picture of the lack of toxicity from HDPE microplastics on *Drosophila melanogaster*. We used a wide range of concentrations in the

developmental toxicity assay to determine acute mortality while performing further tests at a more environmentally relevant concentration of 100 mg/kg HDPE in food to assess multigenerational and sublethal effects. Moreover, we performed our experiments in multiple blocks, which affords us greater confidence in stating that no significant toxicity was observed from the HDPE microplastics on *Drosophila melanogaster*.

Acknowledgements

The authors acknowledge financial support from the Natural Sciences and Engineering Research Council of Canada (NSERC) for the Discovery, Strategic, and PURE CREATE programs, the Canada Research Chairs Program, the Killam Research Fellowship, the Canada Foundation for Innovation, and the FRQNT. S. Chahal acknowledges NSERC for a PGS D scholarship, McGill University for a MEDA fellowship, the support of the EUL fund in the Department of Chemical Engineering, and EcotoQ. J.-R. M acknowledges an NSERC Postdoctoral Fellowship. The authors acknowledge Sara Matthews and Eva Roubeau Dumont for helpful discussions.

References

- (1) Geyer, R.; Jambeck, J. R.; Law, K. L. Production, use, and fate of all plastics ever made. *Science Advances* **2017**, *3* (7), e1700782. DOI: 10.1126/sciadv.1700782.
- (2) Zhang, K.; Hamidian, A. H.; Tubić, A.; Zhang, Y.; Fang, J. K. H.; Wu, C.; Lam, P. K. S. Understanding plastic degradation and microplastic formation in the environment: A review. *Environmental Pollution* **2021**, *274*, 116554. DOI: 10.1016/j.envpol.2021.116554.
- (3) Hale, R. C.; Seeley, M. E.; La Guardia, M. J.; Mai, L.; Zeng, E. Y. A Global Perspective on Microplastics. *Journal of Geophysical Research: Oceans* **2020**, *125* (1), e2018JC014719. DOI: 10.1029/2018JC014719.
- (4) Fuller, S.; Gautam, A. A Procedure for Measuring Microplastics using Pressurized Fluid Extraction. *Environmental Science & Technology* **2016**, *50* (11), 5774-5780. DOI: 10.1021/acs.est.6b00816.
- (5) Feng, S.; Lu, H.; Tian, P.; Xue, Y.; Lu, J.; Tang, M.; Feng, W. Analysis of microplastics in a remote region of the Tibetan Plateau: Implications for natural environmental response to human activities. *Science of The Total Environment* **2020**, *739*, 140087. DOI: 10.1016/j.scitotenv.2020.140087.
- (6) Ribeiro, F.; Garcia, A. R.; Pereira, B. P.; Fonseca, M.; Mestre, N. C.; Fonseca, T. G.; Ilharco, L. M.; Bebianno, M. J. Microplastics effects in *Scrobicularia plana*. *Marine Pollution Bulletin* **2017**, *122* (1), 379-391. DOI: 10.1016/j.marpolbul.2017.06.078.
- (7) Redondo-Hasselerharm, P. E.; Falahudin, D.; Peeters, E. T. H. M.; Koelmans, A. A. Microplastic Effect Thresholds for Freshwater Benthic Macroinvertebrates. *Environmental Science & Technology* **2018**, *52* (4), 2278-2286. DOI: 10.1021/acs.est.7b05367.

- (8) Paffenhöfer, G.-A.; Köster, M. The Effects of Microplastics on *Dolioletta gegenbauri* (Tunicata, Thaliacea). *Archives of Environmental Contamination and Toxicology* **2020**, *78* (1), 94-105. DOI: 10.1007/s00244-019-00676-z.
- (9) Jabeen, K.; Li, B.; Chen, Q.; Su, L.; Wu, C.; Hollert, H.; Shi, H. Effects of virgin microplastics on goldfish (*Carassius auratus*). *Chemosphere* **2018**, *213*, 323-332. DOI: 10.1016/j.chemosphere.2018.09.031.
- (10) Bringer, A.; Cachot, J.; Dubillot, E.; Prunier, G.; Huet, V.; Clérandeau, C.; Evin, L.; Thomas, H. Intergenerational effects of environmentally-aged microplastics on the *Crassostrea gigas*. *Environmental Pollution* **2022**, *294*, 118600. DOI: 10.1016/j.envpol.2021.118600.
- (11) Mak, C. W.; Ching-Fong Yeung, K.; Chan, K. M. Acute toxic effects of polyethylene microplastic on adult zebrafish. *Ecotoxicology and Environmental Safety* **2019**, *182*, 109442. DOI: 10.1016/j.ecoenv.2019.109442.
- (12) Ong, C.; Yung, L.-Y. L.; Cai, Y.; Bay, B.-H.; Baeg, G.-H. *Drosophila melanogaster* as a model organism to study nanotoxicity. *Nanotoxicology* **2015**, *9* (3), 396-403. DOI: 10.3109/17435390.2014.940405.
- (13) Panacek, A.; Pucek, R.; Safarova, D.; Dittrich, M.; Richtrova, J.; Benickova, K.; Zboril, R.; Kvitek, L. Acute and Chronic Toxicity Effects of Silver Nanoparticles (NPs) on *Drosophila melanogaster*. *Environmental Science & Technology* **2011**, *45* (11), 4974-4979. DOI: 10.1021/es104216b.
- (14) Gardette, M.; Perthue, A.; Gardette, J.-L.; Janecska, T.; Földes, E.; Pukánszky, B.; Therias, S. Photo- and thermal-oxidation of polyethylene: Comparison of mechanisms and

- influence of unsaturation content. *Polymer Degradation and Stability* **2013**, 98 (11), 2383-2390. DOI: 10.1016/j.polymdegradstab.2013.07.017.
- (15) Bartholomew, N. R.; Burdett, J. M.; VandenBrooks, J. M.; Quinlan, M. C.; Call, G. B. Impaired climbing and flight behaviour in *Drosophila melanogaster* following carbon dioxide anaesthesia. *Sci Rep* **2015**, 5, 15298-15298. DOI: 10.1038/srep15298 PubMed.
- (16) Matthews, S.; Xu, E. G.; Roubeau Dumont, E.; Meola, V.; Pikuda, O.; Cheong, R. S.; Guo, M.; Tahara, R.; Larsson, H. C. E.; Tufenkji, N. Polystyrene micro- and nanoplastics affect locomotion and daily activity of *Drosophila melanogaster*. *Environmental Science: Nano* **2021**, 8 (1), 110-121. DOI: 10.1039/D0EN00942C.
- (17) Feany, M. B.; Bender, W. W. A *Drosophila* model of Parkinson's disease. *Nature* **2000**, 404 (6776), 394-398. DOI: 10.1038/35006074.
- (18) Hama, H.; Hioki, H.; Namiki, K.; Hoshida, T.; Kurokawa, H.; Ishidate, F.; Kaneko, T.; Akagi, T.; Saito, T.; Saido, T.; et al. ScaleS: an optical clearing palette for biological imaging. *Nature Neuroscience* **2015**, 18 (10), 1518-1529. DOI: 10.1038/nn.4107.
- (19) Harris, C. R.; Millman, K. J.; van der Walt, S. J.; Gommers, R.; Virtanen, P.; Cournapeau, D.; Wieser, E.; Taylor, J.; Berg, S.; Smith, N. J.; et al. Array programming with NumPy. *Nature* **2020**, 585 (7825), 357-362. DOI: 10.1038/s41586-020-2649-2.
- (20) McKinney, W. Data Structures for Statistical Computing in Python. In *Python in Science*, Austin, Texas, June 28 - July 3, 2010; van der Walt, S., Millman, J., Eds.; 2010; Vol. 445, pp 56 - 61. DOI: 10.25080/Majora-92bf1922-00a.
- (21) Virtanen, P.; Gommers, R.; Oliphant, T. E.; Haberland, M.; Reddy, T.; Cournapeau, D.; Burovski, E.; Peterson, P.; Weckesser, W.; Bright, J.; et al. SciPy 1.0: fundamental

- algorithms for scientific computing in Python. *Nature Methods* **2020**, *17* (3), 261-272.
DOI: 10.1038/s41592-019-0686-2.
- (22) Seabold, S.; Perktold, J. Statsmodels: Econometric and statistical modeling with python. In *Proceedings of the 9th Python in Science Conference*, Austin, TX, 2010; Vol. 57, p 61.
- (23) Hunter, J. D. Matplotlib: A 2D Graphics Environment. *Computing in Science & Engineering* **2007**, *9* (3), 90-95. DOI: 10.1109/MCSE.2007.55.
- (24) Demir, E. Adverse biological effects of ingested polystyrene microplastics using *Drosophila melanogaster* as a model *in vivo* organism. *Journal of Toxicology and Environmental Health, Part A* **2021**, *84* (16), 649-660. DOI: 10.1080/15287394.2021.1913684.
- (25) Liu, H.-P.; Cheng, J.; Chen, M.-Y.; Chuang, T.-N.; Dong, J.-C.; Liu, C.-H.; Lin, W.-Y. Neuromuscular, retinal, and reproductive impact of low-dose polystyrene microplastics on *Drosophila*. *Environmental Pollution* **2022**, *292*, 118455. DOI: 10.1016/j.envpol.2021.118455.
- (26) Jimenez-Guri, E.; Roberts, K. E.; García, F. C.; Tourmente, M.; Longdon, B.; Godley, B. J. Transgenerational effects on development following microplastic exposure in *Drosophila melanogaster*. *PeerJ* **2021**, *9*, e11369. DOI: 10.7717/peerj.11369.
- (27) Shen, J.; Liang, B.; Zhang, D.; Li, Y.; Tang, H.; Zhong, L.; Xu, Y. Effects of PET microplastics on the physiology of *Drosophila*. *Chemosphere* **2021**, *283*, 131289. DOI: 10.1016/j.chemosphere.2021.131289.
- (28) Zhang, Y.; Wolosker, M. B.; Zhao, Y.; Ren, H.; Lemos, B. Exposure to microplastics cause gut damage, locomotor dysfunction, epigenetic silencing, and aggravate cadmium (Cd) toxicity in *Drosophila*. *Science of The Total Environment* **2020**, *744*, 140979. DOI: 10.1016/j.scitotenv.2020.140979.

- (29) Liang, B.; Zhang, D.; Liu, X.; Xu, Y.; Tang, H.; Li, Y.; Shen, J. Sex-specific effects of PET-MPs on *Drosophila* lifespan. *Archives of Insect Biochemistry and Physiology* **2022**, *110* (3), e21909. DOI: 10.1002/arch.21909.

Supplementary information

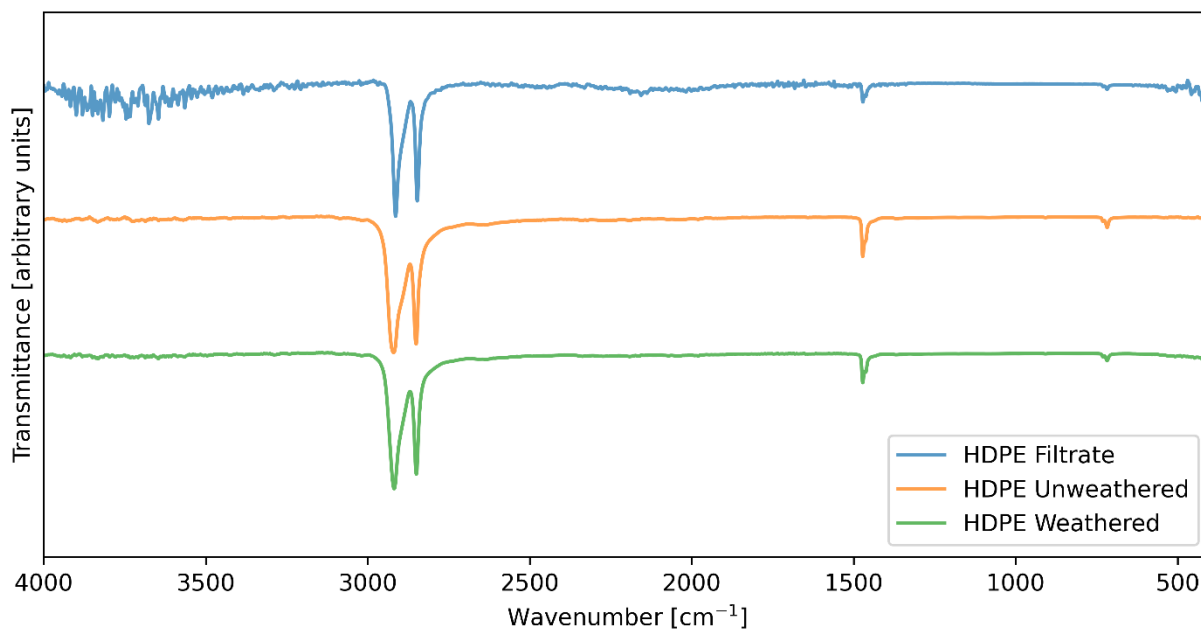


Figure S5.1. FTIR spectra from: HDPE suspension filtrate which passed through a 0.2 μm filter, unweathered HDPE microplastics, and UV weathered HDPE microplastics. The spectra of all samples were virtually identical and consistent with the spectra for HDPE. “HDPE Unweathered” and “HDPE Weathered” spectra were measured three times and one spectra from each was selected to show here as a representative sample. “HDPE Filtrate” spectra was measured once.

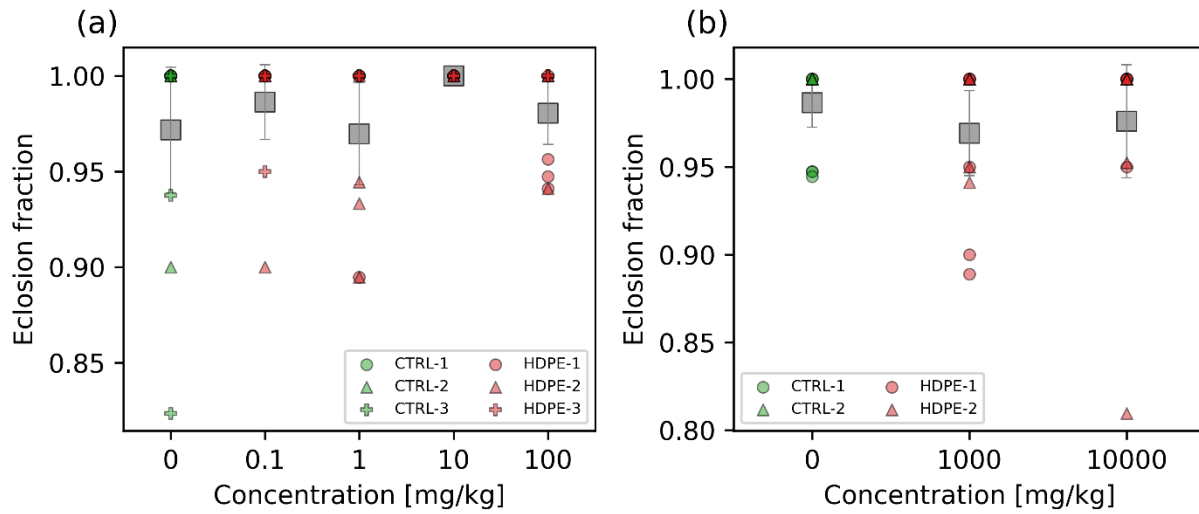


Figure S5.2. Eclosion fraction of *Drosophila melanogaster* that were raised on (a) 0, 0.1, 1, 10, or 100 mg/kg HDPE microplastics and (b) 0, 1000, or 10 000 mg/kg HDPE microplastics. Legend labels are formatted as X-Y, where X is the treatment, and Y is the experimental block ID. Grey squares represent the mean value of all markers that appear in that column and error bars represent $2 \times$ the standard error of the mean. Eclosion fraction is defined here as the fraction of pupae that successfully eclosed into adult flies.

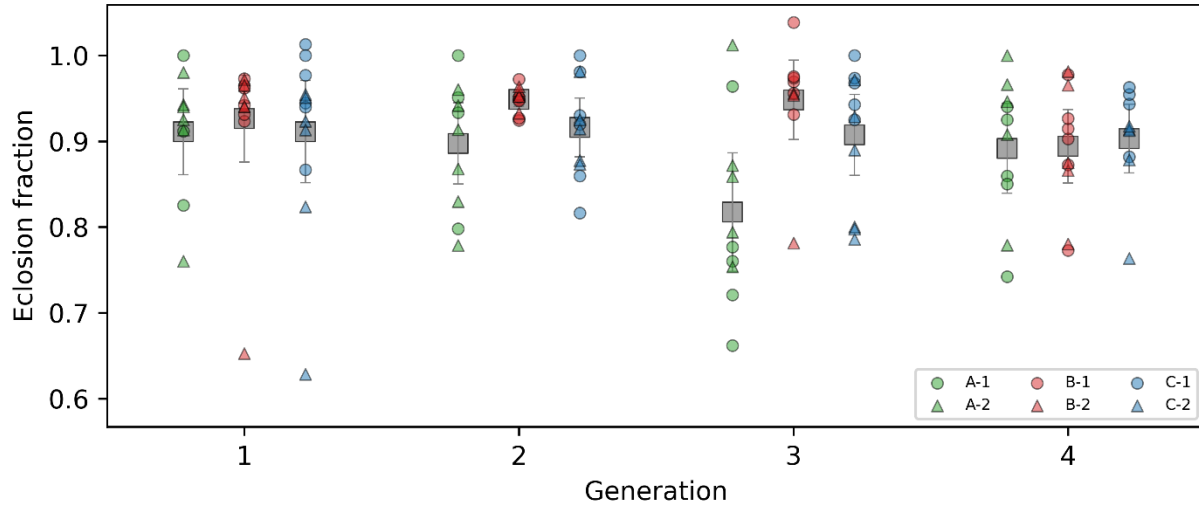


Figure S5.3. Eclosion fraction of *Drosophila melanogaster* that were raised on three streams of food treatments (Table 5.1). Legend labels are formatted as X-Y, where X is the stream ID as indicated in Table 5.1, and Y is the experimental block ID. Grey squares represent the mean value of all markers that appear in that column and error bars represent $2 \times$ the standard error of the mean. The flies were monitored over 4 generations. Eclosion fraction is defined here as the fraction of pupae that successfully eclosed into adult flies.

Preamble to Chapter 6

In Chapter 5, we evaluated the toxicity of HDPE microplastics in an animal organism. Both acute and chronic multigenerational toxicity were measured and no toxicity from the HDPE microplastics was found in *Drosophila melanogaster*. To conclude the research component of this thesis, we expand our evaluation of HDPE microplastic toxicity to strawberry plants and soil microorganisms. Moreover, the study was conducted outdoors over the span of two years to truly evaluate long term effects in a real-world environment. The HDPE microplastics used in Chapter 6 were sourced from the same HDPE sheet as those used in Chapter 5. Considering that no direct toxicity was previously observed from these HDPE microplastics, we also decided to evaluate if they can amplify or inhibit the ability of pharmaceutically active compounds to alter the soil microbial community composition. To summarize, in Chapter 6 we examined the effect of HDPE microplastics and pharmaceutically active compounds on soil microbial community composition, soil enzyme activity, and strawberry plant growth. A key finding from this chapter was that although the pharmaceutically active compounds, consisting of a variety of common household drugs and antibiotics, were able to alter the composition of the microorganisms found in the soil microbial community, they were unable to do so in the presence of 100 mg/kg HDPE microplastics in soil. This shows the importance of evaluating not only the direct toxicity of microplastics, but also their interaction with other emerging contaminants that may be present in the system being assessed. We also showed that no toxicity was observed towards strawberry plant growth and soil enzyme activity, and that the HDPE microplastics alone were unable to directly alter the microbial community composition of the soil.

Chapter 6: Effect of emerging contaminants on soil microbial community composition, soil enzyme activity, and strawberry plant growth in polyethylene microplastic-containing soils

Abstract

Microplastic pollution is commonly found in terrestrial ecosystems, yet few studies have investigated their impact on agricultural soils. Herein, we examine the effects of eight common pharmaceutically active compounds typically found in wastewater (*i.e.*, acetaminophen, caffeine, carbamazepine, gemfibrozil, ibuprofen, sulfamethoxazole, sulfanilamide, and triclosan) and high-density polyethylene (HDPE) microplastics (<1 mm) on soil microbial community composition, soil enzyme activity, and strawberry plant growth in a two-year outdoor study conducted near Montreal, Canada. We found that the pharmaceutically active compounds were able to alter the soil microbial community composition but were unable to do so in the presence of 100 mg/kg HDPE microplastics. This suggests that HDPE microplastics may mitigate the impact of pharmaceutically active compounds on the soil microbial community. Conversely, no significant differences among treatments were observed in the Shannon's diversity index of the soil microbial community throughout the study. Significant differences in the soil enzyme activity among treatments were rare. At the end of each year's growing season, there were no significant differences in the dry plant biomass, strawberry yield, and the number of leaves and flower stalks between treatments. While many of the endpoints measured showed no significant differences between treatments, we believe that sharing the results of this two-year study, performed outdoors using environmentally relevant concentrations, is important to prevent a biased literature and the repetition of resource intensive experiments.

6.1 Introduction

The occurrence of microplastics (plastic particles less than 5 mm in size) in our terrestrial and aquatic systems is an environmental problem that is expected to persist even if global plastic use were to end.¹ A survey by Machado *et al.* found that less than 10 % of scientific publications on microplastic pollution focused on terrestrial systems whereby most studies focused on aquatic systems.² Meanwhile, in Europe, it is estimated that 4 – 23 times as much plastic waste is released into continental environments when compared to oceans.³ Microplastics have even been found in remote catchments of the Pyrenees mountain range and have been shown to travel up to 95 km *via* atmospheric transport.⁴ A survey of soils from an industrial area in Sydney, Australia, found that microplastic concentrations varied from 300 to 67 500 mg kg⁻¹.⁵ Moreover, besides landfills, urban areas, and beaches, agroecosystems are suspected to be the most plastic-contaminated terrestrial system.⁶ For instance, Piehl *et al.* measured the quantity of microplastics found in agricultural soils in which microplastic-containing fertilizers and plastic applications were never used and found 0.34 microplastic particles per kg dry soil, with polyethylene being the most common plastic.⁷ They hypothesized that plastics may have entered the field through manure or atmospheric transport of plastic litter which then degraded into microplastics over time. In general, microplastic concentrations in the environment vary greatly. A study measuring microplastic concentrations in floodplain soils from 29 locations across Switzerland determined that the average microplastic concentration in the soils was 5 mg kg⁻¹, but could reach as high as 55.5 mg kg⁻¹.⁸ Despite increasing evidence that microplastics are ubiquitous in terrestrial environments, there is little work being done to determine their environmental and socioeconomic consequences.⁹

Agricultural soils can be contaminated with microplastics either directly (*e.g.*, plastic mulch films) or indirectly (*e.g.*, biosolids application).¹ Plastic mulch films with a thickness of ~10

µm are used to cover agricultural fields to help regulate soil temperatures, retain soil moisture, and control the growth of weeds.⁶ While these plastic mulch films are present on agricultural fields, they may degrade into microplastics through abrasion and erosion.⁹ Earthworms have also been shown to break down microplastics into even smaller microplastics, likely through ingestion.¹⁰ UV irradiation is also known to physically and chemically degrade certain plastics into microplastics,⁹ which causes anionic or other polar groups to form on their surface, increasing their potential to interact with soil and other compounds or ions.⁶ For instance, polyethylene microplastics have been shown to sorb polychlorinated biphenyls and polycyclic aromatic hydrocarbons.¹¹ Potential human pathogens, such as *Vibrio parahaemolyticus*, have also been observed on various types of microplastics.¹²

Biosolids application and the use of wastewater for irrigation of agricultural soils are also becoming increasingly common.¹³ Microplastics that enter wastewater treatment plants generally end up in the settled sludge which is then applied to agricultural soils as a fertilizer in the form of biosolids.^{14, 15} Nizzetto *et al.* estimated that 107 000 to 730 000 tonnes of microplastics make their way into agricultural soils through biosolids every year in North America and Europe.¹⁶ Similarly, several emerging chemical contaminants are often present in wastewater and end up in biosolids.¹³ The behaviour of these contaminants may differ in the presence of plastic particles. For example, Liu *et al.* found that polystyrene nanoplastics were able to enhance the transport of nonpolar and weakly polar compounds in soil, while polar compound transport was unaffected.¹⁷ Similarly in our work, we chose chemical contaminants that cover a wide range of polarities to investigate their ability to impact the soil ecosystem in the absence or presence of high-density polyethylene (HDPE) microplastics.

Microorganisms, such as bacteria and fungi, are an important source of soil enzymes.¹⁸ Therefore, it is important to measure changes to the soil microbial community, in conjunction with soil enzyme activity, to determine if they play any role in observed changes in plant growth. Soil enzyme activity has long been used as a measure of soil health due to the importance of extracellular soil enzymes in the carbon, nitrogen, sulfur, and phosphorus cycles.¹⁸ For instance, β -glucosidase (EC 3.2.1.21) is responsible for the degradation of organic matter and plant residues; in particular, it degrades cellulose, providing the soil microbial community with simple sugars.¹⁹ Likewise, chitinase (EC 3.2.1.14) degrades chitin.²⁰ Xylan 1,4- β -xylosidase (EC 3.2.1.37) is involved in hemicellulose degradation.²¹ Alkaline (EC 3.1.3.1) and acid (EC 3.1.3.2) phosphatase are responsible for the degradation of organophosphates.^{22, 23} Monitoring changes in the soil microbial community composition and soil enzyme activity over time will allow us to gain a deeper understanding of how selected emerging, pharmaceutically-active contaminants can affect the soil ecosystem and strawberry plant growth in the presence and absence of HDPE microplastics.

Herein, we report our findings on the effects of eight common wastewater chemical contaminants on soil microbial community composition, soil enzyme activity, and strawberry plant growth in HDPE microplastic-contaminated soil in a two-year outdoor study. The chemical contaminants covered a wide range of octanol-water partition coefficients, allowing them to interact, to varying degrees, with the components of the soil ecosystem, water, and microplastics. A unique aspect of our study is that the experiments were performed outdoors, and the soil was reused in the second year after being exposed to winter conditions near Montreal, Canada. Moreover, we measured the impact of these chemical contaminants on the soil ecosystem, in the presence and absence of HDPE microplastics, to determine if the microplastics can influence any effects of the chemical contaminants. We used microplastic concentrations that are typically found

in non-urban soils as these are more representative of the concentrations one may expect to find in agricultural soils. Strawberry plants were chosen because it is a high-value agricultural product. The global strawberry market had a compound annual growth rate of 5 % from 2007 to 2016.²⁴ The inherent variability of outdoor conditions (*e.g.*, changes in temperature, light, precipitation, the presence of animals, *etc.*) may make it difficult to characterize certain system responses which would otherwise have been detected in a controlled laboratory environment.

6.2 Experimental

6.2.1 Production of high-density polyethylene microplastics

High-density white polyethylene sheets (48" × 96" × 1/16", McMaster-Carr 8619K112) were cut into strips of approximately 15 cm × 3 cm and washed with 70 v/v% ethanol and rinsed with reverse osmosis water (Type II, >1 MΩ) (Mar Cor Purification reverse osmosis water purifier). In a single batch, three strips were placed in a 500 W glass blender (T-fal Blendforce) and the blender was filled with water until the HDPE strips were approximately half submerged. The blender was then operated in pulse mode for up to 10 min or until there was no further visible degradation of the HDPE strips. The contents of the blender were then passed through a ~1 mm stainless steel mesh into a clean glass tray. The HDPE microplastics floated as a thin layer on the water in the glass tray. To retrieve the HDPE microplastics, a scoop made from the same HDPE sheet was used to skim the surface layer of HDPE microplastics off the water. An aluminum weighing tray was then used to scrape any HDPE microplastics off the scoop where they were left to dry in the dark at room temperature for several days until there was no more weight change so that the dry mass of the HDPE microplastics could be measured before application to soils. The HDPE microplastics

were also imaged using an Olympus SZX16 microscope to visualize the variety of microplastic shapes produced by the blending process.

To determine the mass-weighted size distribution in each year of the experiment, the dried HDPE microplastics were passed through a series of 500 μm , 250 μm , and 125 μm sieves. The mass of HDPE microplastics retained by each sieve was recorded.

6.2.2 Preparation of contaminated soils

Soil (sand: 30 %, silt: 31 %, clay: 38 %) was collected from an agricultural site at the Macdonald campus of McGill University (Sainte-Anne-de-Bellevue, Canada) and had a pH of 6.9 based on the pH of 8 g of soil in 40 mL of 0.01 M CaCl_2 solution.²⁵ Eight chemical contaminants known to be found in wastewater and covering a range of octanol-water partition coefficients (K_{ow}) were examined; namely, sulfanilamide ($\log K_{\text{ow}} = -0.62$),²⁶ caffeine ($\log K_{\text{ow}} = -0.07$),²⁶ acetaminophen ($\log K_{\text{ow}} = 0.46$),²⁷ sulfamethoxazole ($\log K_{\text{ow}} = 0.89$),²⁶ carbamazepine ($\log K_{\text{ow}} = 2.45$),²⁸ ibuprofen ($\log K_{\text{ow}} = 3.97$),²⁹ gemfibrozil ($\log K_{\text{ow}} = 4.24$),³⁰ and triclosan ($\log K_{\text{ow}} = 4.76$).³¹ To ensure the homogenization of these chemical contaminants in soil, 4.2 mL of a chemical contaminants stock solution (Table S6.1) containing these mixed contaminants in acetone was added to 220 g of soil in a glass beaker. For treatments without chemical contaminants, the stock solution consisted of only acetone. Additional acetone was then added until the soil was completely submerged and was then shaken to allow for mixing of the contaminants in the suspended soil. The mixture was left to dry overnight in a fume hood after which the acetone had evaporated, resulting in 220 g of contaminated dry soil. From this batch, 40 g of chemically contaminated (or control) dry soil would be added to ~18 kg of fresh uncontaminated soil as described in the following section.

6.2.3 Strawberry field experiment

Plant pots (length \times width \times height: 81 cm \times 22 cm \times 17 cm) were wrapped in aluminum with holes at the bottom for drainage. Pots were positioned in 6 rows and 5 columns in a randomized design. The treatments and controls were randomly distributed such that each column contained one pot from each treatment and two control pots. In early June 2018, 40 g of the dry soil as prepared in section 6.2.2 (with or without chemical contaminants) and 0, 180, or 1800 mg of HDPE microplastics were mixed with \sim 18 kg of fresh soil in each pot. The five treatments were: control (CTRL), 10 mg HDPE microplastic kg^{-1} soil (P10), 100 mg HDPE microplastic kg^{-1} soil (P100), chemical contaminants (C), and chemical contaminants + 100 mg HDPE microplastic kg^{-1} soil (CP100). The concentration, $\log K_{\text{OW}}$, molar mass, and chemical structure of the contaminants in C and CP100 soils are listed in Table S6.2. The soil was then transferred into an aluminum wrapped pot and these pots were placed \sim 1.5 m apart from each other. Each pot was elevated on a wooden platform that allowed for the collection of soil leachate from the bottom of each pot into a metal container. Four strawberry bare root plants (*Fragaria \times ananassa* cv. Seascape) (Production Lareault Inc.) were planted into each pot with two drip irrigation sources. Irrigation was applied on days with no rain, and fertilizers (Table S6.3) were applied twice a week through the irrigation system. In September 2018, the end of the first year's growing season, the strawberry plants were removed from the pots. The pots were then covered with aluminum foil and left outdoors. In June 2019, the start of the second year's growing season, the pots were uncovered, and the same treatments were reapplied to the same pots containing the same soil from the first year by removing the soil from the pot into a wheelbarrow and mixing in the respective amount of HDPE microplastics and/or chemical contaminants. Strawberry bare root plants were once again planted in the same manner as the previous year. A schematic diagram of the field

layout is shown in Figure S6.1. The placement of strawberry plants, drip irrigation, and soil sampling locations in each pot is shown in Figure S6.2.

6.2.4 Soil sampling

Soil was sampled vertically at three locations in each pot (Figure S6.2) while ensuring that ~24 h had passed since the last rainfall or irrigation. The three soil cores (diameter \times height: 1.5 cm \times 12 cm) were homogenized in an aluminum tray. Soil samples were then dried in an aluminum weighing tray overnight at room temperature. The soil was then passed through a 2-mm stainless steel sieve to remove any large materials such as rocks or plant roots. Soil for enzyme activity assays were used immediately. Soil for microbial community assays were stored at -80 °C until further use. Soil used for the detection of chemical contaminants was stored at -20 °C until further use. In each year, the soil was sampled just before the application (or reapplication for year 2) of treatments (*i.e.*, day 0), and after approximately 1 week, 1 month, 2 months, and 3 months. For contaminant concentration analysis in soil samples, the soil was sampled just after the application of the chemical contaminants at the start of each growing season to establish a starting point for C and CP100 samples relative to the CTRL.

6.2.5 Chemical contaminants analysis

Chemical contaminants were measured over time in two types of samples: 1) excess water that was released from holes at the bottom of the pot and subsequently captured (referred to as leachate samples), and 2) contaminants measured in soil samples.

The extraction of contaminants from leachate samples consisted of sampling directly in the field with a syringe, followed by filtration through a 0.22 μ m PTFE filter (polytetrafluoroethylene,

Chrom4; Thuringen, Germany) into HPLC amber glass vials (Agilent Technologies). The sample size on days 3, 8, 51, and 391 was N=3, whereas the sample size on days 366, 369, 372, and 377 was N=5.

The extraction of contaminants from soil samples consisted of shaking 1 g of soil in 2 mL of acetonitrile for 30 min, followed by centrifugation (2240 g, 5 min, 20 °C) and filtration of the supernatant through a 0.22 µm PTFE filter into HPLC glass vials. The sample size was N=3.

Samples were analyzed using a 1290 Infinity II LC System coupled with a 6545 Q-TOF mass spectrometer (Agilent Technologies) operating once in positive (ESI+) and again in negative (ESI-) electrospray ionization modes. The liquid chromatography separation was conducted on an InfinityLab Poroshell 120 (Phenyl-Hexyl, particle size: 2.7 µm, inner diameter: 3 mm, length: 100 mm, Agilent) fitted with an InfinityLab Poroshell 120 (EC-C18, particle size: 2.7 µm, inner diameter: 3 mm, length: 100 mm, Agilent) guard column. The mobile phase (0.4 mL min⁻¹) consisted of a mixture of water (solvent A) and acetonitrile:methanol (1:1 volume ratio, solvent B). Both solvents contained 5 mM ammonium acetate. In positive mode, 0-0.5 min: 99 % A; 0.5-2 min: B increased from 1 to 50 %; 2-4 min: B increased from 50 to 100 %; 4-8 min: 100 % B; 8-9 min: 99 % A. In negative mode, 0-0.5 min: 95 % A; 0.5-3 min: B increased from 5 to 100 %; 3-7 min: 100 % B, 7-9 min: 95 % A. The injection volume was 4 µL in ESI+ mode and 10 µL in ESI- mode. The column temperature was maintained at 30 °C. Nitrogen was used as the drying gas (positive mode: 150 °C, 11 L min⁻¹; negative mode: 175 °C, 10 L min⁻¹). The fragmentor voltage was 125 V. Mass spectrometry data was acquired in the 50-750 mass-to-charge ratio (*m/z*) range in the full scan mode. Any sample with a signal less than 3× the standard deviation of the blank was considered to be below the instrument detection limit (IDL). Any values recorded below the IDL were converted to IDL/2.

6.2.6 Soil microbial community composition

Microbial genomic DNA was extracted from soil (N=3) using a DNeasy PowerSoil Pro Kit (QIAGEN). Double stranded DNA concentration was then quantified using a Quant-iT PicoGreen dsDNA Assay Kit (Invitrogen) to ensure that the concentration of the samples met the submission requirements of Genome Quebec (Montreal, Canada). Polymerase chain reaction (PCR) was performed to amplify the extracted DNA and was sequenced using Illumina MiSeq (PE250) at Genome Quebec using the 515F (5'-GTGCCAGCMGCCGCGGTAA-3') and 806R (5'-GGACTACHVGGGTWTCTAAT-3') primers to target the V4 region of the 16S rRNA. Data from Genome Quebec was provided in FASTQ format. Analysis of FASTQ data was performed using Qiime2.³² The sequence of commands used in Qiime2 to process the data and calculate the weighted UniFrac distances (and its subsequent principal coordinate analysis (PCoA)), phylum-level taxonomy, and Shannon's diversity index can be found in Supplementary information – Qiime2 commands.

In addition to the previously mentioned treatments, a pseudo-treatment was formed from a composite sample of the uncontaminated soils (day 0), since they were sampled before any treatments were applied. This is referred to as pre-treatment (PRE) and was only used for the microbial community composition analysis.

6.2.7 Soil enzyme activity measurements

Soil enzyme activities were measured according to previously reported methods,^{33, 34} with some modifications. Dry soil (~1.6 g) was mixed into 50 mM sodium acetate buffer (pH 6.9, ~100 mL) in a glass jar such that the final concentration of soil in buffer was 16 g L⁻¹. The exact volume of buffer was based on the measured mass of the dry soil to ensure a consistent concentration

throughout experiments. The resulting soil slurry was placed on an orbital shaker at 240 rpm for 30 min and was then centrifuged at 4000 g for 2 min. This soil extract (*i.e.*, the supernatant) was then used for further analysis.

Soil extracts, containing the natural enzymes found in the soil, were mixed with 4-methylumbelliferone (MUB) or 4-methylumbelliferyl-linked substrates (MUB-substrates) (Table S6.4). Stock solutions of 5 mM MUB and 30 mM MUB-substrate were prepared in dimethyl sulfoxide and stored at 4 °C. The stock solutions were diluted in 50 mM sodium acetate buffer (pH 6.9) (hereafter referred to simply as “buffer”) to a concentration of 10 μM MUB and 200 μM MUB-substrate which was then used in the enzyme activity assay. In a 96-well black microplate (Corning Costar), 200 μL of soil extract was mixed with 50 μL of MUB, MUB-substrate, or buffer solution. To account for the fluorescence and fluorescence quenching effects of the soil extract, similar wells containing 200 μL buffer in place of soil extract were also prepared. The prepared plate was kept in darkness at room temperature for 2 h (while the soil enzymes catalyze their respective MUB-substrates), after which 10 μL of a 1 M NaOH solution was added to each well to enhance fluorescence. The plate was then immediately analysed in a Tecan Infinite m200 Pro microplate reader at excitation/emission wavelengths of 365/450 nm. The concentration of MUB in buffer at the time of measurement (*i.e.*, 1.92 μM) was shown to be within its linear fluorescence range (Figure S6.3). CTRL samples had a sample size of $N \leq 10$, whereas P10, P100, C, and CP100 treatments had a sample size of $N \leq 5$. A more detailed description of the enzyme activity calculation procedure can be found in Supplementary information - Calculation of enzyme activity.

6.2.8 Strawberry plant growth

Data was recorded from one plant in each pot (chosen from the middle). Plant parts were wrapped individually with aluminum foil and placed in a zippered storage bag. The samples were stored at -20 °C or lower. The fresh mass (marketable and non-marketable) of strawberry fruit produced by the plant over the course of the growing season was measured. The remaining plant biomass was dried, and the dry biomass was recorded. The number of leaves and flower stalks were counted every week. For the measurement of dry biomass (both years), strawberry yield (year 1) and the number of leaves (year 1) and flower stalks (year 1), CTRL samples had a sample size of N=6, whereas P10, P100, C, and CP100 treatments had a sample size of N=3. For the measurement of strawberry yield (year 2) and the number of leaves (year 2) and flower stalks (year 2), CTRL samples had a sample size of N=10, whereas P10, P100, C, and CP100 treatments had a sample size of N=5.

6.2.9 Statistical analysis

Data is reported as the mean \pm 2 standard errors of the mean unless stated otherwise. For each dependant variable at each timepoint, statistical tests were performed to determine any significant differences between treatments at that timepoint. The following procedure applies to these dependant variables: dry biomass, strawberry yield, number of leaves, number of flower stalks, each enzyme's respective activity, each chemical contaminant's measured mass in leachate and measured concentration in soil, Shannon's diversity index, and phylum-level relative abundance of the soil microbial community. The Shapiro-Wilk test was performed to verify that the residuals of the data were normally distributed. If all the residuals were equal then the Shapiro-Wilk test was not performed, and the data was considered not normally distributed. Bartlett's test

was performed to verify that the variance of the data from each treatment was equal. If any treatment had a variance of 0, then Bartlett's test was not performed, and it was considered that the variance among treatments were not equal. If the data was determined to have normally distributed residuals (Shapiro-Wilk test: $p > 0.05$) and equal variance among treatment groups (Bartlett's test: $p > 0.05$), then a one-way ANOVA was performed, otherwise a Kruskal-Wallis H test was performed. If any treatment group had $N < 5$, and the configuration (*i.e.*, number of treatments and number of replicates in each treatment) could not be found in a lookup table or the p-value would be higher than the highest p-value in the lookup table, then the result of the Kruskal-Wallis H test was deemed insignificant in that there were no significant differences in the means between treatments. If all the values in the data were equal (*e.g.*, all values were below the limit of detection), then no significance test was performed, and a symbolic p-value of 1 was assigned to the test. A baseline for significance was $\alpha=0.05$. Since for each dependent variable, a statistical test was performed at each timepoint, a Holm-Bonferroni correction was applied to α such that $\alpha_{HB} \leq \alpha$, whereby the correction factor was equal to the number of time points. Therefore, a result of $p < \alpha_{HB}$ was determined to be significant. Significant differences observed in a one-way ANOVA were followed by Tukey's HSD test. Significant differences observed in a Kruskal-Wallis H test were followed by the Mann-Whitney U test with Bonferroni correction. Tables S6.7-S6.15 contain the results to these tests. These tests were performed in Python 3.9.7 using numpy 1.21.2,³⁵ pandas 1.3.3,³⁶ scipy 1.7.1,³⁷ and statsmodels 0.13.1 packages.³⁸ Plots were made using matplotlib 3.4.2.³⁹

To determine if the weighted UniFrac distances of the soil microbial communities' amplicon sequence variants (ASVs) (*i.e.*, 100% similarity operational taxonomic units) between two treatments across all timepoints was significant, PERMANOVA was performed with $q < 0.05$

being considered significant. A principal coordinate analysis (PCoA) was performed on the weighted UniFrac distances as well to visualize the data.

6.3 Results and discussion

6.3.1 Characterization of HDPE microplastics

Microscope images of the HDPE microplastics are shown in Figure S6.4. The mechanical weathering caused by the blender resulted in HDPE microplastics, not only of varying size, but also of vastly diverse shapes and aspect ratios, ranging from simple flat micrometer-sized fragments to long twisted microfibrils. Therefore, a size distribution was measured on a mass basis by sieving the HDPE microplastics through a series of meshes and recording the mass retained by each mesh (Table 6.1). The initial mesh size used to separate the HDPE microplastics from the larger HDPE particles was ~1 mm. Any plastic retained by this mesh was discarded and not used in experiments. The particle size distribution in both years was relatively similar, with decreasing mass proportion with decreasing size.

Table 6.1. Size distribution on a mass basis of HDPE microplastics in both years of the study. Microplastics were first passed through a ~1 mm mesh size sieve before further use.

Sieve mesh size	2018 HDPE microplastic	2019 HDPE microplastic
> 500 μm	69.8 %	79.5 %
250 – 500 μm	25.3 %	17.2 %
125 – 250 μm	4.4 %	3.1 %
< 125 μm	0.4 %	0.2 %

Although the size distribution shows a decrease in mass concentration as microplastic size decreases, the opposite may be true when considering a particle count concentration. For instance,

a 500- μm spherical microplastic would have the same mass as sixty-four 125- μm spherical microplastics. This would suggest that there could be more microplastic particles in the 125-250 μm range than there are $> 500 \mu\text{m}$. A study by Wang *et al.* examined the distribution of several microplastic properties in agricultural soils, whereby they also observed a trend of increasing microplastic particle concentration as size decreased.⁴⁰ They also found that polyethylene was the most prevalent microplastic found in the soil, making up 21 % of microplastics found, followed closely by polyamide at 20 %.⁴⁰ They classified 54 % of the microplastics they found as fragments and 27 % as fibres.⁴⁰ Overall, our results confirm that we have polydisperse microplastic-sized HDPE for our study.

6.3.2 Contaminant transport

The chemical contaminants covered a range of octanol-water partition coefficients (K_{ow}) (Table S6.2). The leachate and soil from the CTRL pots were examined to ascertain any background presence of these chemical contaminants. It was found that none of the chemical contaminants were observed in measurable quantities (*i.e.*, none were above the instrument detection limit) in the CTRL soils or leachate at any time point throughout the study. Overall, the HDPE microplastics had no clear impact on the extent of these chemical contaminants leaching from the soil (Figure 6.1, S6.5). Similarly, no significant differences in the concentration of any of the chemical contaminants in soil between CTRL, C, and CP100 treatments at any timepoint were observed (Figures 6.2, S6.6). We note that due to having a low sample size ($N=3$) in addition to applying a Holm-Bonferroni correction, we did not have the statistical power to distinguish the CTRL concentrations from C and CP100 soils. In year 1, most of the gemfibrozil and sulfamethoxazole was no longer present in the soil by day 35 (Figure 6.2a,d). Similarly, ibuprofen

was absent from the soils by day 6 (Figure S6.6c) and caffeine was almost absent by day 69 (Figure S6.6b). Conversely, triclosan and carbamazepine were still present in the soil for the duration of year 1, but did show a decline in concentration over the year (Figure 6.2b,c). This indicates that the addition of some chemical contaminants may only have a short period in which they directly impact the soil, whereas others may stay in the soil for an extended period. However, these short-lived contaminants may still alter the soil during their time there, which may have lasting consequences even after they are no longer detected, for instance, by conversion into biologically active metabolites.

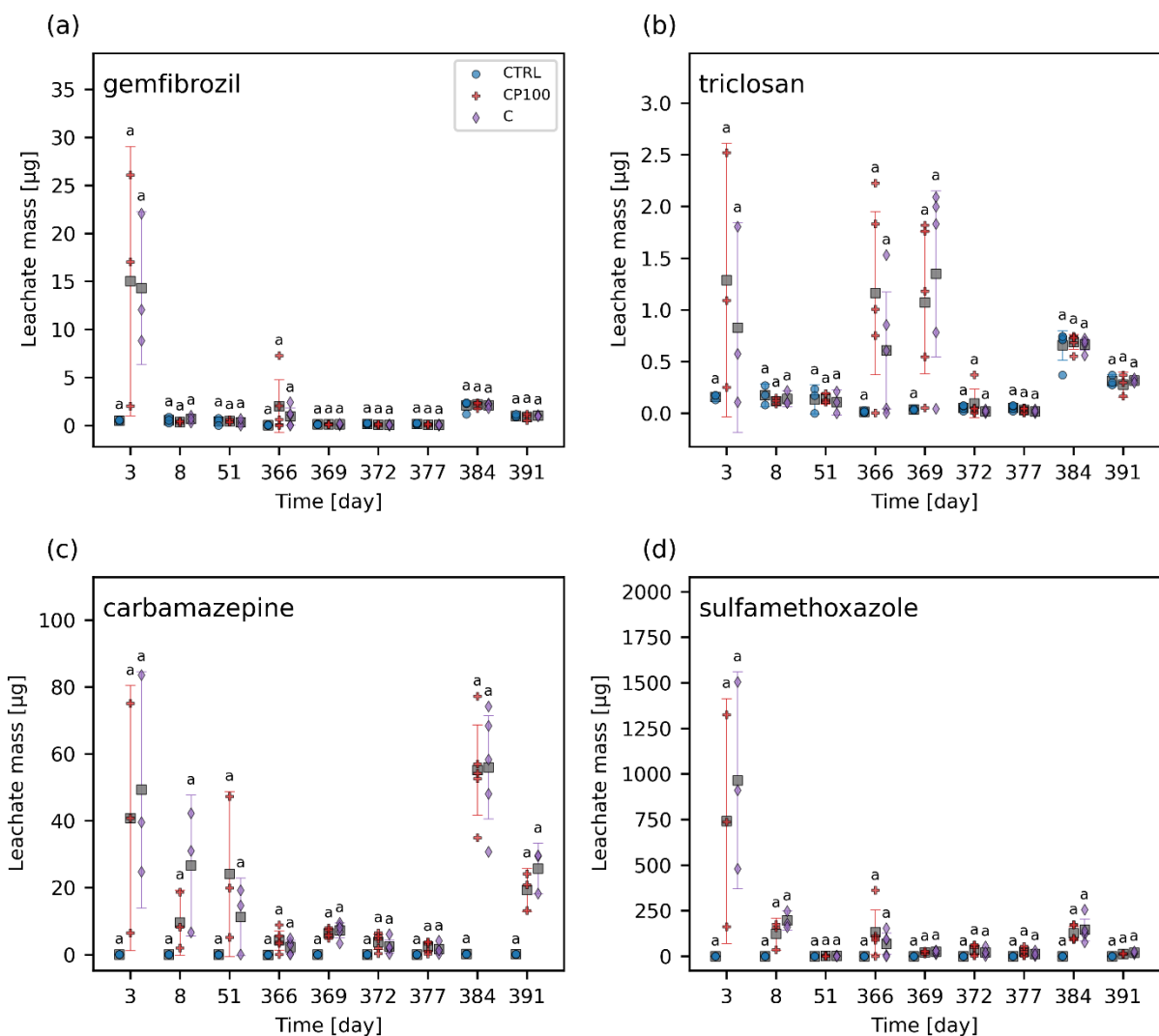


Figure 6.1. Leachate mass data for (a) gemfibrozil, (b) triclosan, (c) carbamazepine, and (d) sulfamethoxazole in control (CTRL), chemical contaminants + 100 mg HDPE microplastic kg^{-1} soil (CP100), and chemical contaminants (C) treated soils. No leachate data was collected for the intervals including day 52 – 363, 392 – 456. For each timepoint, treatments with the same letter have no significant difference between them. Markers represent individual replicates. Grey squares represent the means. Error bars show $2 \times$ the standard error of the mean.

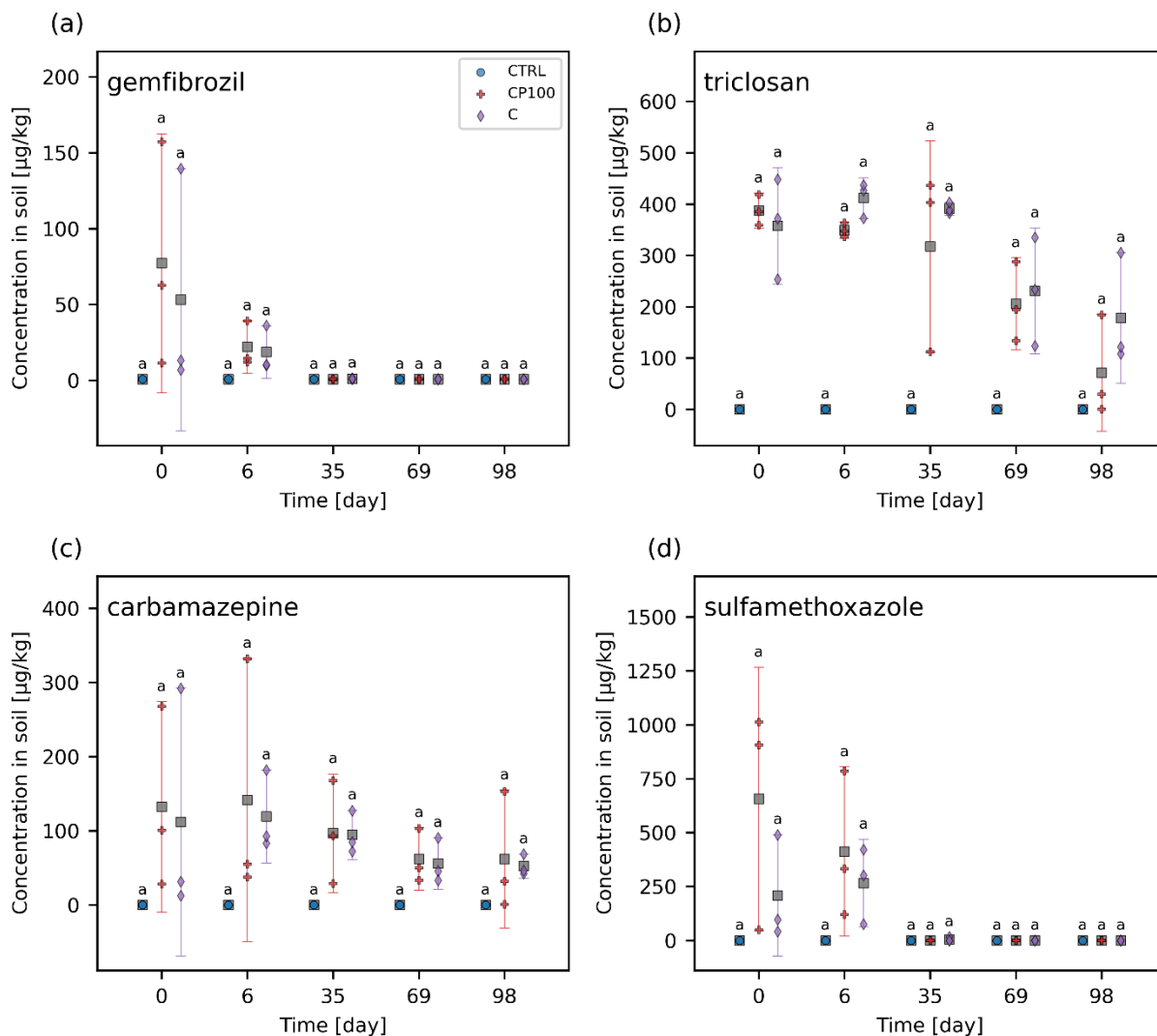


Figure 6.2. Concentration of (a) gemfibrozil, (b) triclosan, (c) carbamazepine, and (d) sulfamethoxazole in control (CTRL), chemical contaminants + 100 mg HDPE microplastic kg^{-1} soil (CP100), and chemical contaminants (C) treated soils. For each timepoint, treatments with the same letter have no significant difference between them. Markers represent individual replicates. Grey squares represent the means. Error bars show $2 \times$ the standard error of the mean.

6.3.3 Effect on soil microbial community composition

The soil's microbial community consists of a variety of bacteria, many of which play a vital role in the cycling of nutrients – in part by releasing extracellular enzymes – which can then be used by the plant.¹⁸ Therefore, monitoring changes to the soil microbial community composition can help explain observations regarding soil enzyme activity and, in turn, plant growth. The most abundant phyla were *Acidobacteria* (24.9 %) and *Actinobacteria* (22.2 %) followed by *Chloroflexi* (13.5 %) and *Proteobacteria* (13.1 %). Values in parentheses represent the number of reads from that phylum divided by the total reads across all samples. Phyla that represented less than 1 % of the overall sequence counts across all samples were grouped together and labelled as “Other”. *Acidobacteria* engage in the general breakdown of soil organic matter, specifically, genes have been identified for the production of enzymes that may decompose cellulose, hemicellulose, chitin, xylan, and lignans.⁴¹ It has also been suggested that *Acidobacteria* can be manipulated to increase the productivity of agricultural crops.⁴¹ *Actinobacteria* has been shown to play a role in plant growth promotion as well.⁴² Interestingly, some *Chloroflexi* bacteria are organohalide respirers,⁴³ while forms of *Proteobacteria* play a role in nitrogen fixation.⁴⁴ Significant differences in the phylum-level microbial community were rare, occurring only on day 35, whereby C soils had a significantly lower relative abundance of *Proteobacteria* than CTRL and P10 soils, and on day 397, whereby CTRL soils had a significantly lower relative abundance of *Actinobacteria* than C, CP100, and P10 soils. The complete phylum-level taxonomy data is shown in Figure 6.3.

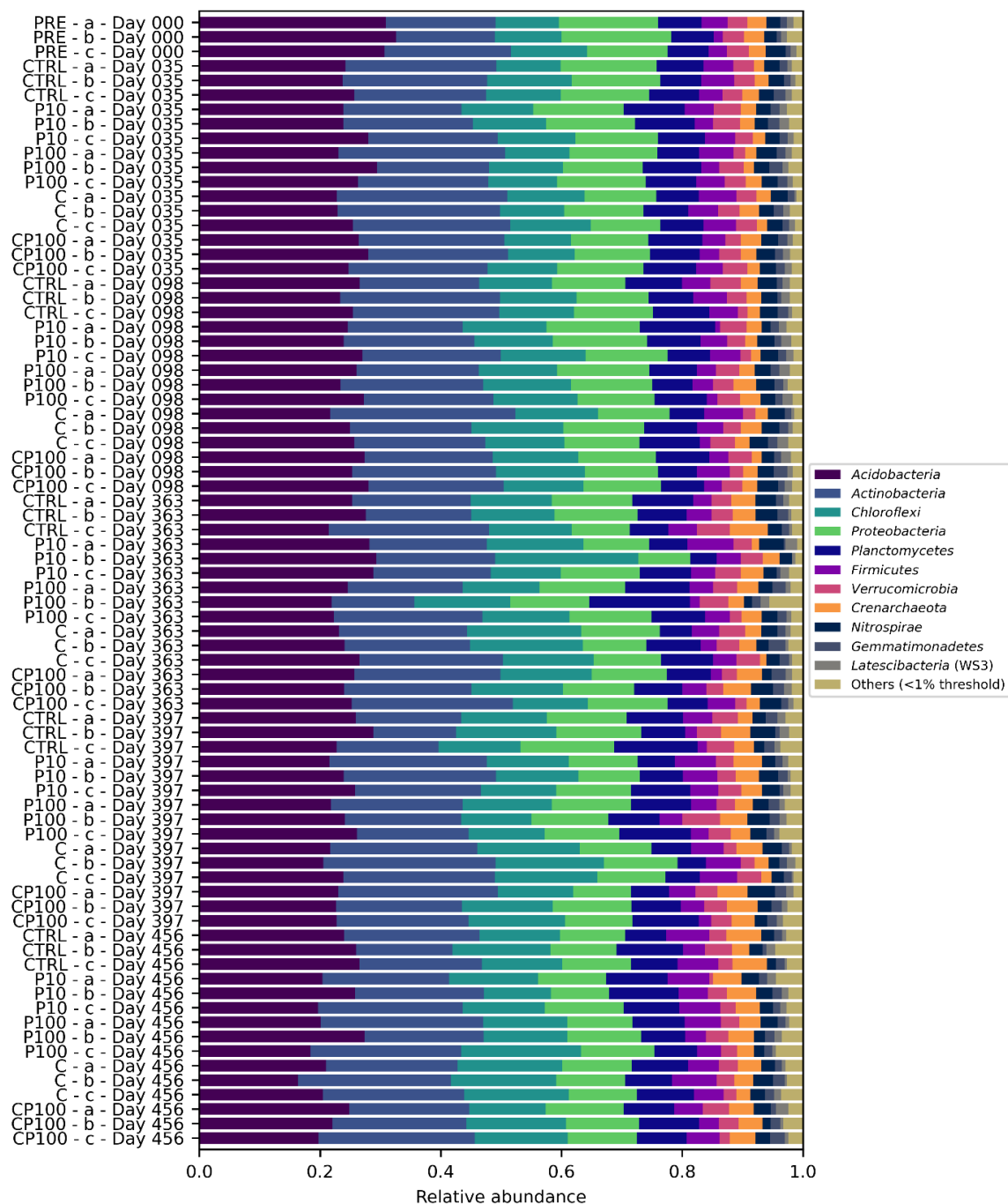


Figure 6.3. Soil microbial community composition based on the relative abundance of phyla found in control (CTRL), 10 mg HDPE microplastic kg⁻¹ soil (P10), 100 mg HDPE microplastic kg⁻¹ soil (P100), chemical contaminants + 100 mg HDPE microplastic kg⁻¹ soil (CP100), and chemical contaminants (C) treated soils. PRE (pre-treatment) is a composite sample of the uncontaminated soils. Row labels have the following nomenclature: A-B-C, where A is the treatment, B is the replicate ID, and C is the timepoint.

The alpha and beta diversity of the soils' microbial community composition based on ASVs were assessed. There were no significant differences in the Shannon's diversity index of the soil microbial community (Figure S6.7) among treatments for any of the timepoints measured. A PERMANOVA was performed on the pairwise weighted UniFrac distances of the soils' ASVs. The complete results can be found in Table S6.5. To get an overall picture of these differences across the entire two-year study, the soil samples obtained across all timepoints for a given treatment were compared against the soil samples obtained across all timepoints for another treatment. This was performed for all possible pairwise comparisons between treatments. The chemical contaminant (C) soils had a significant weighted UniFrac distance from the CTRL ($q=0.0076$), P100 ($q=0.0050$), PRE ($q=0.0062$), and CP100 ($q=0.0329$) treatments. The CP100 treatment also had a significant weighted UniFrac distance from the PRE ($q=0.0062$) soils. However, the most noteworthy observation is the fact that although the CTRL-C pair showed a significant distance ($q=0.0076$), no significance was observed in the CTRL-P100 pair ($q=0.421$) or the CTRL-CP100 pair ($q=0.186$). Moreover, the significant distance observed in the C-CP100 pair ($q=0.0329$), but not the CTRL-P100 pair ($q=0.421$) clearly shows that the HDPE microplastics only play a role in the composition of the microbial community in the presence of the chemical contaminants. This suggests that HDPE microplastics may play a role in minimizing the impact of chemical contaminants on the microbial community composition of soils, especially since an increase in significance (*i.e.*, a decreasing q -value) is observed when moving from the CTRL-P100 pair ($q=0.4214$) to the CTRL-CP100 pair ($q=0.186$) to the significant CTRL-C pair ($q=0.0076$). These results are similar to those found by Kleinteich *et al.* whereby polyethylene microplastics were able to reduce the impact of polycyclic aromatic hydrocarbons, such as phenanthrene and anthracene, on the bacterial community of freshwater sediments.⁴⁵

To visualize these results, a principal coordinate analysis (PCoA) of the weighted UniFrac distances is shown in Figure 6.4 where the C soils are clustered on the left, whereas the CTRL has a larger cluster towards the right. We note that the first and second principal coordinate axes combined only account for 28 % of the total variance, and therefore the significant distances mentioned previously are not easily visible in the PCoA plot. Interestingly, Figure S6.8 shows that changes in the soil microbial community composition over time are readily apparent. This helps confirm the validity of our microbial community analytical methods, since these temporal changes were easily distinguishable.

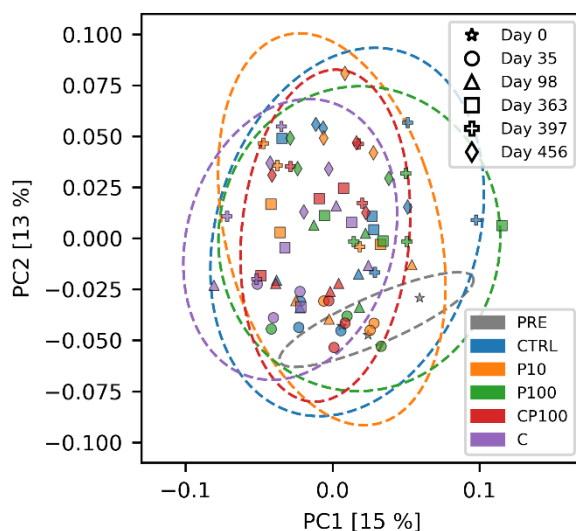


Figure 6.4. Principal coordinate analysis (PCoA) of the weighted UniFrac distance of the soil microbial communities' ASVs in control (CTRL), 10 mg HDPE microplastic kg⁻¹ soil (P10), 100 mg HDPE microplastic kg⁻¹ soil (P100), chemical contaminants + 100 mg HDPE microplastic kg⁻¹ soil (CP100), and chemical contaminants (C) treated soils. PRE (pre-treatment) is a composite sample of the uncontaminated soils. Ellipses represent the zone where 95 % of samples from a bivariate normal distribution with the same mean and covariance matrix as the respective treatment would be drawn from. Numbers in brackets indicate the amount of variance captured by that principal coordinate (PC).

In a study by Dunmei *et al.*, low-density polyethylene (LDPE) with a volume-weighted mean diameter of 37 μm was applied to field soil at concentrations up to 15 g m^{-2} and the soil was then sampled after 287 days.⁴⁶ They found that the addition of LDPE was associated with a significant decrease in the abundance of various types of microarthropods and nematodes, but had no significant impact on the overall abundance of microorganisms.⁴⁶ Previously, Huang *et al.* exposed soil to 76 mg kg^{-1} LDPE microplastic films (2 mm \times 2 mm \times 0.01 mm) over 90 days, and observed increasingly pronounced changes in the soil microbial community composition as the experiment progressed.⁴⁷ However, they did not see any change in the Shannon's diversity index between the control soil and the soil exposed to LDPE microplastics. Ren *et al.* exposed soil to a much higher load of 50 000 mg kg^{-1} polyethylene microplastics at two size distributions ($< 13 \mu\text{m}$ and $< 150 \mu\text{m}$) in separate experiments over 30 days.⁴⁸ While they saw minimal changes to the Shannon's diversity index of the bacterial community, the larger polyethylene microplastics lowered the diversity of the fungal community, while the smaller microplastics increased it at 3 days and 30 days. Similarly, Li *et al.* conducted a microplastic study on the sediments found in the Huangjinxia Reservoir and saw no significant difference in the Shannon's diversity index between sediment samples containing less than 400 microplastics per kg and those sediment samples containing over 600 microplastics per kg.⁴⁹

The effects of chemical contaminants on soil microbial communities have also been assessed previously. Feng *et al.* showed that 100 mg kg^{-1} sulfamethoxazole can reduce the Shannon's diversity index of the soil microbial community after 7 days of exposure, but this effect disappeared after 21 days.⁵⁰ Meanwhile, Park *et al.* found that triclosan (10 or 50 mg kg^{-1} soil) had a minimal effect on the soil microbial community composition and, similar to our findings, observed that the passage of time played a greater role in soil microbial community composition

changes than triclosan.⁵¹ Zhang *et al.* found that wastewater treated with 250 $\mu\text{g L}^{-1}$ caffeine reduced the bacterial community diversity during a 210-day exposure in a wetland system.⁵² Thehusmond *et al.* showed that carbamazepine can decrease (0.05-5 mg kg^{-1} soil) the Shannon's diversity index of soil under aerobic conditions, but can increase (0.5-5 mg kg^{-1} soil) it under anaerobic conditions after 14 days of exposure.⁵³

In our study, we saw no effect of any of the treatments on the Shannon's diversity index of the soil microbial community (Figure S6.7). This is in agreement with scientific literature on the impact of microplastics on the Shannon's diversity index of soil, however, the literature suggests that the presence of chemical contaminants can increase or decrease the Shannon's diversity index of the soil. Since our study consisted of an exposure involving eight chemical contaminants simultaneously, it is perhaps not so surprising that they collectively had no effect on the microbial biodiversity of the soils as their individual abilities to increase or decrease diversity may have negated each other to some extent. From the weighted UniFrac distances, it was clear that the presence of the chemical contaminants was able to significantly alter the microbial community composition of the soil relative to the control (CTRL-C pair, $q=0.0076$), but was unable to significantly change it in the co-presence of 100 mg kg^{-1} HDPE microplastics (CTRL-CP100 pair, $q=0.1862$).

6.3.4 Effect on soil enzyme activity

The enzyme activity of four extracellular soil enzymes were measured. Figure 6.5 shows the enzyme activities for β -glucosidase, chitinase, and xylan 1,4- β -xylosidase for each treatment and timepoint. The enzyme activity for phosphatase (day 0 and day 69 onward) can be found in Figure S6.9. No significant difference in xylan 1,4- β -xylosidase activity between treatments were

observed at any timepoint. The only significant differences observed were on day 6 whereby chitinase activity was significantly higher in P10 soils than CTRL and CP100 soils. Also, on day 425, β -glucosidase activity was significantly higher in CP100 and C soils when compared to CTRL and phosphatase activity was significantly higher in C and P10 soils when compared to CTRL. It is important to note that there were no significant differences in enzyme activity observed at day 0, which signifies that the soil in all the treatments had similar baseline enzyme activities, since day 0 measurements were taken just before the addition of HDPE microplastics and/or chemical contaminants.

A study by Fei *et al.* showed that soil containing 10 000 mg kg⁻¹ LDPE microplastics (678 μ m) for 50 days exhibited an increase in soil urease and acid phosphatase activity and a decrease in fluorescein diacetate hydrolase activity.⁵⁴ Furthermore, Huang *et al.* treated soil with a relatively low dose of 76 mg kg⁻¹ LDPE microplastic films (2 mm \times 2 mm \times 0.01 mm) over 90 days, and found that urease and catalase activity increased while invertase activity showed no significant change.⁴⁷ Yang *et al.* showed that contamination of soil with 70 000 mg kg⁻¹ polypropylene microplastics (<250 μ m) had no significant effect on β -glucosidase and urease activity, but caused a 12 % increase in phosphatase activity over 30 days.⁵⁵ In a separate study, it was shown that 70 000 mg kg⁻¹ polypropylene microplastics (<180 μ m) contaminated soil can increase fluorescein diacetate hydrolase activity, but does not affect phenyl oxidase activity over 30 days.⁵⁶ These studies have shown that in general, microplastics can have a variety of effects on the activity of different soil enzymes ranging from decreasing activity to increasing it, or having no effect altogether.

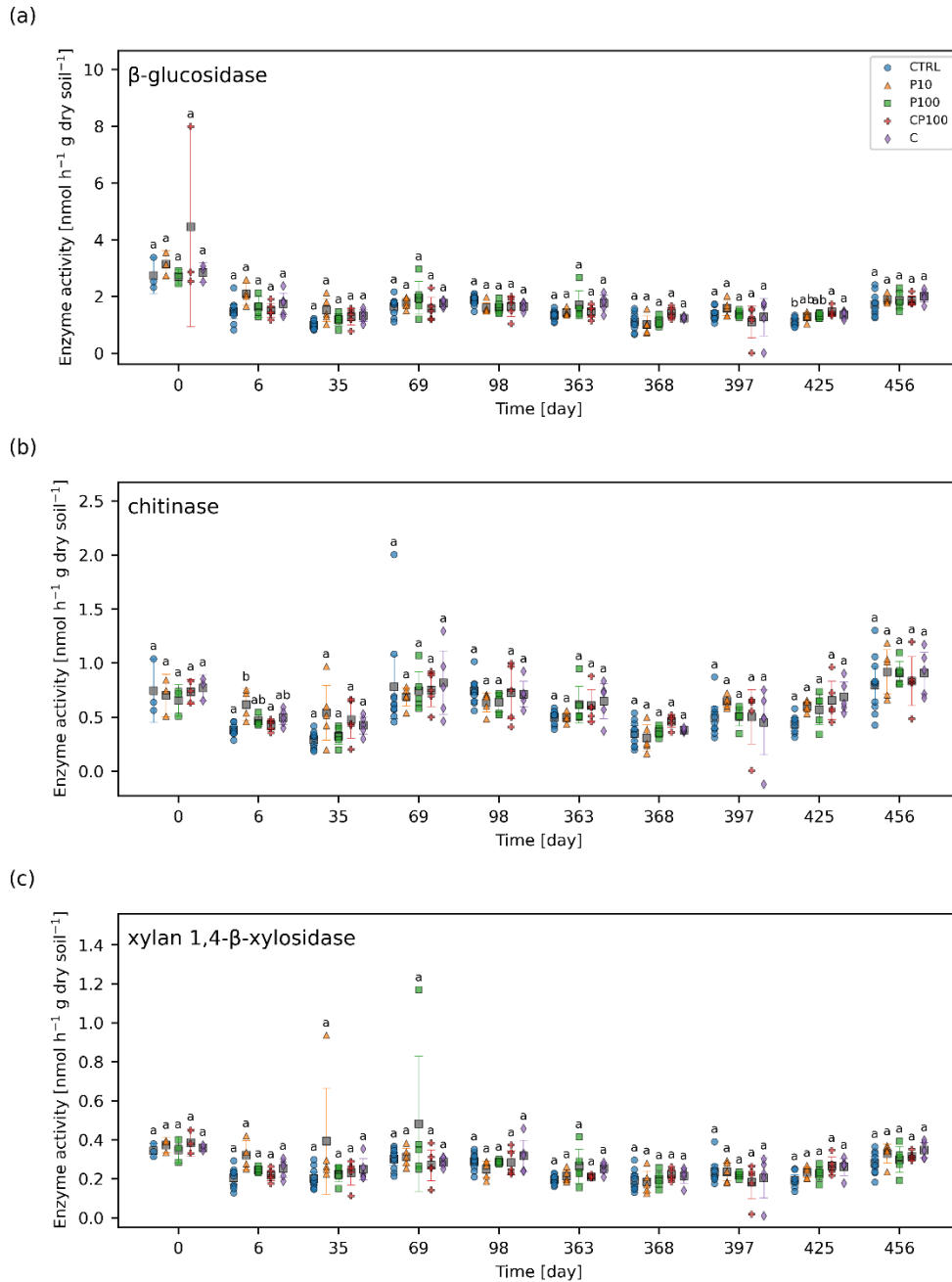


Figure 6.5. (a) β -glucosidase, (b) chitinase, and (c) xylan 1,4- β -xylosidase activities over the course of two growing seasons in control (CTRL), 10 mg HDPE microplastic kg^{-1} soil (P10), 100 mg HDPE microplastic kg^{-1} soil (P100), chemical contaminants + 100 mg HDPE microplastic kg^{-1} soil (CP100), and chemical contaminants (C) treated soils. For each time point, treatments with the same letter have no significant difference between them. Markers represent individual replicates. Grey squares represent the means. Error bars show $2 \times$ the standard error of the mean.

The observed effects of some of the chemical contaminants on soil enzyme activity have been previously reported in the literature. Waller and Kookana measured the effects of triclosan (1-100 mg kg⁻¹ soil) on enzyme activity in clay and sandy soils.⁵⁷ They found that triclosan increased acid phosphatase activity in sandy soil, but not clay soil, and alkali phosphatase activity was largely unaffected in both soil types. They also noted that triclosan reduced β -glucosidase activity in sandy soil, but not clay soil, and that chitinase activity was mostly unaffected except for a significant decrease in clay soil when exposed to 50-100 mg triclosan kg⁻¹ soil. Liu *et al.* also studied the effects of triclosan (0.1-50 mg kg⁻¹ soil) and found that its initial addition to the soil inhibits phosphatase activity, but this activity slowly recovers over time.⁵⁸ They suggested that this could be due to the degradation of triclosan in the soil over time. In a separate study, sulfamethoxazole (1-100 mg kg⁻¹ soil) was shown to inhibit soil phosphatase activity over a 22 day exposure period.⁵⁹ These studies reveal that triclosan has been shown to have variable effects on soil enzyme activity, whereas sulfamethoxazole may decrease it. In our study, we added 1.42 mg kg⁻¹ sulfamethoxazole and 3.14 mg kg⁻¹ triclosan along with six other chemical contaminants to soil, but significant effects were rare. This could be due to the outdoor exposure conditions of our experiment which could have affected the transport or degradation of these chemical contaminants in our soils. For instance, we observed greater leaching of sulfamethoxazole from soil in year 1 relative to year 2 (Figure 6.1d). Heavy rain could also cause these contaminants to leach out faster than they may have otherwise under drip irrigation alone or in an indoor environmental chamber. Therefore, although the same mass of chemical contaminants was applied to the soil in each year, the amount present at each timepoint was likely variable.

6.3.5 Effect on strawberry plant growth

The total yield of fresh strawberries, the dry biomass of the remaining plant (*i.e.*, without any strawberry fruit remaining), the number of leaves, and the number of flower stalks at the end of each year was measured (Figure 6.6). No significant differences were observed in any of these endpoints between any of the treatments at any timepoint suggesting that any impact of the HDPE microplastics and/or chemical contaminants on these endpoints was smaller than the general variance that occurs from growing strawberries under outdoor conditions. This variance can be caused by several factors such as the interaction of the strawberry plants with birds, land animals, and insects, as well as variations in the weather, precipitation, and temperature which would not be present in a climate-controlled lab environment.

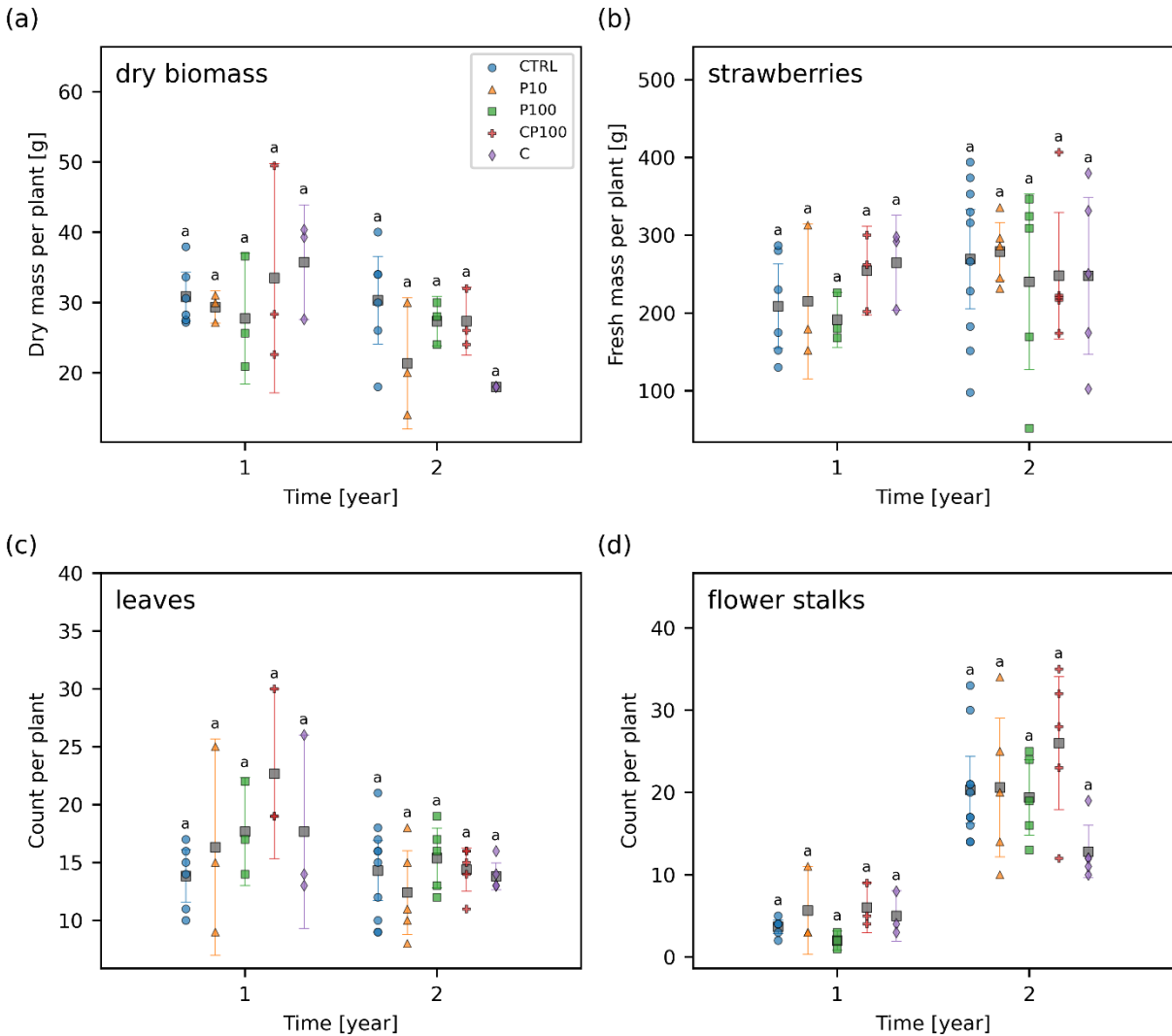


Figure 6.6. (a) Dry biomass of the remaining plant without any strawberry fruit, (b) total yield of fresh strawberries, (c) number of leaves, and (d) number of flower stalks in control (CTRL), 10 mg HDPE microplastic kg^{-1} soil (P10), 100 mg HDPE microplastic kg^{-1} soil (P100), chemical contaminants + 100 mg HDPE microplastic kg^{-1} soil (CP100), and chemical contaminants (C) treated soils. For each time point, treatments with the same letter have no significant difference between them. Markers represent individual replicates. Grey squares represent the means. Error bars show $2 \times$ the standard error of the mean.

The effect of microplastics on other plant species has previously been studied. For instance, our results are similar to those of a previous study by Meng *et al.* whereby soil containing 250-

1000 μm LDPE microplastics at 25 000 mg kg^{-1} dry soil had no significant effect on the shoot, root, or fruit biomass of *Phaseolus vulgaris L.* in an outdoor experiment over approximately 4 months.⁶⁰ Conversely, Pignattelli *et al.* examined the effect of 184 mg kg^{-1} polyethylene microplastics ($< 125 \mu\text{m}$) on garden cress (*Lepidium sativum*) over 21 days.⁶¹ They found that soil containing polyethylene microplastics had a significantly higher germination inhibition of 7.1 % when compared to 0 % in the control, and reduced shoot biomass by 38 % relative to the control soil; however, there was no significant effect on the plant height or the number of leaves.⁶¹ Similarly, Boots *et al.* showed that 1000 mg kg^{-1} HDPE microplastics ($\sim 100 \mu\text{m}$) exposure resulted in an 8 % reduction in perennial ryegrass (*Lolium perenne*) shoot growth, but only a 2.5 % reduction in germination rate.⁶² While both of these studies used considerably smaller microplastics than our work, Qi *et al.* examined the effect of LDPE microplastics ($< 1 \text{ mm}$) on wheat (*Triticum aestivum*) growth.⁶³ Over a 4-month period, there was generally little or no significant difference between wheat grown in soil contaminated with 10 000 mg kg^{-1} LDPE microplastics and the control soil over a variety of factors including: plant height, number of tillers, number of fruits, shoot and root biomass, leaf area, number of leaves, stem diameter, and relative chlorophyll content.⁶³ Likewise, our results show that a similar phenomenon was observed in strawberry plants with HDPE microplastics, in an outdoor environment over a similar time frame. Moreover, our study was done at a lower exposure concentration than these previous studies.

When considering the chemical contaminants added to the soil, triclosan has previously been shown to have no adverse effects on maize, soybean, and spring wheat.⁶⁴ Barbera *et al.* exposed rice (*Oryza sativa*) to a mixture of ibuprofen and caffeine which resulted in a 51 % increase in rice grain yield.⁶⁵ Conversely, sulfamethoxazole (8.0 μM in Murashige and Skoog solid medium) has been shown to decrease the root length and shoot biomass of *Arabidopsis thaliana* by 95 % and

90 %, respectively.⁶⁶ In our work, we added 5.6 μmol sulfamethoxazole per kg fresh soil along with triclosan, ibuprofen, caffeine, and other chemical contaminants at various concentrations (Table S6.2). The combination of these growth enhancing and growth inhibiting effects as well as the nature of the experiment being outdoors in a highly variable environment is consistent with our results that indicate that there is no significant effect of the chemical contaminants on the dry biomass, strawberry yield, number of leaves, and number of flower stalks (Figure 6.6).

6.4 Conclusions

The effects of eight common wastewater chemical contaminants in the presence and absence of HDPE microplastics on soil microbial community composition, soil enzyme activity, and strawberry plant growth were examined over a two-year period in an outdoor study. It was found that when comparing the abundance and presence of various ASVs between treated soils across all timepoints using a weighted UniFrac distance, the distance between the CTRL-C soils were significant, but were not significant for the CTRL-CP100 and CTRL-P100 pairs, suggesting that the presence of HDPE may have mitigated the ability of the chemical contaminants to alter the soil microbial community composition. Moreover, significant differences in the soil enzyme activity, and the phylum-level soil microbial community composition among treatments were rare. No significant differences in the strawberry yield, plant dry biomass, the number of leaves, the number of flower stalks, and the Shannon's diversity index were found among treatments at any time point.

Although our two-year outdoor study largely demonstrates the lack of any overall trend of the treatments on strawberry plant growth, soil enzyme activity, and phylum-level soil microbial community composition, it is worth noting that this study was done in one region of the world on one type of soil, and that these results may vary when conducted in different parts of the world,

for example, due to different soil types, climate, *etc.* Moreover, although no measurable impacts from the chemical contaminants and HDPE microplastics on strawberry yield were detected, we did not assess the potential health effects of eating strawberries grown in such a soil.

Other researchers have also observed no effect of microplastics on *Tripneustes gratilla* larvae survival;⁶⁷ *Lemna minor* growth and photosynthetic efficiency, as well as the mortality and mobility of *Gammarus duebeni* that ingested the microplastic-contaminated *L. minor*;⁶⁸ *Echinogammarus marinus* growth or food consumption;⁶⁹ and the foraging activity and survival of *Acanthurus triostegus*.⁷⁰ While there were little to no significant differences among treatments in many of the endpoints studied in this work, we believe there are several aspects that make this study of interest. For instance, the study was designed to mimic real world conditions as closely as possible without having to contaminate an open field. This was done by using agricultural soil in pots outdoors over a long two-year period with environmentally relevant concentrations of microplastics and chemical contaminants. It is also important to share “no negative effects” data in an effort to contribute to an unbiased microplastic literature and to prevent the duplication of similar resource-intensive experiments by other researchers.⁷¹ We believe the data presented here is particularly important to the agriculture industry due to the widespread usage of HDPE and other plastics in agriculture (*e.g.*, irrigation parts, plastic mulch, *etc.*) and should help in deciding the pros and cons of plastic use in agricultural soils.

Acknowledgements

The authors acknowledge funding from the Natural Sciences and Engineering Research Council of Canada (Discovery and Strategic Project programs), the Canada Research Chairs Program, the Canada Foundation for Innovation (grants to NT, SB, SG, and VG), the Killam

Research Fellowship, and the Fonds de recherche du Québec – Nature et technologies (grant no. 286120). We appreciate the support of Environment and Climate Change Canada, Health Canada, the Canadian Food Inspection Agency, the Mass Spectrometry Platform at the Macdonald Campus of McGill University, and Vive Crop Protection. S. Chahal acknowledges NSERC for a PGS D scholarship, McGill University for a MEDA fellowship, the support of the EUL fund in the Department of Chemical Engineering, and EcotoQ. V.B. was supported in part by the McGill Engineering Doctoral Award. The authors would like to thank S. Fan, P. Gopal, I. Hader, M. Bleho, L. Caralampides, and the team at the Macdonald Campus Horticulture Research Centre for their assistance during the field experiment.

References

- (1) Barnes, D. K. A.; Galgani, F.; Thompson, R. C.; Barlaz, M. Accumulation and fragmentation of plastic debris in global environments. *Philosophical Transactions of the Royal Society B: Biological Sciences* **2009**, *364* (1526), 1985-1998. DOI: 10.1098/rstb.2008.0205.
- (2) de Souza Machado, A. A.; Kloas, W.; Zarfl, C.; Hempel, S.; Rillig, M. C. Microplastics as an emerging threat to terrestrial ecosystems. *Global Change Biology* **2018**, *24* (4), 1405-1416. DOI: 10.1111/gcb.14020.
- (3) Horton, A. A.; Walton, A.; Spurgeon, D. J.; Lahive, E.; Svendsen, C. Microplastics in freshwater and terrestrial environments: Evaluating the current understanding to identify the knowledge gaps and future research priorities. *Science of The Total Environment* **2017**, *586*, 127-141. DOI: 10.1016/j.scitotenv.2017.01.190.
- (4) Allen, S.; Allen, D.; Phoenix, V. R.; Le Roux, G.; Durántez Jiménez, P.; Simonneau, A.; Binet, S.; Galop, D. Atmospheric transport and deposition of microplastics in a remote mountain catchment. *Nature Geoscience* **2019**, *12* (5), 339-344. DOI: 10.1038/s41561-019-0335-5.
- (5) Fuller, S.; Gautam, A. A Procedure for Measuring Microplastics using Pressurized Fluid Extraction. *Environmental Science & Technology* **2016**, *50* (11), 5774-5780. DOI: 10.1021/acs.est.6b00816.
- (6) Ng, E.-L.; Huerta Lwanga, E.; Eldridge, S. M.; Johnston, P.; Hu, H.-W.; Geissen, V.; Chen, D. An overview of microplastic and nanoplastic pollution in agroecosystems. *Science of The Total Environment* **2018**, *627*, 1377-1388. DOI: 10.1016/j.scitotenv.2018.01.341.

- (7) Piehl, S.; Leibner, A.; Löder, M. G. J.; Dris, R.; Bogner, C.; Laforsch, C. Identification and quantification of macro- and microplastics on an agricultural farmland. *Scientific Reports* **2018**, 8 (1), 17950. DOI: 10.1038/s41598-018-36172-y.
- (8) Scheurer, M.; Bigalke, M. Microplastics in Swiss Floodplain Soils. *Environmental Science & Technology* **2018**, 52 (6), 3591-3598. DOI: 10.1021/acs.est.7b06003.
- (9) Mai, L.; Bao, L.-J.; Wong, C. S.; Zeng, E. Y. Chapter 12 - Microplastics in the Terrestrial Environment. In *Microplastic Contamination in Aquatic Environments*, Zeng, E. Y. Ed.; Elsevier, 2018; pp 365-378.
- (10) Huerta Lwanga, E.; Gertsen, H.; Gooren, H.; Peters, P.; Salánki, T.; van der Ploeg, M.; Besseling, E.; Koelmans, A. A.; Geissen, V. Incorporation of microplastics from litter into burrows of *Lumbricus terrestris*. *Environmental Pollution* **2017**, 220, 523-531. DOI: 10.1016/j.envpol.2016.09.096.
- (11) Rochman, C. M.; Hoh, E.; Hentschel, B. T.; Kaye, S. Long-Term Field Measurement of Sorption of Organic Contaminants to Five Types of Plastic Pellets: Implications for Plastic Marine Debris. *Environmental Science & Technology* **2013**, 47 (3), 1646-1654. DOI: 10.1021/es303700s.
- (12) Kirstein, I. V.; Kirmizi, S.; Wichels, A.; Garin-Fernandez, A.; Erler, R.; Löder, M.; Gerdt, G. Dangerous hitchhikers? Evidence for potentially pathogenic *Vibrio* spp. on microplastic particles. *Marine Environmental Research* **2016**, 120, 1-8. DOI: 10.1016/j.marenvres.2016.07.004.
- (13) Mohapatra, D. P.; Cledón, M.; Brar, S. K.; Surampalli, R. Y. Application of Wastewater and Biosolids in Soil: Occurrence and Fate of Emerging Contaminants. *Water, Air, & Soil Pollution* **2016**, 227 (3), 77. DOI: 10.1007/s11270-016-2768-4.

- (14) Carr, S. A.; Liu, J.; Tesoro, A. G. Transport and fate of microplastic particles in wastewater treatment plants. *Water Research* **2016**, *91*, 174-182. DOI: 10.1016/j.watres.2016.01.002.
- (15) Corradini, F.; Meza, P.; Eguiluz, R.; Casado, F.; Huerta-Lwanga, E.; Geissen, V. Evidence of microplastic accumulation in agricultural soils from sewage sludge disposal. *Science of The Total Environment* **2019**, *671*, 411-420. DOI: 10.1016/j.scitotenv.2019.03.368.
- (16) Nizzetto, L.; Futter, M.; Langaas, S. Are Agricultural Soils Dumps for Microplastics of Urban Origin? *Environmental Science & Technology* **2016**, *50* (20), 10777-10779. DOI: 10.1021/acs.est.6b04140.
- (17) Liu, J.; Ma, Y.; Zhu, D.; Xia, T.; Qi, Y.; Yao, Y.; Guo, X.; Ji, R.; Chen, W. Polystyrene Nanoplastics-Enhanced Contaminant Transport: Role of Irreversible Adsorption in Glassy Polymeric Domain. *Environmental Science & Technology* **2018**, *52* (5), 2677-2685. DOI: 10.1021/acs.est.7b05211.
- (18) Itziar Alkorta; Ana Aizpurua; Patrick Riga; Isabel Albizu; Ibone Amézaga; Carlos Garbisu. Soil Enzyme Activities as Biological Indicators of Soil Health. *Reviews on Environmental Health* **2003**, *18* (1), 65-73. DOI: 10.1515/REVEH.2003.18.1.65.
- (19) Stott, D. E.; Andrews, S. S.; Liebig, M. A.; Wienhold, B. J.; Karlen, D. L. Evaluation of β -Glucosidase Activity as a Soil Quality Indicator for the Soil Management Assessment Framework. *Soil Science Society of America Journal* **2010**, *74* (1), 107-119. DOI: 10.2136/sssaj2009.0029.
- (20) Sinsabaugh, R. L.; Lauber, C. L.; Weintraub, M. N.; Ahmed, B.; Allison, S. D.; Crenshaw, C.; Contosta, A. R.; Cusack, D.; Frey, S.; Gallo, M. E.; et al. Stoichiometry of soil enzyme activity at global scale. *Ecology Letters* **2008**, *11* (11), 1252-1264. DOI: 10.1111/j.1461-0248.2008.01245.x.

- (21) Selmants, P. C.; Hart, S. C.; Boyle, S. I.; Stark, J. M. Red alder (*Alnus rubra*) alters community-level soil microbial function in conifer forests of the Pacific Northwest, USA. *Soil Biology and Biochemistry* **2005**, *37* (10), 1860-1868. DOI: 10.1016/j.soilbio.2005.02.019.
- (22) Rodríguez, H.; Fraga, R. Phosphate solubilizing bacteria and their role in plant growth promotion. *Biotechnology Advances* **1999**, *17* (4), 319-339. DOI: 10.1016/S0734-9750(99)00014-2.
- (23) Li, X.; Sarah, P. Arylsulfatase activity of soil microbial biomass along a Mediterranean-arid transect. *Soil Biology and Biochemistry* **2003**, *35* (7), 925-934. DOI: 10.1016/S0038-0717(03)00143-3.
- (24) IndexBox. *World: Strawberries – Market Report. Analysis And Forecast To 2025*; 2017.
- (25) Schofield, R. K.; Taylor, A. W. The Measurement of Soil pH. *Soil Science Society of America Journal* **1955**, *19* (2), 164-167. DOI: 10.2136/sssaj1955.03615995001900020013x.
- (26) Hansch, C. L., A; Hoekman, D Exploring QSAR: Hydrophobic, electronic, and steric constants In *Exploring QSAR: Hydrophobic, Electronic, and Steric Constants*, Hansch, C. L., A; Hoekman, DH Ed.; ACS Professional Reference Book American Chemical Society, 1995.
- (27) Snyder, S. A.; Westerhoff, P.; Yoon, Y.; Sedlak, D. L. Pharmaceuticals, Personal Care Products, and Endocrine Disruptors in Water: Implications for the Water Industry. *Environmental Engineering Science* **2003**, *20* (5), 449-469. DOI: 10.1089/109287503768335931.

- (28) Dal Pozzo, A.; Donzelli, G.; Rodriguez, L.; Tajana, A. “*In vitro*” model for the evaluation of drug distribution and plasma protein-binding relationships. *International Journal of Pharmaceutics* **1989**, *50* (2), 97-101. DOI: 10.1016/0378-5173(89)90133-6.
- (29) Avdeef, A. pH-Metric log *P*. II: Refinement of Partition Coefficients and Ionization Constants of Multiprotic Substances. *Journal of Pharmaceutical Sciences* **1993**, *82* (2), 183-190. DOI: 10.1002/jps.2600820214.
- (30) Krascenits, Z.; Hiller, E.; Bartal, M. Distribution of four human pharmaceuticals, carbamazepine, diclofenac, gemfibrozil, and ibuprofen between sediment and water. *J. Hydrol. Hydromech* **2008**, *56* (4), 237-246.
- (31) Pintado-Herrera, M. G.; Lara-Martín, P. A.; González-Mazo, E.; Allan, I. J. Determination of silicone rubber and low-density polyethylene diffusion and polymer/water partition coefficients for emerging contaminants. *Environmental Toxicology and Chemistry* **2016**, *35* (9), 2162-2172. DOI: 10.1002/etc.3390.
- (32) Bolyen, E.; Rideout, J. R.; Dillon, M. R.; Bokulich, N. A.; Abnet, C. C.; Al-Ghalith, G. A.; Alexander, H.; Alm, E. J.; Arumugam, M.; Asnicar, F.; et al. Reproducible, interactive, scalable and extensible microbiome data science using QIIME 2. *Nature Biotechnology* **2019**, *37* (8), 852-857. DOI: 10.1038/s41587-019-0209-9.
- (33) Asadishad, B.; Chahal, S.; Akbari, A.; Cianciarelli, V.; Azodi, M.; Ghoshal, S.; Tufenkji, N. Amendment of Agricultural Soil with Metal Nanoparticles: Effects on Soil Enzyme Activity and Microbial Community Composition. *Environmental Science & Technology* **2018**, *52* (4), 1908-1918. DOI: 10.1021/acs.est.7b05389.

- (34) Peyrot, C.; Wilkinson, K. J.; Desrosiers, M.; Sauvé, S. Effects of silver nanoparticles on soil enzyme activities with and without added organic matter. *Environmental Toxicology and Chemistry* **2014**, *33* (1), 115-125. DOI: 10.1002/etc.2398.
- (35) Harris, C. R.; Millman, K. J.; van der Walt, S. J.; Gommers, R.; Virtanen, P.; Cournapeau, D.; Wieser, E.; Taylor, J.; Berg, S.; Smith, N. J.; et al. Array programming with NumPy. *Nature* **2020**, *585* (7825), 357-362. DOI: 10.1038/s41586-020-2649-2.
- (36) McKinney, W. Data Structures for Statistical Computing in Python. In *Python in Science*, Austin, Texas, June 28 - July 3, 2010; van der Walt, S., Millman, J., Eds.; 2010; Vol. 445, pp 56 - 61. DOI: 10.25080/Majora-92bf1922-00a.
- (37) Virtanen, P.; Gommers, R.; Oliphant, T. E.; Haberland, M.; Reddy, T.; Cournapeau, D.; Burovski, E.; Peterson, P.; Weckesser, W.; Bright, J.; et al. SciPy 1.0: fundamental algorithms for scientific computing in Python. *Nature Methods* **2020**, *17* (3), 261-272. DOI: 10.1038/s41592-019-0686-2.
- (38) Seabold, S.; Perktold, J. Statsmodels: Econometric and statistical modeling with python. In *Proceedings of the 9th Python in Science Conference*, Austin, TX, 2010; Vol. 57, p 61.
- (39) Hunter, J. D. Matplotlib: A 2D Graphics Environment. *Computing in Science & Engineering* **2007**, *9* (3), 90-95. DOI: 10.1109/MCSE.2007.55.
- (40) Wang, J.; Li, J.; Liu, S.; Li, H.; Chen, X.; Peng, C.; Zhang, P.; Liu, X. Distinct microplastic distributions in soils of different land-use types: A case study of Chinese farmlands. *Environmental Pollution* **2021**, *269*, 116199. DOI: 10.1016/j.envpol.2020.116199.
- (41) Kalam, S.; Basu, A.; Ahmad, I.; Sayyed, R. Z.; El-Enshasy, H. A.; Dailin, D. J.; Suriani, N. L. Recent Understanding of Soil *Acidobacteria* and Their Ecological Significance: A

Critical Review. *Frontiers in Microbiology* **2020**, *11* (2712). DOI:
10.3389/fmicb.2020.580024.

- (42) Hazarika, S. N.; Thakur, D. Chapter 21 - *Actinobacteria*. In *Beneficial Microbes in Agro-Ecology*, Amaresan, N., Senthil Kumar, M., Annapurna, K., Kumar, K., Sankaranarayanan, A. Eds.; Academic Press, 2020; pp 443-476.
- (43) Krzmarzick, M. J.; Crary, B. B.; Harding, J. J.; O., O. O.; Leri, A. C.; Myneni, S. C. B.; Novak, P. J. Natural Niche for Organohalide-Respiring *Chloroflexi*. *Applied and Environmental Microbiology* **2012**, *78* (2), 393-401. DOI: 10.1128/AEM.06510-11.
- (44) Kersters, K.; De Vos, P.; Gillis, M.; Swings, J.; Vandamme, P.; Stackebrandt, E. Introduction to the *Proteobacteria*. In *The Prokaryotes: Volume 5: Proteobacteria: Alpha and Beta Subclasses*, Dworkin, M., Falkow, S., Rosenberg, E., Schleifer, K.-H., Stackebrandt, E. Eds.; Springer New York, 2006; pp 3-37.
- (45) Kleinteich, J.; Seidensticker, S.; Marggrander, N.; Zarfl, C. Microplastics Reduce Short-Term Effects of Environmental Contaminants. Part II: Polyethylene Particles Decrease the Effect of Polycyclic Aromatic Hydrocarbons on Microorganisms. *International Journal of Environmental Research and Public Health* **2018**, *15* (2), 287. DOI: 10.3390/ijerph15020287.
- (46) Lin, D.; Yang, G.; Dou, P.; Qian, S.; Zhao, L.; Yang, Y.; Fanin, N. Microplastics negatively affect soil fauna but stimulate microbial activity: insights from a field-based microplastic addition experiment. *Proceedings of the Royal Society B: Biological Sciences* **2020**, *287* (1934), 20201268. DOI: 10.1098/rspb.2020.1268.

- (47) Huang, Y.; Zhao, Y.; Wang, J.; Zhang, M.; Jia, W.; Qin, X. LDPE microplastic films alter microbial community composition and enzymatic activities in soil. *Environmental Pollution* **2019**, *254*, 112983. DOI: 10.1016/j.envpol.2019.112983.
- (48) Ren, X.; Tang, J.; Liu, X.; Liu, Q. Effects of microplastics on greenhouse gas emissions and the microbial community in fertilized soil. *Environmental Pollution* **2020**, *256*, 113347. DOI: 10.1016/j.envpol.2019.113347.
- (49) Li, C.; Gan, Y.; Dong, J.; Fang, J.; Chen, H.; Quan, Q.; Liu, J. Impact of microplastics on microbial community in sediments of the Huangjinxia Reservoir—water source of a water diversion project in western China. *Chemosphere* **2020**, *253*, 126740. DOI: 10.1016/j.chemosphere.2020.126740.
- (50) Liu, F.; Wu, J.; Ying, G.-G.; Luo, Z.; Feng, H. Changes in functional diversity of soil microbial community with addition of antibiotics sulfamethoxazole and chlortetracycline. *Applied Microbiology and Biotechnology* **2012**, *95* (6), 1615-1623. DOI: 10.1007/s00253-011-3831-0.
- (51) Park, I.; Zhang, N.; Ogunyoku, T. A.; Young, T. M.; Scow, K. M. Effects of Triclosan and Biosolids on Microbial Community Composition in an Agricultural Soil. *Water Environment Research* **2013**, *85* (12), 2237-2242. DOI: 10.2175/106143012x13560205144335.
- (52) Zhang, D.; Luo, J.; Lee, Z. M. P.; Gersberg, R. M.; Liu, Y.; Tan, S. K.; Ng, W. J. Characterization of microbial communities in wetland mesocosms receiving caffeine-enriched wastewater. *Environmental Science and Pollution Research* **2016**, *23* (14), 14526-14539. DOI: 10.1007/s11356-016-6586-4.

- (53) Thelusmond, J.-R.; Strathmann, T. J.; Cupples, A. M. The identification of carbamazepine biodegrading phylotypes and phylotypes sensitive to carbamazepine exposure in two soil microbial communities. *Science of The Total Environment* **2016**, *571*, 1241-1252. DOI: 10.1016/j.scitotenv.2016.07.154.
- (54) Fei, Y.; Huang, S.; Zhang, H.; Tong, Y.; Wen, D.; Xia, X.; Wang, H.; Luo, Y.; Barceló, D. Response of soil enzyme activities and bacterial communities to the accumulation of microplastics in an acid cropped soil. *Science of The Total Environment* **2020**, *707*, 135634. DOI: 10.1016/j.scitotenv.2019.135634.
- (55) Yang, X.; Bento, C. P. M.; Chen, H.; Zhang, H.; Xue, S.; Lwanga, E. H.; Zomer, P.; Ritsema, C. J.; Geissen, V. Influence of microplastic addition on glyphosate decay and soil microbial activities in Chinese loess soil. *Environmental Pollution* **2018**, *242*, 338-347. DOI: 10.1016/j.envpol.2018.07.006.
- (56) Liu, H.; Yang, X.; Liu, G.; Liang, C.; Xue, S.; Chen, H.; Ritsema, C. J.; Geissen, V. Response of soil dissolved organic matter to microplastic addition in Chinese loess soil. *Chemosphere* **2017**, *185*, 907-917. DOI: 10.1016/j.chemosphere.2017.07.064.
- (57) Waller, N. J.; Kookana, R. S. Effect of triclosan on microbial activity in australian soils. *Environmental Toxicology and Chemistry* **2009**, *28* (1), 65-70. DOI: 10.1897/08-224.1.
- (58) Liu, F.; Ying, G.-G.; Yang, L.-H.; Zhou, Q.-X. Terrestrial ecotoxicological effects of the antimicrobial agent triclosan. *Ecotoxicology and Environmental Safety* **2009**, *72* (1), 86-92. DOI: 10.1016/j.ecoenv.2008.06.009.
- (59) Liu, F.; Ying, G.-G.; Tao, R.; Zhao, J.-L.; Yang, J.-F.; Zhao, L.-F. Effects of six selected antibiotics on plant growth and soil microbial and enzymatic activities. *Environmental Pollution* **2009**, *157* (5), 1636-1642. DOI: 10.1016/j.envpol.2008.12.021.

- (60) Meng, F.; Yang, X.; Riksen, M.; Xu, M.; Geissen, V. Response of common bean (*Phaseolus vulgaris* L.) growth to soil contaminated with microplastics. *Science of The Total Environment* **2021**, 755, 142516. DOI: 10.1016/j.scitotenv.2020.142516.
- (61) Pignattelli, S.; Broccoli, A.; Renzi, M. Physiological responses of garden cress (*L. sativum*) to different types of microplastics. *Science of The Total Environment* **2020**, 727, 138609. DOI: 10.1016/j.scitotenv.2020.138609.
- (62) Boots, B.; Russell, C. W.; Green, D. S. Effects of Microplastics in Soil Ecosystems: Above and Below Ground. *Environmental Science & Technology* **2019**. DOI: 10.1021/acs.est.9b03304.
- (63) Qi, Y.; Yang, X.; Pelaez, A. M.; Huerta Lwanga, E.; Beriot, N.; Gertsen, H.; Garbeva, P.; Geissen, V. Macro- and micro- plastics in soil-plant system: Effects of plastic mulch film residues on wheat (*Triticum aestivum*) growth. *Science of The Total Environment* **2018**, 645, 1048-1056. DOI: 10.1016/j.scitotenv.2018.07.229.
- (64) Shahmohamadloo, R. S.; Lissemore, L.; Prosser, R. S.; Sibley, P. K. Evaluating the effects of triclosan on 3 field crops grown in 4 formulations of biosolids. *Environmental Toxicology and Chemistry* **2017**, 36 (7), 1896-1908. DOI: 10.1002/etc.3712.
- (65) Barbera, A. C.; Leonardi, G.; Ferrante, M.; Zuccarello, P.; Maucieri, C. Effects of pharmaceuticals (Caffeine and Ibuprofen) and AMF inoculation on the growth and yield of *Oryza sativa* L. *Agricultural Water Management* **2020**, 232, 106005. DOI: 10.1016/j.agwat.2020.106005.
- (66) Xu, D.; Pan, H.; Yao, J.; Feng, Y.; Wu, P.; Shao, K. Stress responses and biological residues of sulfanilamide antibiotics in *Arabidopsis thaliana*. *Ecotoxicology and Environmental Safety* **2020**, 199, 110727. DOI: 10.1016/j.ecoenv.2020.110727.

- (67) Kaposi, K. L.; Mos, B.; Kelaher, B. P.; Dworjanyn, S. A. Ingestion of Microplastic Has Limited Impact on a Marine Larva. *Environmental Science & Technology* **2014**, *48* (3), 1638-1645. DOI: 10.1021/es404295e.
- (68) Mateos-Cárdenas, A.; Scott, D. T.; Seitmaganbetova, G.; Frank N.A.M, v. P.; John, O. H.; Marcel A.K, J. Polyethylene microplastics adhere to *Lemna minor* (L.), yet have no effects on plant growth or feeding by *Gammarus duebeni* (Lillj.). *Science of The Total Environment* **2019**, *689*, 413-421. DOI: 10.1016/j.scitotenv.2019.06.359.
- (69) Bruck, S.; Ford, A. T. Chronic ingestion of polystyrene microparticles in low doses has no effect on food consumption and growth to the intertidal amphipod *Echinogammarus marinus*? *Environmental Pollution* **2018**, *233*, 1125-1130. DOI: 10.1016/j.envpol.2017.10.015.
- (70) Jacob, H.; Gilson, A.; Lanctôt, C.; Besson, M.; Metian, M.; Lecchini, D. No Effect of Polystyrene Microplastics on Foraging Activity and Survival in a Post-larvae Coral-Reef Fish, *Acanthurus triostegus*. *Bulletin of Environmental Contamination and Toxicology* **2019**, *102* (4), 457-461. DOI: 10.1007/s00128-019-02587-0.
- (71) Lynch, I.; Klaper, R. Telling the important stories of “no adverse effect” nanomaterials data. *Environmental Science: Nano* **2021**, *8* (6), 1496-1499. DOI: 10.1039/D1EN90018H.

Supplementary information

Table S6.1. Chemical contaminants stock solution.

Compound	Mass [mg]
acetaminophen	14.8
caffeine	41.1
carbamazepine	69.8
gemfibrozil	30.0
ibuprofen	100.5
sulfamethoxazole	677.6
sulfanilamide	199.3
triclosan	1493.5
acetone	15831.8

Table S6.2. Spiked chemical contaminant concentration [mg per kg fresh soil] in C and CP100 pots and their octanol-water partition coefficient ($\log K_{ow}$), molar mass, and chemical structure.

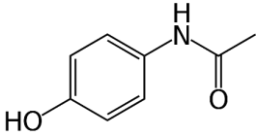
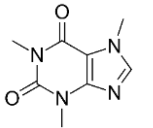
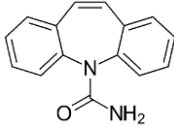
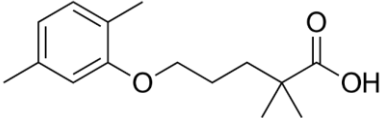
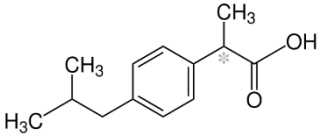
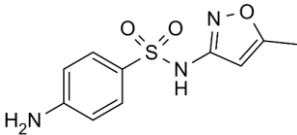
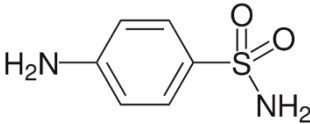
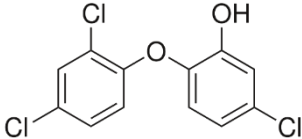
Compound	Concentration [mg/kg]	$\log K_{ow}$	Molar mass [g/mol]	Chemical structure
acetaminophen	0.03	0.46	151.2	
caffeine	0.09	-0.07	194.2	
carbamazepine	0.15	2.45	236.3	
gemfibrozil	0.06	4.24	250.3	
ibuprofen	0.21	3.97	206.3	
sulfamethoxazole	1.42	0.89	253.3	
sulfanilamide	0.42	-0.62	172.2	
triclosan	3.14	4.76	289.5	

Table S6.3. The composition of the fertilizer used on soils.

Concentrate	Fertilizer	Concentration [mg/L]
A	CaNO ₃	7.1
	NH ₄ NO ₃ (34%)	0.375
	Mg(NO ₃) ₂	3.62
	Fe (EDTA)	0.18
B	monopotassium phosphate (MKP)	1.6
	K ₂ SO ₄	1.87
	KNO ₃	0.62
C	Mn(SO ₄) ₂ (32.5%)	0.115
	ZnSO ₄ (23%)	0.031
	Borax (11.3%)	0.058
	CuSO ₄ (24%)	0.002
	Mo (39.6%)	0.011

Table S6.4. Enzyme and substrate pairings. (MUB = 4-methylumbelliferyl)

Enzyme	EC number	Substrate
β-glucosidase	3.2.1.21	MUB β-D-glucopyranoside
chitinase	3.2.1.14	MUB N-acetyl-β-D-glucosaminide
xylan 1,4-β-xylosidase	3.2.1.37	MUB-β-D-xylopyranoside
phosphatase	3.1.3.x	MUB phosphate (free acid)

Table S6.5. Weighted UniFrac distance of the soil microbial communities' amplicon sequence variants pairwise PERMANOVA results for control (CTRL), 10 mg HDPE microplastic kg⁻¹ soil (P10), 100 mg HDPE microplastic kg⁻¹ soil (P100), chemical contaminants + 100 mg HDPE microplastic kg⁻¹ soil (CP100), and chemical contaminants (C) treated soils. PRE (pre-treatment) is a composite sample of the uncontaminated soils. $q < 0.05$ is significant.

Group 1	Group 2	Sample size	Permutations	pseudo-F	p-value	q-value
C	CP100	30	1000000	1.95	0.0110	0.0329
C	CTRL	30	1000000	2.55	0.0020	0.0076
C	P10	30	1000000	1.76	0.0265	0.0517
C	P100	30	1000000	3.06	0.0003	0.0050
C	PRE	18	1000000	3.70	0.0012	0.0062
CP100	CTRL	30	1000000	1.31	0.1366	0.1862
CP100	P10	30	1000000	1.26	0.1636	0.2036
CP100	P100	30	1000000	1.64	0.0315	0.0517
CP100	PRE	18	1000000	2.88	0.0012	0.0062
CTRL	P10	30	1000000	0.58	0.9699	0.9699
CTRL	P100	30	1000000	1.02	0.3933	0.4214
CTRL	PRE	18	1000000	1.92	0.0330	0.0517
P10	P100	30	1000000	1.23	0.1764	0.2036
P10	PRE	18	1000000	2.02	0.0282	0.0517
P100	PRE	18	1000000	1.95	0.0345	0.0517

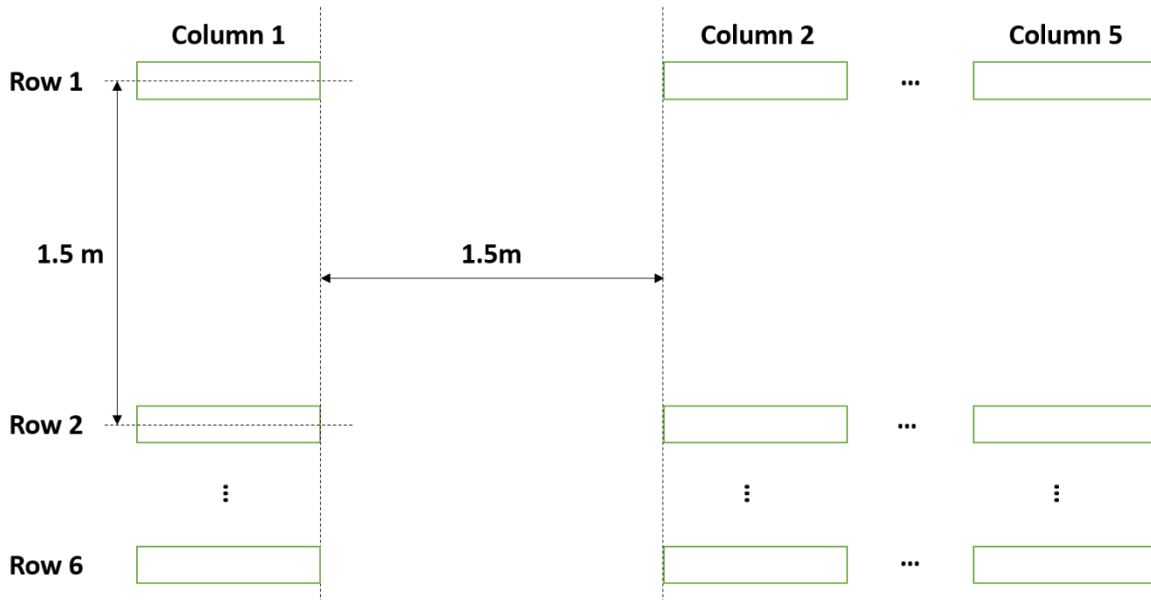


Figure S6.1. Top-down view of outdoor layout of strawberry pots (green rectangles).

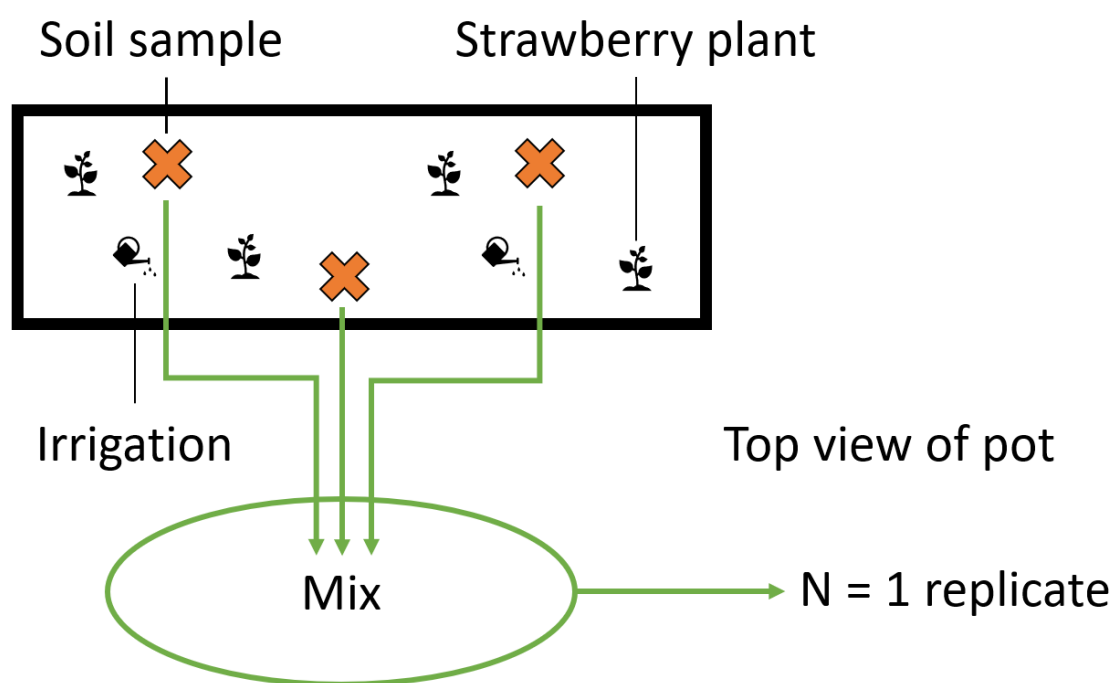


Figure S6.2. Approximate location of strawberry plants, irrigation, and soil sampling in each pot. The mixing was performed in an aluminum tray near the pot, before being transferred to glassware for transportation and further analysis in a lab setting.

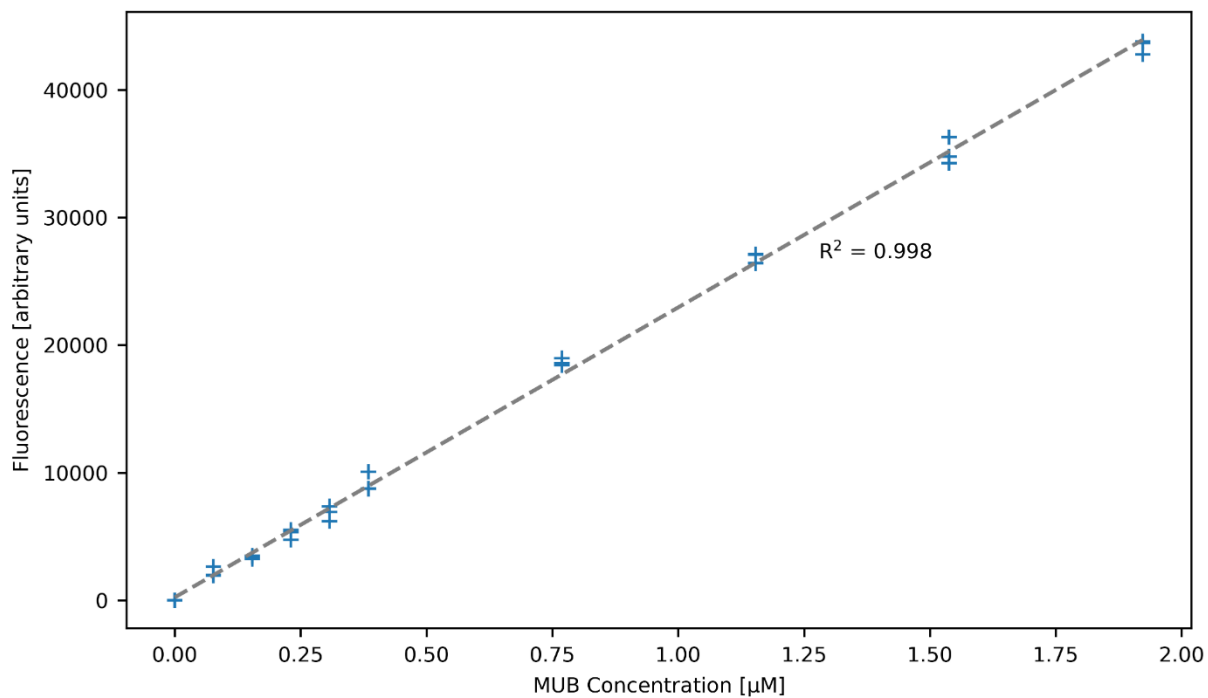


Figure S6.3. Fluorescence of 4-methylumbelliferone (MUB) in buffer at various concentrations and after NaOH addition. This plot shows that the fluorescence of MUB is linearly correlated to its concentration when the MUB concentration is below 1.92 μM. The highest concentration shown here is equivalent to Well C in Table S6.6.

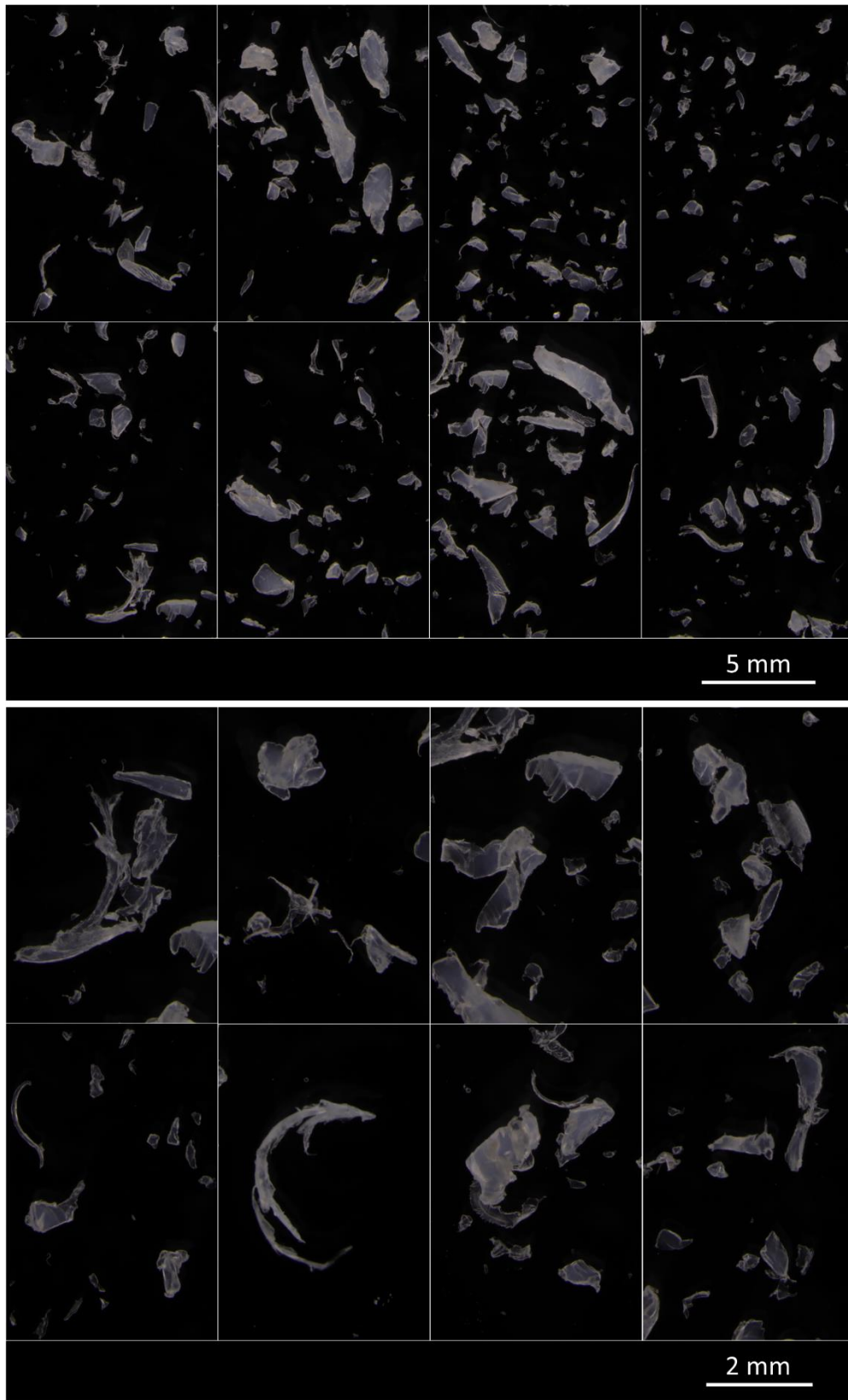


Figure S6.4. Images of HDPE microplastics taken under a stereomicroscope in dark-field mode.

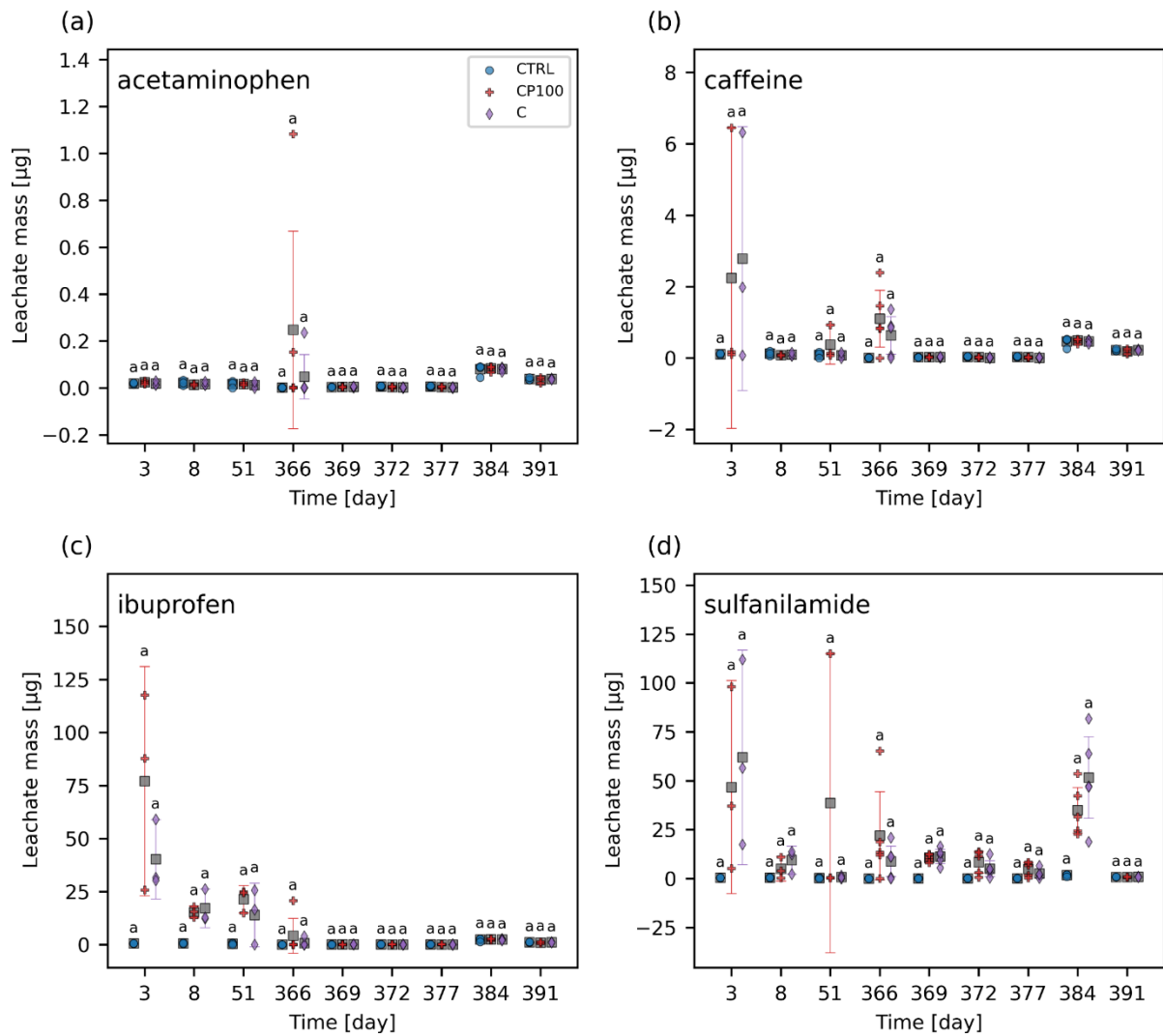


Figure S6.5. Leachate mass data for (a) acetaminophen, (b) caffeine, (c) ibuprofen, and (d) sulfanilamide in control (CTRL), chemical contaminants + 100 mg HDPE microplastic kg⁻¹ soil (CP100), and chemical contaminants (C) treated soils. No leachate data was collected for the intervals including day 52 – 363, 392 – 456. For each timepoint, treatments with the same letter have no significant difference between them. Markers represent individual replicates. Grey squares represent the mean. Error bars show 2 × the standard error of the mean.

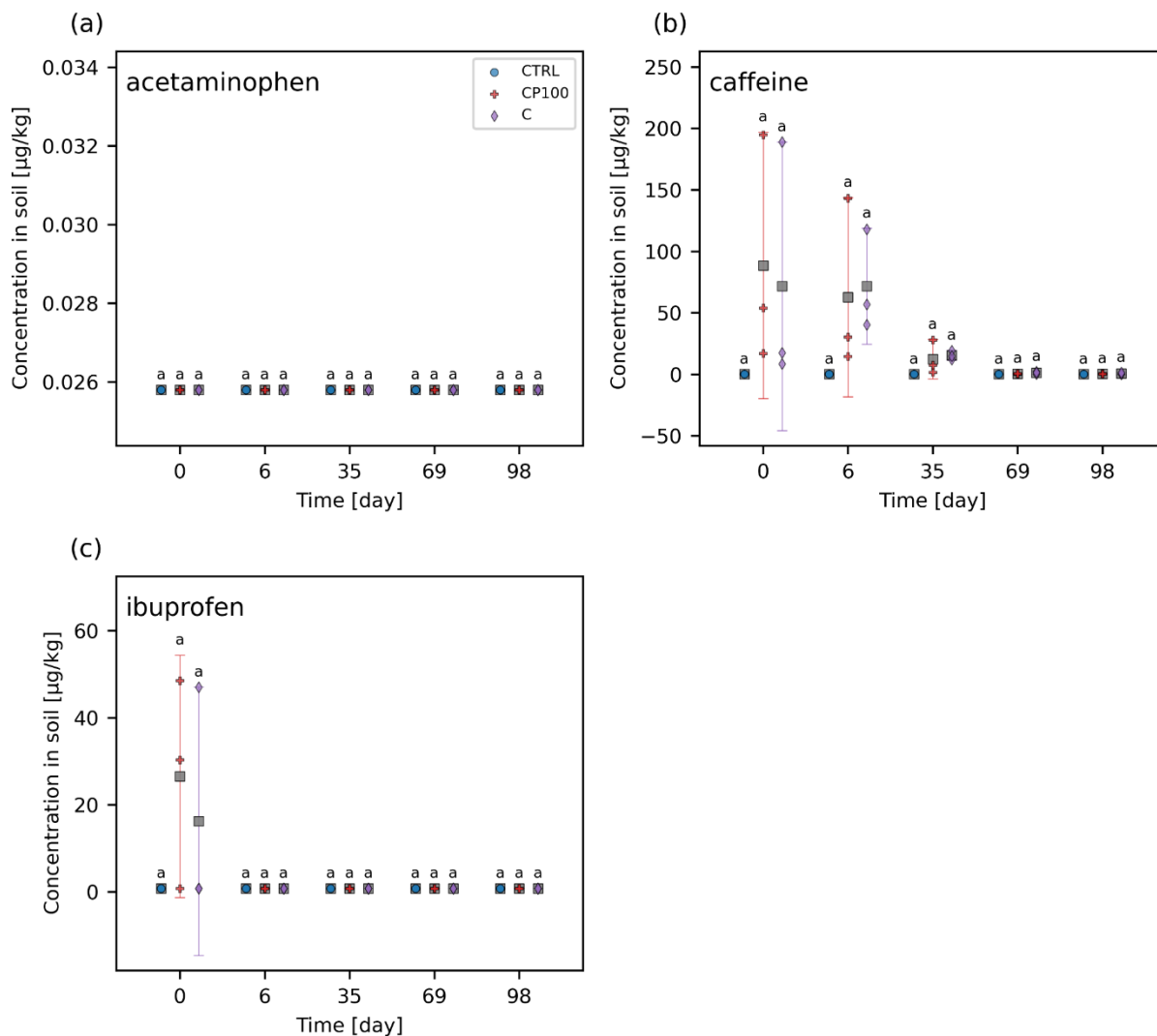


Figure S6.6. Concentration of (a) acetaminophen, (b) caffeine, and (c) ibuprofen in control (CTRL), chemical contaminants + 100 mg HDPE microplastic kg^{-1} soil (CP100), and chemical contaminants (C) treated soils. For each timepoint, treatments with the same letter have no significant difference between them. Markers represent individual replicates. Grey squares represent the mean. Error bars show $2 \times$ the standard error of the mean.

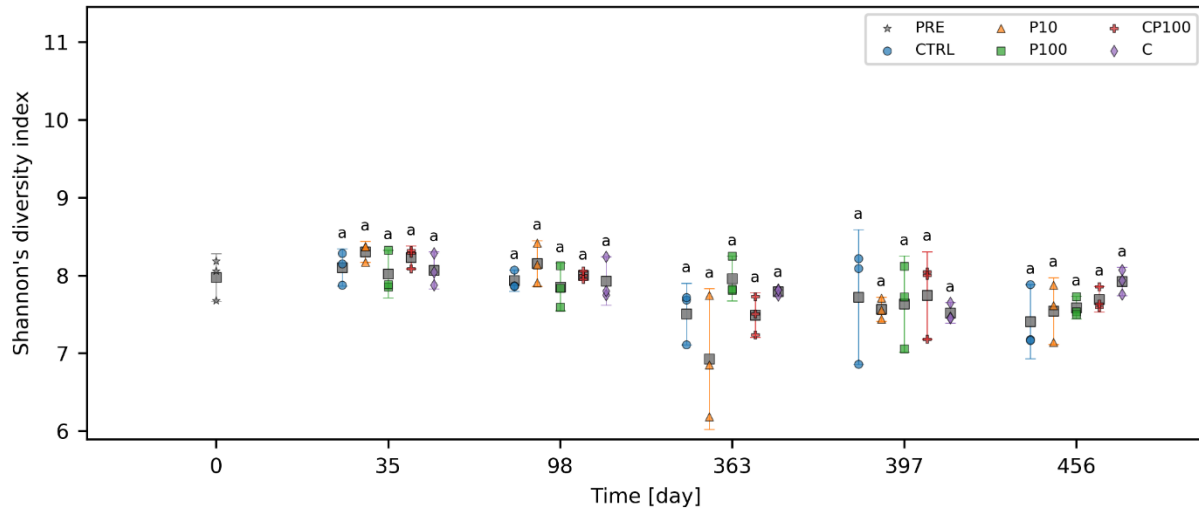


Figure S6.7. Shannon's diversity index of control (CTRL), 10 mg HDPE microplastic kg^{-1} soil (P10), 100 mg HDPE microplastic kg^{-1} soil (P100), chemical contaminants + 100 mg HDPE microplastic kg^{-1} soil (CP100), and chemical contaminants (C) treated soils. PRE (pre-treatment) is a composite sample of the uncontaminated soils. For each timepoint, treatments with the same letter have no significant difference between them. No letters are present for PRE, since there were no other treatments to compare it to on day 0. Markers represent individual replicates. Grey squares represent the mean. Error bars show $2 \times$ the standard error of the mean.

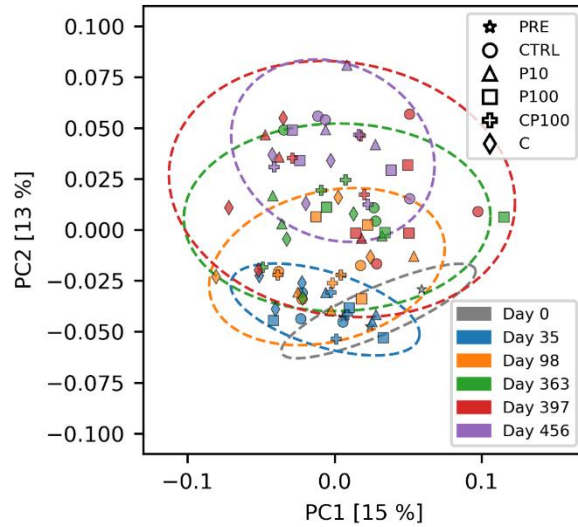


Figure S6.8. Principal coordinate analysis (PCoA) of the weighted UniFrac distance of the soil microbial communities' amplicon sequence variants in control (CTRL), 10 mg HDPE microplastic kg⁻¹ soil (P10), 100 mg HDPE microplastic kg⁻¹ soil (P100), chemical contaminants + 100 mg HDPE microplastic kg⁻¹ soil (CP100), and chemical contaminants (C) treated soils. PRE (pre-treatment) is a composite sample of the uncontaminated soils. Ellipses represent the zone where 95 % of samples from a bivariate normal distribution with the same mean and covariance matrix as the respective treatment would be drawn from. Numbers in brackets indicate the amount of variance captured by that principal coordinate (PC). This figure shows the same data as Figure 6.4, but with markers representing treatments and colour representing time to better illustrate the temporal effects on the microbial community composition.

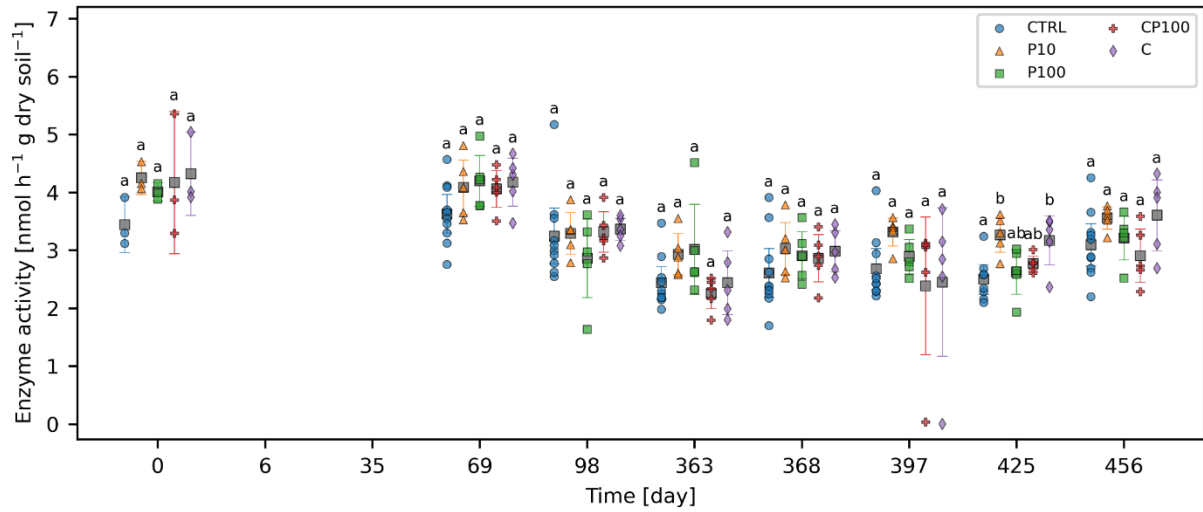


Figure S6.9. Phosphatase activity over the course of two growing seasons in control (CTRL), 10 mg HDPE microplastic kg⁻¹ soil (P10), 100 mg HDPE microplastic kg⁻¹ soil (P100), chemical contaminants + 100 mg HDPE microplastic kg⁻¹ soil (CP100), and chemical contaminants (C) treated soils. Day 6 and 35 data were omitted due to a potential contamination of the MUB-linked substrates. For each timepoint, treatments with the same letter have no significant difference between them. Markers represent individual replicates. Grey squares represent the mean. Error bars show 2 × the standard error of the mean.

Calculation of enzyme activity

Enzyme activity was calculated by measuring the fluorescence from 4-methylumbelliferone (MUB). When a 4-methylumbelliferyl-linked substrate (MUB-substrate) is exposed to soil extract, the enzymes extracted from the soil begin to catalyze the MUB-substrate, releasing MUB in the process. To isolate the fluorescence originating from the MUB, the background fluorescence and/or fluorescence quenching from the soil extract and the MUB-substrate after the 2-hour incubation period would have to be measured and subtracted. However, this is not possible, given that the MUB-substrate readily reacts in soil extract. Therefore, a quench coefficient (q) must be calculated which estimates the degree to which the soil extract quenches fluorescence. The net fluorescence from the produced MUB and the remaining unreacted MUB-substrate after the 2-hour incubation period ($F_B - F_F$) is then corrected using the quench coefficient to estimate what the fluorescence of this mixture would have been without the quenching effect of the soil extract. This value can then be subtracted by the net fluorescence of the MUB-linked substrate in buffer ($F_A - F_E$). The data is then normalized as outlined below.

Table S6.6. Each plate contained the following types of wells.

Well	200 μ L	50 μ L	10 μ L	Wells per plate
A	50 mM sodium acetate buffer	200 μ M MUB-substrate solution	1 M NaOH	4
B	soil extract	200 μ M MUB-substrate solution	1 M NaOH	2
C	50 mM sodium acetate buffer	10 μ M MUB solution	1 M NaOH	4
D	soil extract	10 μ M MUB solution	1 M NaOH	2
E	50 mM sodium acetate buffer	50 mM sodium acetate buffer	1 M NaOH	4
F	soil extract	50 mM sodium acetate buffer	1 M NaOH	2

The mean fluorescence F from these wells was used to calculate the enzyme activity as follows:

$$q = \frac{F_D - F_F}{F_C - F_E}$$

$$e = \frac{F_C - F_E}{0.5 \text{ nmol MUB}}$$

$$E = \frac{\left(\frac{F_B - F_F}{q} - (F_A - F_E) \right)}{e \times t \times c \times v}$$

Where:

- E is the enzyme activity [(nmol MUB)/(h \times (g soil))]
- q is the quench coefficient
- e is the emission coefficient [(net fluorescence) / (nmol MUB)]
- t is the reaction time (~2 h, exact value recorded from timestamps)
- c is the soil in buffer concentration (16 g soil / L buffer)
- v is the soil extract volume (200×10^{-6} L)

Qiime2 commands

```
qiime tools import \  
  --type 'SampleData[PairedEndSequencesWithQuality]' \  
  --input-path manifest.tsv \  
  --output-path paired-end-demux.qza \  
  --input-format PairedEndFastqManifestPhred33V2  
  
qiime demux summarize \  
  --i-data paired-end-demux.qza \  
  --o-visualization paired-end-demux.qzv  
  
qiime dada2 denoise-paired \  
  --i-demultiplexed-seqs paired-end-demux.qza \  
  --p-trim-left-f 6 \  
  --p-trim-left-r 6 \  
  --p-trunc-len-f 244 \  
  --p-trunc-len-r 244 \  
  --o-table table.qza \  
  --o-representative-sequences rep-seqs.qza \  
  --o-denoising-stats denoising-stats.qza  
  
qiime feature-table summarize \  
  --i-table table.qza \  
  --o-visualization table.qzv \  
  --m-sample-metadata-file sample-metadata.tsv  
  
qiime feature-table tabulate-seqs \  
  --i-data rep-seqs.qza \  
  --o-visualization rep-seqs.qzv  
  
qiime metadata tabulate \  
  --m-input-file denoising-stats.qza \  
  --o-visualization denoising-stats.qzv  
  
qiime phylogeny align-to-tree-mafft-fasttree \  
  --i-sequences rep-seqs.qza \  
  --o-alignment aligned-rep-seqs.qza \  
  --o-masked-alignment masked-aligned-rep-seqs.qza \  
  --o-tree unrooted-tree.qza \  
  --o-rooted-tree rooted-tree.qza  
  
qiime diversity core-metrics-phylogenetic \  
  --i-phylogeny rooted-tree.qza \  
  --i-table table.qza \  
  --p-sampling-depth 12462 \  
  --m-metadata-file sample-metadata.tsv \  
  --output-dir core-metrics-results  
  
qiime tools export \  
  --input-path core-metrics-results/weighted_unifrac_pcoa_results.qza \  
  --output-path exported-data/weighted_unifrac_pcoa_results
```

```

qiime diversity alpha-group-significance \
  --i-alpha-diversity core-metrics-results/shannon_vector.qza \
  --m-metadata-file sample-metadata.tsv \
  --o-visualization core-metrics-results/shannon-group-significance.qzv

qiime diversity alpha-correlation \
  --i-alpha-diversity core-metrics-results/shannon_vector.qza \
  --m-metadata-file sample-metadata.tsv \
  --o-visualization core-metrics-results/shannon-correlation.qzv

qiime diversity beta-group-significance \
  --i-distance-matrix core-metrics-results/weighted_unifrac_distance_matrix.qza \
  --m-metadata-file sample-metadata.tsv \
  --m-metadata-column Treatment \
  --o-visualization core-metrics-results/weighted-unifrac-treatment-significance.qzv \
  --p-pairwise \
  --p-permutations 1000000

qiime diversity alpha-rarefaction \
  --i-table table.qza \
  --i-phylogeny rooted-tree.qza \
  --p-max-depth 30000 \
  --m-metadata-file sample-metadata.tsv \
  --o-visualization alpha-rarefaction.qzv

qiime feature-classifier classify-sklearn \
  --i-classifier gg-13-8-99-515-806-nb-classifier.qza \
  --i-reads rep-seqs.qza \
  --o-classification taxonomy.qza

qiime taxa barplot \
  --i-table table.qza \
  --i-taxonomy taxonomy.qza \
  --m-metadata-file sample-metadata.tsv \
  --o-visualization taxa-bar-plots.qzv

qiime metadata tabulate \
  --m-input-file taxonomy.qza \
  --o-visualization taxonomy.qzv

```

Significance tests

Table S6.7. Significance testing for contaminants leachate samples found in Figures 6.1 and S6.5. HB = Holm-Bonferroni.

Dependent variable	Time	Test	Statistic	p-value	α with HB correction	Is $p < \alpha$?
Acetaminophen	3	One-way ANOVA	0.51	0.623	0.013	FALSE
Acetaminophen	8	One-way ANOVA	0.52	0.619	0.010	FALSE
Acetaminophen	51	One-way ANOVA	0.11	0.895	0.025	FALSE
Acetaminophen	366	Kruskal-Wallis H-test	1.24	0.538	0.008	FALSE
Acetaminophen	369	One-way ANOVA	0.11	0.900	0.050	FALSE
Acetaminophen	372	One-way ANOVA	4.32	0.039	0.006	FALSE
Acetaminophen	377	One-way ANOVA	4.32	0.039	0.006	FALSE
Acetaminophen	384	Kruskal-Wallis H-test	1.85	0.396	0.007	FALSE
Acetaminophen	391	One-way ANOVA	0.33	0.733	0.017	FALSE
Caffeine	3	Kruskal-Wallis H-test	1.16	> 0.1	0.025	FALSE
Caffeine	8	One-way ANOVA	0.52	0.619	0.010	FALSE
Caffeine	51	Kruskal-Wallis H-test	0.97	> 0.1	0.050	FALSE
Caffeine	366	Kruskal-Wallis H-test	4.88	0.087	0.007	FALSE
Caffeine	369	One-way ANOVA	0.11	0.900	0.017	FALSE
Caffeine	372	One-way ANOVA	4.32	0.039	0.006	FALSE
Caffeine	377	One-way ANOVA	4.32	0.039	0.006	FALSE
Caffeine	384	Kruskal-Wallis H-test	1.85	0.396	0.008	FALSE
Caffeine	391	One-way ANOVA	0.33	0.733	0.013	FALSE
Carbamazepine	3	Kruskal-Wallis H-test	5.42	0.086	0.025	FALSE
Carbamazepine	8	Kruskal-Wallis H-test	5.96	0.029	0.013	FALSE
Carbamazepine	51	Kruskal-Wallis H-test	4.36	> 0.1	0.050	FALSE
Carbamazepine	366	Kruskal-Wallis H-test	9.78	0.008	0.006	FALSE
Carbamazepine	369	Kruskal-Wallis H-test	9.98	0.007	0.006	FALSE
Carbamazepine	372	Kruskal-Wallis H-test	9.62	0.008	0.007	FALSE
Carbamazepine	377	Kruskal-Wallis H-test	9.42	0.009	0.008	FALSE
Carbamazepine	384	Kruskal-Wallis H-test	9.40	0.009	0.010	FALSE
Carbamazepine	391	Kruskal-Wallis H-test	5.96	0.029	0.017	FALSE
Gemfibrozil	3	Kruskal-Wallis H-test	5.42	0.086	0.007	FALSE
Gemfibrozil	8	One-way ANOVA	0.89	0.457	0.013	FALSE
Gemfibrozil	51	One-way ANOVA	0.11	0.895	0.025	FALSE
Gemfibrozil	366	Kruskal-Wallis H-test	2.54	0.281	0.008	FALSE
Gemfibrozil	369	One-way ANOVA	0.11	0.900	0.050	FALSE
Gemfibrozil	372	One-way ANOVA	4.32	0.039	0.006	FALSE
Gemfibrozil	377	One-way ANOVA	4.32	0.039	0.006	FALSE
Gemfibrozil	384	Kruskal-Wallis H-test	1.85	0.396	0.010	FALSE
Gemfibrozil	391	One-way ANOVA	0.33	0.733	0.017	FALSE
Ibuprofen	3	Kruskal-Wallis H-test	5.60	0.050	0.007	FALSE
Ibuprofen	8	Kruskal-Wallis H-test	5.42	0.086	0.008	FALSE

Ibuprofen	51	Kruskal-Wallis H-test	3.47	> 0.1	0.050	FALSE
Ibuprofen	366	Kruskal-Wallis H-test	1.24	0.538	0.013	FALSE
Ibuprofen	369	One-way ANOVA	0.11	0.900	0.025	FALSE
Ibuprofen	372	One-way ANOVA	4.32	0.039	0.006	FALSE
Ibuprofen	377	One-way ANOVA	4.32	0.039	0.006	FALSE
Ibuprofen	384	Kruskal-Wallis H-test	1.85	0.396	0.010	FALSE
Ibuprofen	391	One-way ANOVA	0.33	0.733	0.017	FALSE
Sulfamethoxazole	3	Kruskal-Wallis H-test	5.60	0.050	0.025	FALSE
Sulfamethoxazole	8	Kruskal-Wallis H-test	6.49	0.029	0.013	FALSE
Sulfamethoxazole	51	Kruskal-Wallis H-test	1.42	> 0.1	0.050	FALSE
Sulfamethoxazole	366	Kruskal-Wallis H-test	9.50	0.009	0.008	FALSE
Sulfamethoxazole	369	Kruskal-Wallis H-test	9.62	0.008	0.006	FALSE
Sulfamethoxazole	372	Kruskal-Wallis H-test	9.62	0.008	0.006	FALSE
Sulfamethoxazole	377	Kruskal-Wallis H-test	9.62	0.008	0.007	FALSE
Sulfamethoxazole	384	Kruskal-Wallis H-test	9.44	0.009	0.010	FALSE
Sulfamethoxazole	391	Kruskal-Wallis H-test	5.96	0.029	0.017	FALSE
Sulfanilamide	3	Kruskal-Wallis H-test	5.60	0.050	0.013	FALSE
Sulfanilamide	8	Kruskal-Wallis H-test	4.36	> 0.1	0.025	FALSE
Sulfanilamide	51	Kruskal-Wallis H-test	0.47	> 0.1	0.050	FALSE
Sulfanilamide	366	Kruskal-Wallis H-test	8.34	0.015	0.010	FALSE
Sulfanilamide	369	Kruskal-Wallis H-test	9.42	0.009	0.008	FALSE
Sulfanilamide	372	Kruskal-Wallis H-test	9.62	0.008	0.007	FALSE
Sulfanilamide	377	Kruskal-Wallis H-test	9.78	0.008	0.006	FALSE
Sulfanilamide	384	Kruskal-Wallis H-test	10.00	0.007	0.006	FALSE
Sulfanilamide	391	One-way ANOVA	0.33	0.733	0.017	FALSE
Triclosan	3	Kruskal-Wallis H-test	3.20	> 0.1	0.050	FALSE
Triclosan	8	One-way ANOVA	0.52	0.619	0.013	FALSE
Triclosan	51	One-way ANOVA	0.11	0.895	0.025	FALSE
Triclosan	366	Kruskal-Wallis H-test	4.74	0.093	0.008	FALSE
Triclosan	369	Kruskal-Wallis H-test	8.18	0.017	0.006	FALSE
Triclosan	372	Kruskal-Wallis H-test	5.16	0.076	0.007	FALSE
Triclosan	377	One-way ANOVA	4.32	0.039	0.006	FALSE
Triclosan	384	Kruskal-Wallis H-test	1.85	0.396	0.010	FALSE
Triclosan	391	One-way ANOVA	0.33	0.733	0.017	FALSE

Table S6.8. Significance testing for contaminants soil samples found in Figures 6.2 and S6.6. HB = Holm-Bonferroni.

Dependent variable	Time	Test	Statistic	p-value	α with HB correction	Is $p < \alpha$?
Acetaminophen	0	None (All values equal)	None (All values equal)	1.000	0.010	FALSE
Acetaminophen	6	None (All values equal)	None (All values equal)	1.000	0.013	FALSE
Acetaminophen	35	None (All values equal)	None (All values equal)	1.000	0.017	FALSE
Acetaminophen	69	None (All values equal)	None (All values equal)	1.000	0.025	FALSE
Acetaminophen	98	None (All values equal)	None (All values equal)	1.000	0.050	FALSE
Caffeine	0	Kruskal-Wallis H-test	5.79	0.029	0.010	FALSE
Caffeine	6	Kruskal-Wallis H-test	5.79	0.029	0.013	FALSE
Caffeine	35	Kruskal-Wallis H-test	5.79	0.029	0.017	FALSE
Caffeine	69	Kruskal-Wallis H-test	3.23	> 0.1	0.025	FALSE
Caffeine	98	Kruskal-Wallis H-test	2.10	> 0.1	0.050	FALSE
Carbamazepine	0	Kruskal-Wallis H-test	5.61	0.050	0.025	FALSE
Carbamazepine	6	Kruskal-Wallis H-test	5.79	0.029	0.010	FALSE
Carbamazepine	35	Kruskal-Wallis H-test	5.61	0.050	0.050	FALSE
Carbamazepine	69	Kruskal-Wallis H-test	5.79	0.029	0.013	FALSE
Carbamazepine	98	Kruskal-Wallis H-test	5.79	0.029	0.017	FALSE
Gemfibrozil	0	Kruskal-Wallis H-test	5.79	0.029	0.010	FALSE
Gemfibrozil	6	Kruskal-Wallis H-test	6.16	0.029	0.013	FALSE
Gemfibrozil	35	Kruskal-Wallis H-test	2.88	> 0.1	0.017	FALSE
Gemfibrozil	69	None (All values equal)	None (All values equal)	1.000	0.025	FALSE
Gemfibrozil	98	None (All values equal)	None (All values equal)	1.000	0.050	FALSE
Ibuprofen	0	Kruskal-Wallis H-test	2.54	> 0.1	0.010	FALSE
Ibuprofen	6	None (All values equal)	None (All values equal)	1.000	0.013	FALSE
Ibuprofen	35	None (All values equal)	None (All values equal)	1.000	0.017	FALSE
Ibuprofen	69	None (All values equal)	None (All values equal)	1.000	0.025	FALSE
Ibuprofen	98	None (All values equal)	None (All values equal)	1.000	0.050	FALSE
Sulfamethoxazole	0	Kruskal-Wallis H-test	6.16	0.029	0.010	FALSE
Sulfamethoxazole	6	Kruskal-Wallis H-test	5.79	0.029	0.013	FALSE
Sulfamethoxazole	35	Kruskal-Wallis H-test	2.00	> 0.1	0.017	FALSE
Sulfamethoxazole	69	None (All values equal)	None (All values equal)	1.000	0.025	FALSE
Sulfamethoxazole	98	None (All values equal)	None (All values equal)	1.000	0.050	FALSE
Triclosan	0	Kruskal-Wallis H-test	5.61	0.050	0.017	FALSE
Triclosan	6	Kruskal-Wallis H-test	7.45	0.004	0.010	TRUE
Triclosan	35	Kruskal-Wallis H-test	5.61	0.050	0.025	FALSE
Triclosan	69	Kruskal-Wallis H-test	5.61	0.050	0.050	FALSE
Triclosan	98	Kruskal-Wallis H-test	6.16	0.029	0.013	FALSE

Table S6.9. Post hoc analysis for contaminants soil samples found in Figure 6.2.

Dependent variable	Time	Treatment 1	Treatment 2	Test	α	Is $p < \alpha$?
Triclosan	6	C	CP100	Mann-Whitney U test	0.017	FALSE
Triclosan	6	CTRL	C	Mann-Whitney U test	0.017	FALSE
Triclosan	6	CTRL	CP100	Mann-Whitney U test	0.017	FALSE

Table S6.10. Significance testing for enzyme activities found in Figures 6.5 and S6.9. HB = Holm-Bonferroni.

Dependent variable	Time	Test	Statistic	p-value	α with HB correction	Is $p < \alpha$?
chitinase	0	One-way ANOVA	0.24	0.912	0.050	FALSE
chitinase	6	One-way ANOVA	7.75	0.000	0.005	TRUE
chitinase	35	Kruskal-Wallis H-test	10.10	0.039	0.006	FALSE
chitinase	69	Kruskal-Wallis H-test	1.73	0.786	0.017	FALSE
chitinase	98	One-way ANOVA	0.68	0.615	0.013	FALSE
chitinase	363	Kruskal-Wallis H-test	5.23	0.265	0.010	FALSE
chitinase	368	Kruskal-Wallis H-test	5.97	0.201	0.008	FALSE
chitinase	397	Kruskal-Wallis H-test	6.96	0.138	0.007	FALSE
chitinase	425	One-way ANOVA	3.64	0.019	0.006	FALSE
chitinase	456	One-way ANOVA	0.40	0.808	0.025	FALSE
β -glucosidase	0	Kruskal-Wallis H-test	3.03	> 0.05	0.050	FALSE
β -glucosidase	6	One-way ANOVA	2.12	0.111	0.008	FALSE
β -glucosidase	35	One-way ANOVA	3.66	0.018	0.006	FALSE
β -glucosidase	69	Kruskal-Wallis H-test	2.90	0.575	0.025	FALSE
β -glucosidase	98	One-way ANOVA	1.74	0.173	0.010	FALSE
β -glucosidase	363	Kruskal-Wallis H-test	7.59	0.108	0.007	FALSE
β -glucosidase	368	Kruskal-Wallis H-test	7.75	0.101	0.006	FALSE
β -glucosidase	397	Kruskal-Wallis H-test	3.65	0.456	0.013	FALSE
β -glucosidase	425	One-way ANOVA	5.02	0.005	0.005	TRUE
β -glucosidase	456	One-way ANOVA	0.82	0.525	0.017	FALSE
phosphatase	0	One-way ANOVA	1.06	0.426	0.017	FALSE
phosphatase	69	One-way ANOVA	1.83	0.154	0.010	FALSE
phosphatase	98	Kruskal-Wallis H-test	2.85	0.584	0.025	FALSE
phosphatase	363	Kruskal-Wallis H-test	9.34	0.053	0.007	FALSE
phosphatase	368	One-way ANOVA	0.71	0.591	0.050	FALSE
phosphatase	397	Kruskal-Wallis H-test	7.20	0.126	0.008	FALSE
phosphatase	425	One-way ANOVA	4.89	0.005	0.006	TRUE
phosphatase	456	One-way ANOVA	1.78	0.163	0.013	FALSE
xylan 1,4- β -xylosidase	0	One-way ANOVA	0.50	0.738	0.017	FALSE
xylan 1,4- β -xylosidase	6	One-way ANOVA	4.20	0.011	0.005	FALSE
xylan 1,4- β -xylosidase	35	Kruskal-Wallis H-test	6.11	0.191	0.007	FALSE
xylan 1,4- β -xylosidase	69	Kruskal-Wallis H-test	1.86	0.761	0.025	FALSE
xylan 1,4- β -xylosidase	98	Kruskal-Wallis H-test	2.95	0.565	0.010	FALSE
xylan 1,4- β -xylosidase	363	Kruskal-Wallis H-test	9.76	0.045	0.006	FALSE
xylan 1,4- β -xylosidase	368	One-way ANOVA	0.54	0.710	0.013	FALSE
xylan 1,4- β -xylosidase	397	Kruskal-Wallis H-test	0.74	0.947	0.050	FALSE
xylan 1,4- β -xylosidase	425	One-way ANOVA	3.17	0.032	0.006	FALSE
xylan 1,4- β -xylosidase	456	One-way ANOVA	1.60	0.206	0.008	FALSE

Table S6.11. Post hoc analysis for enzyme activities found in Figures 6.5 and S6.9.

Dependent variable	Time	Treatment 1	Treatment 2	Test	α	Is $p < \alpha$?
chitinase	6	C	CP100	Tukey's HSD	0.05	FALSE
chitinase	6	C	CTRL	Tukey's HSD	0.05	FALSE
chitinase	6	C	P10	Tukey's HSD	0.05	FALSE
chitinase	6	C	P100	Tukey's HSD	0.05	FALSE
chitinase	6	CP100	CTRL	Tukey's HSD	0.05	FALSE
chitinase	6	CP100	P10	Tukey's HSD	0.05	TRUE
chitinase	6	CP100	P100	Tukey's HSD	0.05	FALSE
chitinase	6	CTRL	P10	Tukey's HSD	0.05	TRUE
chitinase	6	CTRL	P100	Tukey's HSD	0.05	FALSE
chitinase	6	P10	P100	Tukey's HSD	0.05	FALSE
β -glucosidase	425	C	CP100	Tukey's HSD	0.05	FALSE
β -glucosidase	425	C	CTRL	Tukey's HSD	0.05	TRUE
β -glucosidase	425	C	P10	Tukey's HSD	0.05	FALSE
β -glucosidase	425	C	P100	Tukey's HSD	0.05	FALSE
β -glucosidase	425	CP100	CTRL	Tukey's HSD	0.05	TRUE
β -glucosidase	425	CP100	P10	Tukey's HSD	0.05	FALSE
β -glucosidase	425	CP100	P100	Tukey's HSD	0.05	FALSE
β -glucosidase	425	CTRL	P10	Tukey's HSD	0.05	FALSE
β -glucosidase	425	CTRL	P100	Tukey's HSD	0.05	FALSE
β -glucosidase	425	P10	P100	Tukey's HSD	0.05	FALSE
phosphatase	425	C	CP100	Tukey's HSD	0.05	FALSE
phosphatase	425	C	CTRL	Tukey's HSD	0.05	TRUE
phosphatase	425	C	P10	Tukey's HSD	0.05	FALSE
phosphatase	425	C	P100	Tukey's HSD	0.05	FALSE
phosphatase	425	CP100	CTRL	Tukey's HSD	0.05	FALSE
phosphatase	425	CP100	P10	Tukey's HSD	0.05	FALSE
phosphatase	425	CP100	P100	Tukey's HSD	0.05	FALSE
phosphatase	425	CTRL	P10	Tukey's HSD	0.05	TRUE
phosphatase	425	CTRL	P100	Tukey's HSD	0.05	FALSE
phosphatase	425	P10	P100	Tukey's HSD	0.05	FALSE

Table S6.12. Significance testing for plant growth found in Figure 6.6. HB = Holm-Bonferroni, LUT = Lookup table.

Dependent variable	Time	Test	Statistic	p-value	α with HB correction	Is $p < \alpha$?
dry biomass	1	One-way ANOVA	0.56	0.698	0.025	FALSE
dry biomass	2	None (LUT unavailable)	None (LUT unavailable)	N/A	0.050	FALSE
flower stalks	1	One-way ANOVA	1.42	0.283	0.050	FALSE
flower stalks	2	One-way ANOVA	2.28	0.089	0.025	FALSE
leaves	1	One-way ANOVA	1.35	0.305	0.025	FALSE
leaves	2	One-way ANOVA	0.55	0.700	0.050	FALSE
strawberries	1	One-way ANOVA	0.83	0.529	0.025	FALSE
strawberries	2	One-way ANOVA	0.15	0.960	0.050	FALSE

Table S6.13. Significance testing for Shannon entropy found in Figure S6.7. HB = Holm-Bonferroni.

Dependent variable	Time	Test	Statistic	p-value	α with HB correction	Is $p < \alpha$?
Shannon entropy	35	One-way ANOVA	1.14	0.392	0.017	FALSE
Shannon entropy	98	One-way ANOVA	0.85	0.523	0.025	FALSE
Shannon entropy	363	One-way ANOVA	2.72	0.091	0.010	FALSE
Shannon entropy	397	One-way ANOVA	0.12	0.970	0.050	FALSE
Shannon entropy	456	One-way ANOVA	1.51	0.272	0.013	FALSE

Table S6.14. Significance testing for phylum-level relative abundance found in Figure 6.3. HB = Holm-Bonferroni.

Dependent variable	Time	Test	Statistic	p-value	α with HB correction	Is $p < \alpha$?
Acidobacteria	35	One-way ANOVA	0.88	0.507	0.050	FALSE
Acidobacteria	98	One-way ANOVA	1.00	0.451	0.025	FALSE
Acidobacteria	363	One-way ANOVA	4.39	0.026	0.010	FALSE
Acidobacteria	397	One-way ANOVA	1.44	0.292	0.017	FALSE
Acidobacteria	456	One-way ANOVA	1.50	0.275	0.013	FALSE
Actinobacteria	35	One-way ANOVA	2.92	0.077	0.013	FALSE
Actinobacteria	98	One-way ANOVA	0.42	0.789	0.025	FALSE
Actinobacteria	363	Kruskal-Wallis H-test	4.77	> 0.05	0.050	FALSE
Actinobacteria	397	One-way ANOVA	7.92	0.004	0.010	TRUE
Actinobacteria	456	One-way ANOVA	1.08	0.415	0.017	FALSE
Chloroflexi	35	One-way ANOVA	0.74	0.587	0.017	FALSE
Chloroflexi	98	One-way ANOVA	2.44	0.115	0.013	FALSE
Chloroflexi	363	Kruskal-Wallis H-test	3.93	> 0.05	0.025	FALSE
Chloroflexi	397	One-way ANOVA	4.91	0.019	0.010	FALSE
Chloroflexi	456	Kruskal-Wallis H-test	6.57	> 0.05	0.050	FALSE
Crenarchaeota	35	One-way ANOVA	0.47	0.754	0.050	FALSE
Crenarchaeota	98	One-way ANOVA	2.29	0.131	0.010	FALSE
Crenarchaeota	363	One-way ANOVA	2.26	0.134	0.013	FALSE
Crenarchaeota	397	One-way ANOVA	1.36	0.315	0.025	FALSE
Crenarchaeota	456	One-way ANOVA	1.74	0.217	0.017	FALSE
Firmicutes	35	One-way ANOVA	1.24	0.353	0.013	FALSE
Firmicutes	98	One-way ANOVA	0.76	0.577	0.050	FALSE
Firmicutes	363	One-way ANOVA	0.85	0.524	0.025	FALSE
Firmicutes	397	One-way ANOVA	4.37	0.027	0.010	FALSE
Firmicutes	456	One-way ANOVA	1.06	0.427	0.017	FALSE
Gemmatimonadetes	35	One-way ANOVA	1.15	0.390	0.017	FALSE
Gemmatimonadetes	98	One-way ANOVA	0.36	0.830	0.050	FALSE
Gemmatimonadetes	363	One-way ANOVA	4.60	0.023	0.010	FALSE
Gemmatimonadetes	397	One-way ANOVA	1.30	0.335	0.013	FALSE
Gemmatimonadetes	456	One-way ANOVA	0.53	0.720	0.025	FALSE

Nitrospirae	35	Kruskal-Wallis H-test	9.37	0.050	0.010	FALSE
Nitrospirae	98	One-way ANOVA	0.56	0.699	0.025	FALSE
Nitrospirae	363	One-way ANOVA	0.74	0.587	0.017	FALSE
Nitrospirae	397	One-way ANOVA	0.23	0.915	0.050	FALSE
Nitrospirae	456	One-way ANOVA	0.95	0.475	0.013	FALSE
Other	35	One-way ANOVA	0.94	0.478	0.013	FALSE
Other	98	One-way ANOVA	0.32	0.861	0.017	FALSE
Other	363	Kruskal-Wallis H-test	4.77	> 0.05	0.050	FALSE
Other	397	One-way ANOVA	3.31	0.057	0.010	FALSE
Other	456	One-way ANOVA	0.31	0.866	0.025	FALSE
Planctomycetes	35	One-way ANOVA	2.21	0.140	0.013	FALSE
Planctomycetes	98	One-way ANOVA	0.59	0.675	0.050	FALSE
Planctomycetes	363	One-way ANOVA	2.51	0.108	0.010	FALSE
Planctomycetes	397	One-way ANOVA	2.11	0.154	0.017	FALSE
Planctomycetes	456	One-way ANOVA	1.53	0.266	0.025	FALSE
Proteobacteria	35	One-way ANOVA	6.10	0.009	0.010	TRUE
Proteobacteria	98	One-way ANOVA	4.12	0.031	0.013	FALSE
Proteobacteria	363	One-way ANOVA	1.26	0.349	0.025	FALSE
Proteobacteria	397	One-way ANOVA	3.90	0.037	0.017	FALSE
Proteobacteria	456	One-way ANOVA	0.69	0.616	0.050	FALSE
Verrucomicrobia	35	Kruskal-Wallis H-test	1.73	> 0.05	0.025	FALSE
Verrucomicrobia	98	One-way ANOVA	0.17	0.950	0.017	FALSE
Verrucomicrobia	363	One-way ANOVA	1.64	0.239	0.010	FALSE
Verrucomicrobia	397	Kruskal-Wallis H-test	6.40	> 0.05	0.050	FALSE
Verrucomicrobia	456	One-way ANOVA	0.59	0.676	0.013	FALSE
WS3	35	One-way ANOVA	1.73	0.221	0.010	FALSE
WS3	98	One-way ANOVA	0.41	0.801	0.050	FALSE
WS3	363	One-way ANOVA	1.52	0.270	0.013	FALSE
WS3	397	One-way ANOVA	1.27	0.343	0.017	FALSE
WS3	456	One-way ANOVA	0.41	0.801	0.025	FALSE

Table S6.15. Post hoc analysis for phylum-level relative abundance found in Figure 6.3.

Dependent variable	Time	Treatment 1	Treatment 2	Test	α	Is $p < \alpha$?
Actinobacteria	397	C	CP100	Tukey's HSD	0.05	FALSE
Actinobacteria	397	C	CTRL	Tukey's HSD	0.05	TRUE
Actinobacteria	397	C	P10	Tukey's HSD	0.05	FALSE
Actinobacteria	397	C	P100	Tukey's HSD	0.05	FALSE
Actinobacteria	397	CP100	CTRL	Tukey's HSD	0.05	TRUE
Actinobacteria	397	CP100	P10	Tukey's HSD	0.05	FALSE
Actinobacteria	397	CP100	P100	Tukey's HSD	0.05	FALSE
Actinobacteria	397	CTRL	P10	Tukey's HSD	0.05	TRUE
Actinobacteria	397	CTRL	P100	Tukey's HSD	0.05	FALSE
Actinobacteria	397	P10	P100	Tukey's HSD	0.05	FALSE
Proteobacteria	35	C	CP100	Tukey's HSD	0.05	FALSE
Proteobacteria	35	C	CTRL	Tukey's HSD	0.05	TRUE
Proteobacteria	35	C	P10	Tukey's HSD	0.05	TRUE
Proteobacteria	35	C	P100	Tukey's HSD	0.05	FALSE
Proteobacteria	35	CP100	CTRL	Tukey's HSD	0.05	FALSE
Proteobacteria	35	CP100	P10	Tukey's HSD	0.05	FALSE
Proteobacteria	35	CP100	P100	Tukey's HSD	0.05	FALSE
Proteobacteria	35	CTRL	P10	Tukey's HSD	0.05	FALSE
Proteobacteria	35	CTRL	P100	Tukey's HSD	0.05	FALSE
Proteobacteria	35	P10	P100	Tukey's HSD	0.05	FALSE

Chapter 7: Comprehensive discussion

This chapter is a comprehensive discussion of Chapters 2 – 6. Whereas those chapters are standalone chapters that could be understood without reading any other parts of this thesis, Chapter 7 aims to form a discussion around the relationship between the chapters and how they contribute to answering the underlying research objectives outlined in Chapter 1. The limitations of any results obtained and analyses performed are also discussed along with avenues for future work to expand upon the findings discussed here. To avoid repetition, this chapter will mainly focus on discussing results in the context of this thesis. For a more comprehensive discussion of results in the context of the wider literature, please refer to the discussions contained within individual chapters.

7.1 Gaps in the green carbon dot synthesis literature

We began with a critical review of the green CD synthesis literature in Chapter 2 to identify knowledge gaps that are holding these CDs back from having equivalent features as those CDs synthesized from traditional methods. For instance, we revealed that approximately 78 % of green syntheses involved the use of renewable raw materials such as plants (Figure 2.1b). While using raw materials is more sustainable than using refined chemicals since fewer processing steps are required, a compromise can be made by using refined chemicals that are derived from naturally occurring renewable resources. We demonstrated this in Chapter 3 through a green synthesis of CDs from citric acid and phenylalanine which resulted in CDs with a quantum yield of 65 %. While we acknowledge that renewable refined compounds that are mass-produced in Nature are often synthesized from synthetic precursors when sold for commercial purposes, there often exists processes to create these compounds *via* biosynthesis as well.¹ Moreover, the use of renewable

refined compounds that exist in the natural environment can be a good starting point for identifying renewable raw materials that could make good potential precursors. For instance, we showed that high quantum yields can be achieved using citric acid and phenylalanine in a synthesis. This could lead to future research whereby water, citric acid, and phenylalanine is replaced by juice from a citrus fruit, such as lemons, and combined with phenylalanine, making the synthesis more sustainable overall. Going a step further, one may attempt to identify plants with high phenylalanine content to use in a synthesis in conjunction with lemon juice.

In Chapter 2, we showed that approximately 69 % of green syntheses were performed hydrothermally (Figure 2.1b). Indeed, we also performed a hydrothermal synthesis in Chapter 3, and this method remains popular for good reason. Most chemical labs will have access to a heating source that can reach temperatures up to 250 °C. A Teflon-lined autoclave chamber is a relatively cheap type of batch reactor. Moreover, hydrothermal syntheses are typically one-pot. Overall, the method is easy to implement and low cost to perform. However, hydrothermal synthesis times are long, and energy is not used as efficiently as in a microwave synthesis which heats the reaction medium directly. In Chapter 4, we repeated our citric acid and phenylalanine formula in a microwave setting and produced CDs with a quantum yield of 17 % when synthesizing with a solute mixture of 80 mol% phenylalanine and 20 mol% citric acid. While this is considerably lower than the 65 % quantum yield we achieved from hydrothermal synthesis in Chapter 3, we can not make any statistical comparison, since their quantum yields were measured using different instrumentation and control environments. Moreover, a comparison would not tell the entire story, since the synthesis performed in Chapter 4 was optimized more in favour of producing a larger product yield (*i.e.*, mass of CDs obtained), rather than quantum yield. However, such a comparison would be interesting to make in the future under a more standardized processing and

characterization protocol. We also note that this thesis stops short of performing a comprehensive direct comparison of how a starting reaction media with the same precursors could potentially result in CDs with different physicochemical properties when undergoing either a hydrothermal or a microwave synthesis with the same purification methods. It would be a very interesting study to conduct in the future whereby a common precursor is divided into two parts, one undergoes hydrothermal synthesis, another microwave, and their respective outputs undergo similar purification methods and characterization to observe differences.

Carbon dots, especially those synthesized *via* green synthesis methods, are perhaps best known for their characteristic blue-violet fluorescence. In Chapter 2, we showed that 89 % of green synthesized CDs had a peak emission wavelength less than 500 nm with the highest peak emission wavelength being 537 nm,² falling in the green light region (Figure 2.2f). This is in stark contrast to CdTeQDs which are readily available in a variety of peak fluorescence wavelengths with nearly nanometer precision. Moreover, several CDs synthesized by conventional methods from synthetic precursors have also shown emission at higher wavelengths. This phenomenon is displayed prominently in Chapter 4, whereby the blue-violet fluorescence from the green-synthesized NCDs was similar to the autofluorescence of the flies, but the SCDs and CdTeQDs had an easily distinguishable red fluorescence (Figure 4.6). This lack of higher wavelength emission is an area where green-synthesized CDs need significant improvement. One limitation may be that by restricting oneself to compounds or raw materials found in Nature, it can become difficult to find a combination of precursors to produce CDs with a higher peak fluorescence. Moreover, considering that the vast majority of green CD syntheses use plant products as starting materials, one must question how diverse these precursors truly are when many may consist of similar components such as cellulose.

An often-ignored aspect of CD synthesis is the relationship between synthesis inputs (*e.g.*, precursor material and synthesis and purification methods) and the resulting CD output properties (*e.g.*, peak fluorescence, quantum yield). Moreover, there is an important intermediary factor that needs to be studied further to understand how these inputs affect the output properties. A CD's physical and chemical properties are determined by the synthesis conditions. The physicochemical properties then determine the optical properties of the CD. The general gap in the literature is determining how one can control the physicochemical properties of CDs to achieve a certain result. While it is beyond the scope of any thesis to answer this question in its entirety given the endless combination of precursor, synthesis, and purification options possible, we can at the very least contribute a few pieces to the puzzle.

7.2 Understanding the relationship between carbon dot synthesis conditions, chemical structure, and optical properties

In Chapter 3, we performed a green CD synthesis with nine ratios of citric acid to phenylalanine, including only citric acid and only phenylalanine. It has already been established in the literature that nitrogen doping increases the quantum yield of CDs.³ This led to the question of whether increasing the nitrogen-to-carbon ratio of the reactants will continuously increase the quantum yield of the carbon dot. The results in Figure 3.1a were surprising, showing that the CDs that were synthesized using a phenylalanine mole fraction of 0.1 – 0.8 had minimal differences in their quantum yield despite having such a wide range of N:C ratios. This led us to investigate whether the N:C ratio in the carbon dot was actually the same as the ratio found in the reactants. Figure 3.1b showed that these two ratios are rarely equivalent. It was shown that the addition of an initial quantity of phenylalanine results in its reaction with citric acid in a 1:1 ratio of

phenylalanine to citric acid despite the excess citric acid. The stoichiometric ratio was revealed to be a 2:1 ratio of phenylalanine to citric acid. At this ratio, both the reactant mixture and carbon dot have a N:C ratio of 1:12.

Now that we have established a connection between the synthesis conditions (phenylalanine mole fraction) and the chemical properties (N:C ratio) of the carbon dot, we come back to the question of whether increasing nitrogen content will increase the quantum yield of a carbon dot. Figure 3.1c shows that there is a correlation between the $(\text{N:C})_{\text{CD}}$ and quantum yield, up until only phenylalanine is used in which case the quantum yield drops considerably and breaks the correlation. From here we developed a model (Equation 3.4, Figure 3.3) which illustrates that there is a strong correlation between quantum yield and the $(\text{O:C})_{\text{CD}}$ and the relative amount of oxygen found in carboxyl groups. This finding clearly demonstrates that while nitrogen plays a role in increasing the quantum yield of CDs, it is far from the only factor, nor is it necessarily the most important, since our model makes no use of nitrogen content or the type of functional groups the nitrogen is found in. This key finding helped us bridge gaps in the CD literature on how the chemical composition of a CD can influence its fluorescence quantum yield.

While we did provide methods to better understand the stoichiometry of CD syntheses and the role of the chemical structure in determining quantum yield, there are many other factors that may be at play that were not evaluated and would be great opportunities for further research. For instance, QDs experience the quantum confinement effect. This results in the peak fluorescence of QDs moving to higher wavelengths as their size becomes larger. While CDs experience many QD-like properties, the origin of their fluorescence is still not completely understood and, as a result, their peak fluorescence wavelength does not strictly depend on their size. Therefore, understanding how size can impact the peak fluorescence wavelengths and quantum yield of a CD can be critical

in advancing the impact that CDs can have in a variety of applications. If one could produce multiple CDs that differed only in size with similar chemical properties (*e.g.*, similar FTIR and XPS spectra) then we would be able to isolate the effect that size has on a CD's optical properties. However, controlling the chemical structure of a CD requires better understanding of how the synthesis conditions affect chemical structure. These two relationships, effect of synthesis conditions on CD physicochemical properties, and the effect of these properties on the CD optical properties are strongly linked and both will need to be investigated thoroughly to unlock the maximum potential of CDs, especially those made using green synthesis methods.

The ultimate goal of understanding the relationship between synthesis conditions, physicochemical properties, and optical properties is so that these CDs can be deployed in various applications. While the focus of Chapter 3 was to understand the role of stoichiometry and nitrogen doping on the physicochemical and optical properties of CDs, we also demonstrated that our CDs are capable of sensing Fe^{3+} (Figure 3.6). However, we also acknowledge in Chapter 2 that the use of green synthesized CDs in the applications of bioimaging and chemical sensing appears to be taking the attention away from other applications that are in need of more research such as light-emitting diodes and photovoltaics. Future research that reports on novel green CD syntheses should consider examining potential optoelectronic applications, if they have the means to do so, or if a bioimaging or chemical sensing application is to be shown, then screening for new cell types, organisms, or compounds should be attempted, when possible, to further expand the reach of green synthesized CDs.

7.3 Relative toxicity of carbon dots and CdTe quantum dots in *Drosophila melanogaster*

Alongside their potential to be synthesized sustainably, the other half of what makes the advancement of CD technology worth pursuing is their reduced toxicity when compared to cadmium-derived quantum dots. In Chapter 3, we synthesized CDs from phenylalanine and citric acid in a hydrothermal synthesis. In Chapter 4, we used the same precursors, but in a microwave synthesis to produce nitrogen-doped CDs (NCDs). We also used another CD that was previously reported in the literature by Macairan *et al.* consisting of glutathione and formamide in a microwave synthesis, resulting in nitrogen/sulfur-codoped CDs (SCDs).⁴ The NCDs had not yet been evaluated for toxicity, whereas the SCDs were found to have an IC₅₀ value of 148 mg/L in HeLa cells.⁴ However, the authors did show that 100 mg/L was suitable for bioimaging purposes without inducing considerable toxicity.⁴ When evaluating a dose-response effect from the NCDs, SCDs, and CdTeQDs on *Drosophila melanogaster*, this value became our upper limit on the assumption that higher concentrations were unlikely to be used in a biological organism in practice. We do acknowledge that in Chapter 3, we demonstrated a concentration dependent fluorescence quenching from < 50 μM Fe³⁺ when using a CD concentration of ~140 mg/L, however this was not in a biological system, and we also demonstrated fluorescence quenching from several ions with an ion concentration of 1000 μM and CD concentration of ~15 mg/L (Figure 3.6). A further investigation into the minimum CD concentration needed to still be suitable for low concentration ion sensing applications would be required if the system were to be used in a biological system. We had also conducted preliminary experiments with CdTeQDs to assess that 10 mg/kg in food would be the concentration where lethality would begin to be noticeable. These observations led

to the use of 0, 10, 40, 70, and 100 mg/kg as our concentrations for evaluating the developmental toxicity of NCDs, SCDs, and CdTeQDs in *Drosophila melanogaster*.

We determined that a CdTeQD concentration of 46 mg/kg in food was able to inhibit the development of 50 % of 1st instar larvae into adult flies (Figure S4.7b). Also concerning is that every additional 1 mg CdTeQD added per kg food would delay the emergence of adult flies by approximately 68 minutes in the 10 – 100 mg/kg range (Figure S4.9b). This is in contrast to NCDs and SCDs which showed no lethality or signs of developmental delays in the concentration range measured. We note that while the concentration range studied was justified as it is unlikely that higher concentrations would be used in practice, one limitation of our analysis is that we were unable to calculate precise EC₅₀ values for NCDs and SCDs beyond stating that their EC₅₀ > 100 mg/kg. Moreover, SCDs showed minor signs of inducing a dose-dependent biological response (Figure S4.9) whereby a significant, but weak, negative correlation between SCD concentration and development time was found. Similarly male flies exposed to 100 mg/kg SCDs had a greater mass than those raised on CTRL food, but only in the 2nd experimental block (Figure 4.3b). No significant differences were found in the 1st block. Investigating a higher concentration of SCD could have clarified if this result was simply noise, or the start of a larger trend that would only be observable at higher concentrations. When conducting sublethal toxicity assays at 100 mg/kg for NCDs and SCDs and 5 mg/kg for CdTeQDs, no toxicity was found on the reproductive performance, climbing ability, larvae crawling, fly mass, or locomotor activity of *Drosophila melanogaster*.

7.4 Ecotoxicology of HDPE microplastics

Carbon dots have emerged as an interesting class of nanoparticles. However, much work needs to be done before we begin to see their widespread use in consumer products. Therefore, while it is certainly important to test for their ability to induce toxicity in organisms, they are not currently considered a contaminant or pollutant of major concern to the environment or public health. Plastics on the other hand are a well know carbon-based material that have become essential in our everyday lives. Most plastics are released into the environment or landfills when disposed of,⁵ where they then break down into microplastics and possibly further into nanoplastics.⁶ While many toxicity studies exist evaluating the toxicity of nanoplastics and microplastics, efforts have largely focused on studying their effects in aquatic environments. While such studies are certainly valuable in furthering our understanding of the effects of microplastic pollution, there is a disconnect with the current situation we find ourselves in, which is that the majority of microplastics are found in terrestrial environments.⁷ Moreover, a disproportionate fraction of studies have evaluated the effects of polystyrene on organisms, whereas polyethylene and polypropylene are far more prevalent.⁵ Given that the use of plastics has been widespread for decades, it is generally understood that acute exposure to plastics, rarely results in toxicity. It would be difficult to imagine a scenario where someone who holds and drinks from a plastic water bottle everyday for a few days were to become severely ill from that action alone unless some other contaminant, such as cadmium or lead, was found in the plastic bottle. What is not as clear, is what the effects of such exposure are over the long term, or even over multiple generations. Moreover, the key difference between nano- and microplastics and their macroplastic counterparts, is their size. Specifically, nanoplastics are typically much smaller than eukaryotic cells, introducing the potential for cytotoxicity. These considerations set the stage for Chapters 5 and 6, whereby the

toxicity of HDPE microplastics are evaluated in animal and plant organisms, and soil microorganisms.

The microplastics used in Chapter 5 and 6 came from the same HDPE sheet. In both instances, the sheets were cut into small squares before undergoing mechanical weathering. In Chapter 5 a spice grinder was used to obtain < 38 µm microplastics, whereas in Chapter 6 a kitchen blender was used to obtain < 1 mm microplastics. These sizes were selected based on their relevance to each project. Fruit flies are small so smaller plastics which they would potentially be able to consume were used. For example, while a 1 mm plastic particle would be considered a microplastic to humans, to a fruit fly, it would be quite large. For context, it would be similar to evaluating whether 50 cm wide objects made of HDPE are toxic to adult humans. Conversely, the microplastics found in agricultural soils tend to cover a wider range of sizes. The microplastics used in the fruit fly studies were also UV weathered, a step that was deemed unnecessary in the agricultural study since it was performed outdoors where the soil and microplastics would be exposed to natural UV radiation.

In Chapter 5, the developmental toxicity of HDPE microplastics on *Drosophila melanogaster* was evaluated over the range of 0.1 – 10 000 mg/kg in food (Figure 5.2, 5.3). This range was used to cover the diverse concentrations of HDPE microplastics found in the environment, ranging from pristine environments to industrialized sites.⁸ No developmental toxicity was found in *Drosophila melanogaster* in this concentration range and no developmental delays were observed. Further experiments were conducted at 100 mg/kg HDPE microplastics to be better representative of the HDPE concentrations most likely to be found in the environment, rather than focusing on highly industrialized areas. No decline in reproductive performance of the flies over four generations was observed after exposure to HDPE microplastics (Figure 5.4).

Moreover, no sublethal toxic effects from the HDPE microplastics were observed in the climbing ability, larvae crawling, or fly mass as well (Figure 5.5).

In Chapter 6, soil was exposed to 100 mg/kg HDPE microplastics and pharmaceutically active compounds, either alone or together. Similar to Chapter 5, no decline was observed in the health of the strawberry plants throughout the two-year outdoor study from any of the treatments (Figure 6.6). Additionally, no overall trends were observed which would distinguish the soil enzyme activities between treatments throughout the study (Figure 6.5). The soils containing 100 mg/kg HDPE microplastics did not have a significant weighted UniFrac distance from the control soils. In other words, the HDPE microplastics were unable to alter the composition of the microorganisms found in the soil. However, not so surprisingly, the pharmaceutically active compounds were able to induce a biological response in the soil microorganisms and alter their composition. When adding the pharmaceutically active compounds to soil containing HDPE, an interesting phenomenon was observed. In the presence of 100 mg/kg HDPE microplastics, the pharmaceutically active compounds were no longer able to alter the soil microbial community composition. This implies that the HDPE microplastics could potentially be inhibiting the availability of the compounds to the soil microbial community. Future work could include determining a mechanism behind this interaction. For instance, determining the affinity of these compounds to adsorb to HDPE could provide an explanation. Another question to consider is whether it is these compounds directly, or rather some metabolite of these compounds that are interacting with the HDPE microplastics. This would be more complex to determine since there are any number of compound-bacteria interactions that could lead to a variety of metabolites. Another limitation of this analysis is that we did not look at how these treatments alter the number of bacteria in the soil as a whole, but only the relative abundance of the different types of bacteria

found in the soil. For instance, it remains unclear whether these significant changes to the soil microbial community are due to toxicity in certain bacteria species, growth promotion, or some combination of both. This limitation makes it difficult to state whether this ability of HDPE microplastics to inhibit the alteration of the soil microbial community is a positive effect or a toxic effect. However, one thing we can observe is that none of these treatments were able to significantly affect plant growth over the two-year outdoor study, so it appears that the impact of HDPE microplastics on our soil ecosystem was neutral.

A reoccurring limitation in Chapter 6 was that in some instances, the sample size was too small, making certain results appear as not significant, whereas they may have been significant with a higher replicate count. However, conducting an outdoor study is very resource and labour intensive, requiring the transportation of hundreds if not thousands of kilograms of soil and preparation of the field and irrigation to ensure that the soil from the experiment is contained and does not make its way into the natural environment. Therefore, instead of suggesting an overall higher sample size, I would recommend future outdoor studies to carefully consider which treatments are necessary to answer the research questions proposed. For instance, in Chapter 6, the removal of the 10 mg/kg HDPE microplastics treatment would result in the inability to make any statements about a dose-dependent effect but could also be used to increase the sample size of other treatments. Ultimately, there are many avenues that one can consider before embarking on a study of this scale, but one must also be prepared for the inherently higher variance expected from data that is obtained in an outdoor environment, and how this may impact statistical analyses moving forward. Valuable information could also be derived from an outdoor and indoor study being conducted in parallel. For instance, questions such as how variance is different between the two environments, or how many extra replicates would one need per treatment to obtain a similar

standard error on their data. This type of information can be useful for planning future studies if the goal is to conduct multiple outdoor studies over several years.

7.5 References

- (1) Kumar, D.; Jain, V. K.; Shanker, G.; Srivastava, A. Citric acid production by solid state fermentation using sugarcane bagasse. *Process Biochemistry* **2003**, *38* (12), 1731-1738. DOI: 10.1016/S0032-9592(02)00252-2.
- (2) Zhou, J.; Sheng, Z.; Han, H.; Zou, M.; Li, C. Facile synthesis of fluorescent carbon dots using watermelon peel as a carbon source. *Materials Letters* **2012**, *66* (1), 222-224. DOI: 10.1016/j.matlet.2011.08.081.
- (3) Liao, J.; Cheng, Z.; Zhou, L. Nitrogen-Doping Enhanced Fluorescent Carbon Dots: Green Synthesis and Their Applications for Bioimaging and Label-Free Detection of Au³⁺ Ions. *ACS Sustainable Chemistry & Engineering* **2016**, *4* (6), 3053-3061. DOI: 10.1021/acssuschemeng.6b00018.
- (4) Macairan, J.-R.; Jaunky, D. B.; Piekny, A.; Naccache, R. Intracellular ratiometric temperature sensing using fluorescent carbon dots. *Nanoscale Advances* **2019**, *1* (1), 105-113. DOI: 10.1039/C8NA00255J.
- (5) Geyer, R.; Jambeck, J. R.; Law, K. L. Production, use, and fate of all plastics ever made. *Science Advances* **2017**, *3* (7), e1700782. DOI: 10.1126/sciadv.1700782.
- (6) Zhang, K.; Hamidian, A. H.; Tubić, A.; Zhang, Y.; Fang, J. K. H.; Wu, C.; Lam, P. K. S. Understanding plastic degradation and microplastic formation in the environment: A review. *Environmental Pollution* **2021**, *274*, 116554. DOI: 10.1016/j.envpol.2021.116554.
- (7) Horton, A. A.; Walton, A.; Spurgeon, D. J.; Lahive, E.; Svendsen, C. Microplastics in freshwater and terrestrial environments: Evaluating the current understanding to identify the knowledge gaps and future research priorities. *Science of The Total Environment* **2017**, *586*, 127-141. DOI: 10.1016/j.scitotenv.2017.01.190.

(8) Fuller, S.; Gautam, A. A Procedure for Measuring Microplastics using Pressurized Fluid Extraction. *Environmental Science & Technology* **2016**, *50* (11), 5774-5780. DOI: 10.1021/acs.est.6b00816.

Chapter 8: Conclusions and summary

This chapter concludes a thorough investigation into the applications and environmental impacts of anthropogenic carbon-based nanoparticles and microparticles. We began with a comprehensive literature review of what constitutes a typical green CD synthesis. From there we concluded that the vast majority of green CD syntheses were conducted hydrothermally and typically used some form of plant matter as a carbon source. We then surveyed the physical and chemical properties of these green-synthesized CDs obtaining a distribution of the size and O:C and N:C ratios found in green-synthesized CDs. However, a key analysis of the CDs was from their optical properties. It was noted that the quantum yield of green-synthesized CDs lagged those CDs synthesized from traditional methods. Moreover, the peak emission wavelength of these CDs' fluorescence was typically in the blue-violet zone and rarely went into green colour territory. Longer wavelengths were exceedingly rare, with us unable to find any at the time that fit our strict green synthesis criteria outlined in Chapter 2. This contrasts with traditionally synthesized CDs that have a wider span of peak fluorescence wavelengths and, of course, CdTeQDs that can be tuned during synthesis to emit virtually any visible light wavelength desired. The applications in which these green synthesized CDs were used in focussed largely around bioimaging and chemical sensing, with few optoelectronic applications such as photovoltaics and light-emitting diodes compared to their traditionally synthesized counterparts. These findings collectively showed us that the current green CD synthesis literature has become too uniform and lacks diversity. Most green CD synthesis publications can be described as a plant undergoing a hydrothermal synthesis to produce CDs to be used for bioimaging or chemical sensing. While there is nothing inherently wrong with using established methods to focus research efforts on applications where CDs are known to excel, it does leave much untapped potential in the field of optoelectronics, which is also

the more likely category in which we can aim to replace quantum dots in consumer goods such as television sets. By performing more green CD syntheses using renewable refined compounds (*e.g.*, citric acid, amino acids, *etc.*), trying new synthesis routes such as microwave synthesis, and exploring new applications, we can develop a more diverse green CD synthesis literature.

A major knowledge gap observed when surveying the literature for Chapter 2 was that there is a general lack of understanding of how the choice of synthesis conditions impacts the resulting CD's chemical structure, and how that chemical structure impacts the CD's optical properties such as quantum yield. In Chapter 3, we performed a green hydrothermal synthesis using nine ratios of phenylalanine to citric acid. We found that when the concentration of phenylalanine is considerably lower than that of citric acid, the two compounds will still react in a 1:1 ratio during synthesis. This ratio increases as the phenylalanine to citric acid ratio increases. The stoichiometric ratio was found to be a 2:1 phenylalanine to citric acid ratio whereby the reactants and the resulting CD have the same N:C ratio. The CDs with the highest quantum yield were created using 95 mol% phenylalanine and 5 mol% citric acid in the solute of the precursor solution and had a quantum yield of 65 % with a peak excitation/emission of 350/413 nm. Although we were able to confirm that nitrogen doping does increase quantum yield, we also showed that this is not always the case. We found that the quantum yield of our CDs had a stronger correlation with the O:C ratio and the fraction of oxygen found in the carboxyl groups than it did with nitrogen content. We also demonstrated that Fe^{3+} were able to quench the fluorescence of our CDs via a static fluorescence quenching mechanism. Chapter 3 provides us with greater insight into how synthesis conditions, in this case reactant ratios, can have a great impact on the quantum yield of a CD by influencing its chemical structure. Moreover, the use of the stoichiometric ratio can be further investigated to maximize the efficiency with which the reactants are used during synthesis.

We have established that green synthesis methods are a viable route to making CDs. This is one aspect that makes CDs an attractive alternative to inorganic quantum dots, the other is their reduced toxicity. Here it is important to note that although carbon dots are typically less toxic than CdTeQDs, CDs are not necessarily non-toxic altogether depending on the path through which they were synthesized. Therefore, we believe it is important to make two considerations when evaluating their toxicity: 1) examine a concentration range that they are likely to be used in; 2) evaluate their toxicity in parallel with a positive control that can be used in similar applications and is hypothesized to be more toxic than the CD being assessed. In Chapter 4, we measured the developmental toxicity of NCDs, SCDs, and CdTeQDs on *Drosophila melanogaster* in the range of 10 – 100 mg/kg in food. No toxicity was observed from the NCDs or SCDs. Conversely, toxicity from the CdTeQDs was readily apparent with an EC₅₀ of 46 mg/kg affecting the ability of larvae to grow into adult flies. Moreover, the development of the larvae into flies was delayed by approximately 68 minutes for every 1 mg/kg increase in CdTeQDs in the fly food. No differences in development time were observed among NCD concentrations, however, SCDs showed a significant, but weak, negative correlation with concentration. Further sublethal toxicity was evaluated at 100 mg/kg for NCDs and SCDs and 5 mg/kg for CdTeQDs approximately corresponding to the EC₁ of CdTeQDs. No sublethal toxicity was observed in the reproductive performance of the flies, their climbing ability, larvae crawling, mass, or locomotor activity. This chapter confirmed that two types of CDs with diverse elemental compositions were considerably less toxic than CdTeQDs. Moreover, the fact that a concentration of 5 mg/kg did not result in any measurable sublethal CdTeQD toxicity, but at 46 mg/kg it already prevents half of the larvae from ever growing into adult flies, indicates how sensitive *Drosophila melanogaster* can be to changes in CdTeQD concentration.

In Chapter 5, we examined the toxicity of HDPE microplastics in *Drosophila melanogaster*. No developmental toxicity or delays in development were observed from the HDPE microplastics in the 0.1 – 10 000 mg/kg HDPE in food range. Further sublethal exposures were conducted at 100 mg/kg. In particular, the flies were exposed to HDPE microplastics over four generations and their reproductive performance was measured. No toxicity was observed throughout the multigenerational exposure. Interestingly, the eclosion fraction of the pupae raised on HDPE microplastics was 5.7 % higher than those raised on control food throughout the multigenerational exposure. While the result was statistically significant, we do acknowledge that the magnitude of this difference is low and therefore the difference may not entirely be indicative of a larger trend whereby HDPE microplastics enhance reproduction. Moreover, the HDPE microplastics had no effect on the climbing ability, larvae crawling, or mass of the organism.

To complete our investigation of the effects of chronic HDPE microplastic exposure, we shift to their impact on soil microbial community composition, soil enzyme activity, and strawberry plant growth. Up to 100 mg/kg HDPE and a mixture of pharmaceutically active compounds (*i.e.*, acetaminophen, caffeine, carbamazepine, gemfibrozil, ibuprofen, sulfamethoxazole, sulfanilamide, and triclosan), alone and together, were added to soil in pots placed outdoors over two summers. We found that the pharmaceutically active compounds were able to alter the composition of the soil microbial community but were unable to do so in the presence of HDPE microplastics. This suggests that the HDPE microplastics may play a role in inhibiting the ability of the compounds to affect the soil microbial community. Strawberry plants were grown in the soil and no effects from any of the treatments were observed on their growth. While there were occasionally significant differences in the enzyme activity at certain time points throughout the study, there was no clear trend over the entire time span of the experiment. This

work shows that HDPE microplastics may have indirect consequences on a soil ecosystem in the presence of other compounds and more work needs to be done to investigate not only HDPE toxicity alone, but its interaction with other emerging contaminants.

Bibliography of non-manuscript chapters

Listed alphabetically by author last name.¹⁻³¹ Press releases with no author appear first.¹

- (1) Environment: EU ban on hazardous substances in electrical and electronic products takes effect. European Commission: 2006.
- (2) Bano, D.; Kumar, V.; Singh, V. K.; Hasan, S. H. Green synthesis of fluorescent carbon quantum dots for the detection of mercury(ii) and glutathione. *New Journal of Chemistry* **2018**, *42* (8), 5814-5821. DOI: 10.1039/C8NJ00432C.
- (3) Boots, B.; Russell, C. W.; Green, D. S. Effects of Microplastics in Soil Ecosystems: Above and Below Ground. *Environmental Science & Technology* **2019**, *53* (19), 11496-11506. DOI: 10.1021/acs.est.9b03304.
- (4) Carr, S. A.; Liu, J.; Tesoro, A. G. Transport and fate of microplastic particles in wastewater treatment plants. *Water Research* **2016**, *91*, 174-182. DOI: 10.1016/j.watres.2016.01.002.
- (5) Corradini, F.; Meza, P.; Eguiluz, R.; Casado, F.; Huerta-Lwanga, E.; Geissen, V. Evidence of microplastic accumulation in agricultural soils from sewage sludge disposal. *Science of The Total Environment* **2019**, *671*, 411-420. DOI: 10.1016/j.scitotenv.2019.03.368.
- (6) de Souza, S. S.; Freitas, Í. N.; Gonçalves, S. d. O.; Luz, T. M. d.; Araújo, A. P. d. C.; Rajagopal, R.; Balasubramani, G.; Rahman, M. M.; Malafaia, G. Toxicity induced via ingestion of naturally-aged polystyrene microplastics by a small-sized terrestrial bird and its potential role as vectors for the dispersion of these pollutants. *Journal of Hazardous Materials* **2022**, *434*, 128814. DOI: 10.1016/j.jhazmat.2022.128814.
- (7) Fuller, S.; Gautam, A. A Procedure for Measuring Microplastics using Pressurized Fluid Extraction. *Environmental Science & Technology* **2016**, *50* (11), 5774-5780. DOI: 10.1021/acs.est.6b00816.

- (8) Geyer, R.; Jambeck, J. R.; Law, K. L. Production, use, and fate of all plastics ever made. *Science Advances* **2017**, *3* (7), e1700782. DOI: 10.1126/sciadv.1700782.
- (9) Habeebu, S. S. M.; Liu, J.; Klaassen, C. D. Cadmium-Induced Apoptosis in Mouse Liver. *Toxicology and Applied Pharmacology* **1998**, *149* (2), 203-209. DOI: 10.1006/taap.1997.8334.
- (10) Hale, R. C.; Seeley, M. E.; La Guardia, M. J.; Mai, L.; Zeng, E. Y. A Global Perspective on Microplastics. *Journal of Geophysical Research: Oceans* **2020**, *125* (1), e2018JC014719. DOI: 10.1029/2018JC014719.
- (11) Hochreiner, A.; Schwarzl, T.; Eibelhuber, M.; Heiss, W.; Springholz, G.; Kolkovsky, V.; Karczewski, G.; Wojtowicz, T. Midinfrared electroluminescence from PbTe/CdTe quantum dot light-emitting diodes. *Applied Physics Letters* **2011**, *98* (2), 021106. DOI: 10.1063/1.3531760 (accessed 2022/08/02).
- (12) Horton, A. A.; Walton, A.; Spurgeon, D. J.; Lahive, E.; Svendsen, C. Microplastics in freshwater and terrestrial environments: Evaluating the current understanding to identify the knowledge gaps and future research priorities. *Science of The Total Environment* **2017**, *586*, 127-141. DOI: 10.1016/j.scitotenv.2017.01.190.
- (13) Kumar, D.; Jain, V. K.; Shanker, G.; Srivastava, A. Citric acid production by solid state fermentation using sugarcane bagasse. *Process Biochemistry* **2003**, *38* (12), 1731-1738. DOI: 10.1016/S0032-9592(02)00252-2.
- (14) Lahive, E.; Walton, A.; Horton, A. A.; Spurgeon, D. J.; Svendsen, C. Microplastic particles reduce reproduction in the terrestrial worm *Enchytraeus crypticus* in a soil exposure. *Environmental Pollution* **2019**, *255*, 113174. DOI: 10.1016/j.envpol.2019.113174.

- (15) Li, H.; Ye, S.; Guo, J.; Wang, H.; Yan, W.; Song, J.; Qu, J. Biocompatible carbon dots with low-saturation-intensity and high-photobleaching-resistance for STED nanoscopy imaging of the nucleolus and tunneling nanotubes in living cells. *Nano Research* **2019**, *12* (12), 3075-3084. DOI: 10.1007/s12274-019-2554-x.
- (16) Liao, J.; Cheng, Z.; Zhou, L. Nitrogen-Doping Enhanced Fluorescent Carbon Dots: Green Synthesis and Their Applications for Bioimaging and Label-Free Detection of Au³⁺ Ions. *ACS Sustainable Chemistry & Engineering* **2016**, *4* (6), 3053-3061. DOI: 10.1021/acssuschemeng.6b00018.
- (17) Liu, W.; Zhang, S.; Wang, L.; Qu, C.; Zhang, C.; Hong, L.; Yuan, L.; Huang, Z.; Wang, Z.; Liu, S.; et al. CdSe Quantum Dot (QD)-Induced Morphological and Functional Impairments to Liver in Mice. *PLOS ONE* **2011**, *6* (9), e24406. DOI: 10.1371/journal.pone.0024406.
- (18) Macairan, J.-R.; Jaunky, D. B.; Piekny, A.; Naccache, R. Intracellular ratiometric temperature sensing using fluorescent carbon dots. *Nanoscale Advances* **2019**, *1* (1), 105-113. DOI: 10.1039/C8NA00255J.
- (19) Pignattelli, S.; Broccoli, A.; Renzi, M. Physiological responses of garden cress (*L. sativum*) to different types of microplastics. *Science of The Total Environment* **2020**, *727*, 138609. DOI: 10.1016/j.scitotenv.2020.138609.
- (20) Qi, Y.; Yang, X.; Pelaez, A. M.; Huerta Lwanga, E.; Beriot, N.; Gertsen, H.; Garbeva, P.; Geissen, V. Macro- and micro- plastics in soil-plant system: Effects of plastic mulch film residues on wheat (*Triticum aestivum*) growth. *Science of The Total Environment* **2018**, *645*, 1048-1056. DOI: 10.1016/j.scitotenv.2018.07.229.

- (21) Qin, X.; Lu, W.; Asiri, A. M.; Al-Youbi, A. O.; Sun, X. Green, low-cost synthesis of photoluminescent carbon dots by hydrothermal treatment of willow bark and their application as an effective photocatalyst for fabricating Au nanoparticles-reduced graphene oxide nanocomposites for glucose detection. *Catalysis Science & Technology* **2013**, 3 (4), 1027-1035. DOI: 10.1039/C2CY20635H.
- (22) Radhakrishnan, K.; Panneerselvam, P. Green synthesis of surface-passivated carbon dots from the prickly pear cactus as a fluorescent probe for the dual detection of arsenic(iii) and hypochlorite ions from drinking water. *RSC Advances* **2018**, 8 (53), 30455-30467. DOI: 10.1039/C8RA05861J.
- (23) Shen, X.; Jia, J.; Lin, Y.; Zhou, X. Enhanced performance of CdTe quantum dot sensitized solar cell via anion exchanges. *Journal of Power Sources* **2015**, 277, 215-221. DOI: 10.1016/j.jpowsour.2014.12.022.
- (24) Song, Y.; Cao, C.; Qiu, R.; Hu, J.; Liu, M.; Lu, S.; Shi, H.; Raley-Susman, K. M.; He, D. Uptake and adverse effects of polyethylene terephthalate microplastics fibers on terrestrial snails (*Achatina fulica*) after soil exposure. *Environmental Pollution* **2019**, 250, 447-455. DOI: 10.1016/j.envpol.2019.04.066.
- (25) Urbina, M. A.; Correa, F.; Aburto, F.; Ferrio, J. P. Adsorption of polyethylene microbeads and physiological effects on hydroponic maize. *Science of The Total Environment* **2020**, 741, 140216. DOI: 10.1016/j.scitotenv.2020.140216.
- (26) Wang, Y.; Wang, S.; Xu, T.; Cui, W.; Shi, X.; Xu, S. A new discovery of polystyrene microplastics toxicity: The injury difference on bladder epithelium of mice is correlated with the size of exposed particles. *Science of The Total Environment* **2022**, 821, 153413. DOI: 10.1016/j.scitotenv.2022.153413.

- (27) Wei, X.; Li, L.; Liu, J.; Yu, L.; Li, H.; Cheng, F.; Yi, X.; He, J.; Li, B. Green Synthesis of Fluorescent Carbon Dots from *Gynostemma* for Bioimaging and Antioxidant in Zebrafish. *ACS Applied Materials & Interfaces* **2019**, *11* (10), 9832-9840. DOI: 10.1021/acsami.9b00074.
- (28) Wu, X.; Liu, Y.; Yin, S.; Xiao, K.; Xiong, Q.; Bian, S.; Liang, S.; Hou, H.; Hu, J.; Yang, J. Metabolomics revealing the response of rice (*Oryza sativa* L.) exposed to polystyrene microplastics. *Environmental Pollution* **2020**, *266*, 115159. DOI: 10.1016/j.envpol.2020.115159.
- (29) Yang, S.-T.; Wang, X.; Wang, H.; Lu, F.; Luo, P. G.; Cao, L.; Meziani, M. J.; Liu, J.-H.; Liu, Y.; Chen, M.; et al. Carbon Dots as Nontoxic and High-Performance Fluorescence Imaging Agents. *The Journal of Physical Chemistry C* **2009**, *113* (42), 18110-18114. DOI: 10.1021/jp9085969.
- (30) Zhang, K.; Hamidian, A. H.; Tubić, A.; Zhang, Y.; Fang, J. K. H.; Wu, C.; Lam, P. K. S. Understanding plastic degradation and microplastic formation in the environment: A review. *Environmental Pollution* **2021**, *274*, 116554. DOI: 10.1016/j.envpol.2021.116554.
- (31) Zhou, J.; Sheng, Z.; Han, H.; Zou, M.; Li, C. Facile synthesis of fluorescent carbon dots using watermelon peel as a carbon source. *Materials Letters* **2012**, *66* (1), 222-224. DOI: 10.1016/j.matlet.2011.08.081.